



National Library
of Canada

Acquisitions and
Bibliographic Services Branch

395 Wellington Street
Ottawa, Ontario
K1A 0N4

Bibliothèque nationale
du Canada

Direction des acquisitions et
des services bibliographiques

395, rue Wellington
Ottawa (Ontario)
K1A 0N4

Notice - Avis d'importance

Notice - Avis d'importance

NOTICE

The quality of this microform is heavily dependent upon the quality of the original thesis submitted for microfilming. Every effort has been made to ensure the highest quality of reproduction possible.

If pages are missing, contact the university which granted the degree.

Some pages may have indistinct print especially if the original pages were typed with a poor typewriter ribbon or if the university sent us an inferior photocopy.

Reproduction in full or in part of this microform is governed by the Canadian Copyright Act, R.S.C. 1970, c. C-30, and subsequent amendments.

AVIS

La qualité de cette microforme dépend grandement de la qualité de la thèse soumise au microfilmage. Nous avons tout fait pour assurer une qualité supérieure de reproduction.

S'il manque des pages, veuillez communiquer avec l'université qui a conféré le grade.

La qualité d'impression de certaines pages peut laisser à désirer, surtout si les pages originales ont été dactylographiées à l'aide d'un ruban usé ou si l'université nous a fait parvenir une photocopie de qualité inférieure.

La reproduction, même partielle, de cette microforme est soumise à la Loi canadienne sur le droit d'auteur, SRC 1970, c. C-30, et ses amendements subséquents.

Canada

University of Alberta

**Fluid Flow and Heat Transfer in Rotating
Curved Channels**

by



Liqui Wang

A thesis submitted to the Faculty of Graduate Studies and Research in partial
fulfillment of the requirements for the degree of **Doctor of Philosophy**

Department of Mechanical Engineering

Edmonton, Alberta

Spring 1995



National Library
of Canada

Bibliothèque nationale
du Canada

Acquisitions and
Bibliographic Services Branch

Direction des acquisitions et
des services bibliographiques

395 Wellington Street
Ottawa, Ontario
K1A 0N4

395, rue Wellington
Ottawa (Ontario)
K1A 0N4

Number / Votre référence

Date / Votre référence

THE AUTHOR HAS GRANTED AN
IRREVOCABLE NON-EXCLUSIVE
LICENCE ALLOWING THE NATIONAL
LIBRARY OF CANADA TO
REPRODUCE, LOAN, DISTRIBUTE OR
SELL COPIES OF HIS/HER THESIS BY
ANY MEANS AND IN ANY FORM OR
FORMAT, MAKING THIS THESIS
AVAILABLE TO INTERESTED
PERSONS.

L'AUTEUR A ACCORDE UNE LICENCE
IRREVOCABLE ET NON EXCLUSIVE
PERMETTANT A LA BIBLIOTHEQUE
NATIONALE DU CANADA DE
REPRODUIRE, PRETER, DISTRIBUER
OU VENDRE DES COPIES DE SA
THESE DE QUELQUE MANIERE ET
SOUS QUELQUE FORME QUE CE SOIT
POUR METTRE DES EXEMPLAIRES DE
CETTE THESE A LA DISPOSITION DES
PERSONNE INTERESSEES.

THE AUTHOR RETAINS OWNERSHIP
OF THE COPYRIGHT IN HIS/HER
THESIS. NEITHER THE THESIS NOR
SUBSTANTIAL EXTRACTS FROM IT
MAY BE PRINTED OR OTHERWISE
REPRODUCED WITHOUT HIS/HER
PERMISSION.

L'AUTEUR CONSERVE LA PROPRIETE
DU DROIT D'AUTEUR QUI PROTEGE
SA THESE. NI LA THESE NI DES
EXTRAITS SUBSTANTIELS DE CELLE-
CI NE DOIVENT ETRE IMPRIMES OU
AUTREMENT REPRODUITS SANS SON
AUTORISATION.

ISBN 0-612-01773-7

Canada

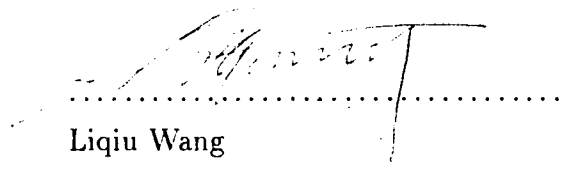
University of Alberta

Library Release Form

Name of Author: Liqiu Wang
Title of Thesis: Fluid Flow and Heat Transfer
in Rotating Curved Channels
Degree: Doctor of Philosophy
Year this Degree Granted: 1995

Permission is hereby granted to the University of Alberta Library to reproduce single copies of this thesis and to lend or sell such copies for private, scholarly, or scientific research purposes only

The author reserves all other publication and other rights in association with the copyright in the thesis, and except as hereinbefore provided, neither the thesis nor any substantial portion thereof may be printed or otherwise reproduced in any material form whatever without the author's prior written permission.



.....
Liqiu Wang

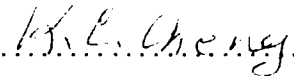
School of Mech. & Product. Eng.
Nanyang Technological University
Singapore 2263

Date : January 31, 1995

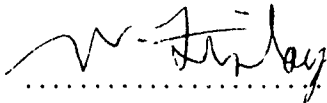
University of Alberta

Faculty of Graduate Studies and Research

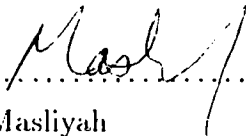
The undersigned certify that they have read, and recommend to the Faculty of Graduate Studies and Research for acceptance, a thesis entitled **Fluid Flow and Heat Transfer in Rotating Curved Channels** submitted by **Liqui Wang** in partial fulfillment of the requirements for the degree of **Doctor of Philosophy**.

.....

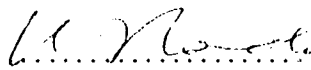
K.C. Cheng (Supervisor)

.....

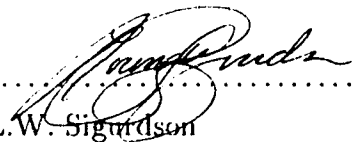
W.H. Finlay (Supervisor)

.....

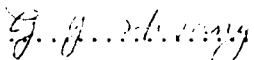
J.H. Masliyah

.....

K. Nandakumar

.....

L.W. Sigurdson

.....

G.J. Hwang (External examiner)

Date : *January 30, 1995*

To
my parents
and
all of my teachers

Abstract

Three different approaches are used to study the laminar flow transitions, instabilities, and combined free and forced convective heat transfer problems for fully developed flows in rotating, curved channels with circular and rectangular cross sections.

In particular, a three-parameter regular perturbation method and a finite volume numerical method are developed to solve the governing equations for the flow and heat transfer in channels with simultaneous curvature, rotation and heating/cooling. The perturbation method is for the circular tubes, and the numerical method for the rectangular channels. In these two parts of the work, we constrain ourselves to the steady, hydrodynamically and thermally fully developed flow under the condition of uniform wall heat flux with peripherally uniform wall temperature. We also confine ourselves to examine the symmetric flows with respect to the horizontal center plane of the channel by imposing a symmetric condition on the plane in our numerical scheme. The results cover the nature of the flow transition and its effect on the flow resistance and combined free and forced convective heat transfer for both heating and cooling cases under positive or negative rotations.

Using air as the fluid, the flows in channels with curvature and/or rotation are visualized in terms of end-view at the exit of the test sections through injecting smoke into the flows. In this part of the work, we also confine ourselves to the fully developed flows, and focus our attention on the phenomena due to the stabilizing/destabilizing influence of the curvature and/or rotation. Several test sections

are used, and the results shown here are some typical ones for the four test sections.

Acknowledgements

The author would like to thank Drs. K.C. Cheng and W.H. Finlay, his supervisors, for their guidance, patience, understanding and encouragement through the author's entire stay at University of Alberta.

The author is indebted to Drs. K. Nandakumar, D.J. Steigmann and J.H. Masliyah for their encouragement and valuable suggestions.

The author wishes to thank Mr. B.G. Faulkner, Mr. A. Yuen and Mr. A.M. Muir for their help in the experimental work. The author would also like to express his deep appreciation to his fellow graduate students in the Department of Mechanical Engineering for creating a good social and working environment.

Financial assistance in the form of fellowships and dissertation fellowships from Province of Alberta and University of Alberta is gratefully acknowledged. Financial support from NSERC through Dr. K.C. Cheng is also acknowledged.

The author owes much thanks to his family and friends. Special thanks to his wife, Lai, and his son, Su-Su, for their love, support and understanding which make it possible to see the completion of this work today.

Contents

1	Introduction	1
1.1	The Origins of Centrifugal and Coriolis Forces	1
1.2	The Conditions for the Centrifugal and Coriolis Forces to Generate Vortices	5
1.3	General Outline of the Available Approaches	7
1.4	Present Work and Organization of the Thesis	11
	References	22
2	Flow Transitions and Combined Free and Forced Convective Heat Transfer in a Rotating Curved Circular Tube–I: Perturbation So- lution	24
2.1	Introduction	25
2.2	Formulation of the problem	31
2.3	Perturbation solution	37
2.4	Concluding Remarks	54

References 57

3 Flow Transitions and Combined Free and Forced Convective Heat

Transfer in a Rotating Curved Circular Tube–II: Flow and Heat

Transfer Characteristics 64

3.1 Introduction 65

3.2 Flow Transitions in Secondary Flow 68

3.2.1 First-order approximation 68

3.2.2 Second-order approximation 72

3.3 Flow Transitions in Main Flow 75

3.4 Temperature Distribution 77

3.5 Mean Friction Factor and Nusselt Number 79

3.5.1 The friction factor 79

3.5.2 The Nusselt Number 81

3.6 The structure of solutions 81

3.7 Concluding Remarks 89

References 104

4 Flow Transitions and Combined Free and Forced Convective Heat

Transfer in Rotating Curved Channels: The Case of Positive Ro-

tation Flow 106

4.1	Introduction	108
4.2	Formulation of the Problem	113
4.3	Numerical Method of Solution	122
4.4	Results and Discussion	125
4.4.1	Flow transition and temperature distributions	129
4.4.2	The disappearance and reappearance of Dean-, Coriolis- and buoyancy-vortices	145
4.4.3	Distributions of friction factor and Nusselt number	147
4.5	Concluding Remarks	152
	References	185

**5 Flow Transitions and Combined Free and Forced Convective Heat
Transfer in Rotating Curved Channels: The Case of Negative Ro-
tation Flow** **195**

5.1	Introduction	196
5.2	Flow Transition and Temperature Distributions	198
5.2.1	The case without the effect of buoyancy force ($L_2 = 0$)	198
5.2.2	The heating case with ($L_2 > 0$)	207
5.2.3	The cooling case with ($L_2 < 0$)	211
5.3	Distributions of Friction Factor and Nusselt Number	213

5.3.1	Distributions along the upper half of the inner wall	214
5.3.2	Distributions along the upper wall	216
5.3.3	Distributions along the upper half of the outer wall	217
5.3.4	Mean friction factor and Nusselt Number	219
5.4	Concluding Remarks	220
	References	248

6 Visualization of Stabilizing/Destabilizing Flows in Channels with Curvature and/or Rotation 250

6.1	Introduction	251
6.2	Generalized Rayleigh' Theory and Mechanics of Streak Formation and Breakup in Turbulent Boundary Layers	255
6.2.1	Generalized Rayleigh' theory	255
6.2.2	Mechanics of streak formation and breakup in turbulent boundary layers	261
6.3	Brief Review of Previous Works	263
6.3.1	Dean flow	263
6.3.2	Straight channel flow with spanwise rotation	270
6.3.3	Curved channel flow with spanwise rotation	273
6.4	Experimental Apparatus and Technique	275

6.5	Results and Discussion	278
6.5.1	Visual results for $Ts-B$ at $Re = 110$	281
6.5.2	Visual results for $Ts-B$ at $Re = 452$	284
6.5.3	Visual results for $Ts-C$ at $Re = 3000$	286
6.5.4	The Dean/Coriolis vortices and flows in the region with two unstable layers	287
6.6	Concluding Remarks	295
	References	336
7	Conclusions and Recommendations	344
7.1	Perturbation Solutions	345
7.2	Numerical Solutions	349
7.3	Visualization of Flows	352
	Appendix A: Two Fundamental Theorems for the Perturbation Method	354
	Theorem 1	354
	Theorem 2	358

List of Tables

1.1	Expressions of correction terms for three typical rotating configurations	4
3.1	Distribution of the solution with L_1 and L_2	70
3.2	Physical implications of $\hat{D}c^2$, $\hat{D}\Omega$, $\hat{D}r$, L_1 and L_2	89
4.1	Variations of Dc , $ \psi _{max}$, u_{max} , t_{max} and CPU time in seconds with different grids	121
4.2	The variations of several representative properties with L_1 at $\gamma = 1$, $Dk = 100$, $\sigma = 0.02$, $Pr = 0.7$ and $L_2 = 0$ ($(fRe)_0 = 14.23$, $Nu_0 = 3.608$)	130
4.3	The variations of several representative properties with L_1 at $\gamma = 1$, $Dk = 100$, $\sigma = 0.02$, $Pr = 0.7$ and $L_2 = 5$ ($(fRe)_0 = 14.23$, $Nu_0 = 3.608$)	140
4.4	The variations of several representative properties with L_1 at $\gamma = 1$, $Dk = 100$, $\sigma = 0.02$, $Pr = 0.7$ and $L_2 = -5$ ($(fRe)_0 = 14.23$, $Nu_0 = 3.608$)	141
5.1	The variations of several representative properties with L_1 at $\gamma = 1$, $Dk = 500$, $\sigma = 0.02$, $Pr = 0.7$ and $L_2 = 0$ ($(fRe)_0 = 14.23$, $Nu_0 = 3.608$)	199
5.2	The variations of several representative properties with L_1 at $\gamma = 1$, $Dk = 500$, $\sigma = 0.02$, $Pr = 0.7$ and $L_2 = 1$ ($(fRe)_0 = 14.23$, $Nu_0 = 3.608$)	208
5.3	The variations of several representative properties with L_1 at $\gamma = 1$, $Dk = 500$, $\sigma = 0.02$, $Pr = 0.7$ and $L_2 = -1$ ($(fRe)_0 = 14.23$, $Nu_0 = 3.608$)	212
6.1	Sign of Π for the case of small gap and low rotation rate	259

6.2	Sign of Π for the case of small gap and high rotation rate	260
6.3	Test Sections	277

List of Figures

1.1	Streamwise rotating straight channels (Morris 1981)	18
1.2	Radially rotating straight channels (Morris 1981)	19
1.3	Spanwise rotating curved channels	20
2.1	Geometrical configuration and toroidal coordinate system	56
3.1	Geometrical configuration and toroidal coordinate system	93
3.2	Secondary flow patterns at $\sigma = 0.02$, $c = 60$, $Pr = 0.7$ and $L_2 = -1.0$. First column: first-order; Second column: second order	94
3.3	Secondary flow patterns at $\sigma = 0.01$, $c = 50$, $Pr = 0.7$ and $L_2 = 1.5$. First column: first-order; Second column: second order	95
3.4	The radial distance of the centre of screw motion	96
3.5	Secondary flow with one, two or three factors of curvature, rotation and heating/cooling at $\sigma = 0.01$, $c = 50$, $Pr = 0.7$, $L_1 = 15.0$ and $L_2 = 1.5$ ((a), (b), (c)-first-order terms due to single effect of curvature, rotation or heating/cooling; (d), (e), (f)- second-order terms due to single effect of curvature, rotation or heating/cooling; (g), (h), (i)- first-order terms + second-order terms due to single effect of curvature, rotation or heating/cooling; (j), (k), (l)-second-order terms due to combined effect of curvature & rotation, curvature & heating/cooling or rotation & heating/cooling; (m), (n), (o)-first-order terms + second-order terms due to combined effect of curvature & rotation, curvature & heating/cooling or rotation & heating/cooling; (p), (q), (r)-first-order terms, second-order terms or first-order terms + second-order terms due to combined effect of all three factors) . . .	97

3.6	Secondary flow with one, two or three factors of curvature, rotation and heating/cooling at $\sigma = 0.01$, $c = 100$, $Pr = 0.7$, $L_1 = 1.1$ and $L_2 = 0.5$ ((a), (b), (c)-first-order terms due to single effect of curvature, rotation or heating/cooling; (d), (e), (f)- second-order terms due to single effect of curvature, rotation or heating/cooling; (g), (h), (i)- first-order terms + second-order terms due to single effect of curvature, rotation or heating/cooling; (j), (k), (l)-second-order terms due to combined effect of curvature & rotation, curvature & heating/cooling or rotation & heating/cooling; (m), (n), (o)-first-order terms + second-order terms due to combined effect of curvature & rotation, curvature & heating/cooling or rotation & heating/cooling; (p), (q), (r)-first-order terms, second-order terms or first-order terms + second-order terms due to combined effect of all three factors) . . .	98
3.7	Main velocity distributions at $\sigma = 0.02$, $c = 60$, $Pr = 0.7$ and $L_2 = -1.0$. First column: isovels; Second column: profiles	99
3.8	Temperature distributions at $\sigma = 0.02$, $c = 60$, $Pr = 0.7$ and $L_2 = -1.0$. First column: isothermals; Second column: profiles	100
3.9	The influence of secondary flow on flow resistance	101
3.10	The influence of secondary flow on heat transfer	102
3.11	Variations of Nusselt number based on bulk temperature	103
4.1	Physical problem and rotating toroidal coordinate system	157
4.2	Variations of friction factor and Nusselt number with Dean number for a stationary square channel- a comparison of present results with available theoretical, experimental and numerical findings: (a) friction factor (Baylis 1971: experiments; Cheng & Akiyama 1970: numerical analysis; Cheng <i>et al.</i> 1976: numerical analysis; Thangam & Hur 1990: numerical analysis; Ghia & Sokhey 1977: numerical analysis; Ludwig 1951: Experiments; Mori <i>et al.</i> 1971: boundary layer correlations); (b) Nusselt number (Mori <i>et al.</i> 1971: experiments; Cheng & Akiyama 1970: numerical analysis; Cheng <i>et al.</i> 1975: numerical analysis; Mori & Uchida 1967: boundary layer correlations) .	158
4.3	Weak curvature and rotation ($Dk = 5$, $\sigma = 0.02$, $L_2 = 0$, $Re = 35$. Maxima of stream function, axial velocity and temperature are 0.0592, 0.0737 and 4.064, respectively.)	160
4.4	Flow transitions and temperature distributions at $Dk = 100$, $\sigma = 0.02$ and $L_2 = 0$ (Three values for each case are the maxima of stream function, axial velocity and temperature)	161

4.5	Axial velocity distributions at $Dk = 100, \sigma = 0.02$ and $L_2 = 0$: (a) along the vertical centreline of the channel; (b) along the horizontal centreline of the channel	164
4.6	Flow transitions and temperature distributions at $Dk = 100, \sigma = 0.02$ and $L_2 = 5$ (Three values for each case are maxima of stream function, axial velocity and temperature)	166
4.7	Axial velocity distributions at $Dk = 100, \sigma = 0.02$ and $L_2 = 5$: (a) along the vertical centreline of the channel; (b) along the horizontal centreline of the channel	168
4.8	Flow transitions and temperature distributions at $Dk = 100, \sigma = 0.02$ and $L_2 = -5$ (Three values for each case are maxima of stream function, axial velocity and temperature)	170
4.9	Axial velocity distributions at $Dk = 100, \sigma = 0.02$ and $L_2 = -5$: (a) along the vertical centreline of the channel; (b) along the horizontal centreline of the channel	174
4.10	Isopiestic contour at $Dk = 100, \sigma = 0.02, Pr = 0.7$ and $L_2 = -5$. . .	176
4.11	Disappearance and reappearance of Dean-vortices and buoyancy-vortices	177
4.12	Distributions of friction factor and Nusselt number at $Dk = 100, \sigma = 0.02$ and $L_2 = -5$ (Curves 1–12 correspond to $L_1 = 1, 1.5, 2, 3, 5, 8, 10, 11.5, 12, 13.5, 15$ and 70 . Curve 0 is for the case of $L_1 = L_2 = 0$.) (a) along the inner wall; (b) along the upper wall; (c) along the outer wall	178
4.13	Mean friction factor and Nusselt number at $Dk = 100, \sigma = 0.02$ and $L_2 = -5$	184
5.1	Flow transitions and temperature distributions at $\gamma = 1, Dk = 500, \sigma = 0.02, Pr = 0.7$ and $L_2 = 0$ (Three values for each case are the maxima of the stream function, main velocity and temperature)	222
5.2	Main velocity distributions at $\gamma = 1, Dk = 500, \sigma = 0.02, Pr = 0.7$ and $L_2 = 0$: (a) along the vertical centreline of the channel; (b) along the horizontal centreline of the channel	226
5.3	Isopiestic contour at $\gamma = 1, Dk = 500, \sigma = 0.02, Pr = 0.7, L_1 = -3.5$ and $L_2 = 0$	228
5.4	Flow transitions and temperature distributions at $\gamma = 1, Dk = 500, \sigma = 0.02, Pr = 0.7$ and $L_2 = 1$. (Three values for each case are the maxima of the stream function, main velocity and temperature)	229
5.5	Main velocity distributions at $\gamma = 1, Dk = 500, \sigma = 0.02, Pr = 0.7$ and $L_2 = 1$: (a) along the vertical centreline of the channel; (b) along the horizontal centreline of the channel	233

5.6	Isopiestic contour at $\gamma = 1, Dk = 500, \sigma = 0.02, Pr = 0.7, L_1 = -4.0$ and $L_2 = 1$	235
5.7	Flow transitions and temperature distributions at $\gamma = 1, Dk = 500, \sigma =$ $0.02, Pr = 0.7$ and $L_2 = -1$. (Three values for each case are the max- ima of the stream function, main velocity and temperature)	236
5.8	Main velocity distributions at $\gamma = 1, Dk = 500, \sigma = 0.02, Pr = 0.7$ and $L_2 = -1$: (a) along the vertical centreline of the channel; (b) along the horizontal centreline of the channel	238
5.9	Isopiestic contour at $\gamma = 1, Dk = 500, \sigma = 0.02, Pr = 0.7, L_1 = -3.0$ and $L_2 = -1$	240
5.10	Distributions of friction factor and Nusselt number at $\gamma = 1, Dk =$ $500, \sigma = 0.02, Pr = 0.7$ and $L_2 = 1$ (Curves 1–12 correspond to $L_1 =$ $-0.5, -1.0, -1.5, -1.65, -1.75, -2.0, -2.1, -2.25, -2.3, -2.5, -3.0$ and -4.0 . Curve 0 is for the case of $L_1 = L_2 = 0$.) (a) along the inner wall; (b) along the upper wall; (c) along the outer wall	241
5.11	Mean friction factor and Nusselt number at $\gamma = 1, Dk = 500, \sigma =$ $0.02, Pr = 0.7$ and $L_2 = 1$	247
6.1	Sketch relating to displaced particle discussion	298
6.2	Stable/unstable regions for the case of small gap with low rotation rate	299
6.3	Stable/unstable regions for the case of small gap with high rotation rate	300
6.4	Sketch of flow model in wall layers of fully developed turbulent bound- ary layer (Kline & Runstadler 1959)	301
6.5	The mechanics of streak formation (Kline <i>et. al.</i> 1967)	302
6.6	The mechanics of streak breakup (Kline <i>et. al.</i> 1967)	303
6.7	Schematic diagram of experimental apparatus	304
6.8	Four typical test sections	305
6.9	Variations of flows with Ro	309
6.10	Variations of flows with Ro and time at $Re = 110$ for $Ts-B$	310
6.11	Variations of flows with Ro and time at $Re = 452$ for $Ts-B$	318
6.12	Variations of flows with Ro and time at $Re = 3000$ for $Ts-C$	326
6.13	Symmetric Coriolis vortices for $Ts-D$	327
6.14	Symmetric Coriolis vortices at $Re = 193.6, Ro = -1.18$ for $Ts-B$) . . .	328
6.15	Radial oscillating Coriolis vortices	329

6.16	Spanwise oscillating Dean/Coriolis vortices	330
6.17	Simultaneous spanwise and radial oscillating Dean/Coriolis vortices	331
6.18	Twisting Dean/Coriolis vortices	332
6.19	Small vortex pairs for $Ts-B$	333
6.20	Complex oscillating Dean/Coriolis vortices for $Ts-B$	334
6.21	Flows in the region with two unstable layers for $Ts-A$	335

Nomenclature

a	radius of tube, width of rectangular channel
b	height of rectangular channel
a_0	acceleration of the origin
a_i	acceleration
c	pseudo Reynolds number
c_1	axial pressure gradient
c_2	axial temperature gradient
c^l, c^h	constants
c_1^l, c_1^h	constants
c_p	specific heat
d	diameter
De	Dean number, Eq.(3.15)
$\hat{D}e$	modified Dean number, Eq.(3.20)
De_c	critical Dean number
d_h	hydrodynamic diameter
Dk	modified Dean number, $\frac{\sigma d_h W_1}{4\nu}$
D_Ω	dynamical parameter, Eq.(3.15)
\hat{D}_Ω	modified D_Ω , Eq.(3.20)
D_r	dynamical parameter, Eq.(3.15)
\hat{D}_r	modified D_r , Eq.(3.20)

$\{\mathbf{e}_x, \mathbf{e}_y, \mathbf{e}_z\}$	orthonormal basis
f	stream function of secondary flow
f_s	mean friction factor for a stationary straight tube
h	heat transfer coefficient
I_n, \hat{I}_n	integrals
k^{-1}	radius of curvature
l	length
L_1	parameter defined by $3Rc_\Omega/2\sigma c$
L_2	parameter defined by $Ra_\Omega/16\sigma c$
n	rotation speed (<i>rpm</i>)
Nu	mean Nusselt number
Nu_0	mean Nusselt number for a stationary straight tube
\mathbf{r}	position vector
r, R	coordinates
Ra	Rayleigh number
Ra_Ω	rotational Rayleigh number, $\frac{Pr\beta\Omega^2 c_2 a^4 R_c}{\nu^2}$
R_c	curvature radius
Re	Reynolds number
Re_c	critical Reynolds number
Re_Ω	rotational Reynolds number, $\frac{4\Omega a^2}{\nu}$
$\hat{R}e$	modified Reynolds number, Eq.(3.20)
Ro	ratio of the Coriolis force to the inertia force

$o'z'$	axis of curvature and rotation
p	fluid pressure
p'	pseudo pressure
$P_n(x)$	polynomial
Pr	Prandtl number
Q	flow rate, Eq.(3.3)
Q_1	modified flow rate, Eq.(3.4)
Q_s	flow rate through a stationary straight tube
q_w	wall heat flux
t	temperature of fluid, time
t_w	wall temperature
T	temperature
T_0	reference temperature
T_b	bulk mean temperature
T_w	temperature difference ($t_w - t$)
u, v, w	non-dimensional velocity components
U, V, W	velocity components
\mathbf{v}	velocity vector
w	non-dimensional main velocity
W_1	$d_h^2 c_1 / \mu$
w_{ijk}	expansion coefficient for w
W_m	average main velocity

\vec{W}	velocity
x, y	non-dimensional coordinates
x_i	variable

Greek Symbols

α	thermal diffusivity, constant, small positive number
α_i	constant
β	coefficient of thermal expansion
β^k, β^l	constants
β_i^k, β_i^l	constants
δ	boundary layer thickness, arbitrary small positive number
η	non-dimensional temperature
η_e	extreme value of η
η_{ijk}	expansion coefficient for η
η_{ijk}^{lm}	parameter free expansion coefficients for η
η_m	mean temperature across the tube
γ	aspect ratio
Γ	c/Re
λ	conductivity of fluid
\in	in
Δt	time period

ΔT	$Pr d_h c_2$
ν	kinematic viscosity
ω	angular velocity vector
Ω	angular velocity
ϕ	non-dimensional stream function
ϕ_{ijk}	expansion coefficient for ϕ
ϕ_{ijk}^{lm}	parameter free expansion coefficients for ϕ
Π	defined by Eq.(6.8)
ρ	density of fluid
ρ_0	density at T_0
ρ_w	density of fluid based on wall temperature
σ	curvature ratio
θ	polar coordinate
Θ	defined by Eq.(6.7)
$\varepsilon_1, \varepsilon_2, \varepsilon_3$	$\sigma, Rc_\Omega, Ra_\Omega$
φ	coordinate
ξ	vorticity

Chapter 1

Introduction

1.1 The Origins of Centrifugal and Coriolis Forces

Fluid flow and heat transfer in rotating curved channels arise in various practical processes. Examples are: cooling systems for conductors of electric generators and generator motors for pumped-storage stations (Ito & Motai 1974, Miyazaki 1971 & 1973, Morris 1981), particle separation (Lennartz *et al.* 1987, Papanu *et al.* 1986, Hoover *et al.* 1984, Stöber & Flachshart 1969, Hochrainer 1971 and Kotrappa & Light 1972), heat exchangers (Qiu *et al.* 1988 and 1990) and physiological field (Ito & Motai 1974, Berman 1985 and Pedley 1980). Studies on the hydrodynamics and transport phenomena in the rotating curved channels are, therefore, not only of considerable theoretical interest, but also of great practical importance.

The goal of hydrodynamics is to describe and predict the motion of a body of

fluid under applied forces. The so-called Newton's second law of motion relates the resultant force acting on the body to the change in momentum experienced by the body. However for the second law to be valid it is necessary to ensure that the motion concerned is referred to an inertial frame of reference, a reference system permitting uniform motion of the body to be specified when there is no resultant force acting. This requires a reference frame either at rest in space or moving with uniform velocity, and can be understood by noting that the motion of the body is reference frame dependent but the applied forces are not.

If the motion of a fluid particle moving inside a stationary channel is required, a convenient reference frame is one fixed to the channel itself. Since the channel is stationary, the second law of motion can be employed to relate the force to the motion of the particle. If the channel is rotating and/or acceleratively translating, however, a reference frame fixed to the channel is no longer inertial any more.

In practical engineering, it is the relative motion between bodies that determines the performances such as friction resistance and heat transfer characteristics. Thus it is often more convenient to choose a non-inertial frame moving with the channel although an inertial frame of reference can always be defined in principle. For these cases, correction terms must be applied to the usual mathematical description of the Newton's second law of motion to sustain its validity. In other words, the relation is required between accelerations relative to an inertial system and a non-inertial system for a given motion.

A kinetic analysis of the motion establishes such a relation as (Morris 1981)

$$\mathbf{a}_i = \underbrace{\frac{\partial^2 \mathbf{r}}{\partial t^2}}_1 + \underbrace{2(\boldsymbol{\omega} \times \frac{\partial \mathbf{r}}{\partial t})}_2 + \underbrace{\boldsymbol{\omega} \times (\boldsymbol{\omega} \times \mathbf{r})}_3 + \underbrace{\frac{\partial \boldsymbol{\omega}}{\partial t} \times \mathbf{r}}_4 + \mathbf{a}_0. \quad (1.1)$$

Here \mathbf{a}_i is the acceleration with respect to the inertial frame of reference, $\boldsymbol{\omega}$ the angular velocity vector of the non-inertial frame of reference, t the time, and \mathbf{a}_0 is acceleration of the origin of the non-inertial frame of reference with respect to the inertial frame of reference. Since \mathbf{r} is position vector in the non-inertial system, the first term is acceleration with respect to the non-inertial frame of reference.

Expression (1.1) shows that three correction terms involving $\boldsymbol{\omega}$ are required to determine \mathbf{a}_i . Also required is a fourth term \mathbf{a}_0 if the origin of the non-inertial frame is not fixed. The second and the third terms are known as the Coriolis acceleration and the centripetal acceleration, respectively. They appear whenever motion is referred to a reference frame which is itself rotating. If the reference is rotating with non-uniform angular velocity, an additional term (the fourth term in (1.1)) is then required to account for the angular acceleration of the frame. The detailed expressions of these correction terms are listed in Table 1.1 for three typical rotating configurations. Two of them with straight channels have been derived by Morris (1981), but with some errors, resulting in some incorrect conclusions. For each configuration, two typical rotating reference frames are used. They are convenient to be used for the circular and rectangular channels, respectively.

These additional terms of acceleration, with their force implications, will significantly affect the flow behaviour in a rotating channel. In particular, they may

Table 1.1: Expressions of correction terms for three typical rotating configurations

Configurations	streamwise rotating straight channels		radial rotating straight channels		spanwise rotating curved channels	
	Fig.1.1(a)	Fig.1.1(b)	Fig.1.2(a)	Fig.1.2(b)	Fig.1.3(a)	Fig.1.3
coordinate	Cartesian	cylindrical polar	Cartesian	cylindrical polar	Toroidal rectangular	toroidal polar
\mathbf{r}	$ze_x + ye_y + ze_z$	$r\mathbf{e}_r + z\mathbf{e}_z$	$ze_x + ye_y + ze_z$	$r\mathbf{e}_r + z\mathbf{e}_z$	$ze_x + ye_y$	$(R_c \sin\varphi + r)\mathbf{e}_r + R_c \cos\varphi \mathbf{e}_\theta$
$\boldsymbol{\omega}$	$\Omega \mathbf{e}_z$	$\Omega \mathbf{e}_z$	$\Omega \mathbf{e}_y$	$\Omega(\cos\varphi_r - \sin\varphi_\theta) \mathbf{e}_z$	$-\Omega \mathbf{e}_y$	$\Omega(\cos\varphi_r - \sin\varphi_\theta)$
\mathbf{a}_0	$-\Omega^2 H \mathbf{e}_z$	$-\Omega^2 H(\cos\varphi_r - \sin\varphi_\theta)$	$-\Omega^2 H \mathbf{e}_z$	$-\Omega^2 H \mathbf{e}_z$	0	0
$\frac{\partial^2 \mathbf{r}}{\partial t^2}$	$\frac{D_u^2}{Dt} \mathbf{e}_x + \frac{D_v^2}{Dt} \mathbf{e}_y + \frac{D_w^2}{Dt} \mathbf{e}_z$	$(\frac{D_u}{Dt} - \frac{v^2}{r}) \mathbf{e}_r + (\frac{D_v}{Dt} + \frac{uv}{r}) \mathbf{e}_\theta + \frac{D_w}{Dt} \mathbf{e}_z$	$\frac{D_u^2}{Dt} \mathbf{e}_x + \frac{D_v^2}{Dt} \mathbf{e}_y + \frac{D_w^2}{Dt} \mathbf{e}_z$	$(\frac{D_u}{Dt} - \frac{v^2}{r}) \mathbf{e}_r + (\frac{D_v}{Dt} + \frac{uv}{r}) \mathbf{e}_\theta + \frac{D_w}{Dt} \mathbf{e}_z$	$(\frac{D_u}{Dt} - \frac{v^2}{r} - \frac{w^2 \sin\varphi}{R_c + r \sin\varphi}) \mathbf{e}_r + (\frac{D_v}{Dt} + \frac{uv}{r} - \frac{w^2 \cos\varphi}{R_c + r \sin\varphi}) \mathbf{e}_\theta + (\frac{D_w}{Dt} + \frac{uw \sin\varphi}{R_c + r \sin\varphi} + \frac{uw \cos\varphi}{R_c + r \sin\varphi}) \mathbf{e}_\theta$	
$2\boldsymbol{\omega} \times \frac{\partial \mathbf{r}}{\partial t}$	$-2\Omega u \mathbf{e}_z + 2\Omega v \mathbf{e}_y$	$-2\Omega u \mathbf{e}_r + 2\Omega v \mathbf{e}_\theta$	$2\Omega u \mathbf{e}_z - 2\Omega v \mathbf{e}_z$	$-2\Omega u(\sin\varphi_r + \cos\varphi_\theta) + 2\Omega(v \cos\theta + u \sin\theta) \mathbf{e}_z$	$-2\Omega(u \mathbf{e}_r - v \mathbf{e}_\theta)$	$-2\Omega w(\sin\varphi_r + \cos\varphi_\theta) + 2\Omega(u \sin\varphi + v \cos\varphi) \mathbf{e}_\theta$
$\boldsymbol{\omega} \times (\boldsymbol{\omega} \times \mathbf{r})$	$-\omega^2(z \mathbf{e}_x + y \mathbf{e}_y)$	$-\omega^2 r \mathbf{e}_r$	$-\omega^2(z \mathbf{e}_x + z \mathbf{e}_z)$	$-\omega^2 r \sin\varphi (\mathbf{e}_r + \cos\varphi \mathbf{e}_\theta)$	$-\omega^2 z \mathbf{e}_z$	$-\omega^2(R_c + r \sin\varphi)(\sin\varphi_r + \cos\varphi_\theta)$
$\frac{\partial \boldsymbol{\omega}}{\partial t} \times \mathbf{r}$	$-\dot{\Omega}(y \mathbf{e}_x - z \mathbf{e}_y)$	$r \dot{\Omega} \mathbf{e}_\theta$	$\dot{\Omega}(z \mathbf{e}_x - r \mathbf{e}_z)$	$-\dot{\Omega}_z(\sin\theta \mathbf{e}_r + \cos\theta \mathbf{e}_\theta)$	$\dot{\Omega} r \mathbf{e}_\theta$	$\dot{\Omega}(R_c + r \sin\varphi) \mathbf{e}_\theta$

generate vortices in the flow under certain conditions. Since the main objective of the present study is to investigate the effects of the centrifugal and Coriolis forces on the flow and heat transfer, we derive these conditions in the next section.

1.2 The Conditions for the Centrifugal and Coriolis Forces to Generate Vortices

Vorticity is a measure of the angular velocity of a fluid particle at a point in the flow. Mathematically, it is defined as

$$\zeta = \nabla \times \mathbf{v} \quad (1.2)$$

with ζ and \mathbf{v} as the vorticity and velocity, respectively. The equation governing the generation, convection and diffusion of the vorticity is called the vorticity equation which can be obtained by taking the curl of the momentum equation.

To highlight the salient features, assume that the flow is laminar, the reference frame is Cartesian and rotates with uniform angular velocity, and no body forces act on the fluid. In many situations of practical importance (e.g. examples in Table 1.1), the centripetal and the translational acceleration of the origin can be combined to form a conservative field which is described through a scalar function ϕ such that

$$\nabla\phi = \boldsymbol{\omega} \times (\boldsymbol{\omega} \times \mathbf{r}) + \mathbf{a}_0 \quad (1.3)$$

under which circumstances, the momentum equations for a motion of the fluid re-

ferred to a translating and rotating reference frame are (Morris 1981)

$$\frac{D\mathbf{v}}{Dt} + 2\boldsymbol{\omega} \times \mathbf{v} = -\nabla\left(\frac{p}{\rho} + \phi\right) + \nu\nabla^2\mathbf{v} \quad (1.4)$$

for an isothermal flow and

$$\frac{D\mathbf{v}}{Dt} + 2\boldsymbol{\omega} \times \mathbf{v} = -\frac{1}{\rho_0}\nabla p' + \beta(T - T_0)\nabla\phi + \nu\nabla^2\mathbf{v} + \frac{\nu}{3}\nabla(\text{div}\mathbf{v}) \quad (1.5)$$

for a non-isothermal flow. Here T_0 and ρ_0 are the reference temperature and the density at $T = T_0$, β the thermal expansion coefficient, and p' is the deviation of the pressure field from the hydrostatic pressure field. In deriving Eq.(1.5), the usual Boussinesq approximation has been used which states that the density variation need be included only in the effective body force term. This is important since to a first approximation, the temperature-density variation need not be included in the Coriolis term.

By taking the curl of Eqs.(1.4) and (1.5) and enforcing the continuity equation, we obtain the vorticity equations, measured relative to the translating and rotating reference frame, as

$$\frac{D\boldsymbol{\zeta}}{Dt} = (\boldsymbol{\zeta} \cdot \nabla)\mathbf{v} + \nu\nabla^2\boldsymbol{\zeta} + 2(\boldsymbol{\omega} \cdot \nabla)\mathbf{v} \quad (1.6)$$

for an isothermal flow and

$$\frac{D\boldsymbol{\zeta}}{Dt} = (\boldsymbol{\zeta} \cdot \nabla)\mathbf{v} + \nu\nabla^2\boldsymbol{\zeta} + 2(\boldsymbol{\omega} \cdot \nabla)\mathbf{v} + \nabla \times \beta(T - T_0)\nabla\phi \quad (1.7)$$

for a non-isothermal flow.

These show the following important results as discussed by Morris (1981). The centrifugal and translational acceleration terms vanish from the vorticity equation

for the isothermal flows. These terms are clearly purely hydrostatic for this case, analogous to the earth's gravitational field. A term having its origin in the Coriolis acceleration does, however, appear in the vorticity equation (Eq.(1.6)). This implies an additional generation term tending to produce vorticity or relative rotation of the flow provided the term $(\boldsymbol{\omega} \cdot \nabla)\mathbf{v}$ is non-zero.

For the non-isothermal flows, the Coriolis force generates vorticity as that in the isothermal flows provided $(\boldsymbol{\omega} \cdot \nabla)\mathbf{v}$ is non-zero and temperature-induced density variations do not directly affect this term to a first order approximation. The conservative effective body force, describing through the scalar function ϕ , can create vorticity through an interaction between the temperature and density. Therefore, the non-isothermal flows will be simultaneously influenced by the Coriolis and centrifugal-type buoyancy forces. We will examine these effects for several flow geometries by three different approaches in the present work. Before the detailed descriptions of the present work, it appears appropriate to briefly summarize the available approaches to study these effects.

1.3 General Outline of the Available Approaches

In this section a general outline of the approaches, theoretical, numerical and experimental, employed in the past to study the effects of the centrifugal and/or Coriolis forces on the fluid flows and heat transfer will be described. A detailed account for each particular work will be presented in the section dealing with the

relevant problems.

The presence of the centrifugal and Coriolis forces results in a complex mechanism of flow and heat transfer in a rotating channel. This makes the theoretical analysis difficult. The rotation of the system also presents a complex system design for the experimental measurements.

In the theoretical field, work has been centred mainly on employing parameter perturbation methods and boundary layer integral-type methods to solve the equations governing the flow and heat transfer in stationary curved channels, streamwise and radially rotating straight channels.

The parameter perturbation method used in the past usually employs a power sequence of one parameter as the expansion functions. The theoretical basis about the convergence remains to be established in the future. As well, the solution with finite terms is usually believed to be valid only for a limited range of the perturbation parameters with the small values. If applied beyond the range of applicability, it fails to converge and gives erroneous results. Recently, the method of extended perturbation series was developed with an attempt to remove this limitation by combining analysis and numerical computation.

The method consists of three steps: First, the set of perturbation equations is programmed for solution on a computer such that a large number of terms can be obtained. Second, the coefficients of the series are utilized to identify the location and nature of singularities limiting the range of applicability of the series. With this

knowledge, the final step is to recast the perturbation solution series using one or a combination of devices such as the Euler transformation, Shanks transformation, Padé approximants, extraction of singularities, and series reversion. The improved series generally has better accuracy and a wide range of applicability than the original series. However, this techniques has not been extended to analyze the multiple series.

The boundary layer integral-type method may be regarded as one kind of motion decomposition based on flow domains. It recognizes the different nature of flow in different flow regions and considers the whole flow domain to be consisted of two regions. In a core region, the flow is nearly inviscid and only pressure, centrifugal and Coriolis forces are considered to be dominant. The viscous forces are considered to be important in a thin region close to the walls which is called a boundary layer. Momentum and heat balances are usually made in the boundary layer in their integral forms. Careful attention is required to obtain the proper matching conditions between the two regions. This method is generally valid only for the cases with very high rotation speed.

In the past, the applications of these two theoretical methods started by solving the equations for laminar flow without heat transfer and were gradually developed to include the effects of heat transfer and turbulence. From these works, certain formulae have been proposed to estimate the effects of rotation on the flow and heat transfer.

The theoretical methods are valid for the limiting cases of low and high rotation speeds. Numerical computation is, however, more appropriate for calculation of moderate rotation rate. The numerical approaches can be further classified as series truncation methods, finite difference methods, finite-volume methods, finite element methods and spectral methods (one kind of coordinate perturbation methods) etc. (Nandakumar & Masliyah 1986). Most of the numerical works on the topic, to our knowledge, have been confined to laminar and fully-developed flows.

On the experimental side, works have been done mostly for the case of straight channels radially rotating without heat transfer. This is because of the similarity between this situation and the flow in an impeller of a centrifugal compressor. Therefore, most of the experimental data are concerned with the dependence of the flow resistance to the relevant flow parameters. Very few experimental data exist for the heat transfer when the channel is rotated. These experimental data are all for particular cases, limited in number in each case, and not possible to be compared between them beyond an estimate of one order of magnitude. Furthermore, they are not sufficient to check thoroughly the general validity or accuracy of a proposed prediction procedure.

The flow and heat transfer in the rotating systems can be investigated experimentally either through the direct measurements or through some kinds of analogy theories. The later includes the mass transfer - heat transfer analogy, stratified flow - rotating flow analogy and electromagnetic flow - rotating flow analogy. The exper-

iments by the direct measurements and mass transfer - heat transfer analogy must be carried out in a rotating system, which presents difficult problems in designing and running the experimental apparatus. The stratified flow - rotating flow analogy and electromagnetic flow - rotating flow analogy allow one to observe the effects of the centrifugal and the Coriolis forces on the flows and heat transfer in a stationary analogous system, and to examine the flows and heat transfer under the isolated centrifugal force or Coriolis force. They are worthy to be developed in the future.

1.4 Present Work and Organization of the Thesis

In the present work, three different approaches, namely, three-parameter perturbation, finite-volume numerical simulation and experimental visualization of flows, are developed to study the laminar flow transitions, instabilities, and combined free and forced convective heat transfer in rotating curved channels with circular and rectangular cross sections. The three parts are relatively independent and emphasize different aspects of the flow and heat transfer in rotating curved channels.

Perturbation analysis is to obtain an approximate analytical solution of velocity and temperature fields in a curved circular tube rotating spanwisely with an constant angular velocity and to extend the previous analyses to the range where centrifugal, Coriolis and buoyancy forces just neutralize each other. The analytical solution allows one to analyze the structure of the solution and bring out the physical parameters, resulting a better understanding of the physical nature. The

finite-volume numerical analysis is to reveal the laminar flow transitions of the secondary flow and the main flow in a curved rectangular channel rotating spanwisely with an constant angular velocity for a wide range of the characteristic parameters, and to investigate the effects of the flow transitions on temperature distribution, flow resistance and heat transfer characteristics. In these two parts of the work, three factors, namely, curvature, rotation and heating/cooling, are all included in the analysis.

The motivation of the flow visualization comes from the desire to investigate the stabilizing/destabilizing effects of the curvature and rotation on the channels flows. In particular, this experiment presents the visual results of the stabilizing/destabilizing flows in channels with curvature and/or rotation which are believed to be useful for the modeling of the flows.

The thesis consists of seven chapters of which the present one is the Introduction.

In Chapter 1, we present the origins of the centrifugal and Coriolis forces and the conditions for the centrifugal and Coriolis forces to generate vortices in flows relative to a non-inertial frame of reference. It also briefly summarizes the present work and the available approaches (analytical, numerical and experimental) for studying the effects of the centrifugal and Coriolis forces on the flows and heat transfer in rotating/curved channels.

In Chapter 2, we show the existence of a unique, uniformly convergent polynomial for any continuous function of one or more variables which can be used to

approximate the function. Assuming that the stream function of secondary flow, the pressure driven main flow and the temperature are continuous on the curvature ratio, the rotational Reynolds number and the rotational Rayleigh number, a systematic three-parameter, regular perturbation method is developed to study the laminar flow transitions and combined free and forced convective heat transfer in a rotating curved circular tube.

The specific problem considered is the curved tube rotating at a uniform angular velocity about the axis through the centre of the curvature. A full second-order perturbation solution is obtained for the full nonlinear coupled governing equations under the conditions that the flow and temperature fields are fully developed, and the wall heat flux is uniform with peripherally uniform wall temperature. The solution covers both heating and cooling cases, with the rotation of the tube either in the same direction or opposite to the main flow imposed by an axial pressure gradient. By excluding the effect of any one or two of the three factors (curvature, rotation and heating/cooling), the solution reduces to each of the six special problems such as the classical Dean problem and mixed convection problem.

In Chapter 3, we analyze the flow and heat transfer characteristics based on the perturbation solution presented in Chapter 2. The results cover both the nature of flow transitions and the effects of these transitions on temperature distribution, friction factor and Nusselt number. When the rotation is in the same direction as the main flow imposed by a pressure gradient and the fluid is heated, the flow and

heat transfer remain similar to those observed in stationary curved tubes, radially rotating straight tubes or mixed convection in stationary straight tubes. There are, however, quantitative changes due to the combined effects of the centrifugal, Coriolis and buoyancy forces. A more complex behaviour is possible when the rotation is opposite to the flow due to the pressure gradient or when the fluid is cooled. In particular, the inward Coriolis force and/or buoyancy force may cause the direction of the secondary flow to reverse. The flow reversal occurs by passing through a four-cell vortex flow region where overall, the centrifugal, Coriolis and buoyancy force just neutralize each other.

In Chapter 4, we study the flow and heat transfer in the rectangular channels with simultaneous effects of curvature, rotation and heating/cooling. The governing equations are solved numerically by using a finite-volume method. The results contain both the nature of the flow transition and effect of flow transition on the distributions of the friction factor and Nusselt number in a square channel. A one-pair vortex flow, with an ageostrophic and virtually inviscid core, is uncovered between a viscous force dominated one-pair vortex flow and two-pair vortex flow with the presence of the Dean-, Coriolis- or buoyancy-vortices. Different two kinds of one-pair vortex flow exist after the disappearance of the Coriolis-vortices upon increasing the Coriolis force sufficiently. When the fluid is cooled, the inward buoyancy forces cause the buoyancy- vortices (due to the buoyancy force instability) to appear in the low pressure side (rather than the usual high pressure side of the channel), and the

direction of the secondary flow reverses by overcoming the outward centrifugal and Coriolis forces in the plane of the cross section. The flow reversal occurs by passing through a multi-pair vortex flow region where overall, the effect of the buoyancy force just neutralizes those of the centrifugal and Coriolis forces. A two-pair vortex flow may result from two different mechanisms. One is associated with a break-up of the Ekman-type vortices owing to the centrifugal, Coriolis or buoyancy force instabilities. Another, with a smaller size of the resulting second pair of vortices, is characterized by a merging-together of the vortices. The disappearance of the Coriolis- or buoyancy-vortices is observed upon increasing the Coriolis or buoyancy forces. No such phenomena are observed for the Dean- vortices. Furthermore, the reappearance of the buoyancy-vortices, upon increasing the buoyancy force further, is also found in this study.

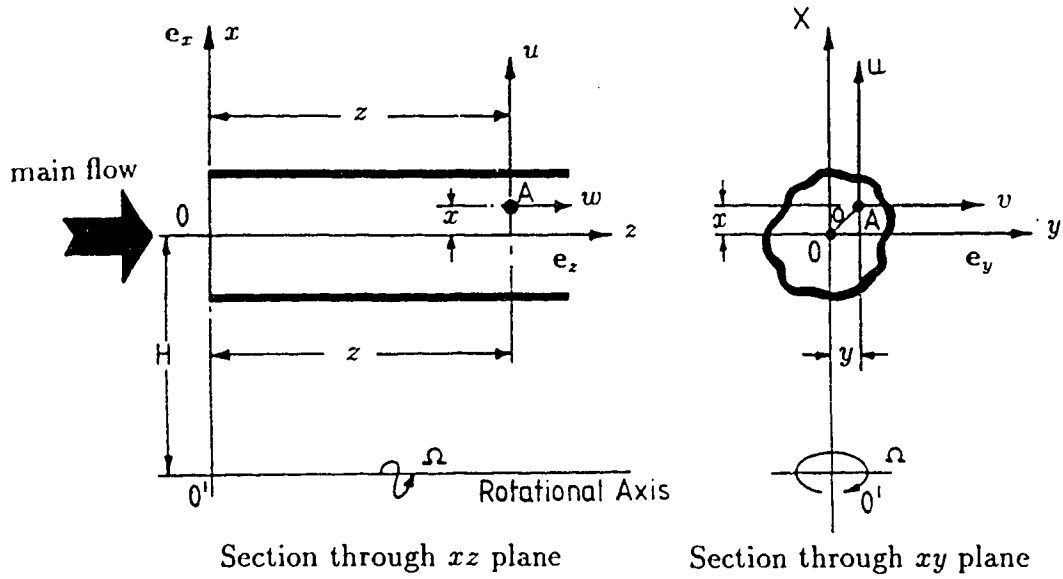
In Chapter 5, the finite-volume scheme developed in Chapter 4 is used to study the laminar flow transitions and combined free and forced convective heat transfer in a rotating curved channel for the case of negative rotation at relatively high Dean number. The results cover both the nature of the flow transition and the effects on temperature distribution, friction resistance and heat transfer between fluid and wall. Several phenomena shown in Chapter 4 are confirmed. As well, several new phenomena are revealed. When the rotation is in the negative direction, the inward Coriolis forces cause the Coriolis vortices (due to the Coriolis force instability) to appear near the inner wall of the channel, and the direction of the secondary flow

to reverse by overcoming the outward centrifugal and/or buoyancy forces. When the Coriolis vortices appear near the inner wall, the inner side of the channel becomes the high pressure side. The flow reversal (due to negative Coriolis forces) occurs by passing through a multi-pair vortex flow region where overall, the Coriolis, centrifugal and buoyancy forces just neutralize each other. The merging-vortices found in Chapter 4 appear to exist only when the buoyancy forces are taken into consideration.

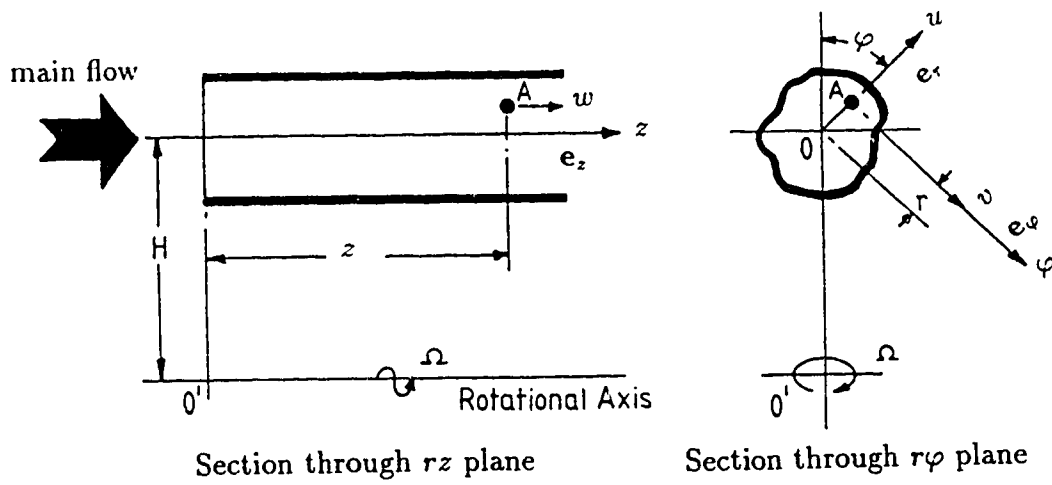
In Chapter 6, experiments on visualization of stabilizing/destabilizing flows in channels with curvature and/or rotation are described. Several test sections have been used, and the results shown here are some typical ones for four test sections. Although the main objective is to draw some general features about the stabilizing/destabilizing flows from the visualization experiments, a generalized Rayleigh criterion is formulated about the primary instability of flows in rotating curved channels to help the understanding of some experimental results. We have observed several stabilizing/destabilizing related phenomena in the channel flows with curvature and/or rotation: (1) For large values of $|Ro|$, both primary and secondary instabilities exhibit a symmetry about the directions of rotation. As well, the flows at large $|Ro|$ are found to be controlled by the secondary instabilities rather than the primary instability. In particular, the secondary instabilities lead the flow at large $|Ro|$ to be unsteady and turbulent like the *bursting* flow in the turbulent boundary layers. This produces the low Reynolds number turbulent flows. (2)

When the curved channels rotate with slow negative speed, two potentially unstable regions, alternated by two stable regions, exist in the cross-plane, resulting a complicated vortex flow. (3) The Dean/Coriolis vortices can also exist on the unstable side in the relaminarization process of the flow from turbulent to laminar. In particular, their formation in the flows with high Reynolds number annihilates the turbulence, and leads to a high Reynolds number laminar flow. (4) Secondary instabilities of the Dean/Coriolis vortices lead the vortices to oscillate in various forms even in the streamwise fully developed flow regions. We have observed several oscillating modes including one with mostly radial motion, one with mostly spanwise motion, one with significant simultaneous radial and spanwise motion, and one with rocking motion. In addition, the oscillating modes are also present with motion so complicated that they are difficult to describe from the flow visualization results. (5) It is possible to completely destroy the Dean vortices by rotation and to give rise to vortices on the convex wall due to the Coriolis force.

In Chapter 7, we summarize the main results of the present study and the conclusions obtained thereof, and present the suggestions for future work.

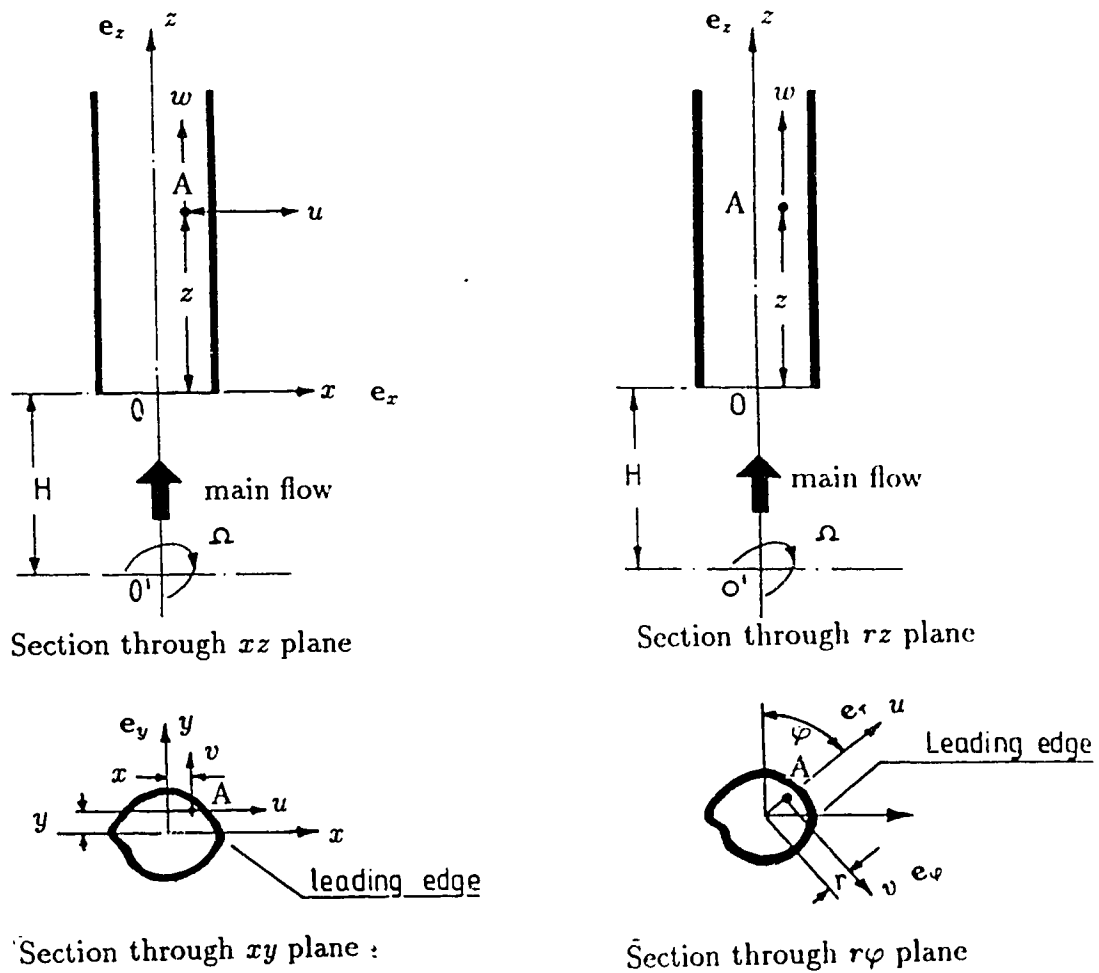


(a) Cartesian frame of reference



(b) Cylindrical polar frame of reference

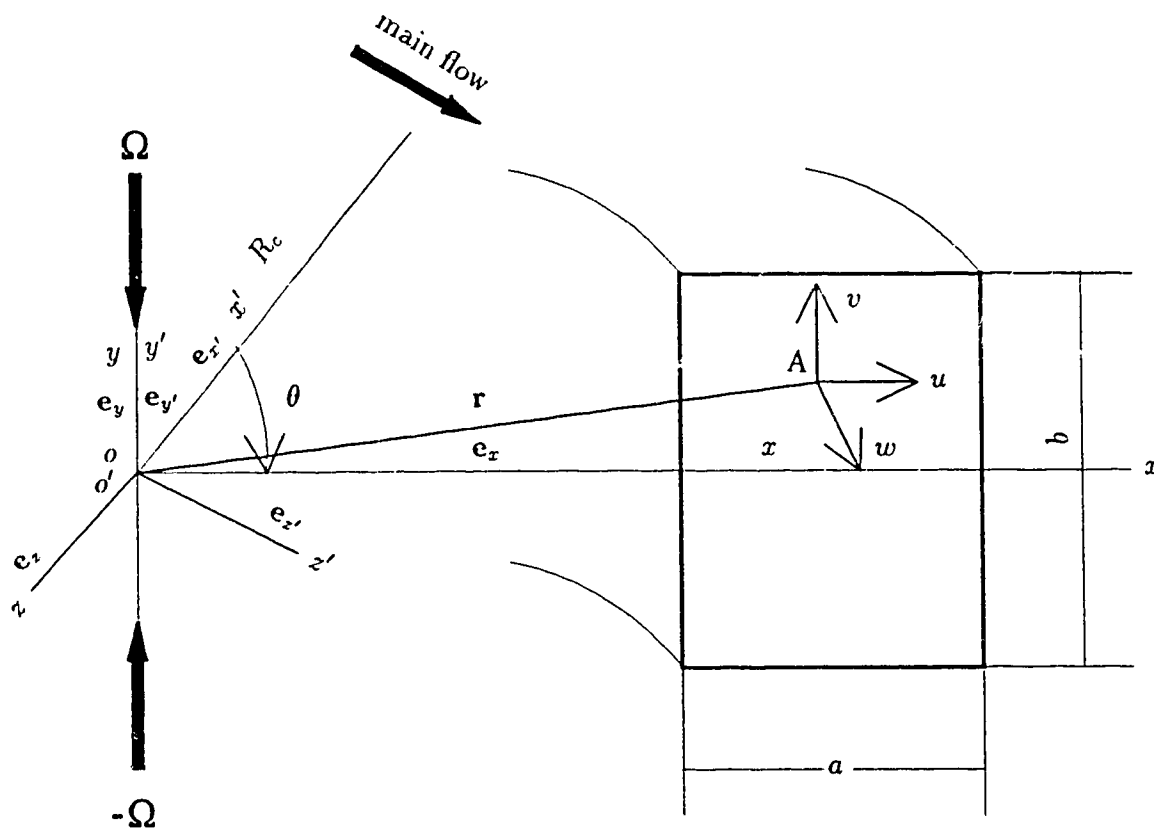
Figure 1.1. Streamwise rotating straight channels (Morris 1981)



(a) Cartesian frame of reference

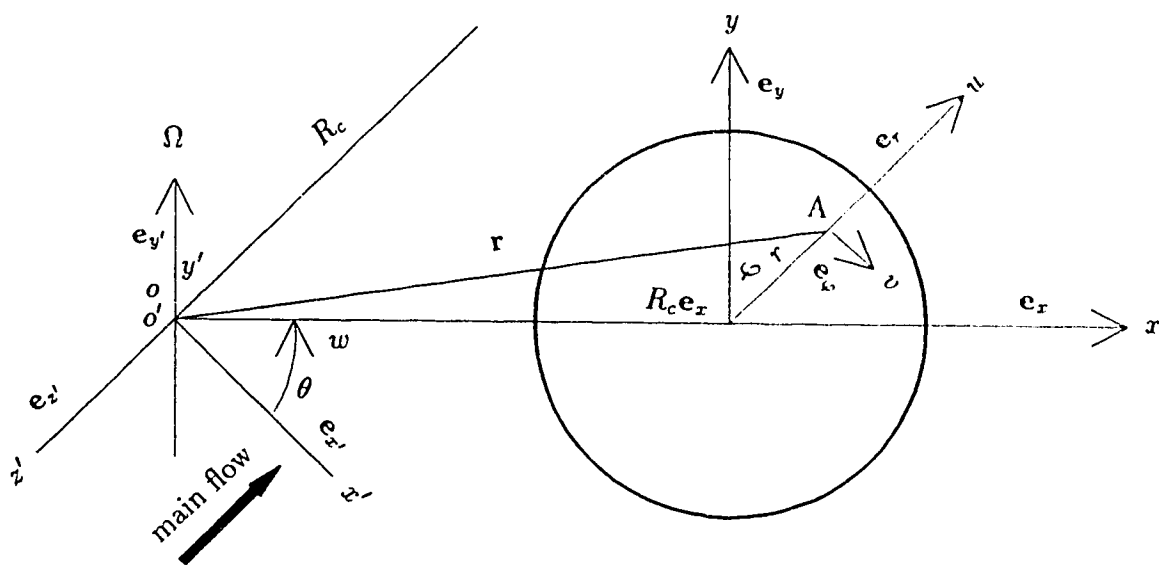
(b) Cylindrical polar frame of reference

Figure 1.2. Radially rotating straight channels (Morris 1981)



(a) Toroidal rectangular frame of reference

Figure 1.3. Spanwise rotating curved channels



(b) Toroidal polar frame of reference

Figure 1.3. Spanwise rotating curved channels

References

- [1] Berman, J. 1985 Fully developed heat transfer in a rotating non-aligned straight tube. *Chem. Eng. Commun.* **39**, 201-216.
- [2] Hochrainer, D. 1971 A new centrifuge to measure the aerodynamic diameter of aerosol particles in the submicron range. *J. of Colloid and Interface Science* **36**, 191-194.
- [3] Hoover, M.D., Stöber, W. & Morawietz, G. 1984 Experiment on laminar flow in a rotating, curved duct of rectangular cross section. *J. Fluids Engi.* **106**, 38-44.
- [4] Ito, H. & Motai, T., 1974 Secondary flow in a rotating curved pipe. *Rep. Inst. High Speed Mech.* **29**, 33-57.
- [5] Kotrappa, P. & Light, M.E. 1972 Design and performance of the Lovelace aerosol particle separator. *Review of Scientific Instruments* **43**, 1106-1112.
- [6] Lennartz, J.W., Gorensek, M.B. & Adler, R.J. 1987 Separation of fine-particle dispersions using periodic flows in a spinning coiled tube. Part III: Batch fractionation experiments. *AIChE J.* **33**, 506-509.
- [7] Miyazaki, H. 1971 Combined free and forced convective heat transfer and fluid flow in a rotating curved circular tube. *Int. J. Heat Mass Transfer* **14**, 1295-1309.
- [8] Miyazaki, H. 1973 Combined free and forced convective heat transfer and fluid flow in a rotating curved rectangular tubes. *J. Heat Transfer* **95**, 64-71.

- [9] Morris, W.D. 1981 *Heat Transfer and Fluid Flow in Rotating Coolant Channels*. Research Studies Press, John Wiley and Sons.
- [10] Nandakumar, K. & Masliyah, J.H. 1986 Swirling flow and heat transfer in coiled and twisted pipes. *Advances in Transport Processes* **4**, 49-112.
- [11] Papanu, J.S., Adler, R.J., Gorenssek, M.B. & Menon, M.M. 1986 Separation of fine particle dispersions using periodic flows in a spinning coiled tube. *AIChE J.* **32**, 798-808.
- [12] Pedley, T.J. 1980 *The Fluid Mechanics of Large Blood Vessels*. Cambridge Univ. Press, pp. 160-234.
- [13] Qiu, L., Wang, L. & Sun, Y. 1988 Experimental study on rotating tube heat exchangers. In Proc. Chinese National Congress on Heat Recovery, pp.200-206.
- [14] Qiu, L., Wang, L. & Sun, Y. 1990 Heat transfer from tubes which extend radially outward from a rotating shaft. In *Heat transfer enhancement and energy conservation* (ed. S.J. Deng, T.N. Veziroğlu, Y.K. Tan and L.Q. Chen), pp.231-236. Hemisphere Publishing Corporation.
- [15] Stöber, W. & Flachsbarth, H. 1969 Size-separating precipitation of aerosols in a spinning spiral duct. *Environmental science and technology* **3**, 1280-1296.

Chapter 2

Flow Transitions and Combined Free and Forced Convective Heat Transfer in a Rotating Curved Circular Tube—I: Perturbation Solution

A three-parameter, regular perturbation method is developed to study laminar flow transitions and combined free and forced convective heat transfer in a rotating curved circular tube. The specific problem considered here is the curved tube rotating at a uniform angular velocity about the axis through the centre of the curvature.

A full second-order perturbation solution is obtained for the full nonlinear coupled governing equations under the conditions that the flow and temperature fields are fully developed, and the wall heat flux is uniform with peripherally uniform wall temperature. The solution covers both heating and cooling cases, with the rotation of the tube either in the same direction or opposite to the main flow imposed by an axial pressure gradient. By excluding the effect of any one or two of the three factors (rotation, curvature and heating/cooling), the solution reduces to each of the six special problems such as the classical Dean problem and mixed convection problem.

2.1 Introduction

Fluid flow and heat transfer in rotating curved channels are not only of theoretical interest, but also of practical importance in many engineering applications (Morris 1981, Papanu *et al.* 1986 and Qiu *et al.* 1988 & 1990). The transport and flow phenomena in the rotating curved channels have, therefore, challenged engineers and scientists for a long time. A remarkable characteristic of the flow and heat transfer in a rotating system is the presence of the centrifugal and Coriolis forces. Under certain conditions, those forces may induce a secondary flow in a plane perpendicular to the direction of main flow. This could significantly affect the resistance to the fluid flow and convective heat transfer. According to its inducing condition (§1.2), the secondary flow could only be created by the Coriolis force for a constant

property fluid, while the centrifugal force is purely hydrostatic, analogous to the earth's gravitational field. When a temperature-induced variation of fluid density is permitted, both Coriolis and centrifugal-type buoyancy force could contribute to the generation of the secondary flow. On the other hand, secondary flow also arises due to centrifugal force when a channel is curved (Dean 1928). Therefore, centrifugal, Coriolis and centrifugal-type buoyancy forces all contribute to the generation of the secondary flow if the channel is both curved and rotating. The nonlinear interaction of these body forces could result in a complicated structure of the flow. We examine this structure and its effects on flow resistance and convective heat transfer in the present study by a three-parameter perturbation method assuming the channel to be of a circular cross section.

The secondary flow under consideration is really a nonlinear combination of the buoyancy force-driven secondary flow in the mixed-convection problem, the centrifugal force-driven secondary flow in the Dean problem and the Coriolis force-driven secondary flow in radially rotating straight channels (hereafter referred to as Coriolis problem). The similarity among these three problems has been recognized by a number of investigators. The dynamical parameters for these three problems are, respectively, $RcRa$, square of the Dean number De^2 ($De = Re\sqrt{\sigma}$) and D_Ω ($= RcRe_\Omega$). Here Re is the Reynolds number, Ra is the Rayleigh number, σ is the curvature ratio of the channel and Re_Ω ($= 4\Omega a^2/\nu$) is the rotational Reynolds number. In all three problems, a typical structure of fully-developed secondary

flow consists of one-pair of counter-rotating vortices in a plane perpendicular to the axis of the channel at sufficiently small values of the dynamical parameter. The interaction of the secondary flow with the pressure-driven main flow shifts the location of the maximum axial velocity away from the centre of the channel and in the direction of the secondary velocities in the middle of the channel (Nandakumar & Weinitschke 1991). Upon increasing the value of the dynamical parameters sufficiently (depending on the value of the Prandtl number Pr , curvature ratio σ or the rotational Reynolds number Rc_Ω for these three problems), the one-pair vortex flow structure becomes unstable and gives way to another form of two-dimensional flow with a two-pair or roll-cell vortex structure (depending on the geometry of the channel) in the cross-plane.

Winters (1987) found such two-pair vortex flows in the Dean problem to be unstable to asymmetric perturbations. Similar results are found in the mixed-convection problem (Nandakumar & Weinitschke 1991) and the Coriolis problem (Nandakumar *et al.* 1991). The stability of these vortices with respect to two-dimensional, spanwise-periodic perturbations (i.e. Eckhaus stability) is examined by Guo and Finlay (1991) for parallel plate channel with curvature and/or rotation. They found that the Eckhaus stability boundary is a small closed loop. Within the boundary, the vortices are stable to spanwise perturbations. Outside the boundary, Eckhaus instability causes the vortex pairs to split apart or merge together. Upon increasing the dynamical parameter even more, all two-dimensional flows become unstable, and

there is evidence for the evolution of streamwise periodic three-dimensional flows in all of the three problems (Nandakumar *et al.* 1991, Nandakumar & Weinitschke 1991 and Ravi Sankar *et al.* 1988). The references concerning these three problems may be found in Cheng & Hwang (1969), Hwang & Cheng (1970), Nandakumar (1985) and Nandakumar & Weinitschke (1991) for the mixed-convection problem; Berger (1991), Berger *et al.* (1983), Cheng *et al.* (1976), Dennis & Ng (1982), Ito (1987), Nandakumar & Masliyah (1986), Winters (1987) and Hwang & Chao (1991) for the Dean problem; Kheshgi & Scriven (1985), Morris (1981), Nandakumar *et al.* (1991), Speziale (1982), Speziale & Thangam (1983), Hwang & Jen (1990), Hwang & Soong (1992), Jen *et al.* (1992), Hwang & Kuo (1993), Hwang & Jen (1987), Hwang & Soong (1989), Hwang & Kuo (1992), Soong *et al.* (1991) and Soong & Hwang (1990) for the Coriolis problem.

In spite of the practical importance and academic interest, the flow and heat transfer in rotating curved channel have not yet sufficiently been examined in details. Most of the previous analytical/numerical investigations have been focused on the two simplified limiting cases (i.e. with weak rotations or with strong rotations). By employing Pohlhausen's method, Hocking (1967) and Ludwig (1951) examined the fully developed laminar boundary layers in rotating curved channel with rectangular and square cross section, respectively. Their results are valid for the large rotational Reynolds number based on the angular velocity of the channel, as compared with the usual Reynolds number based on the mean axial velocity of the fluid. This problem is

not as difficult as the case of the moderate rotation since the flow in the interior of the channel is approximately geostrophic. Considering the channel to be curved tube of circular cross section, the fully developed laminar flow was investigated theoretically by Ito & Motai (1974). They solved the equations of motion by a perturbation method for a small curvature and a low range of angular rotating velocity of the tube. Heat transfer and the effect of centrifugal-type buoyancy force were not considered by these authors. Miyazaki (1971 and 1973) analyzed the fully developed laminar flow and heat transfer in curved rotating circular/rectangular channels by finite-difference method. The effects of the directions of rotation or heat flux were not considered in Miyazaki's works. Because of the convergence difficulties of the iterative solution method used, no solutions in the range where three forces (centrifugal, Coriolis and centrifugal-type buoyancy forces) are of comparable magnitude could be obtained. As for experimental works, it appears that only Piesche (1982) and Piesche & Felsch (1980) have made experimental measurement of the pressure loss in rotating curved square/rectangular channels. By ejecting smoke into the flow, the secondary flow in rotating curved square/rectangular channels has been visualized by Cheng *et al.* (1993) and Cheng & Wang (1993a and 1993b). The photographic results of secondary flow patterns show that the secondary flow in rotating curved channels is very complex. Depending on the range of governing parameters and geometry of channels, the secondary flow may appear as one-pair, two-pair, roll-cell or a large number of small vortex flow patterns.

Since the existing solutions to the problem are only for the asymptotic limits of slow and rapid rotation, the secondary flow revealed by the works mentioned above consists of only one-pair counter-rotating vortices. When the three forces are of comparable magnitude, a complicated structure of the secondary flow might be expected since then the nonlinear effects could be quite strong.

In the present work, the laminar flow transitions and combined free and forced convective heat transfer are investigated theoretically for a curved circular tube rotating at a uniform angular velocity about the axis through the centre of the curvature. A three-parameter perturbation method is developed to solve the full nonlinear governing equations under the conditions that the flow and temperature fields are fully developed, and the wall heat flux is uniform with peripherally uniform wall temperature. The solutions are valid for both heating and cooling cases, and also both cases in which the rotation of the tube is in the same direction or opposite to the main flow imposed by a pressure gradient along the axis of the tube. Attention is focused on transitions of the secondary flow and the main flow, and the effects of these transitions on temperature distribution, friction resistance and heat transfer in terms of friction factor and Nusselt number. The work is divided into two parts. The first part provides a theoretical basis for the perturbation method with the power sequence as the expansion functions, and obtains a full second order perturbation solution for the velocity and temperature fields. The second part presents the flow and heat transfer characteristics obtained by the perturbation solution.

The motivation of the present study comes from the desire of obtaining an approximate analytical solution and extending the previous analysis to the range where centrifugal, Coriolis and buoyancy forces just neutralize each other. From the analytical solution, the structure of the solution may be analyzed. Consequently, the physical nature of the problem may be understood more clearly. However, a perturbation solution with finite terms is usually valid only in the range with small values of the characteristic parameters. This limit may be extended by two techniques developed recently. One is the extended perturbation series technique (Aziz & Na 1984, Aziz 1988 and Van Dyke 1975), in which considerable routine labour of calculating higher approximations is delegated to a computer. After dozens or even hundreds of terms are found, the structure of the solution may be analyzed and the solution may be improved to extend its utility. The other is the matching technique which uses the asymptotic solutions for large or small values of the characteristic parameters to construct a general solution, valid over the whole range of the values of the characteristic parameters.

2.2 Formulation of the problem

The geometrical configuration of the physical model for a rotating curved circular tube and its coordinate system are given in Fig.2.1. Under the action of the pressure gradient, a viscous fluid is allowed to flow through the curved tube of circular cross section of radius a with negligible pitch effect, which is rotated about the axis

through the centre of the curvature $o'z'$ with a constant angular velocity Ω . The tube is being uniformly heated or cooled at the wall with a heat flux q_w . The properties of the fluid, with the exception of density, are taken to be constant.

Consider a toroidal coordinate system (R, φ, θ) fixed to the rotating curved tube as shown in Fig.2.1. The direction of the main flow in the tube is chosen in the direction of increasing θ , while the angular velocity of the tube is taken as $\Omega > 0$ for increasing θ and $\Omega < 0$ for decreasing θ , respectively. The velocity components in the increasing directions of R, φ , and θ are denoted by U, V, W respectively. The buoyancy term is expressed in terms of the coefficient of thermal expansion as is commonly done in free-convection analyses (Boussinesq approximation). The temperature difference used to express density variations in the buoyancy term is $t_w - t$ (t_w = wall temperature; t = temperature of the fluid). In the case of hydrodynamically and thermally fully developed laminar flow, the continuity, Navier-Stokes and energy equations governing the flow and heat transfer are:

Equation of Continuity

$$\frac{\partial U}{\partial R} + \frac{U}{R} + \frac{U \sin \varphi}{R_c + R \sin \varphi} + \frac{1}{R} \frac{\partial V}{\partial \varphi} + \frac{V \cos \varphi}{R_c + R \sin \varphi} = 0 \quad (2.1)$$

Equation of Momentum

$$\begin{aligned} U \frac{\partial U}{\partial R} + \frac{V}{R} \frac{\partial U}{\partial \varphi} - \frac{V^2}{R} - \frac{W^2 \sin \varphi}{R_c + R \sin \varphi} &= -\frac{1}{\rho} \frac{\partial P'}{\partial R} + \beta(t_w - t) \Omega^2 (R_c + R \sin \varphi) \sin \varphi \\ &+ 2\Omega W \sin \varphi + \nu \left(\frac{1}{R} \frac{\partial}{\partial \varphi} + \frac{\cos \varphi}{R_c + R \sin \varphi} \right) \left(\frac{1}{R} \frac{\partial U}{\partial \varphi} - \frac{\partial V}{\partial R} - \frac{V}{R} \right) \quad (2.2) \\ U \frac{\partial V}{\partial R} + \frac{V}{R} \frac{\partial V}{\partial \varphi} + \frac{UV}{R} - \frac{W^2 \cos \varphi}{R_c + R \sin \varphi} &= -\frac{1}{\rho R} \frac{\partial P'}{\partial \varphi} + \beta(t_w - t) \Omega^2 (R_c + R \sin \varphi) \cos \varphi \end{aligned}$$

$$\begin{aligned}
& + 2\Omega W \cos\varphi + \nu \left(\frac{\partial}{\partial R} + \frac{\sin\varphi}{R_c + R \sin\varphi} \right) \left(\frac{\partial V}{\partial R} + \frac{V}{R} \frac{\partial U}{\partial \varphi} \right) \quad (2.3) \\
U \frac{\partial W}{\partial R} + \frac{V}{R} \frac{\partial W}{\partial \varphi} + \frac{UW \sin\varphi}{R_c + R \sin\varphi} + \frac{VW \cos\varphi}{R_c + R \sin\varphi} &= - \frac{1}{\rho(R_c + R \sin\varphi)} \frac{\partial P'}{\partial \theta} - 2\Omega(U \sin\varphi \\
& + V \cos\varphi) + \nu \left[\left(\frac{\partial}{\partial R} + \frac{1}{R} \right) \left(\frac{\partial W}{\partial R} + \frac{W \sin\varphi}{R_c + R \sin\varphi} \right) + \frac{1}{R} \frac{\partial}{\partial \varphi} \left(\frac{1}{R} \frac{\partial W}{\partial \varphi} + \frac{W \cos\varphi}{R_c + R \sin\varphi} \right) \right] \quad (2.4)
\end{aligned}$$

Equation of energy

$$\begin{aligned}
U \frac{\partial t}{\partial R} + \frac{V}{R} \frac{\partial t}{\partial \varphi} + \frac{W}{R_c + R \sin\varphi} \frac{\partial t}{\partial \theta} &= \alpha \left[\frac{\partial^2 t}{\partial R^2} + \frac{1}{R} \frac{\partial t}{\partial R} + \frac{1}{R^2} \frac{\partial^2 t}{\partial \varphi^2} \right. \\
& \left. + \frac{\sin\varphi}{R_c + R \sin\varphi} \frac{\partial t}{\partial R} + \frac{\cos\varphi}{R(R_c + R \sin\varphi)} \frac{\partial t}{\partial \varphi} + \frac{1}{(R_c + R \sin\varphi)^2} \frac{\partial^2 t}{\partial \theta^2} \right] \quad (2.5)
\end{aligned}$$

The boundary conditions at the wall are:

$$U = V = W = 0; \quad t = t_w \quad (2.6)$$

In the equations above, ν and α are the kinematic viscosity and thermal diffusivity of the fluid, respectively. P' is a pseudo pressure which absorbs any force residual implied by the choice of reference temperature for the evaluation of fluid density ($P' = p - \rho_w \Omega^2 (R_c + R \sin\varphi)^2 / 2$ with p as the fluid pressure)

The equation of continuity (Eq.(2.1)) may be satisfied by a secondary flow stream function f as

$$U = - \frac{1}{R(R_c + R \sin\varphi)} \frac{\partial f}{\partial \varphi} \quad V = \frac{1}{R_c + R \sin\varphi} \frac{\partial f}{\partial R} \quad (2.7)$$

Substituting Eq.(2.7) into Eqs.(2.2) and (2.3), and eliminating P' from Eqs.(2.2) and (2.3), we obtain

$$\frac{1}{R(R_c + R \sin\varphi)} \frac{\partial(f, D^2 f)}{\partial(R, \varphi)} - \frac{2}{(R_c + R \sin\varphi)^2} \frac{\partial f}{\partial Y} D^2 f$$

$$:= 2[\Omega(R_c + R\sin\varphi) + W] \frac{\partial W}{\partial Y} + \beta\Omega^2(R_c + R\sin\varphi)^2 \frac{\partial T}{\partial Y} + \nu D^4 f \quad (2.8)$$

Here $T = t_w - t$. Since U, V, W are independent of θ for hydrodynamically developed flow, it follows from Eq.(2.4) that the form of P' is restricted to $f_1(R, \varphi)\theta + f_2(R, \varphi)$, and then from Eqs.(2.2) and (2.3), $f_1(R, \varphi)$ must be a constant. Therefore, we can write

$$-\frac{1}{R_c} \frac{\partial P'}{\partial \theta} = c_1 \quad (2.9)$$

Where c_1 is a positive constant, the direction of flow being always chosen as the direction of increasing θ .

Substitution of Eqs.(2.7) and (2.9) into Eq.(2.4) yields

$$\begin{aligned} & \frac{1}{R} \frac{\partial(f, W)}{\partial(R, \varphi)} + \left(2\Omega + \frac{W}{R_c + R\sin\varphi}\right) \frac{\partial f}{\partial Y} \\ & = \frac{R_c c_1}{\rho} + \nu[(R_c + R\sin\varphi) \nabla^2 W + \frac{\partial W}{\partial X} - \frac{W}{R_c + R\sin\varphi}] \end{aligned} \quad (2.10)$$

Because of fully developed temperature field, the axial temperature gradients must be constant, i.e.,

$$-\frac{1}{R_c} \frac{\partial t}{\partial \theta} = c_2 \quad (2.11)$$

Here c_2 is a constant axial gradient of temperature in θ -direction. $c_2 > 0$ means that the fluid is cooled, and $c_2 < 0$ indicates that the fluid is heated. Furthermore, combining the assumption of fully developed flow and uniform axial heating or cooling and the assumption of high thermal conductivity of the tube wall material to smooth out circumferential variations in wall temperature gives

$$\frac{\partial t}{\partial R} = -\frac{\partial T}{\partial R} \quad \frac{\partial t}{\partial \varphi} = -\frac{\partial T}{\partial \varphi} \quad \frac{\partial t}{\partial \theta} = -\frac{\partial t_w}{\partial \theta} \quad (2.12)$$

Inserting Eqs.(2.7), (2.11) and (2.12) into Eq.(2.5) yields

$$\frac{1}{R(R_c + R\sin\varphi)} \frac{\partial(f, T)}{\partial(R, \varphi)} + \frac{WR_c c_2}{R_c + R\sin\varphi} = \alpha(\nabla^2 T + \frac{1}{R_c + R\sin\varphi} \frac{\partial T}{\partial X}) \quad (2.13)$$

In Eqs.(2.8) (2.10) and (2.13),

$$X = R\sin\varphi \quad Y = R\cos\varphi$$

$$\frac{\partial}{\partial X} = \frac{\sin\varphi}{R} \frac{\partial}{\partial R} + \frac{\cos\varphi}{R} \frac{\partial}{\partial \varphi} \quad \frac{\partial}{\partial Y} = \frac{\cos\varphi}{R} \frac{\partial}{\partial R} - \frac{\sin\varphi}{R} \frac{\partial}{\partial \varphi}$$

The differential operators are

$$D^2 = \nabla^2 - \frac{1}{R_c + R\sin\varphi} \frac{\partial}{\partial X} \quad \nabla^2 = \frac{\partial^2}{\partial R^2} + \frac{1}{R} \frac{\partial}{\partial R} + \frac{1}{R^2} \frac{\partial^2}{\partial \varphi^2}$$

Making use of the non-dimensional variables defined by

$$\phi = \frac{f}{\nu R_c} \quad w = \frac{Wa}{\nu} \quad r = \frac{R}{a} \quad \eta = \frac{T}{Pr c_2 a} \quad (2.14)$$

Eqs.(2.8), (2.10) and (2.13) reduce, respectively, to

$$D^4 \phi = \frac{1}{r(1 + \sigma r \sin\varphi)} \frac{\partial(\phi, D^2 \phi)}{\partial(r, \varphi)} - \frac{2\sigma}{(1 + \sigma r \sin\varphi)^2} \frac{\partial \phi}{\partial y} D^2 \phi - [2\sigma w + \frac{Rc_\Omega}{2}(1 + \sigma r \sin\varphi)] \frac{\partial w}{\partial y} - Ra_\Omega (1 + \sigma r \sin\varphi)^2 \frac{\partial \eta}{\partial y} \quad (2.15)$$

$$\nabla^2 w = \frac{1}{1 + \sigma r \sin\varphi} \left[\frac{1}{r} \frac{\partial(\phi, w)}{\partial(r, \varphi)} - \sigma \frac{\partial w}{\partial x} + \frac{Rc_\Omega}{2} \frac{\partial \phi}{\partial y} - 4c \right] + \frac{\sigma w}{(1 + \sigma r \sin\varphi)^2} \left(\frac{\partial \phi}{\partial y} + \sigma \right) \quad (2.16)$$

$$\nabla^2 \eta = \frac{1}{1 + \sigma r \sin\varphi} \left[\frac{Pr}{r} \frac{\partial(\phi, \eta)}{\partial(r, \varphi)} + w - \sigma \frac{\partial \eta}{\partial x} \right] \quad (2.17)$$

where

$$x = \frac{X}{a} \quad y = \frac{Y}{a}$$

$$\frac{\partial}{\partial x} = \sin\varphi \frac{\partial}{\partial r} + \frac{\cos\varphi}{r} \frac{\partial}{\partial \varphi} \quad \frac{\partial}{\partial y} = \cos\varphi \frac{\partial}{\partial r} - \frac{\sin\varphi}{r} \frac{\partial}{\partial \varphi}$$

$$D^2 = \nabla^2 - \frac{\sigma}{1 + \sigma r \sin\varphi} \frac{\partial}{\partial x}$$

$$\nabla^2 = \frac{\partial^2}{\partial r^2} + \frac{1}{r} \frac{\partial}{\partial r} + \frac{1}{r^2} \frac{\partial^2}{\partial \varphi^2}$$

and

$$Re_\Omega = \frac{4\Omega a^2}{\nu} \quad Ra_\Omega = \frac{Pr\beta\Omega^2 c_2 a^4 R_c}{\nu^2}$$

$$c = \frac{c_1 a^3}{4\rho\nu^2} \quad \sigma = \frac{a}{R_c} \quad Pr = \frac{\nu}{\alpha}$$

We seek the solution of Eqs.(2.15)-(2.17) subject to the condition of no-slip at the wall and the uniform wall heat flux with peripherally uniform wall temperature, namely,

$$\frac{\partial\phi}{\partial r} = \frac{\partial\phi}{\partial\varphi} = w = \eta = 0 \quad \text{at} \quad r = 1 \quad (2.18)$$

Further in the region $0 \leq r \leq 1$ and $-\pi \leq \varphi \leq \pi$

$$\frac{\partial\phi}{\partial r}, \frac{\partial\phi}{\partial\varphi}, w, \text{ and } \eta \quad \text{must be finite} \quad (2.19)$$

The solution of Eqs.(2.15)-(2.17) under the boundary conditions (2.18) and (2.19) are governed by five dimensionless parameters: σ , Pr , Re_Ω , Ra_Ω and c . The curvature ratio σ , a geometry parameter, represents the degree of curvature. Prandtl number Pr , a thermophysical property parameter, represents the ratio of momentum diffusion rate to that of thermal diffusion. The rotational Reynolds number Re_Ω emerges from the Coriolis term of the momentum equations. It indicates the

ratio of the Coriolis force to the viscous force. $Re_{\Omega} > 0$ represents the case of positive rotation. $Re_{\Omega} < 0$ is for the case of negative rotation. The rotational Rayleigh number Ra_{Ω} has its origin in the centrifugal buoyancy terms. It is similar to the Rayleigh number encountered in the study of gravitational buoyancy due to the earth's gravitational field but with the gravitational acceleration replaced by the centrifugal acceleration measured at the centre line of the tube considered. It denotes the ratio of centrifugal-type buoyancy force to the viscous force. $Ra_{\Omega} > 0$ represents the cooling case, while $Ra_{\Omega} < 0$ is for the case of heating. c is defined in an identical mathematical form to the usual Reynolds number Re , but using pseudo pressure instead of the usual fluid pressure. It represents the ratio of inertial force to viscous force.

2.3 Perturbation solution

Although an exact solution of Eqs.(2.15)-(2.17) would be extremely difficult to find, if indeed possible, an approximate solution may readily be obtained using a parameter perturbation method with power sequence as the expansion functions. A theoretical basis for this method is given in Appendix A, which shows that any function of m variables x_1, x_2, \dots, x_m , which is continuous for $c_i^l \leq x_i \leq c_i^h$ ($i = 1, 2, \dots, m$) may be approximated uniformly by a unique polynomial. The reason to choose the power sequence as the expansion functions is because of the uniqueness of the expansion and its uniform convergence rather than just convergence in the mean.

In the literature, the perturbation solution is usually considered to be valid only for small values of perturbation parameters. However, we can always, in principle, find a proper mathematical transformation to make the perturbation parameter small enough so that the solution is valid. The theoretical basis given in the Appendix also shows that we can achieve any accuracy required by a suitable choice of the number of terms in the perturbation series for the entire region of the parameters. And the high order terms can be obtained easily through a computer (Aziz 1988, Aziz & Na 1984 and Van Dyke 1975). The main drawback of the perturbation method with the power sequence as the expansion functions is that it can not be used to obtain a discontinuous solution in parameters which usually exists in the nonlinear problems. This leads to a disagreement between the perturbation solution and the numerical solution for Dean problem and mixed convection problem (Van Dyke 1978 & 1990) by noting that the numerical solution is a discontinuous one due to the bifurcation of the flow at intermediate and large values of the corresponding dynamical parameters.

Applying to the present problem, the method involves the expansion of the stream function, non-dimensional main velocity and temperature fields ϕ, w, η in ascending powers of the suitable small parameters. σ, Re_Ω and Ra_Ω are selected as the parameters in this work. This implies the assumption of continuity of ϕ, w and η on σ, Re_Ω and Ra_Ω . Then each of the coefficients of the expansion series for ϕ, w and η may be obtained from the solutions of the associated nonhomogeneous

harmonic and biharmonic differential equations. In calculating each additional term of the series, the terms on the right hand sides of the harmonic and biharmonic differential equations, are in terms of the functions determined from the solution of the preceding harmonic and biharmonic differential equations. Therefore successive solutions of the three main differential equations will produce as many terms as desired for the three series depending upon the accuracy required. In this work, the solution is carried up to and including the second-order terms.

Let

$$\left. \begin{aligned} \phi &= \sum_{i=0}^{\infty} \sum_{j=0}^{\infty} \sum_{k=0}^{\infty} \phi_{ijk} \varepsilon_1^i \varepsilon_2^j \varepsilon_3^k \\ w &= \sum_{i=0}^{\infty} \sum_{j=0}^{\infty} \sum_{k=0}^{\infty} w_{ijk} \varepsilon_1^i \varepsilon_2^j \varepsilon_3^k \\ \eta &= \sum_{i=0}^{\infty} \sum_{j=0}^{\infty} \sum_{k=0}^{\infty} \eta_{ijk} \varepsilon_1^i \varepsilon_2^j \varepsilon_3^k \end{aligned} \right\} \quad (2.20)$$

where $\varepsilon_1, \varepsilon_2$ and ε_3 denote respectively σ , Re_{Ω} and Ra_{Ω} , and the coefficients depend on the coordinates of the points of the fluid (r, φ) .

On substitution of Eq.(2.20) into Eqs.(2.15)-(2.17), sets of equations for the zeroth, first, and second order coefficients may be obtained by equating the coefficients of equal powers of $\varepsilon_1^i \varepsilon_2^j \varepsilon_3^k$. Since there can be no flow in the (r, φ) -plane when $\sigma = Re_{\Omega} = Ra_{\Omega} = 0$, it follows that $\phi_{000} = 0$. The resulting equations for the coefficients up to and including second order are as follows:

Zeroth-order

$$\nabla^2 w_{000} = -4c \quad (2.21)$$

$$\nabla^2 \eta_{000} = w_{000} \quad (2.22)$$

First-order

$$\nabla^4 \phi_{100} = -2w_{000} \frac{\partial w_{000}}{\partial y} \quad (2.23)$$

$$\nabla^4 \phi_{010} = \frac{1}{2} \frac{\partial w_{000}}{\partial y} \quad (2.24)$$

$$\nabla^4 \phi_{001} = -\frac{\partial \eta_{000}}{\partial y} \quad (2.25)$$

$$\nabla^2 w_{100} = \frac{1}{r} \frac{\partial(\phi_{100}, w_{000})}{\partial(r, \varphi)} - \frac{\partial w_{000}}{\partial y} + 4cr \sin \varphi \quad (2.26)$$

$$\nabla^2 w_{010} = \frac{1}{r} \frac{\partial(\phi_{010}, w_{000})}{\partial(r, \varphi)} \quad (2.27)$$

$$\nabla^2 w_{001} = \frac{1}{r} \frac{\partial(\phi_{001}, w_{000})}{\partial(r, \varphi)} \quad (2.28)$$

$$\nabla^2 \eta_{100} = \frac{Pr}{r} \frac{\partial(\phi_{100}, \eta_{000})}{\partial(r, \varphi)} + w_{100} - \frac{\partial \eta_{000}}{\partial x} - rw_{000} \sin \varphi \quad (2.29)$$

$$\nabla^2 \eta_{010} = \frac{Pr}{r} \frac{\partial(\phi_{010}, \eta_{000})}{\partial(r, \varphi)} + w_{010} \quad (2.30)$$

$$\nabla^2 \eta_{001} = \frac{Pr}{r} \frac{\partial(\phi_{001}, \eta_{000})}{\partial(r, \varphi)} + w_{001} \quad (2.31)$$

Second-order

$$\nabla^2 \phi_{200} = \frac{1}{r} \frac{\partial(\phi_{100}, \nabla^2 \phi_{100})}{\partial(r, \varphi)} + 2 \frac{\partial \nabla^2 \phi_{100}}{\partial x} - 2w_{000} \frac{\partial w_{100}}{\partial y} - 2w_{100} \frac{\partial w_{000}}{\partial y} \quad (2.32)$$

$$\nabla^2 \phi_{020} = \frac{1}{r} \frac{\partial(\phi_{010}, \nabla^2 \phi_{010})}{\partial(r, \varphi)} - \frac{1}{2} \frac{\partial w_{010}}{\partial y} \quad (2.33)$$

$$\nabla^2 \phi_{002} = \frac{1}{r} \frac{\partial(\phi_{001}, \nabla^2 \phi_{001})}{\partial(r, \varphi)} - \frac{\partial \eta_{010}}{\partial y} \quad (2.34)$$

$$\begin{aligned} \nabla^4 \phi_{110} = & \frac{1}{r} \frac{\partial(\phi_{100}, \nabla^2 \phi_{100})}{\partial(r, \varphi)} + \frac{1}{r} \frac{\partial(\phi_{010}, \nabla^2 \phi_{100})}{\partial(r, \varphi)} + 2 \frac{\partial \nabla^2 \phi_{010}}{\partial x} \\ & - 2w_{000} \frac{\partial w_{010}}{\partial y} - 2w_{010} \frac{\partial w_{000}}{\partial y} - \frac{1}{2} \frac{\partial w_{100}}{\partial y} - \frac{1}{2} r \sin \varphi \frac{\partial w_{000}}{\partial y} \end{aligned} \quad (2.35)$$

$$\begin{aligned} \nabla^4 \phi_{101} = & \frac{1}{r} \frac{\partial(\phi_{100}, \nabla^2 \phi_{001})}{\partial(r, \varphi)} + \frac{1}{r} \frac{\partial(\phi_{001}, \nabla^2 \phi_{100})}{\partial(r, \varphi)} + 2 \frac{\partial \nabla^2 \phi_{001}}{\partial x} \\ & - 2w_{000} \frac{\partial w_{001}}{\partial y} - 2w_{001} \frac{\partial w_{000}}{\partial y} - \frac{\partial \eta_{100}}{\partial y} - 2r \sin \varphi \frac{\partial \eta_{000}}{\partial y} \end{aligned} \quad (2.36)$$

$$\nabla^4 \phi_{011} = \frac{1}{r} \frac{\partial(\phi_{010}, \nabla^2 \phi_{001})}{\partial(r, \varphi)} + \frac{1}{r} \frac{\partial(\phi_{001}, \nabla^2 \phi_{010})}{\partial(r, \varphi)} - \frac{1}{2} \frac{\partial w_{001}}{\partial y} - \frac{\partial \eta_{010}}{\partial y} \quad (2.37)$$

$$\begin{aligned} \nabla^2 w_{200} = & \frac{1}{r} \frac{\partial(\phi_{200}, w_{000})}{\partial(r, \varphi)} + \frac{1}{r} \frac{\partial(\phi_{100}, w_{100})}{\partial(r, \varphi)} - \sin \varphi \frac{\partial(\phi_{100}, w_{000})}{\partial(r, \varphi)} + r \sin \varphi \frac{\partial w_{000}}{\partial x} \\ & - \frac{\partial w_{100}}{\partial x} + w_{000} + w_{000} \frac{\partial \phi_{100}}{\partial y} - 4cr^2 \sin^2 \varphi \end{aligned} \quad (2.38)$$

$$\nabla^2 w_{020} = \frac{1}{r} \frac{\partial(\phi_{020}, w_{000})}{\partial(r, \varphi)} + \frac{1}{r} \frac{\partial(\phi_{010}, w_{010})}{\partial(r, \varphi)} + \frac{1}{2} \frac{\partial \phi_{010}}{\partial y} \quad (2.39)$$

$$\nabla^2 w_{002} = \frac{\partial(\phi_{002}, w_{000})}{\partial(r, \varphi)} + \frac{1}{r} \frac{\partial(\phi_{001}, w_{001})}{\partial(r, \varphi)} \quad (2.40)$$

$$\begin{aligned} \nabla^2 w_{110} = & \frac{1}{r} \frac{\partial(\phi_{110}, w_{000})}{\partial(r, \varphi)} + \frac{1}{r} \frac{\partial(\phi_{100}, w_{010})}{\partial(r, \varphi)} + \frac{1}{r} \frac{\partial(\phi_{010}, w_{100})}{\partial(r, \varphi)} \\ & - \sin \varphi \frac{\partial(\phi_{010}, w_{000})}{\partial(r, \varphi)} - \frac{\partial w_{010}}{\partial x} + \frac{1}{2} \frac{\partial \phi_{100}}{\partial y} + w_{000} \frac{\partial \phi_{010}}{\partial y} \end{aligned} \quad (2.41)$$

$$\begin{aligned} \nabla^2 w_{101} = & \frac{1}{r} \frac{\partial(\phi_{101}, w_{000})}{\partial(r, \varphi)} + \frac{1}{r} \frac{\partial(\phi_{100}, w_{001})}{\partial(r, \varphi)} + \frac{1}{r} \frac{\partial(\phi_{001}, w_{100})}{\partial(r, \varphi)} \\ & - \sin \varphi \frac{\partial(\phi_{001}, w_{000})}{\partial(r, \varphi)} - \frac{\partial w_{001}}{\partial x} + w_{000} \frac{\partial \phi_{001}}{\partial y} \end{aligned} \quad (2.42)$$

$$\nabla^2 w_{011} = \frac{1}{r} \frac{\partial(\phi_{011}, w_{000})}{\partial(r, \varphi)} + \frac{1}{r} \frac{\partial(\phi_{010}, w_{001})}{\partial(r, \varphi)} + \frac{1}{r} \frac{\partial(\phi_{001}, w_{010})}{\partial(r, \varphi)} + \frac{1}{2} \frac{\partial \phi_{001}}{\partial y} \quad (2.43)$$

$$\begin{aligned} \nabla^2 \eta_{200} = & \frac{Pr}{r} \frac{\partial(\phi_{200}, \eta_{000})}{\partial(r, \varphi)} + \frac{Pr}{r} \frac{\partial(\phi_{100}, \eta_{100})}{\partial(r, \varphi)} \\ & + w_{200} + \frac{\partial \eta_{100}}{\partial x} + r \sin \varphi \nabla^2 \eta_{100} \end{aligned} \quad (2.44)$$

$$\nabla^2 \eta_{020} = \frac{Pr}{r} \frac{\partial(\phi_{020}, \eta_{000})}{\partial(r, \varphi)} + \frac{Pr}{r} \frac{\partial(\phi_{010}, \eta_{010})}{\partial(r, \varphi)} + w_{020} \quad (2.45)$$

$$\nabla^2 \eta_{002} = \frac{Pr}{r} \frac{\partial(\phi_{020}, \eta_{000})}{\partial(r, \varphi)} + \frac{Pr}{r} \frac{\partial(\phi_{001}, \eta_{001})}{\partial(r, \varphi)} + w_{002} \quad (2.46)$$

$$\begin{aligned} \nabla^2 \eta_{110} = & \frac{Pr}{r} \frac{\partial(\phi_{110}, \eta_{000})}{\partial(r, \varphi)} + \frac{Pr}{r} \frac{\partial(\phi_{100}, \eta_{010})}{\partial(r, \varphi)} + \frac{Pr}{r} \frac{\partial(\phi_{010}, \eta_{100})}{\partial(r, \varphi)} \\ & + w_{110} - \frac{\partial \eta_{010}}{\partial x} - r \sin \varphi \nabla^2 \eta_{010} \end{aligned} \quad (2.47)$$

$$\begin{aligned} \nabla^2 \eta_{101} = & \frac{Pr}{r} \frac{\partial(\phi_{101}, \eta_{000})}{\partial(r, \varphi)} + \frac{Pr}{r} \frac{\partial(\phi_{100}, \eta_{001})}{\partial(r, \varphi)} + \frac{Pr}{r} \frac{\partial(\phi_{001}, \eta_{100})}{\partial(r, \varphi)} \\ & + w_{101} - \frac{\partial \eta_{001}}{\partial x} - r \sin \varphi \nabla^2 \eta_{001} \end{aligned} \quad (2.48)$$

$$\begin{aligned}\nabla^2 \eta_{011} &= \frac{Pr}{r} \frac{\partial(\phi_{011}, \eta_{000})}{\partial(r, \varphi)} + \frac{Pr}{r} \frac{\partial(\phi_{010}, \eta_{001})}{\partial(r, \varphi)} \\ &+ \frac{Pr}{r} \frac{\partial(\phi_{001}, \eta_{010})}{\partial(r, \varphi)} + w_{011}\end{aligned}\quad (2.49)$$

Similarly, we may obtain equations corresponding to the third and higher approximations. Solving Eqs.(2.21)-(2.49) in order gives:

Stream function of secondary flow

$$\phi_{100} = \frac{c^2}{288} r(1-r^2)^2(4-r^2)\cos\varphi \quad (2.50)$$

$$\phi_{010} = \frac{c}{192} r(1-r^2)^2\cos\varphi \quad (2.51)$$

$$\phi_{001} = \frac{c}{4608} r(1-r^2)^2(r^2-10)\cos\varphi \quad (2.52)$$

$$\begin{aligned}\phi_1 &= \sigma\phi_{100} + Re_\Omega\phi_{010} + Ra_\Omega\phi_{001} \\ &= \frac{\sigma c^2}{288} r(1-r^2)^2[4-r^2 + L_2(r^2-10) + L_1]\cos\varphi\end{aligned}\quad (2.53)$$

where

$$L_1 = \frac{3Re_\Omega}{2\sigma c} \quad L_2 = \frac{Ra_\Omega}{16c} \quad (2.54)$$

$$\begin{aligned}\phi_{200} &= \frac{c^4 \sin 2\varphi}{350 \times 1152^2} r^2(1-r^2)^2(4979 - 2792r^2 + 779r^4 - 134r^6 + 5r^8) \\ &- \frac{c^4 \sin 2\varphi}{5760} r^2(1-r^2)^2(16 - 7r^2)\end{aligned}\quad (2.55)$$

$$\phi_{020} = \frac{c^2 \sin 2\varphi}{30 \times 768^2} r^2(1-r^2)^2(17 - 2r^2 - r^4) \quad (2.56)$$

$$\begin{aligned}\phi_{002} &= \frac{Prc^2 \sin 2\varphi}{44800 \times 1152^2} (10518r^2 - 25260r^4 + 21000r^6 - 7280r^8 + 1575r^{10} - 168r^{12} + 5r^{14}) \\ &+ \frac{c^2 \sin 2\varphi}{89600 \times 1152^2} (6743r^2 - 11576r^4 + 840r^6 + 6160r^8 - 2380r^{10} + 192r^{12} - 9r^{14})\end{aligned}\quad (2.57)$$

$$\begin{aligned}\phi_{110} &= \frac{c^3 \sin 2\varphi}{350 \times 1152^2} r^2 (1-r^2)^2 (3111 - 1228r^2 + 208r^4 - 36r^6) \\ &\quad + \frac{c \sin 2\varphi}{1024} r^2 (1-r^2)^2\end{aligned}\quad (2.58)$$

$$\begin{aligned}\phi_{101} &= \frac{Pr c^3 \sin 2\varphi}{2800 \times 1152^2} (-4086r^2 + 10050r^4 - 8400r^6 + 3080r^8 - 735r^{10} + 96r^{12} - 5r^{14}) \\ &\quad + \frac{c^3 \sin 2\varphi}{2800 \times 1152^2} (-7739r^2 + 18608r^4 - 14490r^6 + 4200r^8 - 665r^{10} + 84r^{12} + 2r^{14}) \\ &\quad + \frac{c \sin 2\varphi}{20 \times 32^2} (-37r^2 + 78r^4 - 45r^6 + 4r^8)\end{aligned}\quad (2.59)$$

$$\begin{aligned}\phi_{011} &= \frac{Pr c^2 \sin 2\varphi}{537600 \times 1152^2} (-268r^2 + 650r^4 - 525r^6 + 175r^8 - 35r^{10} + 3r^{12}) \\ &\quad + \frac{c^2 \sin 2\varphi}{5600 \times 1152^2} (-3957r^2 + 8000r^4 - 3675r^6 - 840r^8 + 490r^{10} - 18r^{12})\end{aligned}\quad (2.60)$$

Main velocity

$$w_{000} = c(1 - r^2) \quad (2.61)$$

$$w_{100} = \frac{c^3}{11520} r(1 - r^2)(19 - 21r^2 + 9r^4 - r^6) \sin \varphi - \frac{3c}{4} r(1 - r^2) \sin \varphi \quad (2.62)$$

$$w_{010} = \frac{c^2 r}{4608} r(1 - r^2)(3 - 3r^2 + r^4) \sin \varphi \quad (2.63)$$

$$w_{001} = \frac{c^2}{160 \times 1152} r(r^2 - 1)(49 - 51r^2 + 19r^4 - r^6) \sin \varphi \quad (2.64)$$

$$w_{200} = f_{200} + g_{200} \cos 2\varphi \quad (2.65)$$

Where

$$f_{200} = -\frac{c^5}{2800 \times 1152^2} (1 - r^2)^4 (4119 - 4804r^2 + 2410r^4 - 500r^6 + 35r^8)$$

$$\begin{aligned}
& -\frac{c^3}{230400}(1-r^2)(148+43r^2-132r^4+68r^6-7r^8) \\
& \quad -\frac{c}{32}(1-r^2)(3-11r^2) \\
g_{200} = & -\frac{c^5}{88200 \times 1152^2}r^2(1-r^2)(145690-240206r^2 \\
& +174649r^4-70547r^6+19123r^8-2801r^{10}+160r^{12}) \\
& +\frac{c^3}{276480}r^2(1-r^2)(463-613r^2+296r^4-40r^6) \\
& \quad -\frac{5c}{16}r^2(1-r^2) \\
u_{020} = & f_{020} + g_{020}\cos 2\varphi \tag{2.66}
\end{aligned}$$

where

$$\begin{aligned}
f_{020} = & -\frac{c^3}{360 \times 768^2}(1-r^2)^4(37-32r^2+10r^4) - \frac{c}{4608}(1-r^2)^3 \\
g_{020} = & -\frac{c^3}{12600 \times 768^2}r^2(1-r^2)(923-1457r^2+958r^4-302r^6+48r^8) \\
& +\frac{c}{18432}r^2(1-r^2)(5-3r^2) \\
u_{002} = & f_{002} + g_{002}\cos 2\varphi \tag{2.67}
\end{aligned}$$

with

$$\begin{aligned}
f_{002} = & \frac{c^3}{430080 \times 1152^2}(-16525+82320r^2-170436r^4+189728r^6-122598r^8 \\
& +46032r^{10}-9268r^{12}+768r^{14}-21r^{16}) \\
g_{002} = & \frac{Pr c^3}{9800 \times 1152^3}(-362375r^2+883512r^4-807975r^6+352800r^8 \\
& -76440r^{10}+11340r^{12}-882r^{14}+20r^{16})
\end{aligned}$$

$$\begin{aligned}
& + \frac{c^3}{1400 \times 1152^3} (7325r^2 - 6090r^4 - 17640r^6 + 30366r^8 \\
& \quad - 17850r^{10} + 4194r^{12} - 315r^{14} + 10r^{16}) \\
& + \frac{c^2}{7526400 \times 1152^2} (-88447r^2 + 188804r^4 - 121233r^6 + 4704r^8 \\
& \quad + 21560r^{10} - 5712r^{12} + 336r^{14} - 12r^{16}) \\
& w_{110} = f_{110} + g_{110} \cos 2\varphi
\end{aligned} \tag{2.68}$$

with

$$\begin{aligned}
f_{110} &= -\frac{c^4}{8400 \times 1152^2} (1-r^2)^4 (9797 - 9952r^2 + 4100r^4 - 480r^6) \\
& \quad - \frac{c^2}{73728} (1-r^2) (59 - 81r^2 + 39r^4 - r^6) \\
g_{110} &= -\frac{c^4}{5600 \times 1152^2} r^2 (1-r^2) (6017 - 9735r^2 + 6775r^4 - 2465r^6 + 545r^8 - 47r^{10}) \\
& \quad + \frac{c^2}{92160} r^2 (1-r^2) (101 - 89r^2 + 21r^4) \\
& w_{101} = f_{101} + g_{101} \cos 2\varphi
\end{aligned} \tag{2.69}$$

Here

$$\begin{aligned}
f_{101} &= \frac{c^4}{67200 \times 1152^2} (31951 - 162120r^2 + 344400r^4 - 397880r^6 + 271746r^8 \\
& \quad - 111216r^{10} + 25900r^{12} - 2880r^{14} + 105r^{16}) \\
& \quad + \frac{c^2}{6400 \times 1152} (771 - 510r^2 - 950r^4 + 1000r^6 - 325r^8 + 14r^{10}) \\
g_{101} &= \frac{Pr c^4}{705600 \times 1152^2} (140237r^2 - 343224r^4 + 316575r^6 - 141120r^8 \\
& \quad + 32340r^{10} - 5292r^{12} + 540r^{14} - 20r^{16}) \\
& \quad + \frac{c^4}{470400 \times 1152^2} (146801r^2 - 394184r^4 + 433398r^6 - 263424r^8
\end{aligned}$$

$$\begin{aligned}
& +97510r^{10} - 22512r^{12} + 2499r^{14} - 88r^{16}) \\
& + \frac{c^2}{3840 \times 1152} (253r^2 - 644r^4 + 561r^6 - 180r^8 + 10r^{10}) \\
& w_{011} = f_{011} + g_{011} \cos 2\varphi \tag{2.70}
\end{aligned}$$

Here

$$\begin{aligned}
f_{011} &= \frac{c^3}{8400 \times 4608^2} (25337 - 124740r^2 + 253890r^4 - 275380r^6 \\
& + 170625r^8 - 59472r^{10} + 10220r^{12} - 480r^{14}) \\
& + \frac{c}{32 \times 4608} (13 - 40r^2 + 42r^4 - 16r^6 + r^8) \\
g_{011} &= \frac{Pr c^3}{22400 \times 1152^2} (1763r^2 - 4288r^4 + 3900r^6 \\
& - 1680r^8 + 350r^{10} - 48r^{12} + 3r^{14}) \\
& + \frac{c^3}{89600 \times 1152^2} (7615r^2 - 20264r^4 + 21810r^6 \\
& - 12600r^8 + 4130r^{10} - 720r^{12} + 29r^{14}) \\
& + \frac{c}{160 \times 1152} (-21r^2 + 35r^4 - 15r^6 + r^8)
\end{aligned}$$

Temperature

$$\eta_{000} = -\frac{c}{16} (3 - 4r^2 + r^4) \tag{2.71}$$

$$\begin{aligned}
\eta_{100} &= \frac{Pr c^3 \sin \varphi}{240 \times 1152} (-103r + 240r^3 - 220r^5 + 105r^7 - 24r^9 + 2r^{11}) \\
& + \frac{c^3 \sin \varphi}{1200 \times 1152} (-146r + 285r^3 - 200r^5 + 75r^7 - 15r^9 + r^{11}) \\
& + \frac{c \sin \varphi}{96} (19r - 27r^3 + 8r^5) \tag{2.72}
\end{aligned}$$

$$\begin{aligned}\eta_{010} = & \frac{Pr^2 \sin \varphi}{160 \times 1152} (-27r + 60r^3 - 50r^5 + 20r^7 - 3r^9) \\ & + \frac{c^2 \sin \varphi}{960 \times 1152} (-47r + 90r^3 - 60r^5 + 20r^7 - 3r^9)\end{aligned}\quad (2.73)$$

$$\begin{aligned}\eta_{001} = & \frac{Pr^2 \sin \varphi}{3840 \times 1152} (265r - 600r^3 + 520r^5 - 225r^7 + 42r^9 - 2r^{11}) \\ & + \frac{c^2 \sin \varphi}{19200 \times 1152} (381r - 735r^3 + 500r^5 - 175r^7 + 30r^9 - r^{11})\end{aligned}\quad (2.74)$$

$$\eta_{200} = h_{200} + m_{200} \cos 2\varphi \quad (2.75)$$

Where

$$\begin{aligned}h_{200} = & \frac{Pr^2 c^5}{302400 \times 1152^2} (97207 - 519120r^2 + 1188810r^4 - 1536360r^6 + 1242045r^8 \\ & - 655452r^{10} + 225540r^{12} - 48060r^{14} + 5670r^{16} - 280r^{18}) \\ & + \frac{Pr^5}{525 \times 1152^3} (58721 - 294336r^2 + 618408r^4 - 712488r^6 + 498456r^8 \\ & - 223776r^{10} + 66276r^{12} - 12528r^{14} + 1323r^{16} - 56r^{18}) \\ & + \frac{c^5}{2800 \times 11340 \times 1152^2} (4741147 - 1167736r^2 + 15082200r^4 - 14597100r^6 \\ & + 9823275r^8 - 4516722r^{10} + 1384740r^{12} - 267300r^{14} + 28350r^{16} - 1225r^{18}) \\ & + \frac{Pr^3}{50 \times 1152^2} (-7877 + 51780r^2 - 105300r^4 + 99800r^6 - 48975r^8 + 11592r^{10} - 1020r^{12}) \\ & + \frac{c^3}{19200 \times 1152} (2905 - 2968r^2 - 1080r^4 + 1800r^6 - 825r^8 + 180r^{10} - 12r^{12}) \\ & + \frac{c}{384} (-6 - 28r^2 + 51r^4 - 17r^6) \\ m_{200} = & \frac{Pr^2 c^5}{100800 \times 1152^2} (-2132r^2 - 4620r^4 + 27510r^6 - 41748r^8 \\ & + 31395r^{10} - 13176r^{12} + 3150r^{14} - 400r^{16} + 21r^{18})\end{aligned}$$

$$\begin{aligned}
& + \frac{Pr^5}{1750 \times 1152^3} (806072r^2 - 2292480r^4 + 2711190r^6 - 1762464r^8 \\
& \quad + 680400r^{10} - 167760r^{12} + 27595r^{14} - 2640r^{16} + 87r^{18}) \\
& + \frac{c^5}{3675 \times 1152^3} (239005r^2 - 582760r^4 + 578844r^6 - 331884r^8 \\
& \quad + 122598r^{10} - 30744r^{12} + 5481r^{14} - 564r^{16} + 24r^{18}) \\
& + \frac{Pr^3}{67200 \times 1152} (-12189r^2 + 31220r^4 - 32340r^6 + 17458r^8 - 4585r^{10} + 436r^{12}) \\
& + \frac{c^3}{175 \times 1152^2} (-24034r^2 + 52360r^4 - 42945r^6 + 18396r^8 - 4095r^{10} + 318r^{12}) \\
& \quad + \frac{c}{1536} (149r^2 - 220r^4 + 71r^6) \\
& \eta_{020} = h_{020} + m_{020} \cos 2\varphi \tag{2.76}
\end{aligned}$$

Here

$$\begin{aligned}
h_{020} &= \frac{Pr^2 c^3}{11200 \times 1152^2} (563 - 2835r^2 + 5985r^4 - 6895r^6 + 4725r^8 - 1953r^{10} + 455r^{12} - 45r^{14}) \\
& + \frac{Pr^3}{134400 \times 1152^2} (2071 - 9870r^2 + 19320r^4 - 20090r^6 + 12075r^8 - 4326r^{10} + 910r^{12} - 90r^{14}) \\
& + \frac{c^3}{125440 \times 1152^2} (3029 - 7252r^2 + 8820r^4 - 7840r^6 + 4655r^8 - 1764r^{10} + 392r^{12} - 40r^{14}) \\
& \quad + \frac{c}{768 \times 1152} (25 - 48r^2 + 36r^4 - 16r^6 + 3r^8) \\
m_{020} &= \frac{Pr^2 c^3}{89600 \times 1152^2} (37r^2 - 1680r^4 + 4830r^6 - 5600r^8 + 3220r^{10} - 912r^{12} + 105r^{14}) \\
& + \frac{Pr^3}{134400 \times 1152^2} (5245r^2 - 14000r^4 + 14700r^6 - 7644r^8 + 1855r^{10} - 156r^{12}) \\
& + \frac{c^3}{134400 \times 1152^2} (766r^2 - 1846r^4 + 1785r^6 - 966r^8 + 315r^{10} - 60r^{12} + 6r^{14}) \\
& \quad + \frac{c}{960 \times 1152} (-13r^2 + 25r^4 - 15r^6 + 3r^8)
\end{aligned}$$

$$\eta_{002} = h_{002} + m_{002}\cos 2\varphi \quad (2.77)$$

where

$$\begin{aligned} h_{002} = & \frac{Pr^2c^3}{13440 \times 1152^3} (129578 - 667800r^2 + 1457190r^4 - 1762320r^6 + 1300005r^8 \\ & - 604044r^{10} + 173124r^{12} - 27756r^{14} + 2079r^{16} - 56r^{18}) \\ & + \frac{Pr^3c^3}{67200 \times 1152^3} (197494 - 960120r^2 + 1934226r^4 - 2100588r^6 + 1351413r^8 \\ & - 539784r^{10} + 136080r^{12} - 20016r^{14} + 1323r^{16} - 28r^{18}) \\ & + \frac{c^3}{6125 \times 1152^4} (32277522 - 78080625r^2 + 97240500r^4 - 89478900r^6 + 56029050r^8 \\ & - 23171022r^{10} + 6041700r^{12} - 893700r^{14} + 56700r^{16} - 1225r^{18}) \\ m_{002} = & \frac{Pr^2c^3}{224 \times 537600 \times 1152^2} (843810r^2 - 2640232r^4 + 3586156r^6 - 2779560r^8 \\ & + 1308790r^{10} - 375984r^{12} + 61397r^{14} - 4496r^{16} + 119r^{18}) \\ & + \frac{Pr^3c^3}{960 \times 9800 \times 1152^3} (35391181r^2 - 89303680r^4 + 86668470r^6 - 39870432r^8 \\ & + 6703200r^{10} + 624960r^{12} - 223020r^{14} + 10080r^{16} - 759r^{18}) \\ & + \frac{c^3}{134400 \times 1152^3} (-32212r^2 + 58600r^4 - 18270r^6 - 28224r^8 \\ & + 30366r^{10} - 12240r^{12} + 2097r^{14} - 120r^{16} + 3r^{18}) \\ & + \frac{c^2}{1568000 \times 1152^3} (795951r^2 - 1768940r^4 + 1416030r^6 - 484932r^8 \\ & + 11760r^{10} + 36960r^{12} - 7140r^{14} + 320r^{16} - 9r^{18}) \end{aligned}$$

$$\eta_{110} = h_{110} + m_{110}\cos 2\varphi \quad (2.78)$$

where

$$\begin{aligned}
h_{110} = & \frac{Pr^2c^4}{134400 \times 1152^2} (34163 - 177240r^2 + 390180r^4 - 477400r^6 \\
& + 357420r^8 - 169008r^{10} + 49280r^{12} - 7920r^{14} + 525r^{16}) \\
& + \frac{Pr^4}{268800 \times 1152^2} (20795 - 101696r^2 + 206556r^4 - 226912r^6 \\
& + 148330r^8 - 60480r^{10} + 15596r^{12} - 2336r^{14} + 147r^{16}) \\
& + \frac{c^4}{940800 \times 1152^2} (112955 - 274316r^2 + 343980r^4 - 319480r^6 \\
& + 202615r^8 - 85260r^{10} + 22736r^{12} - 3440r^{14} + 210r^{16}) \\
& + \frac{Pr^2c^2}{19200 \times 1152} (-1027 + 6510r^2 - 12450r^4 + 10600r^6 - 4275r^8 + 642r^{10}) \\
& + \frac{c^2}{38400 \times 1152} (5407 - 8380r^2 + 3900r^4 - 1100r^6 + 25r^8 + 48r^{10}) \\
m_{110} = & \frac{Pr^2c^4}{67200 \times 1152^2} (-508r^2 - 4340r^4 + 16275r^6 \\
& - 21392r^8 + 14070r^{10} - 4920r^{12} + 875r^{14} - 60r^{16}) \\
& + \frac{Pr^4}{1225 \times 1152^3} (364057r^2 - 1010310r^4 + 1143072r^6 \\
& - 688086r^8 + 232260r^{10} - 46746r^{12} + 6195r^{14} - 442r^{16}) \\
& + \frac{c^4}{1225 \times 1152^3} (52085r^2 - 126357r^4 + 124047r^6 \\
& - 69342r^8 + 24255r^{10} - 5418r^{12} + 777r^{14} - 47r^{16}) \\
& + \frac{Pr^2c^2}{7680 \times 1152} (-30r^2 + 40r^4 - 45r^6 + 56r^8 - 21r^{10}) \\
& + \frac{c^2}{1920 \times 1152} (-136r^2 + 277r^4 - 195r^6 + 62r^8 - 8r^{10})
\end{aligned}$$

$$\eta_{101} = h_{101} + m_{101} \cos 2\varphi \quad (2.79)$$

Here

$$\begin{aligned}
h_{101} = & \frac{Pr^2c^4}{4200 \times 1152^3}(-501881 + 2633400r^2 - 5889240r^4 + 7369320r^6 \\
& - 5700870r^8 + 2831976r^{10} - 894600r^{12} + 167400r^{14} - 16065r^{16} + 560r^{18}) \\
& + \frac{Pr^4}{8400 \times 1152^3}(-304597 + 1503936r^2 - 3695820r^4 + 3467184r^6 \\
& - 2331882r^8 + 991872r^{10} - 272916r^{12} + 46080r^{14} - 3969r^{16} + 112r^{18}) \\
& + \frac{c^4}{441000 \times 1152^3}(-24731219 + 60387390r^2 - 76601760r^4 + 72324000r^6 \\
& - 46999575r^8 + 20543544r^{10} - 5838840r^{12} + 999000r^{14} - 85050r^{16} + 2450r^{18}) \\
& + \frac{Pr^2}{800 \times 1152^2}(20201 - 129900r^2 + 254700r^4 - 227000r^6 + 100275r^8 - 19296r^{10} + 1020r^{12}) \\
& + \frac{c^2}{307200 \times 1152}(-7623 + 7728r^2 + 2880r^4 - 4600r^6 + 1975r^8 - 372r^{10} + 12r^{12}) \\
m_{101} = & \frac{Pr^2c^4}{19600 \times 1152^3}(-901994r^2 + 3239712r^4 - 5184816r^6 \\
& + 4770192r^8 - 2672460r^{10} + 913248r^{12} - 181167r^{14} + 17936r^{16} - 651r^{18}) \\
& + \frac{Pr^4}{294000 \times 1152^3}(-28769699r^2 + 79473200r^4 - 89945730r^6 \\
& + 54780768r^8 - 19051200r^{10} + 4049640r^{12} - 584325r^{14} + 47880r^{16} - 534r^{18}) \\
& + \frac{c^4}{49000 \times 1152^3}(-598003r^2 + 1468010r^4 - 1478190r^6 \\
& + 866796r^8 - 329280r^{10} + 83580r^{12} - 14070r^{14} + 1190r^{16} - 33r^{18}) \\
& + \frac{Pr^2}{1075200 \times 1152}(-56141r^2 + 146580r^4 - 144585r^6 + 66262r^8 - 12880r^{10} + 764r^{12}) \\
& + \frac{c^2}{2800 \times 1152^2}(18554r^2 - 33740r^4 + 19845r^6 - 5376r^8 + 735r^{10} - 18r^{12})
\end{aligned}$$

$$\eta_{011} = h_{011} + m_{011}\cos 2\varphi \quad (2.80)$$

where

$$\begin{aligned}
h_{011} = & \frac{Pr^2 c^3}{2150400 \times 1152^2} (-88211 + 449400r^2 - 964740r^4 + 1139320r^6 \\
& - 811020r^8 + 356496r^{10} - 92960r^{12} + 12240r^{14} - 525r^{16}) \\
& + \frac{Pr c^3}{4300800 \times 1152^2} (-53931 + 259616r^2 - 515676r^4 + 548352r^6 \\
& - 341530r^8 + 129696r^{10} - 30156r^{12} + 3776r^{14} - 147r^{16}) \\
& + \frac{c^3}{940800 \times 4608^2} (-294695 + 709436r^2 - 873180r^4 + 789880r^6 \\
& - 481915r^8 + 191100r^{10} - 46256r^{12} + 5840r^{14} - 210r^{16}) \\
& + \frac{c}{9600 \times 4608} (-503 + 975r^2 - 750r^4 + 350r^6 - 75r^8 + 3r^{10}) \\
m_{011} = & \frac{Pr^2 c^3}{6 \times 1120^2 \times 1152^2} (-130520r^2 + 461132r^4 - 711921r^6 \\
& + 613424r^8 - 307230r^{10} + 86856r^{12} - 12257r^{14} + 516r^{16}) \\
& + \frac{Pr c^3}{140^2 \times 1152^3} (-540835r^2 + 1419138r^4 - 1458072r^6 \\
& + 736806r^8 - 167580r^{10} + 9954r^{12} + 567r^{14} + 22r^{16}) \\
& + \frac{c^3}{140^2 \times 1152^3} (-65381r^2 + 159915r^4 - 159579r^6 \\
& + 91602r^8 - 33075r^{10} + 7434r^{12} - 945r^{14} + 29r^{16}) \\
& + \frac{c}{160 \times 48^3} (86r^2 - 168r^4 + 105r^6 - 24r^8 + r^{10})
\end{aligned}$$

It is apparent that w_{000} and η_{000} give the velocity and temperature distributions in a stationary straight tube. The results (2.50), (2.55), (2.62) and (2.65) are the corresponding solutions for a stationary curved tube calculated by Topakoglu (1967).

And the solutions (2.51), (2.56), (2.63) and (2.66) are in agreement with Barua (1954).

Similarly, we may obtain higher order solutions. However, the amount of labour required is considerable. And it is hard to tell exactly that under what conditions the higher order solutions are needed until we get enough terms to unveil the analytic structure of the solution. Usually a perturbation solution is carried to the second approximation. Now, the routine labour of calculating higher approximations may be delegated to a computer. Then, dozens or even hundreds of terms may typically be found. These may suffice to permit the structure of the solution to be analyzed for a single power series, and the solution may be improved to extend its utility (Aziz 1988, Aziz & Na 1984 and Van Dyke 1975). Unfortunately, there is no such approach available for analyzing the multiple series in this problem. Besides, even for single power series, one must obtain the first few terms of the solution by hand in order to use computer to get higher order solutions.

It should be noted that the solutions of ϕ , w and η reduce to the corresponding ones of the six special cases by setting any one or two of σ , Re_Ω and Ra_Ω to be zero. They are Dean problem, Coriolis problem, mixed convection problem, Dean problem with the effect of rotation, Dean problem with the effect of heating/cooling and Coriolis problem with the effect of heating/cooling.

2.4 Concluding Remarks

For any continuous function of one or more variables, there exists a unique, uniformly convergent polynomial which can be used to approximate the function. Assuming that the stream function ϕ , the main velocity w and the temperature η are continuous on the curvature ratio σ , the rotational Reynolds number Re_Ω and the rotational Rayleigh number Ra_Ω , a systematic method is developed to determine an approximate analytical solution for velocity and temperature fields in a rotating curved tube under the conditions that the flow and temperature fields are fully developed, and the wall heat flux is uniform with peripherally uniform wall temperature.

Each of the functions ϕ , w and η is expanded in a triple power series in terms of σ , Re_Ω and Ra_Ω . The coefficients in these expansion series may be obtained from the solutions of the associated nonhomogeneous harmonic and biharmonic differential equations. In calculating each additional term of the series, the terms on the right hand sides of the harmonic and biharmonic differential equations, are in terms of the functions determined from the solution of the preceding harmonic and biharmonic differential equations. Therefore the successive solutions of the three main differential equations will produce as many terms as desired for the three series depending upon the accuracy required. In this work, the solution is carried up to and including the second-order terms. And the analytical expressions for the velocity and temperature distributions are applicable for both heating and cooling cases,

and also for both cases in which the rotation of the tube is in the same direction or opposite to the main flow imposed by the pressure gradient.

By setting any one or two of σ , Re_Ω and Ra_Ω to be zero, the solution reduces to the corresponding six special cases, i.e., Dean problem, Coriolis problem, mixed convection problem, Dean problem with effect of rotation, Dean problem with effect of heating/cooling and Coriolis problem with effect of heating/cooling.

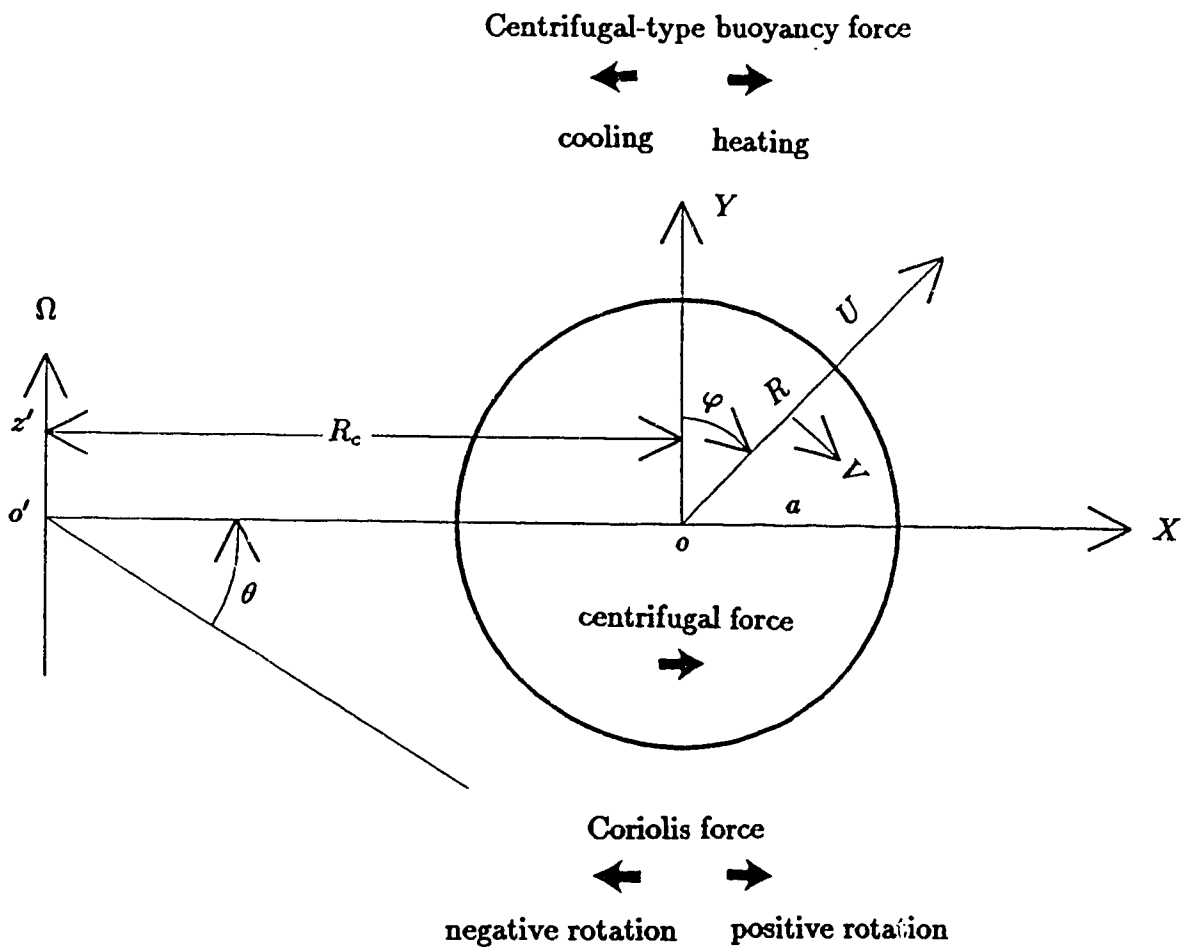


Figure 2.1. Geometrical configuration and toroidal coordinate system

References

- [1] Aziz, A. 1988 Perturbation Methods. In *Handbook of Numerical Heat Transfer* (ed. W.J. Minkowycz, E.M. Sparrow, G.E. Schneider & R.H. Pletcher), pp.625-671. John Wiley & Sons Inc., New York.
- [2] Aziz, A. & Na, T.Y. 1984 *Perturbation Methods in Heat Transfer*. Hemisphere, New York.
- [3] Barua, S.N. 1954 Secondary flow in a rotating straight pipe. *Proc. R. Soc. Lond.* **A227**, 133-139.
- [4] Berger, S.A. 1991 Secondary heat transfer in curved pipes and tubes. AIAA91-0030, 29th Aeronautical Sciences Meeting, Nevada, USA.
- [5] Berger, S.A., Talbot, L. & Yao, L.S. 1983 Flow in curved pipes. *Annu. Rev. Fluid Mech.* **15**, 461-512.
- [6] Cheng, K.C. & Hwang, G.J. 1969 Numerical solution for combined free and forced laminar convection in horizontal rectangular channels. *J. Heat Transfer* **91**, 59-66.
- [7] Cheng, K.C., Lin, R.C. & Ou, J.W. 1976 Fully developed laminar flow in curved rectangular channels. *J. Fluid Eng.* **98**, 41-48.
- [8] Cheng, K.C. & Wang, L. 1993a The effects of Coriolis and centrifugal forces on transition to turbulence in a rotating curved rectangular channel. In *Transport*

Phenomena in Thermal Eng. **3**, 297-304.

- [9] Cheng, K.C. & Wang, L. 1993b The effects of centrifugal and Coriolis forces on secondary flow phenomena in rotating curved square channels-visualizations for positive and negative rotations. *ASME, FED* **172**, 359-367.
- [10] Cheng, K.C., Wang, L. & Faulkner, B.G. 1993 Visualization of instability phenomena in a rotating curved rectangular channel with aspect ratio 10. In *Transport Phenomena and Dynamics of Rotating Machinery*, **A.**, pp.549-560. Hemisphere Publishing Corporation.
- [11] Dean, W.R. 1928 The stream-line motion of a fluid in a curved pipe. *Phil. Mag.* **5**, 673-695.
- [12] Dennis, S.C.R. & Ng, M. 1982 Dual solutions for steady laminar flow through a curved tube. *Q.J. Mech. Appl. Maths.* **35**, 305-324.
- [13] Guo, Y. & Finlay, W.H. 1991 Splitting, merging and wavelength selection of vortices in curved and/or rotating channel flow due to Eckhaus instability. *J. Fluid Mech.* **228**, 661-691.
- [14] Hwang, G.J. & Chao, C.H. 1991 Forced laminar convection in a curved isothermal square duct. *J. Heat Transfer* **113**, 48-55.
- [15] Hwang, G.J. & Cheng, K.C. 1970 Boundary vorticity method for convective heat transfer with secondary flow-applications to the combined free and forced

- convection in horizontal tubes. *Heat Transfer* 1970, paper NC3.5.
- [16] Hwang, G.J. & Jen, T.C. 1987 Forced laminar convection in fully developed flow in a rotating isothermal duct with the effect of axial conduction. *Proc. 2nd ASME-JSME Thermal Engineering Joint Conf.*, Honolulu, USA, **2**, 43-49.
- [17] Hwang, G.J. & Jen, T.C. 1990 Convective heat transfer in rotating isothermal ducts. *Int. J. Heat Mass Transfer* **33**, 1817-1828.
- [18] Hwang, G.J. & Kuo, C.R. 1992 Experimental study of convection heat transfer in a radially rotating square duct with uniform heat flux. *The Fourth Int. Symposium on Transport Phenomena and Dynamics of Rotating Machinery (ISROMAC-4)*, Honolulu, USA, April 5-8.
- [19] Hwang, G.J. & Kuo, C.R. 1993 Experimental study of convective heat transfer in a rotating square duct with radial outward flow. *ASME: Gas Turbine Heat Transfer*, HTD-vol.242.
- [20] Hwang, G.J. & Soong, C.Y. 1989 Experimental automation and heat transfer measurement on a rotating thermal system. *Transport Phenomena in Thermal Control* (Ed. by G.J. Hwang), Hemisphere Pub. Corp., New York, 375-388.
- [21] Hwang, G.J. & Soong, C.Y. 1992 Convective heat transfer in rotating channels. *The Fourth Int. Symposium on Transport Phenomena and Dynamics of Rotating Machinery (ISROMAC-4)*, Honolulu, USA, April 5-8.

- [22] Hocking, L.M. 1967 Boundary and shear layers in a curved rotating pipe. *J. Math. Phys. Sci.* **1**, 123-136.
- [23] Ito, H. 1987 Flow in curved pipes. *JSME Int. J.* **30**, 543-552.
- [24] Ito, H. & Motai, T., 1974 Secondary flow in a rotating curved pipe. *Rep. Inst. High Speed Mech.* **29**, 33-57.
- [25] Jen, T.C., Lavine, A.S. & Hwang, G.J. 1992 Simultaneous developing laminar convection in rotating isothermal square channels. *Int. J. Heat Mass Transfer* **35**, 239-254.
- [26] Kheshgi, H.S. & Scriven, L.E. 1985 Viscous flow through a rotating square channel. *Phys. Fluids* **28**, 2968-2979.
- [27] Ludwig, H. 1951 Die ausgebildete kanalstromung in einem rotierenden system. *Ing.-Arch. Bd.* **19**, 296-308.
- [28] Miyazaki, H. 1971 Combined free and forced convective heat transfer and fluid flow in a rotating curved circular tube. *Int. J. Heat Mass Transfer* **14**, 1295-1309.
- [29] Miyazaki, E. 1973 Combined free and forced convective heat transfer and fluid flow in a rotating curved rectangular tubes. *J. Heat Transfer* **95**, 64-71.
- [30] Morris, W.D. 1981 *Heat transfer and fluid flow in rotating coolant channels*. Research Studies Press, John Wiley and Sons.

- [31] Nandakumar, K. & Masliyah, J.H. 1986 Swirling flow and heat transfer in coiled and twisted pipes. In *Advances in Transport Processes* **4**, 49-112.
- [32] Nandakumar, K., Masliyah, J.H. & Law, H.S. 1985 Bifurcation in steady laminar mixed convection flow in horizontal ducts. *J. Fluid Mech.* **152**, 145-161.
- [33] Nandakumar, K., Raszillier, H. & Durst, F. 1991 Flow through rotating rectangular ducts. *Phys. Fluids* **A3**, 770-781.
- [34] Nandakumar, K. & Weinitschke, H.J. 1991 A bifurcation study of mixed convection heat transfer in horizontal ducts. *J. Fluid Mech.* **231**, 157-187.
- [35] Papanu, J.S., Adler, R.J., Gorenssek, M.B. & Menon, M.M. 1986 Separation of fine particle dispersions using periodic flows in a helically twisted tube. *AIChE J.* **32**, 798-808.
- [36] Piesche, M. 1982 Experimente zum strömungswiderstand in gekrümmten, rotierenden kanalen mit quadratischem querschnitt. *Acta Mech.* **42**, 145-151.
- [37] Piesche, M. & Felsch, K.O. 1980 Experimental investigation of pressure loss in rotating curved rectangular channels. *Archives of Mechanics* **32**, 747-752.
- [38] Qiu, L., Wang, L. & Sun, Y. 1988 Experimental study on rotating tube heat exchangers. In Proc. Chinese National Congress on Heat Recovery, pp.200-206.
- [39] Qiu, L., Wang, L. & Sun, Y. 1990 Heat transfer from tubes which extend radially outward from a rotating shaft. In *Heat transfer enhancement and energy*

- conservation* (ed. S.J. Deng, T.N. Veziroğlu, Y.K. Tan and L.Q. Chen), pp.231-236. Hemisphere Publishing Corporation.
- [40] Ravi Sankar, S., Nandakumar, K. & Masliyah, J.H. 1988 Oscillatory flows in coiled square ducts. *Phys. Fluids* **31**, 1348-1359.
- [41] Soong, C.Y. & Hwang, G.J. 1990 Laminar mixed convection in a radially rotating semiporous channel. *Int. J. Heat Mass Transfer* **33**, 1805-1817.
- [42] Soong, C.Y., Lin, S.T. & Hwang, G.J. 1991 An experimental study of convective heat transfer in radially rotating rectangular ducts. *J. Heat Transfer* **113**, 604-611.
- [43] Speziale, C.G. 1982 Numerical study of viscous flow in rotating rectangular ducts. *J. Fluid Mech.* **122**, 251-271.
- [44] Speziale, C.G. & Thangam, S. 1983 Numerical study of secondary flows and roll cell instabilities in rotating channel flow. *J. Fluid Mech.* **130**, 377-395.
- [45] Topakoglu, H.C. 1967 Steady laminar flows of an incompressible viscous fluid in curved pipes. *J. Math. Mech.* **16**, 1321-1337
- [46] Van Dyke, M. 1975 Computer extension of perturbation series in fluid mechanics. *SIAM J. Appl. Math.* **28**, 720-734.
- [47] Van Dyke, M. 1978 Extended Stokes series: laminar flow through a loosely coiled pipe. *J. Fluid Mech.* **86**, 129-145.

- [48] Van Dyke, M. 1990 Extended Stokes series: laminar flow through a heated horizontal pipe. *J. Fluid Mech.* **212**,289-308.
- [49] Winters, K.H. 1987 A bifurcation study of laminar flow in a curved tube of rectangular cross- section. *J. Fluid Mech.* **180**, 343-369.

Chapter 3

Flow Transitions and Combined Free and Forced Convective Heat Transfer in a Rotating Curved Circular Tube–II: Flow and Heat Transfer Characteristics

The simultaneous effects of curvature, rotation and heating/cooling of the tube complicate the flow and heat transfer characteristics beyond those observed in the tubes with only curvature, rotation or heating/cooling. The phenomena encountered are investigated for steady, hydrodynamically and thermally fully developed

laminar flow in circular tubes based on the perturbation solution for the velocity and temperature distributions obtained in Chapter 2. The results contain both the nature of flow transitions and the effect of these transitions on temperature distribution, friction factor and Nusselt number. When the rotation is in the same direction as the main flow imposed by a pressure gradient and the fluid is heated, the flow and heat transfer remain similar to those observed in stationary curved tubes, radially rotating straight tubes or mixed convection in stationary straight tubes. There are, however, quantitative changes due to the combined effects of centrifugal, Coriolis and buoyancy forces. A more complex behaviour is possible when the rotation is opposite to the flow due to the pressure gradient or when the fluid is cooled. In particular, the inward Coriolis force and/or buoyancy force may cause the direction of the secondary flow to reverse. The flow reversal occurs by passing through a four-cell vortex flow region where overall, the centrifugal, Coriolis and buoyancy force just neutralize each other.

3.1 Introduction

In Chapter 2 (also see Wang & Cheng 1994), we obtained a full second-order perturbation solution for velocity and temperature distributions in a rotating curved circular tube under the conditions that the laminar flow and temperature fields are fully developed, and the wall heat flux is uniform with peripherally uniform wall temperature. The geometrical configuration of the physical model is shown in

Fig.3.1 for convenience. The analytical expressions of the velocity and temperature obtained are applicable for both heating and cooling cases, with the rotation in the same or opposite direction to the main flow imposed by a pressure gradient. The work presented here is to explore the flow and heat transfer characteristics based on the solution obtained in Chapter 2.

In addition to the viscous and inertial forces, the fluid in the rotating curved tube is subjected to centrifugal force (due to the curvature of the tube), Coriolis force (due to the rotation and curvature) and the centrifugal-type buoyancy force (resulting from temperature-induced density variation of the fluid in the rotating field). While the centrifugal and buoyancy forces act in the plane of cross section, the Coriolis forces have components both in the plane of the cross section and along the normal to the plane. That due to the curvature is $-W(U\sin\varphi + V\cos\varphi)/(R_c + R\sin\varphi)$ (θ -component, Eq.(2.4)). Those due to rotation is perpendicular to both the axis of rotation and the direction of the relative velocity of the fluid, i.e. $-2\Omega(U\sin\varphi + V\cos\varphi)$ (θ -component, Eq.(2.4)), $2\Omega W\sin\varphi$ (r -component, Eq.(2.2)), and $2\Omega W\cos\varphi$ (φ -component, Eq.(2.3)). The two θ -components of the Coriolis force may act in the direction or direction opposite to the main flow depending on the signs of $(U\sin\varphi + V\cos\varphi)/(R_c + R\sin\varphi)$ and $\Omega(U\sin\varphi + V\cos\varphi)$. Consequently, they may accelerate or decelerate the main flow. Furthermore, these two components either enhance or cancel each other depending on the rotation direction of the tube. If the rotation is positive, they enhance each other in the flow domain with $R_c + R\sin\varphi > 0$, and

cancel each other in the flow domain with $R_c + R\sin\varphi < 0$ (This hardly happens for the case of loose coils). Otherwise, they cancel each other in the domain with $R_c + R\sin\varphi > 0$, and enhance each other in the domain with $R_c + R\sin\varphi < 0$.

In the plane of the cross section, the centrifugal force always acts outwards irrespective of the directions of rotation and heat flux. However, the Coriolis force may act either radially outwards or radially inwards depending on the rotation direction. If the rotation is positive, it will act radially outwards. When the rotation is negative, however, it will act radially inwards. Similarly, the centrifugal-type buoyancy force may act radially outwards or radially inwards depending on the direction of the heat flux. If the fluid is heated, it will be radially outwards. If the fluid is cooled, it will act radially inwards. From this analysis about force directions, it is clear that centrifugal, Coriolis and buoyancy forces enhance each other for some cases, and cancel each other for other cases. This may result in a richer structure of flow transitions and rather complex characteristics of heat transfer than those of the tube with only rotation, curvature or heating/cooling.

The contents of the present chapter are: Flow transitions in secondary flow and main flow are examined in §3.2 and §3.3, respectively. §3.4 and §3.5 deal with the effects of flow transitions on temperature distributions, and friction resistance and heat transfer, respectively. The structure of solutions for velocity and temperature fields is analyzed in §3.6.

3.2 Flow Transitions in Secondary Flow

3.2.1 First-order approximation

To the first order of approximation, the secondary flow pattern is determined by

ϕ_1

$$\phi_1 = \frac{\sigma c^2}{288} r(1 - r^2)^2 [4 - r^2 + L_2(r^2 - 10) + L_1] \cos \varphi$$

It reaches its extreme values under the conditions

$$\frac{\partial \phi_1}{\partial r} = \frac{\partial \phi_1}{\partial \varphi} = 0$$

which give

$$7(1 - L_2)r^4 - (24 + 5L_1 - 53L_2)r^2 + (4 + L_1 - 10L_2) = 0 \quad (3.1)$$

$$\sin \varphi = 0 \quad (3.2)$$

It is clear that at the extreme points, both the radial and tangential components of the velocity in the cross section vanish by the definition of stream function and the extreme conditions. The streamlines of motion through these points are clearly circles (parallel to the axis of the tube) with the centers located at the axis of the rotation of the tube. The motion of the fluid may be, then, regarded as helical motions about these circular streamlines. In other words, the locations of the extreme points of ϕ_1 represent the centers of the screw motion of the fluid. The extreme values, on the other hand, have two implications. Their absolute values reflect the

strength of the secondary flow, and their sign denotes the direction of the screw motion, namely, positive for counter-clockwise circulation and negative for clockwise circulation.

The locations of the extreme points are determined by the solutions of the Eqs.(3.1) and (3.2). Equation (3.2) has two solutions in the flow domain $0 \leq \varphi < 2\pi$, namely, $\varphi = 0$ and $\varphi = \pi$. Thus, all extreme points are located along the vertical centerline.

The radial distance of the extreme points is determined by the solutions of the Eq.(3.1) which depend on the two dimensionless parameters, namely, L_1 and L_2 . Their physical implications will be analyzed later in this Chapter (ratios of the Coriolis force and buoyancy force over the centrifugal force). In the flow domain $0 \leq r \leq 1$, Eq.(3.1) has only one solution (r_{1m}) which gives a minimum value of ϕ_1 with a negative sign for some L_1 and L_2 . For some other L_1 and L_2 , Eq.(3.1) has only one solution (r_{2m}) which yields a maximum value of ϕ_1 with a positive sign. And for still other L_1 and L_2 , Eq.(3.1) has two solutions (r_{1m} and r_{2m}) which result a minimum value of ϕ_1 with a negative sign and a maximum value of ϕ_1 with a positive sign, respectively. The structure of the solution is summarized in Table 3.1.

This shows that in the laminar flow region, the secondary flow experiences two transitions which occur at $L_1 = 10L_2 - 4$ and $L_1 = 9L_2 - 3$, respectively. Consequently, the secondary flow appears as three different patterns, namely, two-cell

Table 3.1: Distribution of the solution with L_1 and L_2

$L_2 \leq 1$			
Region	$L_1 \leq 10L_2 - 4$	$10L_2 - 4 \leq L_1 \leq 9L_2 - 3$	$L_1 \geq 9L_2 - 3$
Solution	r_{1m}	$r_{1m} \ \& \ r_{2m}$	r_{2m}
$L_2 \geq 1$			
Region	$L_1 \leq 9L_2 - 3$	$9L_2 - 3 \leq L_1 \leq 10L_2 - 4$	$L_1 > 10L_2 - 4$
Solution	r_{1m}	$r_{1m} \ \& \ r_{2m}$	r_{2m}

of counter-rotating and counterclockwisely circulating vortices; two-cell of counter-rotating and clockwisely circulating vortices; and two-pair (four-cell) of counter-rotating vortices which are oppositely directed to each other.

The first column of Fig.3.2 illustrates the secondary flow patterns for several representative values of L_1 with $L_2 = -1.0$. The symmetry about the horizontal centerline allows us to show the upper half of the cross section only. In the figure, the stream function is normalized by its maximum absolute value. The cross in the figure denotes the position at which the stream function reaches its maximum absolute value. And two numbers for each case are the value of the L_1 and the extreme value of the stream function which yields the maximum absolute value. A vortex with a positive (negative) value of the stream function indicates a counterclockwise (clockwise) circulation.

When $L_1 \geq 9L_2 - 3$ ($L_1 \geq 10L_2 - 4$) for $L_2 \leq 1$ ($L_2 \geq 1$), the secondary flow appears as two-cell, counter-rotating vortices as shown in Fig.3.2(a)(b). When L_1 is in the region $10L_2 - 4 < L_1 < 9L_2 - 3$ ($9L_2 - 3 < L_1 < 10L_2 - 4$) for $L_2 \leq 1$ ($L_2 \geq 1$), the secondary flow appears as two-pair (four-cell), counter-rotating vortices with one pair in clockwise circulation and the other in counterclockwise circulation (Fig.3.2(c)(d)(e)). When $L_1 \leq 10L_2 - 4$ ($L_1 \leq 9L_2 - 3$) for $L_2 \leq 1$ ($L_2 \geq 1$), however, the secondary flow becomes two-cell counter-rotating vortices again, but with the direction of clockwise circulation as shown in Fig.3.2(f)(g).

Three points are to be noted regarding the four-cell vortex structure as shown in Fig.3.2(c)(d)(e). First, this four-cell vortex structure is qualitatively different from the four-cell vortex family in Dean, Coriolis or mixed convection problems. Second, its structure is different from the four-cell vortex structure in Dean flow. This is indicated by the maximum absolute value of the stream function in this region. The analysis of force mechanism in §3.1 suggests that the centrifugal forces and the Coriolis forces, overall, just neutralize each other in this region. And third, the vortices occur at the location of the clockwise circulating vortices. They occur near the tube wall if $L_2 \leq 1$, as shown in Fig.3.2(c)(d)(e). If $L_2 \geq 1$, however, they will appear in the central portion of the cross section of the tube as shown in Fig.3.3.

The variations of r_{1m} and r_{2m} with different L_1 and L_2 are shown in Fig.3.4. Two interesting features are evident about the locations of the centers of the screw motion. One is that

$$r_{1m} \rightarrow \sqrt{1/5} \quad \text{as} \quad L_1 \rightarrow -\infty$$

and

$$r_{2m} \rightarrow \sqrt{1/5} \quad \text{as} \quad L_1 \rightarrow \infty$$

Another is that r_{1m} and r_{2m} satisfy

$$r_{1m} \geq \sqrt{1/5}, \quad r_{2m} \leq \sqrt{1/5} \quad \text{for } L_2 \leq 1 \text{ (Fig.3.4(a)(b))}$$

and

$$r_{1m} \leq \sqrt{1/5}, \quad r_{2m} \geq \sqrt{1/5} \quad \text{for } L_2 \geq 1 \text{ (Fig.3.4(c))}$$

3.2.2 Second-order approximation

The second column in Fig.3.2 illustrates the secondary flow patterns for several representative values of L_1 with $\sigma = 0.02$, $c = 60$, $Pr = 0.7$ and $L_2 = -1$ based on full second-order approximation. The corresponding first-order secondary flow patterns are shown in the first column of the figure.

A striking feature of the second order secondary flow is that the symmetry about the vertical centerline exhibited in the first order secondary flow breaks down with the circulation center of vortices shifting away from the vertical centerline. And the corresponding vortices are distorted in some way. In particular, the circulation center for all clockwise circulation vortices moves inward and downward, while that for all counter-clockwise circulation vortices moves outward and upward. As well, this trend is more noticeable in the region with four-cell patterns. Another interesting feature about the second order secondary flow is that the region with four-cell

secondary flow is wider than that of the corresponding first order secondary flow. It is worthy to note that the secondary flow in this region is quite weaker than that in the region far from this region by comparing their extreme values of the stream function.

Three factors contribute to the generation of the secondary flow in this problem: curvature, rotation and heating/cooling. The secondary flow patterns discussed in Fig.3.2 result from the combined effect of all these three factors. The analytical solutions obtained in Chapter 2, however, allow us to visualize the secondary flow produced due to one or any two of these three factors simply by setting some terms in the series to be zero. In other words, the solutions can be used to analyze the secondary flows for several special cases. They are secondary flows in curved tubes (classical Dean problem), radially rotating tubes (Coriolis problem), stationary straight tubes with heating/cooling (mixed convection problem), rotating curved tubes, curved tubes with heating/cooling and radially rotating straight tubes with heating/cooling. Figures 3.5 and 3.6 are two sets of such secondary flows, which exhibit several interesting features to be noted below.

All the first order terms in the series result in a symmetric (about vertical centerline) one pair counter-rotating secondary flow with the centres of circulation located on the vertical centerline. Keeping in mind that the first order approximation is valid for sufficiently small values of the dynamical parameters, the structure of the fully developed secondary flow in Dean problem, Coriolis problem and mixed-convection

problem, then, consists of one pair (two cell) counter-rotating vortices with one vortex flow located in the upper half and the other in the lower half of the cross section at sufficiently small values of the dynamical parameters. As well they are symmetric about the vertical centerline. This is in agreement with the previous works for the corresponding problems.

All the second order terms in the series of the stream function cause the secondary flow to exhibit a four-cell pattern with the center of the circulation located away from the vertical centerline. It is interesting to note that like secondary flow due to the first order terms, the secondary flow due to the second order term itself is still symmetric about the vertical centerline. The symmetry is, however, lost in the secondary flow resulting from all the first order and second order terms in the series. This breakdown of the symmetry comes from the asymmetric effect of second order terms on the first order terms about the vertical centerline, i.e., the secondary flow of the second order terms enhances that of the first order terms in one side of the vertical centerline, but neutralizes it in the other side of the centerline.

Secondary flow with the simultaneous effect of more than one of curvature, rotation and heating/cooling may be qualitatively similar to or completely different from that with only one factor depending on the region of the governing parameters.

3.3 Flow Transitions in Main Flow

Figure 3.7 shows several typical isovels and profiles of main flow based on the second order approximation. The corresponding secondary flows are shown in Fig.3.2. Once again, the symmetry of flow about the horizontal centerline allows us to show the upper half of the cross section only. A cross in the figure denotes the position at which the main flow reach its maximum value. The value of L_1 and the maximum value of the main velocity w are given in the figure for each case.

Some features of the main flow can be expected and understood through the force balance in the governing equation. It is the secondary flow that causes the deviation of the main flow away from the parabolic profile in Poiseuille flow. The secondary flow affects the main flow through three terms (Eq.(2.4)). They are the convection term, and two Coriolis terms due to the curvature and rotation, respectively. The two Coriolis terms may be in the same direction or opposite to the main flow depending on the sign of $U \sin \varphi + V \cos \varphi$ and Ω . The absence of these three terms leads to the Poiseuille solution with an axisymmetric and parabolic profile (Fig.3.7(a)). The relative importance of the five terms in Eq.(2.4) depends on the magnitudes of the governing parameters, and shows different flow patterns for different regions. The driving term is the axial pressure gradient which is always important. The viscous term is always important near the wall, but may not be significant in the core region for certain ranges of the parameters. If the rotation speed is high enough, the Coriolis terms could be of the same order of magnitude as

that of the pressure gradient term. The main flow would, then, exhibit a geostrophic pattern in the center of the cross section surrounded by a thin boundary layer according to the theory of rotating fluid (Greenspan 1968). This is one limiting case examined by Hocking (1967) and Ludwig (1951).

As discussed in §3.2, secondary flow is very weak in the region where centrifugal, Coriolis and buoyancy forces just neutralize each other. Consequently, it is too weak to modify the main flow effectively such that the profiles of the main flow are essentially axisymmetric and parabolic with the maximum value occurring along the horizontal centerline at or very close to the center of the cross section (Fig.3.7(c)). In this region, the inertial force in Eq.(2.4) is very weak as compared with the viscous force. The driving force for the main flow (i.e., pressure term) is mainly balanced by the viscous force in whole flow domain. Other forces (inertial, Coriolis forces) are very weak.

When the value of L_1 is away from the region where the centrifugal, Coriolis and buoyancy forces just neutralize each other, the secondary flow become stronger (Fig.3.2). The profile of the main flow becomes, then, distorted with the peak moving away from the center of the cross section toward the outer wall for the case of increasing value of L_1 (Fig.3.7(b)) or the inner wall for the case of decreasing value of L_1 (Fig.3.7(d)) along the horizontal centerline. In either of the two cases, the location of the maximum main velocity is away from the center of the tube and in the direction of the secondary velocities in the middle of the tube. Accompanied with the

shift of the peak of the main flow, the isovels are more sparsely spaced in the region near the inner wall (outer wall) than near the outer wall (inner wall) in Fig.3.7(b) (Fig.3.7(d)). Consequently, pronounced peripheral variations are expected in the local friction factors. The flow in the tube core is not geostrophic, it is ageostrophic, i.e., pressure gradients are balanced by both Coriolis force and convective inertial force.

A striking feature which can be inferred from Fig.3.7(a)-(d) is that the region of return flow along the walls appears to be far too thick to be described by boundary layer approximations. Consequently, the integral type method developed by Mori *et al.* (1967, 1968 & 1971) may not be valid for these regions of flow.

3.4 Temperature Distribution

Figure 3.8 demonstrates the way in which the secondary flow affects the temperature profiles based on the second order solution of temperature. In the figure, the non-dimensional temperature η has been normalized by its corresponding extreme value η_c , and the extreme point is illustrated by a cross. Two numbers for each case are, respectively, the value of the L_1 and the extreme value of η .

It is the secondary flow that causes the deviation of the temperature from the parabolic profile in the stationary straight tubes. The effect of the secondary flow enters the energy equation through one term, i.e., the convection term ($\nabla \cdot \mathbf{q}$, (2.5)). The absence of this term leads to the parabolic profile which has an axisymmetric

and parabolic profile (Fig.3.8(a)). In the region with the four-cell secondary flow, the secondary flow is too weak to modify the temperature distributions effectively. Consequently, the temperature profile in this region exhibits essentially axisymmetric and parabolic with extreme value appearing along the horizontal centerline at or very close to the center of the cross section (Fig.3.8(c)).

When L_1 moves away from this region in both directions, the stronger secondary flow causes the temperature profile to be distorted with the extreme point shifting from the center of the cross section to the outer wall for the case of increasing L_1 (Fig.3.8(b)) or to the inner wall for the case of decreasing L_1 (Fig.3.8(d)) along the horizontal centerline. The shift of the extreme point results in a more tightly spaced isotherms in the region near the outer wall (Fig.3.8(b)) or near the inner wall (Fig.3.8(d)). This will cause pronounced peripheral variations in the local Nusselt number. The reason for this is that there exists a larger gradient of the main flow in these regions (Fig.3.7(b,d)).

Two interesting results can be inferred from the temperature profiles shown in Fig.3.8(a)-(d). One is that the theory of thermal boundary layer is not valid for the temperature fields in these regions of parameters because the layer along the walls is too thick to be described by the theory. Another is that the temperature distributions are qualitatively similar to the corresponding ones of the main flow in these regions of parameters. This implies that the Coriolis terms in the momentum equation for main flow are not strong enough to dominate by noting that only the

difference between the momentum equation for main flow and energy equation for temperature is the existence of the Coriolis terms in the momentum equation.

3.5 Mean Friction Factor and Nusselt Number

3.5.1 The friction factor

Substituting the expression for w based on the second-order solution into the definition of flow rate Q

$$Q = \int_0^{2\pi} \int_0^a W R dR d\varphi = \int_0^{2\pi} \int_0^1 a \nu w r dr d\varphi$$

we obtain

$$Q = \frac{\pi \nu a c}{2} Q_1 \quad (3.3)$$

where

$$\begin{aligned} Q_1 = 1 - & \left(\frac{1541c^4}{3150 \times 1152^2} + \frac{11c^2}{17280} - \frac{1}{48} \right) \sigma^2 - \left(\frac{c^2}{28 \times 768^2} + \frac{1}{9216} \right) Re_{\Omega}^2 \\ & - \frac{5293c^2 Ra_{\Omega}^2}{350 \times 1152^3} - \left(\frac{111c^2}{280 \times 1152^2} + \frac{1}{1920} \right) c\sigma Re_{\Omega} + \left(\frac{8077c^2}{50400 \times 1152^2} + \frac{29}{240 \times 1152} \right) c\sigma Ra_{\Omega} \\ & + \left(\frac{97c^2}{430080 \times 4608} + \frac{1}{23040} \right) Re_{\Omega} Ra_{\Omega} \end{aligned} \quad (3.4)$$

and the mean main velocity w_m is

$$w_m = \frac{Q}{\pi a^2} = \frac{\nu c Q_1}{2a} \quad (3.5)$$

Then the Reynolds number with diameter of the tube as a characteristic length is

$$Re = \frac{2w_m a}{\nu} = cQ_1 \quad (3.6)$$

From Eq.(2.61) in Chapter 2, the flow rate of the fluid through a stationary straight tube is

$$Q_s = \frac{\pi \nu a c}{2}$$

Then we may define the ratio of the flow rates as

$$\frac{Q}{Q_s} = Q_1 \quad (3.7)$$

This agrees with those obtained by Topakoglu(1967), Dean(1928), and Barua(1954) for the special cases they considered.

Since the mean friction factor for a rotating curved tube is defined by

$$f = -\frac{2a}{\rho w_m^2 / 2} \frac{\partial p'}{R \partial \theta}$$

we have

$$f = \frac{64c}{Re^2} \quad (3.8)$$

and

$$\frac{f}{f_s} = \frac{c}{Re} = \frac{1}{Q_1} \quad (3.9)$$

where $f_s (= 64/Re)$ is the mean friction factor for a stationary straight tube. It is interesting to note that the Prandtl number does not appear explicitly in the expressions of Q/Q_s and f/f_s although it was present in the second order solution of the main velocity (Chapter 2).

Figure 3.9 illustrates the typical trends for the friction factor variation with L_1 and L_2 at $\sigma = 0.02$ and $c = 60$. For any specified L_2 , there exists a region of L_1 where the friction factor is identical or very close to that in stationary straight tube. And this region has already been discussed in §3.2 where centrifugal, Coriolis and buoyancy forces just neutralize each other. This contributes to a very weak secondary flow in this region. As L_1 moves away from this region at a specified value of L_2 , the friction factor increases. Apparently the increased resistance to the flow comes from the stronger secondary flow. Furthermore, the increase in friction factor becomes more significant as $|L_1|$ increases. At a specified value of L_1 , we note an important fact from Fig.3.9 that the flow impediment at higher values of L_2 is relatively greater if the value of L_1 is at the left of the region mentioned above, but is relatively smaller if the value of L_1 is at the right of the region.

3.5.2 The Nusselt Number

From the energy balance

$$\rho c_p c_2 \pi a^2 w_m = 2\pi ah(t_w - t_m)$$

and the definition of the mean Nusselt number

$$Nu = \frac{2ah}{\lambda}$$

we obtain

$$Nu = \frac{cQ_1}{2\eta_m} \quad (3.10)$$

where η_m is an integrated mean temperature across the tube (sometimes referred to as an unweighed mean) and defined as (Morris 1981)

$$\eta_m = \frac{1}{\pi} \int_0^{2\pi} \int_0^1 \eta r dr d\varphi$$

Substituting the second-order solution of η into the expression above, we have

$$\begin{aligned} \eta_m = & -\frac{c}{12} + \sigma^2 \left(\frac{1171Pr^2c^5}{22400 \times 1152^2} + \frac{4169Pr^2c^5}{5 \times 50400 \times 1152^2} + \frac{1171c^5}{22400 \times 1152^2} - \frac{17Pr^2c^3}{6720 \times 1152} \right. \\ & + \frac{481c^3}{6720 \times 1152} - \frac{29c}{1536} \left. \right) + Re_\Omega^2 \left(\frac{17Pr^2c^3}{2293760 \times 1152} + \frac{293Pr^2c^3}{107520 \times 1152^2} + \frac{17c^3}{2293760 \times 1152} \right. \\ & \left. + \frac{c}{80 \times 1152} \right) + Ra_\Omega^2 \left(\frac{72143Pr^2c^3}{44800 \times 1152^3} + \frac{57383Pr^2c^3}{112000 \times 1152^3} + \frac{72143c^3}{44800 \times 1152^3} \right) \quad (3.11) \\ & + \sigma Re_\Omega \left(\frac{2129Pr^2c^4}{50400 \times 1152^2} + \frac{2707Pr^2c^4}{201600 \times 1152^2} + \frac{2129c^4}{50400 \times 1152^2} - \frac{Pr^2c^2}{960 \times 1152} + \frac{19c^2}{320 \times 1152} \right) \\ & - \sigma Ra_\Omega \left(\frac{27571Pr^2c^4}{1400 \times 1152^3} + \frac{7291Pr^2c^4}{134400 \times 1152^3} + \frac{27571c^4}{1400 \times 1152^3} - \frac{Pr^2c^2}{2752512} + \frac{253c^2}{21501 \times 1152} \right) \\ & - Re_\Omega Ra_\Omega \left(\frac{11143Pr^2c^3}{1400 \times 1152^3} + \frac{3551Pr^2c^3}{1400 \times 1152^3} + \frac{11143c^3}{1400 \times 1152^3} + \frac{77c}{3840 \times 4608} \right) \end{aligned}$$

The following implications of Eqs.(3.10) and (3.11) are worthy of note. In the limiting case with no curvature, rotation and heating/cooling, the present problem becomes identical to the asymptotic solution for constant property forced convection in a stationary straight tube and was reported by Goldstein (1957). For this limiting case $Nu_s = 6$ and clearly Eq.(3.10) approaches to this value asymptotically as $\sigma \rightarrow 0$, $Re_\Omega \rightarrow 0$ and $Ra_\Omega \rightarrow 0$. Dividing Eq.(3.10) by Nu_s for a stationary straight tube, we have

$$\frac{Nu}{Nu_s} = \frac{31cQ_1}{95\eta_m} \quad (3.12)$$

Typical variations of the Nusselt number given by Eq.(3.12) are presented in Fig.3.10 for a range of L_2 at $\sigma = 0.02$, $c = 60$, and $Pr = 0.7$. Although it is likely that the solution is being extended beyond its range of validity at the higher values of the L_1 , the physical trends are quite evident. As expected the heat transfer is enhanced significantly due to the presence of the secondary flow, and the similarity between the main flow and temperature distribution leads to a similarity in the results for friction factor and Nusselt number. Like the friction factor, the Nusselt number is also identical or very close to that for constant property forced convection in stationary straight tube in the region with the four-cell secondary flow. An increase in $|L_1|$ from this region causes the secondary flow to become stronger. Consequently, the Nusselt number increases substantially at higher value of the $|L_1|$. The higher value of L_2 results a relatively greater enhancement of heat transfer for the case in which the value of L_1 is at the left of the region with the lowest value of the Nusselt number, but a relatively smaller enhancement when the value of L_1 is at the right of the region.

For future comparison with experimental data, Fig.3.11 shows variations of the Nusselt number based on bulk temperature with L_1 for a range of L_2 at $\sigma = 0.02$, $c = 60$, and $Pr = 0.7$. The bulk temperature is obtained through a numerical double integration by Simpson's 1/3 rule. In the figure, Nu_s is the Nusselt number (based on the bulk temperature) for constant property forced convection in a stationary straight tube, which is 48/11 in value.

At the present stage, the structure of the solutions has not been explored completely. On the other hand, it appears that no experimental results of friction factors or Nusselt numbers for rotating curved tube with heating or cooling effect are available. Thus the range of validity for Eqs.(3.9) and (3.12) remains to be checked in future.

3.6 The structure of solutions

In practical problems, the Reynolds number Re is usually given while the pseudo Reynolds number, which is defined by the pressure gradient along curved tube axis, is often unknown. An expression for the pseudo Reynolds number c in terms of Re, σ, Re_Ω and Ra_Ω may be obtained by inverting (3.6) and ignoring the higher-order terms as

$$c = Rc\Gamma \quad (3.13)$$

with

$$\begin{aligned} \Gamma = 1 + & \left(\frac{1541 Re^4}{3150 \times 1152^2} + \frac{11 Re^2}{17280} - \frac{1}{48} \right) \sigma^2 + \left(\frac{Rc^2}{28 \times 768^2} + \frac{1}{9216} \right) Rc_\Omega^2 + \frac{5203 Rc_\Omega^2 Ra_\Omega^2}{350 \times 1152^3} \\ & + \left(\frac{111 Rc^2}{280 \times 1152^2} + \frac{1}{1920} \right) \sigma Re Re_\Omega - \left(\frac{8077 Rc^2}{50400 \times 1152^2} + \frac{29}{240 \times 1152} \right) \sigma Rc Ra_\Omega \\ & - \left(\frac{97 Re^2}{430080 \times 4608} + \frac{1}{23040} \right) Re_\Omega Ra_\Omega \end{aligned} \quad (3.14)$$

Introducing the following non-dimensional parameters,

$$De = Re\sqrt{\sigma} \quad D_\Omega = Re Rc_\Omega \quad Dr = Rc Ra_\Omega \quad (3.15)$$

the expression of Γ becomes

$$\begin{aligned} \Gamma = 1 - & \frac{\sigma^2}{48} + \frac{1541(D\epsilon^2)^2}{3150 \times 1152^2} + \frac{D_\Omega^2}{28 \times 768^2} + \frac{5293Dr^2}{350 \times 1152^3} + \frac{Re_\Omega^2}{9216} + \frac{11\sigma D\epsilon^2}{17280} \\ & + \frac{\sigma D_\Omega}{1920} - \frac{29\sigma Dr}{240 \times 1152} + \frac{111De^2 D_\Omega}{280 \times 1152^2} - \frac{8077D\epsilon^2 Dr}{50400 \times 1152^2} \\ & - \frac{97D_\Omega Dr}{430080 \times 4608} - \frac{Re_\Omega Dr}{23040Re\epsilon} \end{aligned} \quad (3.16)$$

The second-order solution, (2.20) along with (2.50)-(2.80) in Chapter 2, may be expressed as

$$\begin{aligned} \phi = & \hat{D}\epsilon^2 \phi_{100}^{20} + \hat{D}_\Omega^2 \phi_{010}^{10} + \hat{D}r^2 \phi_{001}^{10} + \hat{D}\epsilon^4 \phi_{200}^{40} + \hat{D}_\Omega^2 \phi_{020}^{20} + \hat{D}r^2 \phi_{002}^{20} \\ & \sigma \hat{D}\epsilon^2 \phi_{200}^{20} + \sigma \hat{D}_\Omega^2 \phi_{110}^{10} + \sigma \hat{D}r^2 \phi_{101}^{10} + \hat{D}\epsilon^2 \hat{D}_\Omega \phi_{110}^{30} + \hat{D}\epsilon^2 \hat{D}r \phi_{101}^{30} \\ & + \hat{D}_\Omega \hat{D}r \phi_{010}^{20} + Pr \hat{D}\epsilon^2 \hat{D}r \phi_{101}^{31} + Pr \hat{D}_\Omega \hat{D}r \phi_{011}^{21} + Pr \hat{D}r^2 \phi_{002}^{21} \end{aligned} \quad (3.17)$$

$$\begin{aligned} w = & \hat{R}\epsilon[w_{000}^{10} + \sigma w_{100}^{10} + \hat{D}\epsilon^2 w_{100}^{30} + \hat{D}_\Omega w_{010}^{20} + \hat{D}r w_{001}^{20} + \sigma^2 w_{200}^{10} + \hat{D}\epsilon^4 w_{200}^{50} \\ & + Re_\Omega^2 w_{020}^{10} + \hat{D}_\Omega^2 w_{020}^{30} + \hat{D}r^2 w_{002}^{30} + \sigma \hat{D}\epsilon^2 w_{200}^{30} + \sigma \hat{D}_\Omega w_{110}^{20} + \sigma \hat{D}r w_{101}^{20} \\ & + \hat{D}\epsilon^2 \hat{D}_\Omega w_{110}^{40} + \hat{D}\epsilon^2 \hat{D}r w_{101}^{40} + \hat{D}_\Omega \hat{D}r w_{011}^{30} + Pr \hat{D}\epsilon^2 \hat{D}r w_{101}^{41} \\ & + Pr \hat{D}r^2 w_{002}^{31} + Pr \hat{D}_\Omega \hat{D}r w_{011}^{31}] + Re_\Omega \hat{D}r w_{011}^{10} + \hat{D}r^2 w_{002}^{20} \end{aligned} \quad (3.18)$$

$$\begin{aligned} \eta = & \hat{R}\epsilon[\eta_{000}^{10} + \sigma \eta_{100}^{10} + \hat{D}\epsilon^2 \eta_{100}^{30} + \hat{D}_\Omega \eta_{010}^{20} + \hat{D}r \eta_{001}^{20} + \sigma^2 \eta_{200}^{10} + \hat{D}\epsilon^4 \eta_{200}^{50} \\ & + Re_\Omega^2 \eta_{020}^{10} + Re_\Omega^2 w_{020}^{10} + \hat{D}_\Omega^2 \eta_{020}^{30} + \hat{D}r^2 \eta_{002}^{30} + \sigma \hat{D}\epsilon^2 \eta_{200}^{30} + \sigma \hat{D}_\Omega \eta_{110}^{20} + \sigma \hat{D}r \eta_{101}^{20} \end{aligned}$$

$$\begin{aligned}
& + Pr \hat{D}c^2 \eta_{100}^{31} + Pr \hat{D}_\Omega \eta_{010}^{21} + Pr \hat{D}r \eta_{001}^{21} + \hat{D}c^2 \hat{D}_\Omega \eta_{110}^{41} + \hat{D}c^2 \hat{D}r \eta_{110}^{40} + \hat{D}_\Omega \hat{D}r \eta_{011}^{30} \\
& + Pr \hat{D}c^4 \eta_{200}^{51} + Pr \hat{D}_\Omega^2 \eta_{020}^{31} + Pr \hat{D}r^2 \eta_{002}^{31} + \sigma Pr \hat{D}c^2 \eta_{200}^{31} + \sigma Pr \hat{D}_\Omega \eta_{110}^{21} \\
& + \sigma Pr \hat{D}r \eta_{110}^{21} + Pr \hat{D}c^2 \hat{D}_\Omega \eta_{110}^{41} + Pr \hat{D}c^2 \hat{D}r \eta_{110}^{41} + Pr \hat{D}_\Omega \hat{D}r \eta_{011}^{31} \\
& + Pr^2 \hat{D}c^4 \eta_{200}^{52} + Pr^2 \hat{D}_\Omega^2 \eta_{020}^{32} + Pr^2 \hat{D}r^2 \eta_{002}^{32} + Pr^2 \hat{D}c^2 \hat{D}_\Omega \eta_{110}^{42} \\
& + Pr^2 \hat{D}c^2 \hat{D}r \eta_{110}^{42} + Pr^2 \hat{D}_\Omega \hat{D}r \eta_{011}^{32} + Re_\Omega \hat{D}r \eta_{011}^{10} + \hat{D}r^2 \eta_{002}^{20} \quad (3.19)
\end{aligned}$$

in which

$$\hat{R}c = Re\Gamma \hat{D}c = Dc\Gamma \hat{D}_\Omega = D_\Omega\Gamma \hat{D}r = Dr\Gamma \quad (3.20)$$

and the parameter-free expansion coefficients ϕ_{ijk}^{lm} , w_{ijk}^{lm} and η_{ijk}^{lm} are introduced by factoring out the parameters c and Pr from ϕ_{xy} , w_{xy} and η_{xy} , i.e.

$\phi_{ijk}^{lm} =$ items in ϕ_{ijk} including i -th power of c and j -th power of Pr divided by $c^i Pr^j$

Similar remark is also true for w_{ijk}^{lm} and η_{ijk}^{lm} .

Since ϕ_{ijk}^{lm} , w_{ijk}^{lm} and η_{ijk}^{lm} depend on r and φ only and are independent of the flow region, the relative size of each term in these series depends on the magnitudes of the parameters; however, the shape of each term is always the same. Note that Re is fixed once De and σ are specified; then the solutions for velocity and temperature may be regarded as the infinite series (higher-order approximations would produce additional types of terms) in powers of σ , $\hat{D}c^2$, Re_Ω , \hat{D}_Ω , Pr and $\hat{D}r$. In view of expressions (3.15) and (3.16) for Γ (In fact $\Gamma \simeq 1$ for small values of the parameters), the series may also be considered as in powers of σ , Dc^2 , Re_Ω , D_Ω , Pr and Dr . The

first pair of parameters, σ and De^2 , characterizes the flow and heat transfer in stationary helically coiled tubes (the Dean problem). The second pair, Re_Ω and D_Ω , determines the characteristics of the flow and heat transfer in radially rotating straight tubes (the Coriolis problem). The third pair, Pr and Dr , characterizes the flow and heat transfer due to the inertial and buoyancy forces (the mixed convection problem). σ , the curvature ratio of the curved tube, is important for the problems in the helical tube with tightly wound coils. Dean number, De , characterizes the flow and heat transfer in the coiled tubes with loosely wound coils. Re_Ω , whose effect for problems in radially rotating straight tube is analogous to that of σ for the stationary curved tube, is the ratio of the Coriolis force to the viscous force. It is important for problems in the radially rotating tube if D_Ω is small. D_Ω , whose effect for the problems in radially rotating straight tube is analogous to that of the square of the Dean number for the stationary curved tube, represents the ratio of the product of the inertial and Coriolis forces to the square of the viscous forces. It determines the flow and heat transfer in radially rotating straight tube if Re_Ω is small (i.e. slowly rotating). Dr represents the ratio of the product of the inertial and buoyancy forces to the square of the viscous forces. Dr and Prandtl number Pr are two characteristic parameters for mixed convection problem.

If each of these parameters is significant, the solution becomes a sixfold series expansion in σ , De , Re_Ω , D_Ω , Pr and Dr . It appears that no successful technique is available for analyzing and improving such a multiple series. However, for some

special cases, the series may be reduced to a single series. For example, the solution series for the fully developed steady laminar flow through a radially rotating straight tube becomes a single series if the tube is rotating slowly and the density of fluid is taken to be constant. Mansour(1985) expanded this single series up to 31 terms in powers of $D\Omega$. Recasting the resulting series for the friction ratio, he predicted that it will grow asymptotically as the 1/8 power of $D\Omega$. Van Dyke(1978) extended Dean's four-term series for the loosely coiled tube to 24 terms in power of $D\epsilon$. The series, re-casted by Van Dyke, is considered to be valid for arbitrarily large Dean number. Similar work has been done by Van Dyke (1990) for Morton's series for fully developed laminar flow through a uniformly heated horizontal tube. He extended the series by computer to 31 terms in powers of a parameter ϵ which is similar to $D\epsilon$ of this work. He found that the Nusselt number grow asymptotically as the 2/15 power of the parameter ϵ .

As discussed in §3.2.1, two dimensionless parameters L_1 and L_2 characterize the secondary flow in rotating curved tube. From their definition (see Eq.(2.54)),

$$L_1 = \frac{3Re_\Omega}{2\sigma c} = \frac{3\hat{D}_\Omega}{2\hat{D}\epsilon^2}$$

$$L_2 = \frac{Ra_\Omega}{16\sigma c} = \frac{\hat{D}r}{16\hat{D}\epsilon^2}$$

Thus, L_1 represents the ratio of the characteristic parameter \hat{D}_Ω for rotating straight tube to the characteristic parameter $\hat{D}\epsilon^2$ for the stationary curved tube. Similarly, L_2 represents the ratio of the characteristic parameter $\hat{D}r$ for mixed heat transfer

Table 3.2: Physical implications of $\hat{D}c^2$, \hat{D}_Ω , $\hat{D}r$, L_1 and L_2

Parameter	Force Ratio
$\hat{D}c^2(Dc^2)$	$\frac{(\text{inertial force}) \times (\text{centrifugal force})}{(\text{viscous force})^2}$
$\hat{D}_\Omega(D_\Omega)$	$\frac{(\text{inertial force}) \times (\text{Coriolis force})}{(\text{viscous force})^2}$
$\hat{D}r(Dr)$	$\frac{(\text{inertial force}) \times (\text{buoyancy force})}{(\text{viscous force})^2}$
L_1	$\frac{\text{Coriolis force}}{\text{centrifugal force}}$
L_2	$\frac{\text{buoyancy force}}{\text{centrifugal force}}$

problem to the characteristic parameter $\hat{D}e^2$ for the stationary curved tube.

In terms of the force ratios, the physical implications of $\hat{D}e^2$, \hat{D}_Ω , $\hat{D}r$, L_1 and L_2 are summarized in Table 3.2.

3.7 Concluding Remarks

The characteristics of flow and heat transfer are studied based on the perturbation solutions for the velocity and temperature fields in a rotating curved circular tube obtained in Chapter 2. The solutions of velocity and temperature are found to be infinite series in powers of three pairs of parameters. The first pair, σ and Dc^2 (or $\hat{D}e^2$), characterizes the flow and heat transfer in helically coiled tubes. The second pair, Re_Ω and D_Ω (or \hat{D}_Ω), determines the characteristics of flow and heat transfer in radially rotating straight tubes. And the third pair, Pr and Dr (or $\hat{D}r$),

characterizes the flow and heat transfer caused by inertial and buoyancy forces.

The centrifugal, Coriolis and buoyancy forces all contribute to the generation of the secondary flow in a rotating curved tube. The resultant secondary flow may be grouped under three broad patterns depending on the values of two dimensionless parameters L_1 and L_2 . The first parameter represents the ratio of the characteristic dimensionless parameter \hat{D}_Ω for radially rotating straight tube to the characteristic dimensionless parameter $\hat{D}c^2$ for a stationary curved tube. The last one, on the other hand, is the ratio of the characteristic dimensionless parameter $\hat{D}r$ for mixed convection to the characteristic dimensionless parameter $\hat{D}c^2$ for the stationary curved tube.

Based on the first order approximation, the secondary flow appears as a two-cell pattern with the direction of the circulation same as that found in the stationary curved tube in the range with $L_1 > 9L_2 - 3$ (for the case of $L_2 \leq 1$) or $L_1 > 10L_2 - 4$ (for the case of $L_2 \geq 1$). This is because the centrifugal and *positive* Coriolis forces are dominant. When L_1 falls in the range with $L_1 < 10L_2 - 4$ (for $L_2 \leq 1$) or $L_1 < 9L_2 - 3$ (for $L_2 \geq 1$), the *negative* Coriolis force predominates and the secondary flow is also of a two-cell pattern, but the direction of the circulation is opposite to that found in the stationary curved tube. In the range where the three effects just neutralize each other, i.e. in the range with $10L_2 - 4 < L_1 < 9L_2 - 3$ for $L_2 \leq 1$ or $9L_2 - 3 < L_1 < 10L_2 - 4$ for $L_2 \geq 1$, two-pair (four-cell) secondary circulations which are oppositely directed to each other occur in the cross section of the tube. If

$L_2 \leq 1$, the second pair of secondary circulation appears along the wall of the tube. On the other hand, it would appear in the central portion of the cross section of the tube if $L_2 > 1$.

The second order solution of secondary flow distorts the vortices of the first order solution, and moves the circulation centres of the vortices away from the vertical centerline. This destroys the symmetry of the secondary flow about the vertical centerline for the first order solution. And the region with four-cell pattern is extended by the second order solution.

The presence of the secondary flow causes the deviation of the main velocity and temperature profiles away from the parabolic profile in Poiseuille flow. In particular, the locations of the maximum main velocity and the extreme temperature are moved away from the center of the tube in the direction of the secondary velocities in the middle of the tube. As a result, one observes the pronounced peripheral variations of friction factor and Nusselt number, and the increase of the mean friction factor and Nusselt number significantly. However, in the region where the secondary flow appears as a four-cell pattern, the secondary flow is too weak to modify the main velocity and temperature profiles effectively, such that they are essentially axisymmetric and parabolic with extreme value appearing along the horizontal centerline at or very close to the center of the cross section. As well in this region, the friction factor and Nusselt number are identical or very close to those for constant property forced convection in a stationary straight tube.

The profiles of the main velocity and temperature show that the boundary layer theory is not valid for the analysis of the flow and heat transfer in a rotating curved tube for a range of parameters considered in this work.

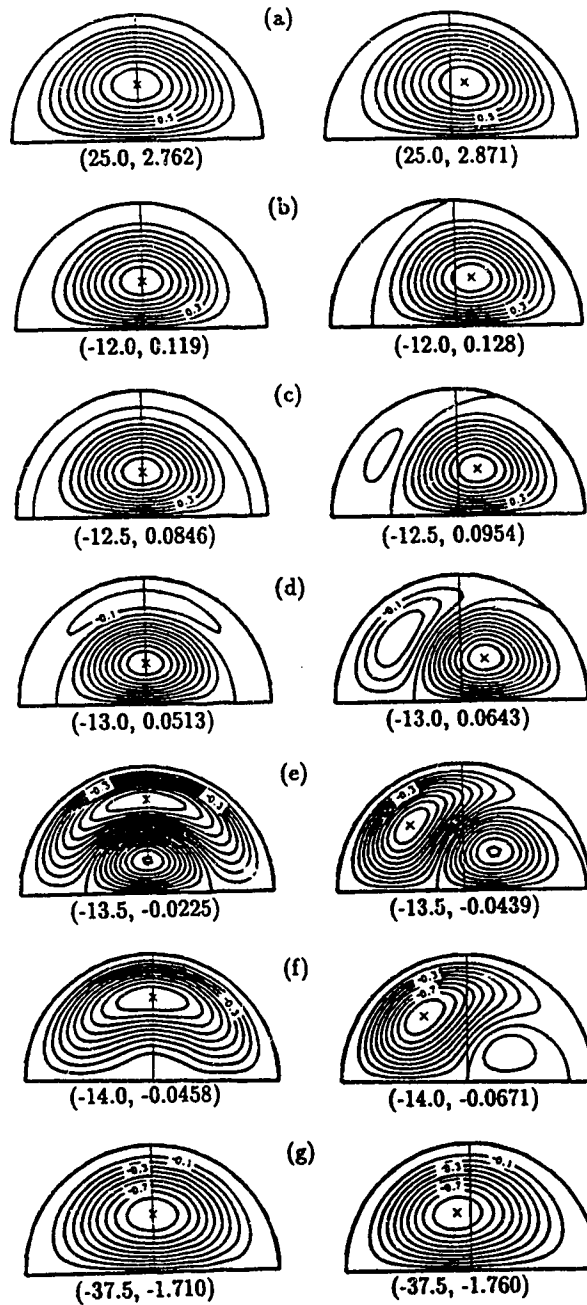


Figure 3.2. Secondary flow patterns at $\sigma = 0.02$, $c = 60$, $Pr = 0.7$ and $L_2 = -1.0$. First column: first-order; Second column: second order

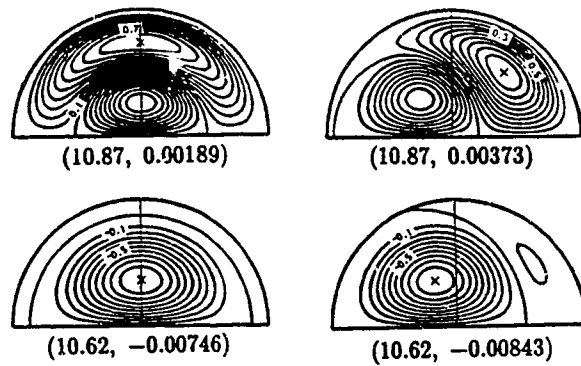


Figure 3.3. Secondary flow patterns at $\sigma = 0.01$, $c = 50$, $Pr = 0.7$ and $L_2 = 1.5$. First column: first-order; Second column: second order

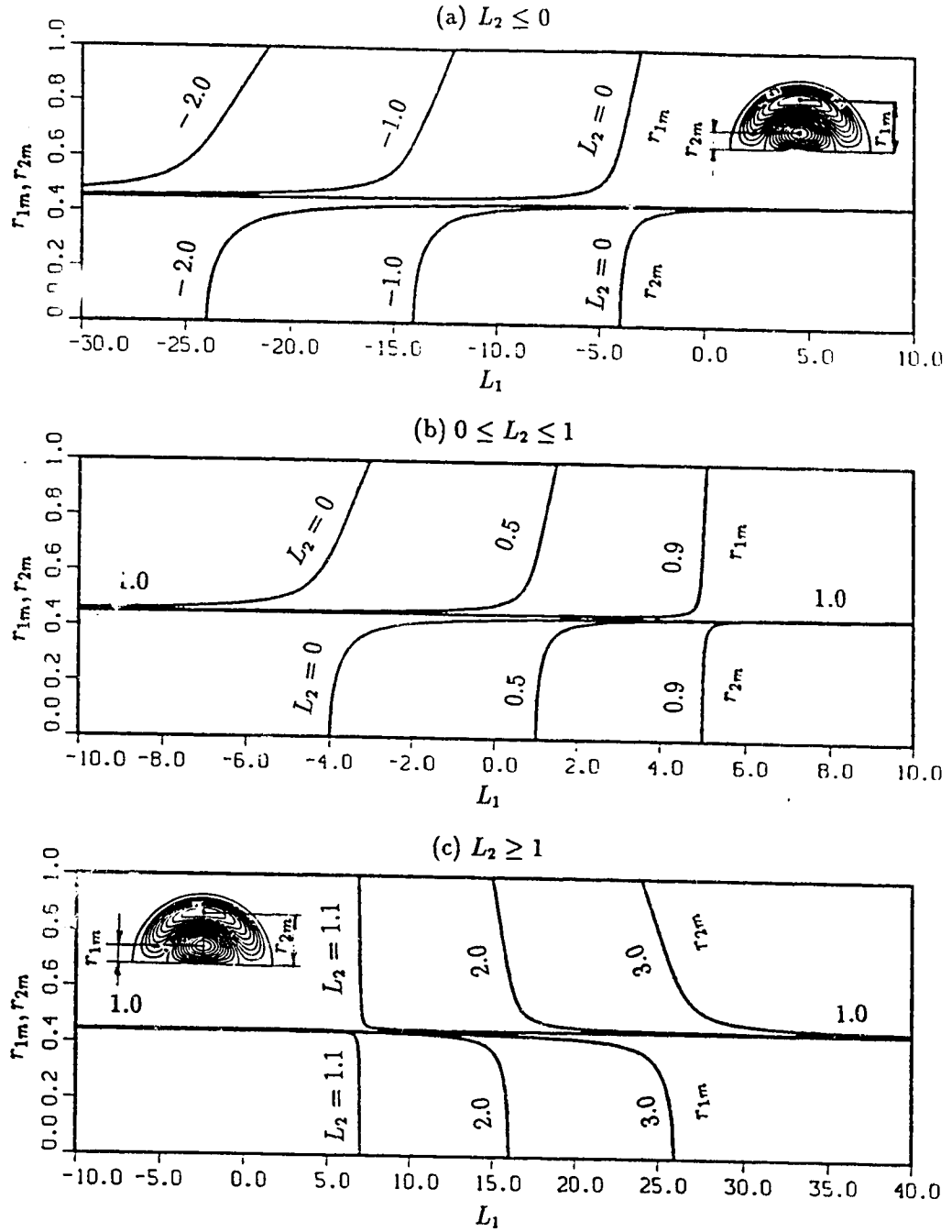


Figure 3.4. The radial distance of the centre of screw motion

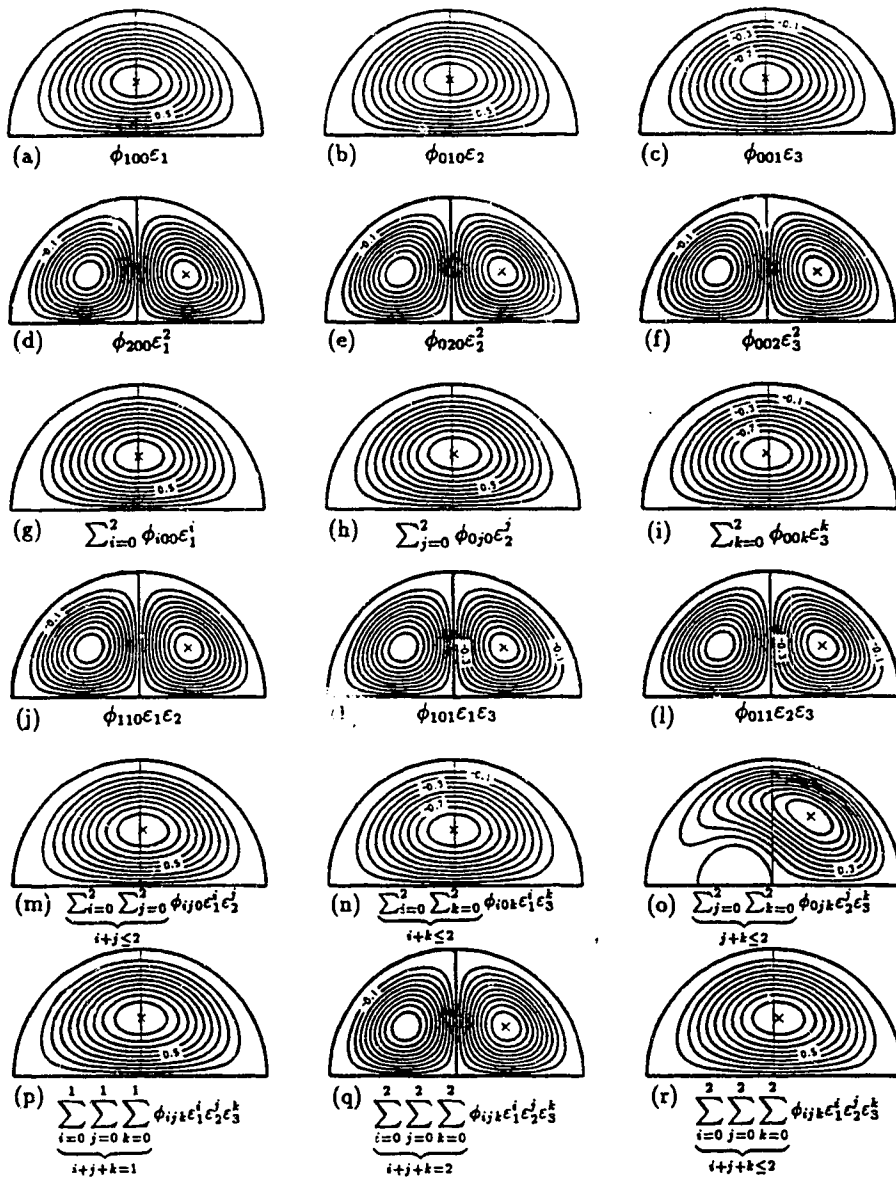


Figure 3.5. Secondary flow with one, two or three factors of curvature, rotation and heating/cooling at $\sigma = 0.01$, $c = 50$, $Pr = 0.7$, $L_1 = 15.0$ and $L_2 = 1.5$ ((a), (b), (c)-first-order terms due to single effect of curvature, rotation or heating/cooling; (d), (e), (f)- second-order terms due to single effect of curvature, rotation or heating/cooling; (g), (h), (i)- first-order terms + second-order terms due to single effect of curvature, rotation or heating/cooling; (j), (k), (l)-second-order terms due to combined effect of curvature & rotation, curvature & heating/cooling or rotation & heating/cooling; (m), (n), (o)-first-order terms + second-order terms due to combined effect of curvature & rotation, curvature & heating/cooling or rotation & heating/cooling; (p), (q), (r)-first-order terms, second-order terms or first-order terms + second-order terms due to combined effect of all three factors)

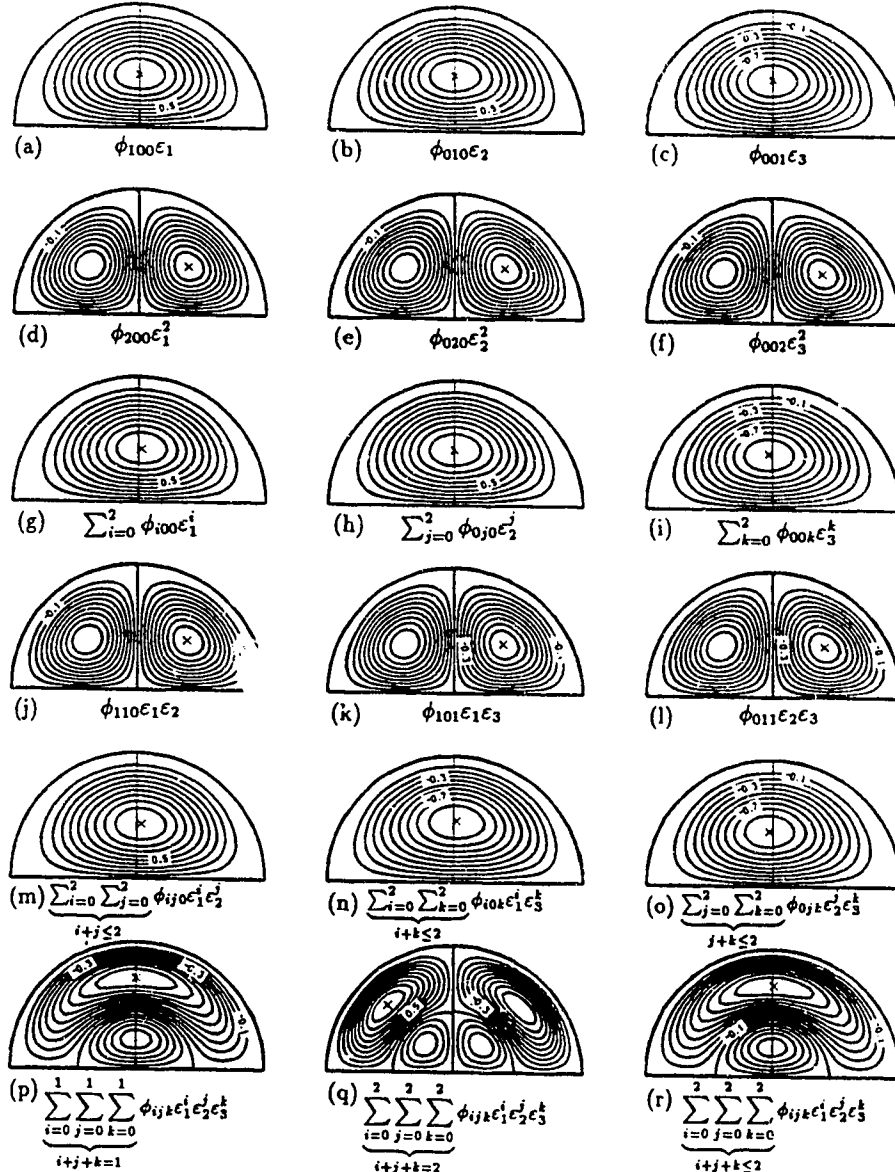


Figure 3.6. Secondary flow with one, two or three factors of curvature, rotation and heating/cooling at $\sigma = 0.01$, $c = 100$, $Pr = 0.7$, $L_1 = 1.1$ and $L_2 = 0.5$ ((a), (b), (c)-first-order terms due to single effect of curvature, rotation or heating/cooling; (d), (e), (f)- second-order terms due to single effect of curvature, rotation or heating/cooling; (g), (h), (i)- first-order terms + second-order terms due to single effect of curvature, rotation or heating/cooling; (j), (k), (l)-second-order terms due to combined effect of curvature & rotation, curvature & heating/cooling or rotation & heating/cooling; (m), (n), (o)-first-order terms + second-order terms due to combined effect of curvature & rotation, curvature & heating/cooling or rotation & heating/cooling; (p), (q), (r)-first-order terms, second-order terms or first-order terms + second-order terms due to combined effect of all three factors)

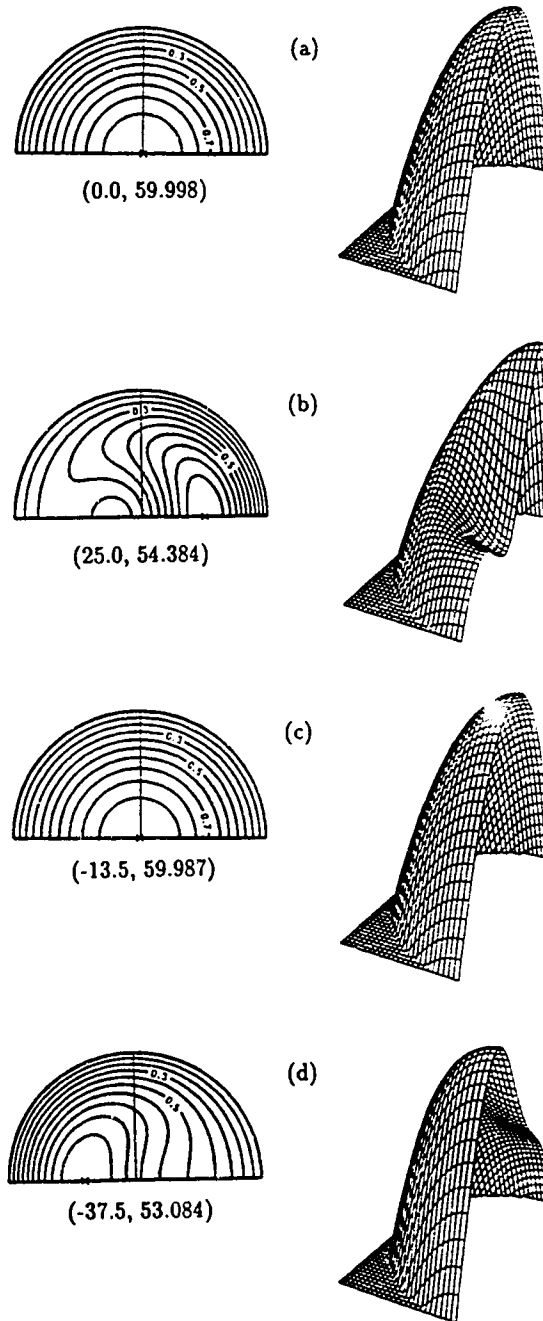


Figure 3.7. Main velocity distributions at $\sigma = 0.02$, $c = 60$, $Pr = 0.7$ and $L_2 = -1.0$. First column: isovels; Second column: profiles

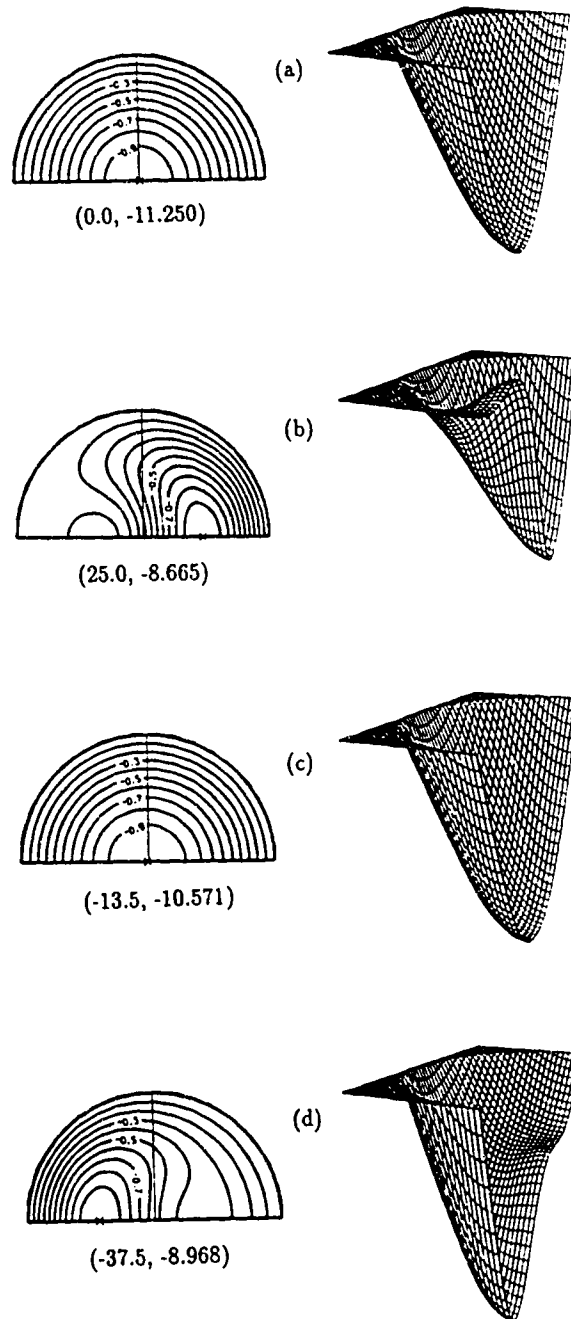


Figure 3.8. Temperature distributions at $\sigma = 0.02$, $c = 60$, $Pr = 0.7$ and $L_2 = -1.0$. First column: isothermals; Second column: profiles

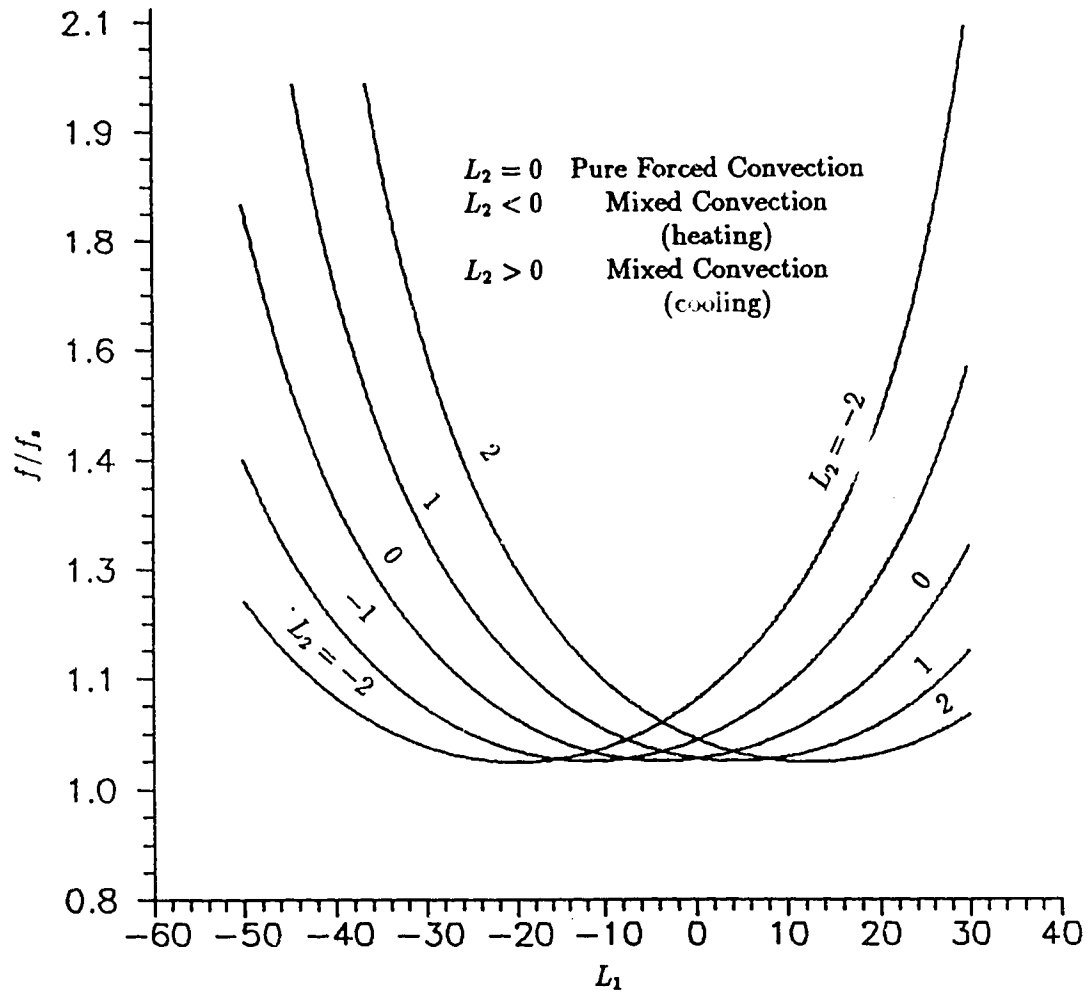


Figure 3.9. The influence of secondary flow on flow resistance

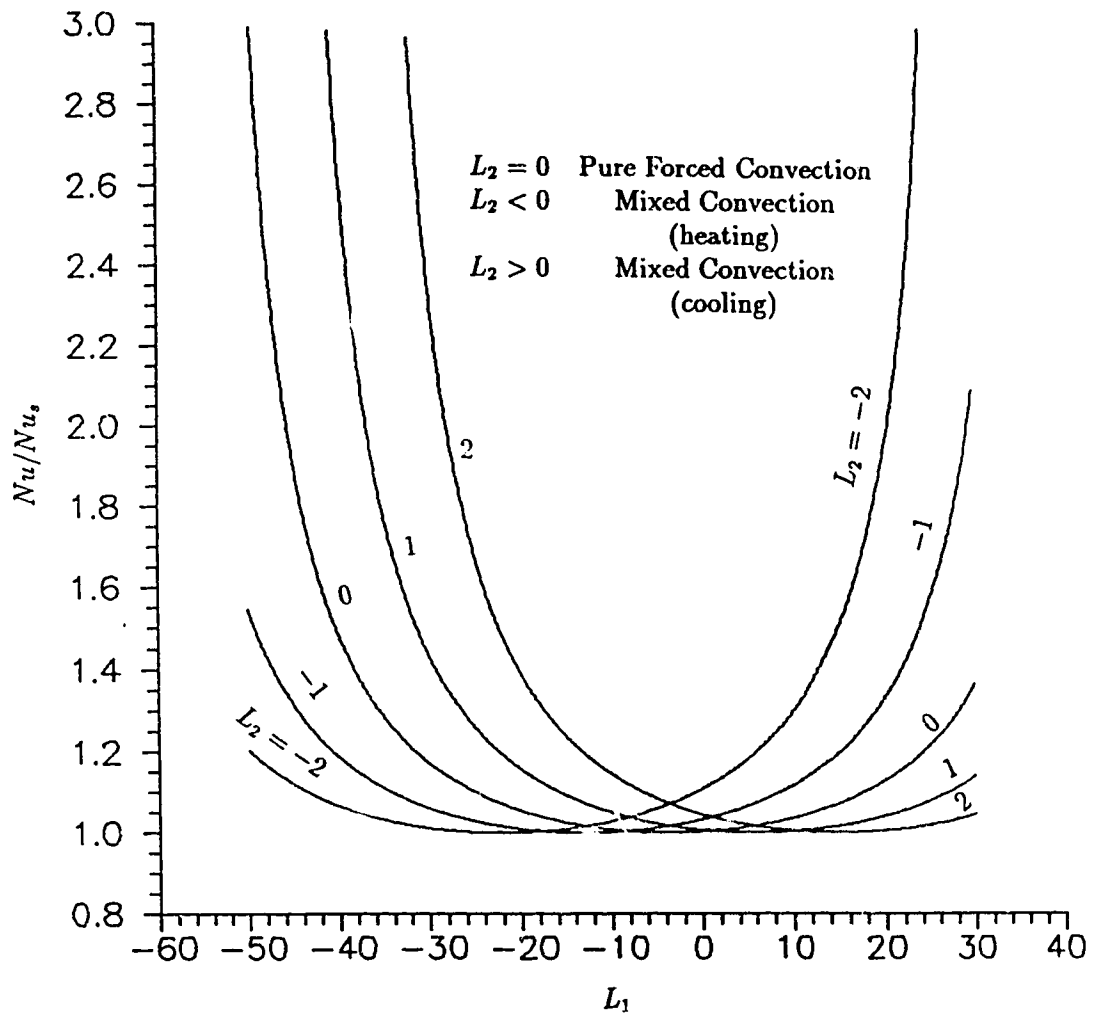


Figure 3.10. The influence of secondary flow on heat transfer

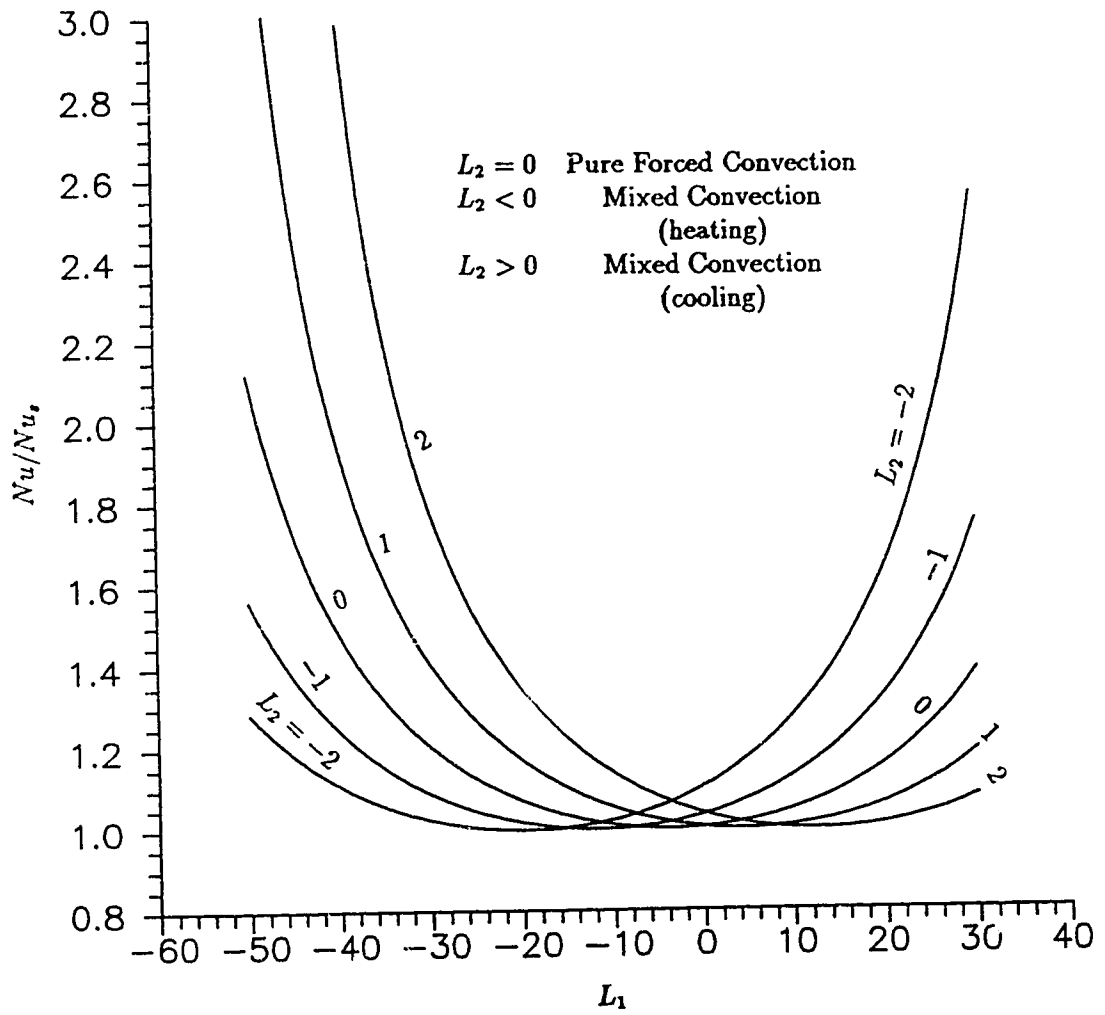


Figure 3.11. Variations of Nusselt number based on bulk temperature

References

- [1] Barua, S.N. 1954 Secondary flow in a rotating straight pipe. *Proc. R. Soc. Lond.* **A227**, 133-139.
- [2] Dean, W.R. 1928 The stream-line motion of a fluid in a curved pipe. *Phil. Mag.* **5**, 673-695.
- [3] Goldstein, S. 1957 *Modern developments in fluid dynamics*, Vol. 2, Oxford University Press, London.
- [4] Greenspan, H.P. 1968 *The theory of rotating fluids*, Cambridge University Press, London.
- [5] Hocking, L.M. 1967 Boundary and shear layers in a curved rotating pipe. *J. Math. Phys. Sci.* **1**, 123-136.
- [6] Ludwig, H. 1951 Die ausgebildete kanalströmung in einem rotierenden system. *Ing.-Arch. Bd.* **19**, 296-308.
- [7] Mansour K. 1985 Laminar flow through a slowly rotating straight pipe. *J. Fluid Mech.* **150**, 1-24.
- [8] Mori, Y., Fukada, T. and Nakayama, W. 1971 Convective heat transfer in rotating radial circular pipes (2nd report). *Int. J. Heat Mass Trans.* **14**, 1807-1824.

- [9] Mori, Y. & Nakayama, W. 1967 Forced convective heat transfer in a straight pipe rotating about a parallel axis (laminar region). *Int. J. Heat Mass Trans.* **10**, 1179-1194.
- [10] Mori, Y. & Nakayama, W. 1968 Convective heat transfer in rotating radial circular pipes (1st report, laminar region). *Int. J. Heat Mass Trans.* **11**, 1027-1040.
- [11] Morris, W.D. 1981 *Heat transfer and fluid flow in rotating coolant channels*. Research Studies Press, John Wiley and Sons.
- [12] Topakoglu, H.C. 1967 Steady laminar flows of an incompressible viscous fluid in curved pipes. *J. Math. Mech.* **16**, 1321-1337.
- [13] Van Dyke, M. 1978 Extended Stokes series: laminar flow through a loosely coiled pipe. *J. Fluid Mech.* **86**, 129-145.
- [14] Van Dyke, M. 1990 Extended Stokes series: laminar flow through a heated horizontal pipe. *J. Fluid Mech.* **212**, 289-308.
- [15] Wang, L. and Cheng, K.C. 1994 Flow transitions and combined free and forced convective heat transfer in a rotating curved circular tube-I: perturbation solution, submitted for publication.

Chapter 4

Flow Transitions and Combined Free and Forced Convective Heat Transfer in Rotating Curved Channels: The Case of Positive Rotation

The simultaneous effects of curvature, rotation and heating/cooling in channel flow complicate the flow and heat transfer characteristics beyond those observed in the channels with simple curvature or rotation. The phenomena encountered are examined for steady, hydrodynamically and thermally fully developed flow in

rectangular channels. The governing equations are solved numerically by using a finite-volume method. The results show both the nature of the flow transition and the effect of this transition on the distributions of the friction factor and Nusselt number in a square channel. A one-pair vortex flow, with an ageostrophic and virtually inviscid core, is uncovered between a viscous force dominated one-pair vortex flow and two-pair vortex flow with the presence of the Dean-, Coriolis- or buoyancy-vortices. Another two kinds of one-pair vortex flow exist after the disappearance of the Coriolis-vortices upon increasing the Coriolis force sufficiently. When the fluid is cooled, the inward buoyancy forces cause the buoyancy- vortices (due to the buoyancy force instability) to appear in the low pressure side (rather than the usual high pressure side of the channel), and the direction of the secondary flow reverses by overcoming the outward centrifugal and Coriolis forces in the plane of the cross section. The flow reversal occurs by passing through a multi-pair vortex flow region where overall, the effect of the buoyancy force just neutralizes those of the centrifugal and Coriolis forces. Two-pair vortex flow may result from two different mechanisms. One is associated with a break-up of the Ekman-type vortices owing to the centrifugal, Coriolis or buoyancy force instabilities. Another, with a smaller size of the resulting second pair of vortices, is characterized by a merging-together of the vortices. The disappearance of the Coriolis- or buoyancy-vortices is observed upon increasing the Coriolis or buoyancy forces. No such phenomena are observed for the Dean- vortices. Furthermore, the reappearance of the buoyancy-vortices,

upon increasing the buoyancy force further, is also found in this study.

4.1 Introduction

Fluid flow and heat transfer in rotating curved channels are encountered in cooling systems for conductors of electric generators and generator motors for pumped-storage stations (Ito & Motai 1974; Miyazaki 1971 and 1973). They are also employed in applications such as separation processes (Lennartz *et al.* 1987; Papanu *et al.* 1986; Hoover *et al.* 1984; Stöber & Flachsbart 1969; Hochrainer 1971 and Kotrappa & Light 1972), heat exchangers (Qiu *et al.* 1988 and 1990), and physiological field (Ito & Motai 1974; Berman 1985). The transport and flow phenomena in the rotating curved channels have, therefore, challenged engineers and scientists for some time. A remarkable characteristic of the flow and heat transfer in a rotating system is the presence of the centrifugal and Coriolis forces. Under certain conditions, these forces may induce a secondary flow in a plane perpendicular to the direction of the main flow. This could significantly affect the resistance to the fluid flow and convective heat transfer.

According to its inducing condition (Chapter 1), the secondary flow could be created by the Coriolis force for a constant property fluid, while the centrifugal force is purely hydrostatic, analogous to the earth's gravitational field. When a temperature-induced variation of fluid density occurs, both Coriolis and centrifugal-type buoyancy force could contribute to the generation of the secondary flow. On

the other hand, secondary flow also arises due to centrifugal force (Dean 1928) when a channel is curved. Therefore, centrifugal, Coriolis and centrifugal-type buoyancy forces all contribute to the generation of the secondary flow if the channel is both curved and rotating. The nonlinear interaction of these body forces with the other forces in the flow field may result in a complicated structure of the secondary flow. We attempt to examine this structure and its effects on pressure-driven main flow and temperature field in a rectangular channel by using a finite-volume method.

The secondary flow under consideration is essentially a nonlinear combination of the buoyancy force-driven secondary flow in the mixed-convection problem, the centrifugal force-driven secondary flow in the Dean problem and the Coriolis force-driven secondary flow in radially rotating straight channels (hereinafter referred to as Coriolis problem). The similarity among these three problems has been recognized by a number of investigators. The dynamical parameters for these three problems are $Dr (= RcRa)$, square of the Dean number De^2 ($De = Re\sqrt{\sigma}$) and $D_\Omega (= ReRe_\Omega)$, respectively, (Chapters 2 and 3, also see Wang & Cheng 1993a,b). Here Re is the Reynolds number, Ra the Rayleigh number, σ the curvature ratio of the channel and $Re_\Omega (= 4\Omega a^2/\nu)$ the rotational Reynolds number. Depending on the value of the dynamical parameter, fully-developed secondary flow exhibits three different structures for all three problems in the laminar flow region.

At a relatively small value of the dynamical parameter, it consists of one-pair of counter-rotating vortices in a plane perpendicular to the axis of the channel.

Upon increasing the value of the dynamical parameters sufficiently (depending on the value of the Prandtl number Pr , curvature ratio σ or the rotational Reynolds number Re_ρ , respectively, for these three problems), the centrifugal, Coriolis or buoyancy force instability may lead this one-pair vortex flow structure to another form of two-dimensional flow with a two-pair or roll-cell vortex structure (depending on the geometry of the channel) in the cross-plane. Such two-pair vortex flows are found to be unstable to asymmetric perturbations in the Dean problem (Winters 1987), in the Coriolis problem (Nandakumar, Raszillier and Durst 1991), and in the mixed-convection problem (Nandakumar & Weinitschke 1991).

Upon increasing the dynamical parameter further, all two-dimensional flows become unstable, and there are evidences for the evolution of streamwise periodic three-dimensional flows in all of the three problems (Sankar, Nandakumar & Masliyan 1988; Nandakumar & Weinitschke 1991 and Nandakumar, Raszillier & Durst 1991). The references concerning these three problems may be found in Cheng & Hwang (1969), Hwang & Cheng (1970), Nandakumar, Masliyah & Law (1985), and Nandakumar & Weinitschke (1991) for the mixed-convection problem; Cheng, Lin & Ou (1976), Pedley (1980), Dennis & Ng (1982), Berger, Talbot & Yao (1983), Nandakumar & Masliyah (1986), Ito (1987), Winters (1987), Berger (1991) and Hwang & Chao (1991) for the Dean problem; Morris (1981), Speziale (1982), Speziale & Thangam (1983), Kheshgi & Scriven (1985), Nandakumar, Raszillier & Durst (1991), Hwang & Jen (1990), Hwang & Soong (1992), Jen *et al.* (1992), Hwang & Kuo

(1993), Hwang & Jen (1987), Hwang & Soong (1989), Hwang & Kuo (1992), Soong *et al.* (1991) and Soong & Hwang (1990) for the Coriolis problem.

In spite of the practical importance and theoretical interest, the flow and heat transfer in rotating curved channel have not yet been examined in sufficient details. Most of the previous analytical/numerical investigations have focused on the two limiting cases with weak rotations or strong rotations. By employing Pohlhausen's method, Hocking (1967) and Ludwig (1951) examined the fully developed laminar boundary layers in rotating curved channel with rectangular and square cross section, respectively. Their results are valid for large rotational Reynolds number based on the angular velocity of the channel, as compared with the usual Reynolds number based on the mean axial velocity of the fluid. This problem is not considered to be as difficult as the case with moderate rotation since the flow in the interior of the channel is approximately geostrophic.

Considering the channel to be curved tube of circular cross section, the fully developed laminar flow was investigated theoretically by Ito & Motai (1974). They solved the equations of motion by a perturbation method for a small curvature and low range of angular rotating velocity of the tube. Heat transfer and the effect of centrifugal-type buoyancy force were not considered by these authors. Miyazaki (1971,1973) analyzed the fully developed laminar flow and heat transfer in curved rotating circular/rectangular channels by finite-difference method. The effects of the directions of rotation or heat flux were not investigated in Miyazaki's works.

Because of the convergence difficulties of the iterative solution method used, no solutions in the range where three forces (centrifugal force due to curvature, Coriolis and centrifugal-type buoyancy forces) are of comparable order of magnitude could be obtained. Besides, the examination of the governing equations employed by Miyazaki show that some errors existed in the viscous terms.

Since the solution to the present problem so far is only for the asymptotic cases of slow and rapid rotation, the secondary flow revealed by the works mentioned above consists of one-pair of counter-rotating vortices. When the three forces are of comparable order of magnitude, a complicated structure of the secondary flow might be expected since then the nonlinear effects could be quite strong. In this work, we present a comprehensive numerical study on the laminar flow and combined free and forced convective heat transfer in a rotating curved rectangular channel at low to relatively rapid rotation rates where both the convective and diffusive terms play an important role and, consequently, the full nonlinear equations must be solved.

Attention is focused on the flow transitions of secondary flow and main flow in the fully developed region and the effects of the flow transitions on temperature distribution, friction factors and Nusselt numbers for a wide range of characteristic parameters. The emphasis is also placed on the primary instabilities (centrifugal, Coriolis and buoyancy force instabilities) arising in the rotating curved rectangular channels, and not their secondary instabilities or the transition to turbulence, although the vortices studied ultimately have an important influence on the tran-

sition. The motivation for the present study arose from the following observations: (1) There exists no detailed study of the flow and heat transfer in rotating curved rectangular channels and (2) the transitions in flow structure due to the action of centrifugal, Coriolis and buoyancy forces have not been fully studied. In particular, the disappearance and reappearance of Dean-vortices, Coriolis-vortices and buoyancy-vortices have in general received less attention in the past.

4.2 Formulation of the problem

The geometrical configuration of the physical model for a rotating curved rectangular channel and its coordinate system are illustrated in Fig.4.1. A viscous fluid is allowed to flow through a channel of rectangular cross section with width \times height = $a \times b$ under the action of the pressure gradient along the channel axis. The channel is uniformly curved around the axis $o'z'$. At same time, the channel is rotating about that axis with a constant angular velocity Ω . The rotation can be *positive* or *negative* as shown in Fig.4.1 in terms of angular velocity vector. If positive, the rotation direction is in the direction of the relative velocity of the fluid inside the channel. When the rotation is negative, however, the rotation direction is in the direction opposite to the relative velocity of the fluid. In addition to the curvature and rotation, the channel is being uniformly heated or cooled at the wall with a uniform peripheral temperature. The properties of the fluid, with the exception of density, are taken to be constant. To facilitate the discussion, each side of

the channel wall is termed the inner, outer, upper and lower walls as shown in the figure. Furthermore, we introduced the horizontal centreline, which is a part of the X -axis cut out by the inner and outer walls, and the vertical centreline which is a part of the line $X = a/2$ between the upper and lower walls.

Consider a non-inertial toriodal coordinate system (O, X, Y, θ) fixed to the curved channel rotating with a constant angular velocity Ω about $o'z'$ axis as shown in Fig.4.1. The direction of the relative velocity of the fluid in the channel is chosen in the direction of increasing θ , while the angular velocity of the channel is taken as $\Omega > 0$ for increasing θ (positive rotation) and $\Omega < 0$ for decreasing θ (negative rotation) respectively. In order to facilitate the numerical programming, the origin of the coordinate system is located at the centre of the inner wall instead of centre of the cross section.

The flow is assumed to be laminar and steady. The axial velocity is so slow that there is no energy dissipation due to friction, and no other internal heat generation sources exist in the fluid. Comparing with the centrifugal force, the gravitational force is negligible. The buoyancy term is expressed in terms of the coefficient of volume expansion as is commonly done in free convection analysis (Boussinesq approximation). By invoking the usual Boussinesq approximation that the density variation need be included only in the effective body force term, the effect of variable fluid density need not be included in the Coriolis terms (Chapter 1). The temperature difference used to express density variations in the buoyancy term is

$(T - T_w)$. Here, T_w is the wall temperature. If the velocity components in the directions of X, Y , and θ are U, V, W respectively, the continuity, Navier-Stokes and energy equations governing the laminar flow and heat transfer with the aforementioned assumptions are:

Continuity equation

$$\frac{\partial}{\partial X} \left(\left(b - \frac{a}{2} + X \right) U \right) + \frac{\partial}{\partial Y} \left(\left(b - \frac{a}{2} + X \right) V \right) + \frac{\partial W}{\partial \theta} = 0 \quad (4.1)$$

Momentum equations

$$\begin{aligned} U \frac{\partial U}{\partial X} + V \frac{\partial U}{\partial Y} + \frac{W}{b - \frac{a}{2} + X} \frac{\partial U}{\partial \theta} - \frac{W^2}{b - \frac{a}{2} + X} - 2\Omega W - \left(1 + \frac{X - \frac{a}{2}}{b} \right) b \Omega^2 \beta (T_w - T) \\ = -\frac{1}{\rho} \frac{\partial P}{\partial X} + \nu \left[\frac{\partial^2 U}{\partial X^2} + \frac{\partial^2 U}{\partial Y^2} + \frac{1}{\left(b - \frac{a}{2} + X \right)^2} \frac{\partial^2 U}{\partial \theta^2} \right. \\ \left. - \frac{2}{\left(b - \frac{a}{2} + X \right)^2} \frac{\partial W}{\partial \theta} - \frac{U}{\left(b - \frac{a}{2} + X \right)^2} + \frac{1}{b - \frac{a}{2} + X} \frac{\partial U}{\partial X} \right] \end{aligned} \quad (4.2)$$

$$\begin{aligned} U \frac{\partial V}{\partial X} + V \frac{\partial V}{\partial Y} + \frac{W}{b - \frac{a}{2} + X} \frac{\partial V}{\partial \theta} \\ = -\frac{1}{\rho} \frac{\partial P}{\partial Y} + \nu \left[\frac{\partial^2 V}{\partial X^2} + \frac{\partial^2 V}{\partial Y^2} + \frac{1}{\left(b - \frac{a}{2} + X \right)^2} \frac{\partial^2 V}{\partial \theta^2} + \frac{1}{b - \frac{a}{2} + X} \frac{\partial V}{\partial X} \right] \end{aligned} \quad (4.3)$$

$$\begin{aligned} U \frac{\partial W}{\partial X} + V \frac{\partial W}{\partial Y} + \frac{W}{b - \frac{a}{2} + X} \frac{\partial W}{\partial \theta} + \frac{UW}{b - \frac{a}{2} + X} + 2\Omega U \\ = -\frac{1}{\rho \left(b - \frac{a}{2} + X \right)} \frac{\partial P}{\partial \theta} + \nu \left[\frac{\partial^2 W}{\partial X^2} + \frac{\partial^2 W}{\partial Y^2} + \frac{1}{\left(b - \frac{a}{2} + X \right)^2} \frac{\partial^2 W}{\partial \theta^2} + \frac{1}{b - \frac{a}{2} + X} \frac{\partial W}{\partial X} \right. \\ \left. + \frac{2}{\left(b - \frac{a}{2} + X \right)^2} \frac{\partial U}{\partial \theta} - \frac{W}{\left(b - \frac{a}{2} + X \right)^2} \right] \end{aligned} \quad (4.4)$$

Energy equation

$$\begin{aligned}
 & U \frac{\partial T}{\partial X} + V \frac{\partial T}{\partial Y} + \frac{W}{b - \frac{a}{2} + X} \frac{\partial T}{\partial \theta} \\
 = & \alpha \left[\frac{\partial^2 T}{\partial X^2} + \frac{\partial^2 T}{\partial Y^2} + \frac{1}{(b - \frac{a}{2} + X)^2} \frac{\partial^2 T}{\partial \theta^2} + \frac{1}{b - \frac{a}{2} + X} \frac{\partial T}{\partial X} \right] \quad (4.5)
 \end{aligned}$$

The terms $W^2/(b - a/2 + X)$, $(1 + (X - a/2)/b)b\Omega^2\beta(T_w - T)$ and $2\Omega W$, on the left-hand side of Eq.(4.2), are the centrifugal force due to the curvature of the channel, the centrifugal-type buoyancy force due to the variation of fluid density in a centrifugal field, and the Coriolis force due to the rotation of the channel, respectively. They drive the flow in the X -direction. The terms $-UW/(b - a/2 + X)$ and $-2\Omega U$, on the left hand of Eq.(4.4), are the Coriolis forces acting in the main flow due to the curvature and rotation of the channel, respectively. They would significantly affect the main flow in some region of the parameters.

For both hydrodynamically and thermally fully developed region, the velocity and temperature are independent of the axial coordinate θ . It follows from equation (4.4) that the form of P is restricted to $\theta f_1(X, Y) + f_2(X, Y)$, and then from equation (4.2) and (4.3) that $f_1(X, Y)$ must be a constant. Therefore, we can write

$$\frac{\partial P}{R_c \partial \theta} = -c_1$$

Where c_1 is a positive constant, the direction of flow being always chosen to the

direction of increasing θ .

In the thermally fully developed region of a long channel with a uniform wall heat flux or a constant axial temperature gradient, the fluid temperature changes linearly in the axial direction for both cases of pure forced convection and combined free and forced convection (Shah & London 1978, Hong *et al.* 1974). Then, the fluid temperature T may be expressed as

$$T = c_2 R_c \theta + F(X, Y)$$

Where c_2 is the axial gradient of temperature and F is a function of the cross stream coordinates X and Y alone. This is also valid at the channel wall which means that the wall temperature will change uniformly in the direction of flow. If the wall material is with sufficiently high thermal conductivity to ignore any circumferential temperature variation, the difference in the wall temperature T_w and local value of temperature T in the flow will also be functionally related to cross stream coordinates alone.

By using the characteristics of velocity and temperature mentioned above for hydrodynamically and thermally fully developed region, the governing equations (4.1)-(4.5) in terms of the dimensionless variables, are reduced to,

Continuity equation

$$\frac{\partial}{\partial x} \left((1 + \sigma(x - (1 + \frac{1}{\gamma})/4))u \right) + \frac{\partial}{\partial y} \left((1 + \sigma(x - (1 + \frac{1}{\gamma})/4))v \right) = 0 \quad (4.6)$$

Momentum equations

$$\begin{aligned}
& u \frac{\partial u}{\partial x} + v \frac{\partial u}{\partial y} - \frac{16Dk^2 w^2}{\sigma(1 + \sigma(x - (1 + \frac{1}{\gamma})/4))} - \frac{4L_1 Dk^2 w}{3\sigma} - 16DkL_2(1 + \sigma(x - (1 + \frac{1}{\gamma})/4))t \\
& = -\frac{\partial p}{\partial x} + \left(\frac{\partial^2 u}{\partial x^2} + \frac{\partial^2 u}{\partial y^2} + \frac{\sigma}{1 + \sigma(x - (1 + \frac{1}{\gamma})/4)} \frac{\partial u}{\partial x} - \frac{\sigma^2 u}{(1 + \sigma(x - (1 + \frac{1}{\gamma})/4))^2} \right) \quad (4.7)
\end{aligned}$$

$$u \frac{\partial v}{\partial x} + v \frac{\partial v}{\partial y} = -\frac{\partial p}{\partial y} + \left(\frac{\partial^2 v}{\partial x^2} + \frac{\partial^2 v}{\partial y^2} + \frac{\sigma}{1 + \sigma(x - (1 + \frac{1}{\gamma})/4)} \frac{\partial v}{\partial x} \right) \quad (4.8)$$

$$\begin{aligned}
& u \frac{\partial w}{\partial x} + v \frac{\partial w}{\partial y} + \frac{\sigma u w}{1 + \sigma(x - (1 + \frac{1}{\gamma})/4)} + \frac{\sigma L_1 u}{12} \\
& = \frac{1}{1 + \sigma(x - (1 + \frac{1}{\gamma})/4)} + \left(\frac{\partial^2 w}{\partial x^2} + \frac{\partial^2 w}{\partial y^2} + \frac{\sigma}{1 + \sigma(x - (1 + \frac{1}{\gamma})/4)} \frac{\partial w}{\partial x} - \frac{\sigma^2 w}{(1 + \sigma(x - (1 + \frac{1}{\gamma})/4))^2} \right) \quad (4.9)
\end{aligned}$$

Energy equation

$$u \frac{\partial t}{\partial x} + v \frac{\partial t}{\partial y} - \frac{4Dkw}{\sigma Pr(1 + \sigma(x - (1 + \frac{1}{\gamma})/4))} = \frac{1}{Pr} \left(\frac{\partial^2 t}{\partial x^2} + \frac{\partial^2 t}{\partial y^2} + \frac{\sigma}{1 + \sigma(x - (1 + \frac{1}{\gamma})/4)} \frac{\partial t}{\partial x} \right) \quad (4.10)$$

The dimensionless variables and parameters are as follows:

$$\begin{aligned}
x &= \frac{X}{d_h} & y &= \frac{Y}{d_h} & \gamma &= \frac{a}{b} \\
\sigma &= \frac{d_h}{R_c} & u &= \frac{d_h U}{\nu} & v &= \frac{d_h V}{\nu} \\
w &= \frac{W}{W_1} & p &= \frac{p'}{\rho(\nu/d_h)^2} & p' &= P - \rho \left(X - \frac{a}{2} + \frac{(X-a)^2}{2R_c} \right) R_c \Omega^2 \\
t &= \frac{T_w - T}{\Delta T} & L_1 &= \frac{3R_c \Omega}{2Dk} & L_2 &= \frac{Ra \Omega}{16Dk} \\
Dk &= \frac{\sigma d_h W_1}{4\nu} & c_1 &= -\frac{\partial p'}{R_c \partial \theta} & c_2 &= -\frac{\partial T}{R_c \partial \theta}
\end{aligned}$$

with

$$d_h = \frac{2ab}{a+b} \quad W_1 = \frac{d_h^2 c_1}{\mu} \quad \Delta T = Pr d_h c_2$$

$$R_\Omega = \frac{d_h^2 \Omega}{\nu} \quad Ra_\Omega = \frac{\beta R c \Omega^2 d_h^3 \Delta T}{\nu^2}$$

It is customary to use the mean velocity W_m , and the difference between the wall temperature and the bulk mean temperature ($T_w - T_b$), for the non-dimensionlization of the axial velocity and temperature, respectively, because they are usually specified as design parameters. However, the employment of these quantities results unavoidably in the appearance of the two unknown dimensional parameters in the governing equations which comprise the unknowns W_m and T_b respectively. Consequently, the iterative procedure should be applied, assuming some initial estimated values to them. It requires an additional computation time. In order to avoid this additional increase in computation time, W_1 and ΔT are used here as a representative axial velocity and a representative temperature difference, respectively. They involve the axial pressure gradient c_1 and the axial temperature gradient c_2 , which are usually given as design parameters so that it does not induce a difficulty in using the computation results for design. The velocity W_1 is proportional to the pressure drop in the axial direction and the mean axial velocity $W_m = W_1/8$ for the flow in a stationary straight circular tube. The temperature difference ΔT is, on the other hand, proportional to the fluid temperature difference between the channel inlet and outlet.

Different scaling quantities used in the non-dimensionlization may generate different parameter groups for the rotation, curvature and heat/cooling effects. In Chapters 2 and 3, we show that L_1 and L_2 represent the ratios of the dynamical parameters D_Ω (in the Coriolis problem) and Dr (in the mixed-convection problem) to that (De^2) in the Dean problem, respectively. They are two parameters to determine the flow transitions in the channel with curvature, rotation and heating/cooling. They are introduced in the governing equations (4.6)-(4.10) explicitly since we mainly concern this transition of the flow in this work.

In this work, we attempt to examine the transition of symmetric secondary flow with respect to the horizontal centreline only. In order to effectively arrange the grid points, the symmetry/antisymmetry of flow and temperature fields about the X axis is used so that it suffices to consider the upper half region alone for the analysis. In fact, it is readily found that u, w and t are even functions of y , while v is odd functions of y . Then the boundary conditions may be written, in terms of dimensionless variables, as

$$u = v = w = t = 0 \quad \text{at } x = 0, \frac{1}{2}(1 + \frac{1}{\gamma}) \quad \text{for } 0 \leq y \leq \frac{1}{4}(1 + \gamma) \quad (4.11)$$

$$u = v = w = t = 0 \quad \text{at } y = \frac{1}{4}(1 + \gamma) \quad \text{for } 0 \leq x \leq \frac{1}{2}(1 + \frac{1}{\gamma}) \quad (4.12)$$

$$\frac{\partial u}{\partial y} = \frac{\partial w}{\partial y} = \frac{\partial t}{\partial y} = 0, v = 0 \quad \text{at } y = 0 \quad \text{for } 0 \leq x \leq \frac{1}{2}(1 + \frac{1}{\gamma}) \quad (4.13)$$

Equations (4.6)-(4.10) under the boundary conditions (4.11)-(4.13) constitute the mathematical model of the problem under consideration. Note that only symmetrical solutions, with respect to the horizontal centreline, will be obtained with the present boundary conditions (4.11)-(4.13) set for half of the channel.

After the velocity and temperature fields are obtained, the computations of the local friction factor and Nusselt number are of practical interest. Following the usual definitions, the expression for the product of the friction factor and Reynolds number fRe and Nusselt number Nu can be written based on the local axial velocity gradient or the temperature gradient at the wall as

$$fRe = \frac{2}{w_m} \left(\frac{\partial w}{\partial n} \right)_{wall} \quad (4.14)$$

$$Nu = \frac{1}{t_b} \left(\frac{\partial t}{\partial n} \right)_{wall} \quad (4.15)$$

Where w_m and t_b are mean axial velocity and bulk mean temperature, respectively.

The mean friction factor and Nusselt number can be obtained either by peripherally averaging the local values or by making the overall force and energy balance along the axis of the channel. The calculated values by these two methods were found to be in good agreement. The result presented in this work is the average of the values obtained by these two methods.

4.3 Numerical Method of Solution

The governing equations (4.6)-(4.10) given in the previous section are a set of convection-diffusion equations with velocity-pressure coupling. In order to obtain solution for this kind of equations by finite-volume method, two factors are considered to be extremely essential: (1) using correct difference scheme for convection term and (2) decoupling the velocity and pressure properly. After discretization in the domain, the governing differential equations become a set of algebraic equations, the so-called discretization equations. The methods of solving these discretization equations are also vital to the success. Therefore, the difference scheme, treatment of the velocity-pressure coupling and the method of solving the discretization equations may be regarded as the three major factors for the success of a finite-volume method. As well they are also the major criteria for distinguishing one scheme from the other.

In the last twenty years, numerous papers were published dealing with the three aspects of the finite-volume method mentioned above. Based on the review and comparison among various methods in terms of their transport and conservative properties, convective numerical stability, economy and exactitude, we chose the power-law scheme to discretize the convection term; employ the SIMPLE scheme to deal with the problem of velocity-pressure coupling; and use an alternating direction line-by-line iterative method (ADI) with block correction technique to solve the discretization equations. The description of the numerical implementation can be

found, for example, in Patankar (1980).

The initial calculation for Dean problem was performed by setting angular velocity $\Omega = 0$ to verify the code. In Fig.4.2, the mean friction factor and Nusselt number for curved square channel obtained by the present analysis are shown together with the available theoretical, numerical and experimental results. In the figure, the friction factor and Nusselt number are shown as a function of the Dean number on the basis of those for a stationary straight square channel. The results of the present analysis are in good agreement with the published results.

In the present computations, four pairs of grid sizes were used to check the grid dependence. They are 35×17 , 43×21 , 51×25 and 59×29 . The results obtained by using these four grid sizes are shown in Table 4.1 for six cases with $L_1 = -30, -5, 1, 5, 8$ and 30 respectively with $\gamma = 1, Dk = 100, \sigma = 0.01, Pr = 0.7$ and $L_2 = -5$. These six cases are chosen because they cover all typical secondary flow patterns obtained in the present work. Four representative properties, namely, the Dean number and the absolute maximum values of secondary flow stream function ($|\psi|_{max}$), maximum axial velocity (w_{max}) and maximum temperature (t_{max}), as well as the CPU time, are listed in Table 4.1 for comparison.

The computations were carried out on the AMDAHL computer. The initial guesses of the fields for ψ , w , t , and p were all set to zero. The general trend of these results as the grid size is decreased tends to indicate that the solutions for the case of (51×25) grids are accurate to within 1% tolerance. We also checked the

Table 4.1: Variations of De , $|\psi|_{max}$, w_{max} , t_{max} , and CPU time in seconds with different grids

$\gamma = 1 \quad Dk = 100 \quad \sigma = 0.01 \quad Pr = 0.7 \quad L_2 = -5$						
L_1	Grids	De	ψ_{max}	w_{max}	t_{max}	CPU (sec)
-30	35×17	46.93	12.86	0.0177	16.79	
	43×21	47.94	12.88	0.0182	17.22	86.5
	51×25	48.66	12.88	0.0184	17.54	184.4
	59×29	49.04	12.88	0.0185	17.66	465.7
-5	35×17	63.33	13.47	0.0252	23.35	
	43×21	64.02	13.38	0.0273	26.75	125.7
	51×25	68.22	13.51	0.0286	28.61	492.7
	59×29	68.50	13.47	0.0286	28.85	1300.8
1	35×17	72.30	11.13	0.0299	29.85	
	43×21	72.75	11.07	0.0301	30.19	170.5
	51×25	73.01	11.03	0.0302	30.38	370.4
	59×29	73.17	11.04	0.0302	30.49	750.9
5	35×17	90.11	10.57	0.0405	49.37	
	43×21	90.45	10.64	0.0407	49.79	106.5
	51×25	90.63	10.63	0.0407	49.95	214.0
	59×29	90.74	10.65	0.0408	50.03	369.0
8	35×17	101.29	9.32	0.0464	66.76	
	43×21	101.45	9.43	0.0465	66.71	162.0
	51×25	101.54	9.51	0.0464	66.83	282.5
	59×29	101.60	9.54	0.0464	66.81	1540.3
30	35×17	51.83	10.37	0.0194	21.24	
	43×21	52.81	10.33	0.0198	21.80	79.6
	51×25	53.50	10.29	0.0201	22.13	180.0
	59×29	53.97	10.26	0.0202	22.28	427.1

detailed variations of the flow and temperature fields for different grid sizes, and found that 51×25 is indeed a reasonably accurate choice for the grid size for square channels. It is worth noting that the CPU time increases rapidly as the grid spacing decreases. In order to have a balance between the cost of the computer time and the accuracy of the solution, we carried out all the computations with a 51×25 meshes for square channels.

Typically, the computations were made for given values of the aspect ratio γ , curvature ratio σ , Dean number Dk , Prandtl number Pr and the parameters L_1 and L_2 . The calculations were performed iteratively using the alternating direction line-solution (ADI) with block correction technique, and the solution was assumed to be convergent in a numerical sense if the maximum relative error in each of the primitive variables (i.e. velocity components, temperature and the pressure) is less than 5×10^{-5} between successive iterations.

4.4 Results and Discussion

In addition to the viscous and inertial forces, the fluid in the rotating curved channel is subject to centrifugal force (due to the curvature of the channel), Coriolis force (due to the rotation and curvature) and the centrifugal-type buoyancy force (resulted from temperature-induced density variation of the fluid in the rotating field). While the centrifugal and buoyancy forces act on the plane of cross section, the Coriolis forces have both X and θ components for the configuration as shown in

Fig.4.1. That due to the curvature is $-UW/(b - a/2 + X)$ (θ - component). Those due to rotation is perpendicular to both the axis of rotation and the direction of the relative velocity of the fluid, i.e. $-2\Omega U$ (θ -component) and $2\Omega W$ (X -component). Two θ -components of the Coriolis force may act in the direction or direction opposite to the main flow depending on the signs of U and ΩU . Consequently, they may accelerate or decelerate the main flow. Furthermore, these two components either enhance or cancel each other depending on the rotation direction of the channel. If the rotation is positive, they enhance each other. Otherwise, they cancel each other.

In the plane of the cross section, the centrifugal force always acts outwards in the positive X - direction. However, the Coriolis force may act in either positive or negative X -direction depending on the rotation direction. If the rotation is positive, it will act along the positive X - direction. When the rotation is negative, however, it will act in the negative X -direction. Similarly, the centrifugal-type buoyancy force may act in the positive or negative X -direction depending on the direction of the heat flux. If the fluid is heated, it will be along the positive X -direction. If fluid is cooled, it will act in the negative X -direction. From this simple analysis about force directions, it is clear that centrifugal, Coriolis and buoyancy forces enhance each other for some cases, and cancel each other for some other cases. This could make the flow and heat transfer more complex than those of channel simple rotation or curvature.

The flow and heat transfer under consideration are characterized by the following men-

sionless parameters: $\gamma, \sigma, Pr, Dk, L_1$ and L_2 . These parameter are coupled with and affect each other, so that the effects of the parameters on the flow and heat transfer are very complex. Extensive computations are required for a large number of cases to cover the entire effect, which requires an extremely long computation time. Fortunately, the introduction of L_1 and L_2 , analogous to the normalization of the problems, enables one to obtain some insight of the problem from not so large number of cases. This results from the fact that they are the dynamical parameters for the Coriolis problem and mixed convection problem based on the dynamical parameter for Dean problem. Even so, however, it is still a lengthy process to describe the typical results covering the whole range of the parameters. The results shown in this chapter will be confined to the case of the positive rotation with $\gamma = 1, Pr = 0.7$ and $\sigma = 0.02$.

Some features of the main flow and temperature distributions can be expected and understood through the force balance and energy balance in the governing equations. It is the secondary flow that makes the axial velocity and temperature profiles different from the parabolic profile in Poiseuille flow. The effect of the secondary flow enters the governing equation for the main flow (Eq.(4.4) or (4.9)) through three terms: the convection term, and two Coriolis terms due to the curvature and rotation, respectively. Two Coriolis terms may be in the same direction or opposite to the main flow depending on the sign of U although they are always in the same direction for the case of positive rotation. The absence of these three terms leads to

the Poiseuille solution which has an axisymmetric and parabolic profile. The relative importance among the five terms in Eq.(4.4) or (4.9) depends on the magnitudes of governing parameters, and shows different flow patterns for different regions. The driving term is the axial pressure gradient which is always important. The viscous term is always important near the wall, but may not be significant in the core region for certain ranges of the parameters. The scales in this work are convenient for the present calculation, but not suitable for detail analysis of the force mechanisms.

If Dk , L_1 and L_2 are small enough, then secondary flow would be too weak to modify the main flow and temperature distributions effectively. Such axial velocity and temperature profiles are essentially axisymmetric and parabolic with the maximum value occurring along the horizontal centreline at or very close to the center of the cross section. One case with this kind of flow and temperature distribution is shown in Fig.4.3. This is one limiting case examined by previous studies (Miyazaki 1973; Ito & Motai 1974). In this flow region, the inertial force in Eq.(4.4) or (4.9) is very weak as compared with the viscous force. The driving force for main flow (i.e. pressure term) is mainly balanced by the viscous force in whole flow domain. Other forces (inertial, Coriolis forces) are very weak. The stability analysis, performed by Yanase *et al.* (1988) and Winters (1987), showed that this one-pair vortex flow to be stable to an arbitrary perturbation in the Dean problem.

The effect of the secondary flow enters the energy equation through one term only, i.e., convection term. When the secondary flow is sufficiently weak such that the

Coriolis terms in the momentum equation in the θ -direction are too weak to modify the main flow effectively, the main flow and temperature distributions should be qualitatively similar. However, they might have qualitatively different distributions if the secondary flow is strong enough.

4.4.1 Flow transitions and temperature distributions

The case without the effect of buoyancy force ($L_2 = 0$)

Figure 4.4. illustrates the secondary flow patterns, axial velocity isopleths and profiles, and isotherms and temperature profiles for several representative values of L_1 at $Dk = 100$, $\sigma = 0.02$ and $L_2 = 0$. The variations of several representative properties, namely, the Reynolds number, the Dean number, the maximum absolute value of the secondary flow stream function, the maximum values of main velocity and temperature, and the mean friction factor ratio and Nusselt number ratio, are listed in Table 4.2. Because of the symmetry about the horizontal centreline, they are shown in the upper half of the cross section only. In the figure, the stream function, axial velocity and temperature are normalized by their corresponding maximum absolute values. A cross is used to denote the position at which they reach the maximum values. A vortex with a positive (negative) value of the stream function indicates a counter-clockwise (clockwise) circulation

With zero value of L_2 , centrifugal-type buoyancy force disappears. Heat transfer

Table 4.2: The variations of several representative properties with L_1 at $\gamma = 1$, $Dk = 100$, $\sigma = 0.02$, $Pr = 0.7$ and $L_2 = 0$ ($(fRc)_0 = 14.23$, $Nu_0 = 3.608$)

L_1	Rc	De	$ \psi _{max}$	w_{max}	t_{max}	$fRc/(fRc)_0$	Nu/Nu_0
0	542	77	5.641	0.0496	39.89	1.314	1.486
1	492	70	6.865	0.0440	31.88	1.441	1.686
2	464	66	7.572	0.0406	28.00	1.533	1.812
2.5	453	64	7.778	0.0394	26.65	1.572	1.860
3	423	60	7.256	0.0353	22.40	1.681	2.012
7.5	366	52	8.697	0.0284	16.92	1.948	2.336
10	363	51	9.239	0.0293	19.16	1.970	2.197
30	271	38	7.342	0.0193	16.53	2.680	2.105
70	195	28	3.606	0.0132	15.06	3.873	1.719

is purely forced convection. In the plane of cross section, both centrifugal (due to curvature) and Coriolis forces (due to the rotation) act radially outwards ($+X$) for the case of positive rotation. If L_1 is also set to zero, the Coriolis force then disappears and the problem reduces to the Dean problem which has been well examined by many investigators. The secondary flow consists of one-pair of counter-rotating vortices as shown in Fig.4.4(a)-(i) for the case of low Dean number. The fluid in the core region is driven in the positive X -direction by the centrifugal force. The outward flow in the core region forces the fluid near the upper and lower walls to flow in the negative X -direction and one-pair of counter-rotating vortices is generated. These are so called Ekman-vortices. The strong inward flow near the upper and lower wall is observed and this induces the Ekman layer (Smirnov 1978, Jen *et al.* 1992)(Fig.4.4(a)-(ii)). A uniform outward secondary flow in the core region has two effects on main flow. One is pushing the axial velocity peak outward, thereby increasing the local shear stress and heat transfer near the outer wall. Another is inducing an upstream Coriolis force, which flattens the axial velocity profile (Fig.4.4(a)-(ii)).

As L_1 increases from zero, the secondary flow becomes stronger since the outward Coriolis force enhances the centrifugal force. However, it consists of the same type one-pair of counter-rotating vortices as shown in Fig.4.4(b)(c)-(i). There exists a weak secondary flow region in triangular form (Fig.4.4(b)-(i)) or stagnation area (Fig.4.4(c)-(i)) near the central part of the outer wall. This foreshadows the onset of an Coriolis instability to be described later.

Shown in Fig.4.4(a)-(c)-(ii) are the axial velocity isopleths and profiles corresponding to the secondary flow patterns in Fig.4.4(a)(b)(c)-(i). It is observed that the isovels are more sparsely spaced in the region near the inner wall than near the outer wall. Consequently, pronounced peripheral variations are expected in the local friction factors. The densely distributed isovels near the center part of the outer wall results in a high pressure region since centrifugal force and Coriolis force are proportional to W and W^2 , respectively. The flow in the channel core is not geostrophic; it is *ageostrophic*, i.e. pressure gradients are balanced by both Coriolis force and convective inertial force. Two axial velocity peaks are observed with one on the upper half of the cross section and the other on the lower half. The regions of maximum velocity are moved toward the upper and lower walls while they are shifted toward the outer wall by the curvature and rotation in the positive direction. There is an indication of peaking of the axial velocity near the boundary layer regions at the upper and lower walls. The peaking results because the boundary layer is being fed by high velocity fluid from the outer wall; the core, however, is being fed by lower velocity fluid from the inner wall. A depression in the axial velocity profile near the outer wall shown in Fig.4.4(b)(c)-(ii) foreshadows the onset of the instability to be described later.

A striking feature of this ageostrophic one-pair vortex structure can be seen from the profiles of the axial velocity along the vertical centreline and the horizontal centreline by curves 0-2 in Fig.4.5. The axial velocity w changes linearly across the

core and a little from lower wall to upper wall. Then the vorticity is nearly constant. Slow-moving fluid from the inner wall is accelerated across the core axially at a constant rate until the outer wall is approached. Coriolis and convective inertial forces dominate the ageostrophic core. Axial velocity falls to zero in viscous layers on the inner and outer walls. The constant-vorticity, inviscid core flow structure suggests a possible analysis by asymptotic method. It appears that no such attempt was made so far in the literature.

Qualitatively similar results are observed for the temperature distribution (Fig.4.4(a)(b)(c)-(iii)). The pronounced peripheral variations in the local Nusselt number will result from the more sparsely spaced isotherms in the region near the inner wall than near the outer wall. The reason for this is that the larger axial velocity gradients exist in the region near the outer wall. Two symmetric (with respect to the horizontal centreline) *high* temperature regions are observed. The physical mechanism can be explained by recalling the secondary flow patterns in Fig.4.4(a)(b)(c)-(i). The larger inward secondary flow near the upper and lower walls brings the relatively *cold* (i.e. non-dimensional temperature close to zero) fluid to the inner wall; the colder fluid near the inner wall returns to the core region of the channel, flows outward and isolates the warmer fluid in the upper and lower sides of the channel. And the fairly uniform outward secondary flow in the core region leads to a flattened isotherm distribution in that region.

When the rotation becomes more rapid, the ageostrophic one-pair vortex breaks

down into a configuration of two pair of counter-rotating vortices that is asymmetric with respect to the vertical centreline of the channel (Fig.4.4(d)(e)(f)-(i)). The additional pair of counter-rotating vortices located in the center of the outer wall are called *Coriolis-vortices*. They result from the Coriolis instability and are similar to the *Dean-vortices* due to the centrifugal instability. A strong inward secondary flow exists between these two vortices and a strong outward secondary flow appears between the original larger vortices (*Ekman-type-vortices*) and the smaller vortices (*Coriolis-vortices*).

The onset of the *Coriolis-vortices* is consistent with the instability explanation given by Cheng et al. (1976) for the Dean problem. In the region near the central outer wall, the pressure gradient across the channel in X-direction is positive but the centrifugal force and Coriolis force decreases from a maximum value to zero at the outer wall. The instability due to the imbalance between the pressure gradient inwards and the Coriolis & centrifugal forces outwards results in an unstable region. If the rotation speed becomes large enough, viscous effects can no longer hold the one-pair vortex structure in place, thus additional vortices may appear. The resulting secondary flow is similar to those obtained by Cheng *et. al.*(1976) for Dean problem and Speziale (1982) for the Coriolis problem. However, the instability here is caused by both Coriolis and centrifugal forces rather than by centrifugal force (Coriolis force) alone as in Dean problem (Coriolis problem). Since no such an instability can exist in the absence of the Coriolis force (Fig.4.4(a)-(i)), we may

still call this instability as the Coriolis instability, and the resulting additional pair of vortices as the Coriolis-vortices.

Figure 4.4(d)(e)(f)-(ii) demonstrate the way in which the Coriolis-vortices affect the isovels and profile of the axial velocity. Significantly distorted isovels are observed in the region with the Coriolis-vortices. Corresponding to the strong inward secondary flow, the isovels in that region are moved inwards by the Coriolis-vortices. Two symmetric high velocity cores are found. The position of maximum axial velocity, at which the centrifugal and Coriolis forces are maximum, is located on the boundary line between the Ekman and Coriolis-vortices. It is clear that the centrifugal and Coriolis forces due to the main flow become the driving forces for the secondary flow. Comparing with those in Fig.4.4(a)(b)(c)-(ii), the isovels in the region near the upper and lower wall are more tightly spaced. The large velocity gradients are also found between each of the two high velocity cores and the outer wall. Thus the higher local friction factors are expected there.

The axial velocity distributions along the vertical and horizontal centrelines are shown by curves 4-5 in Fig.4.5(a)(b). Again, the axial velocity is substantially distorted, with its maximum velocity shifting toward the low-pressure side of the channel (Fig.4.5(b)). The axial velocity profile along the vertical centreline is symmetric and flat with peaks located near the boundary of the boundary layers at the upper and lower walls. The most striking feature is that the axial velocity has inflection points on both the vertical and horizontal centrelines. Similar features were

found in Dean problem (Cheng et al. 1976) and Coriolis problem (Speziale 1982).

From inviscid reasoning, such profiles may be unstable in accordance with Rayleigh's inflection point criterion. Assuming the channel with infinite span, the linear stabilities of Dean-vortices (Dean problem) and Coriolis-vortices (Coriolis problem) were examined by Finlay, Keller & Ferziger 1988 and Finlay 1990. Two different wavy travelling vortex flows, namely *undulating* vortex flow and *twisting* vortex flow, are developed due to the instability of the Dean-vortices and Coriolis-vortices subjected to the streamwise wavy perturbations. These two kinds of vortex flows are confirmed experimentally by Ligrani et al. (1992), Ligrani & Niver (1988) for the Dean problem with large aspect ratio and by Cheng & Wang (1993a,b) and Cheng et al. (1992) for Dean or Coriolis problem with smaller aspect ratio.

The stability of Dean-vortices and Coriolis-vortices subjected to two dimensional, spanwise-periodic perturbations (i.e. Eckhaus stability) was examined numerically by Guo and Finlay (1991) for infinite-span cross section. They found that Eckhaus stability boundary is a small closed loop. Within the boundary, Dean-vortices or Coriolis-vortices are stable to spanwise perturbations. Outside the boundary, Eckhaus instability causes the vortex pairs to split apart or merge together. Experimental observations of splitting and merging of vortex pairs were made by Ligrani & Niver (1988), Alfredsson & Persson (1989), Matsson & Alfredsson (1990), Cheng & Wang (1993a,b) and Cheng et al. (1992). However, this type of hydrodynamic stability analysis has not been extended to the geometries with finite cross sections.

It is also noted that such an analysis has not been made for buoyancy-vortices which will be discussed later.

Figures 4.4(d)(e)(f)-(iii) illustrate isotherms and temperature profile affected by the Coriolis-vortices. The isotherms are drastically distorted inward near the centre of the outer wall where the Coriolis-vortices occur. Two symmetric high temperature cores (with respect to the horizontal centreline) appear in the cross section of the channel. The isotherms in the regions near the upper and lower walls are more tightly spaced than those shown in Fig.4.4(a)(b)(c)-(iii). Larger temperature gradients are also found between each of the two high temperature cores and the outer wall. Thus a higher heat transfer rate is expected in these regions.

If the Coriolis force is now increased to that with $L_1 = 10$ while maintaining the same values for the other parameters, the Coriolis vortex pair presented in Fig.4.4(d)(e)(f)-(i) disappears and the secondary flow restabilizes to a slightly asymmetric one-pair vortex configuration as shown in Fig.4.4(g)-(i). Furthermore, the inflection points in the axial velocity profiles along the vertical and horizontal centrelines also disappear (curve 6 in Fig.4.5). The axial velocity profile assumes a Taylor-Croudman configuration in the core region with a maximum located on the horizontal centreline (Fig.4.4(g)-(ii)). The tightly spaced isovels along the outer wall upper and lower walls signal the high local friction factors in these regions. The similarity between the axial velocity and temperature profiles still holds although the difference between them becomes larger than the previous cases.

After the Coriolis-vortices disappear, there still exists a transition in the main flow upon increasing the Coriolis force further. If the value of L_1 is high enough, as shown in Fig.4.4(h)(i)- (ii), the Coriolis forces tend to dimple the axial velocity profile in the region near the center and create a dumbbell-like profile with two maxima. One is within the Ekman layer along the upper wall. The other is within the Ekman layer along the lower wall. The shifting of the locations of maxima results in even more closely spaced isovels near the upper and lower walls. The fluids flow geostrophically in the channel core and the Stewartson layers (vertical double layers). However, the secondary flow and temperature profile (Fig.4.4(h)(i)-(i)(iii)) remain qualitatively similar as those shown in Fig.4.4(g)-(i)(iii). It appears that this is the first numerical calculation to illustrate two kinds of flow structure after the Coriolis-vortices disappear.

It is worthy to note that near uniformity of the axial velocity in the core region of the rotating curved channels is of great importance in aerosol centrifuges. It allows aerosol centrifuges to function as true particle spectrometers (Hoover & Stöber 1981; Hoover et al. 1984).

The heating case with $L_2 > 0$

If the fluid is heated, both centrifugal and centrifugal-type buoyancy forces act radially outwards in the plane of the cross section. The Coriolis force also acts radially outwards in the case of positive rotation. The flow transitions in both

secondary flow and main flow are qualitatively similar to those for the case of $L_2 = 0$. However, the corresponding transitions will occur at lower values of L_1 than those for $L_2 = 0$. The difference results from the enhancement effect of buoyancy force on Coriolis force and centrifugal forces, and it depends on the relative importance of the buoyancy force, i.e. the value of L_2 .

Figure 4.6 shows the secondary flow patterns, axial velocity isopleths and profiles, and isotherms and temperature profiles for several typical values of L_1 at $Dk = 100$, $\sigma = 0.02$ and $L_2 = 5$. The variations of the Reynolds number, Dean number, maximum absolute value of secondary flow stream function, the maximum values of main velocity and temperature and mean friction factor ratio and Nusselt number ratio, are listed in Table 4.3. The axial velocity profiles, along the vertical and horizontal centrelines, are illustrated in Fig.4.7. Some features such as reflection points, described previously, may be seen more clearly.

The cooling case with $L_2 < 0$

If the fluid is cooled, the inward buoyancy force counteracts the centrifugal and Coriolis forces in the plane of the cross section. The flow situation is more complicated. The flows in various regions of the parameter can be different in nature. Figure 4.8 shows the secondary flow patterns, axial velocity isopleths and profiles, and isotherms and temperature profiles for several representative values of L_1 at $Dk = 100$, $\sigma = 0.02$ and $L_2 = -5$. The variations of the Reynolds number, Dean

Table 4.3: The variations of several representative properties with L_1 at $\gamma = 1$, $Dk = 100$, $\sigma = 0.02$, $Pr = 0.7$ and $L_2 = 5$ ($(fRe)_0 = 14.23$, $Nu_0 = 3.608$)

L_1	Re	De	$ \psi _{max}$	w_{max}	t_{max}	$fRe/(fRe)_0$	Nu/Nu_0
0.1	379	54	10.022	0.0312	16.75	1.875	2.389
1	372	53	10.321	0.0301	16.15	1.912	2.438
4	351	50	10.938	0.0275	14.58	2.027	2.566
5	363	51	11.619	0.0294	16.88	1.962	2.394
10	331	47	11.46	0.0254	15.33	2.163	2.472
70	181	26	3.749	0.0131	13.45	4.184	1.798

number, maximum absolute value of secondary flow stream function, the maximum values of main velocity and temperature and mean friction factor ratio and Nusselt number ratio, are listed in Table 4.4.

Shown in Fig.4.8(a)(b)-(i) are two stream function contours of the secondary flow with an additional pair of vortices shown in the center part near the inner wall. This additional pair of vortices results from the buoyancy force instability which is similar to the centrifugal instability in the Dean problem or the Coriolis instability in the Coriolis problem. They are called *buoyancy-vortices* in this work.

The presence of the buoyancy-vortices gives rise to a highly disturbed main flow field (Fig.4.8(a)(b)-(ii)) and temperature field (Fig.4.8(a)(b)-(iii)), with strong in-

Table 4.4: The variations of several representative properties with L_1 at $\gamma = 1$, $Dk = 100$, $\sigma = 0.02$, $Pr = 0.7$ and $L_2 = -5$ ($(fRe)_0 = 14.23$, $Nu_0 = 3.608$)

L_1	Re	De	$ v _{max}$	w_{max}	t_{max}	$fRe/(fRe)_0$	Nu/Nu_0
1	401	57	9.003	0.0341	18.86	1.781	2.255
1.5	408	58	8.764	0.0349	19.47	1.753	2.214
2	443	63	9.853	0.0396	23.57	1.615	2.027
3	457	65	9.519	0.0414	25.21	1.565	1.949
5	488	69	8.722	0.0460	29.89	1.466	1.770
8	545	77	6.705	0.0543	41.20	1.311	1.479
10	606	86	4.416	0.0624	54.80	1.179	1.253
11.5	652	92	2.716	0.0688	67.66	1.096	1.102
12	484	68	3.635	0.0461	38.25	1.475	1.441
13.5	415	59	5.053	0.0367	27.20	1.722	1.724
15	406	57	5.463	0.0373	29.37	1.762	1.699
70	213	30	3.430	0.0148	17.14	3.542	1.632

flectional profiles developing in both X - and Y -directions (Fig.4.8(a)(b)-(ii) and curves 1-2 in Fig.4.9). This may result a secondary instability as discussed previously. The most striking feature of the buoyancy-vortices shown in Fig.4.8(a)(b)-(i) is that they appear in the low pressure side (inner wall) rather than the usual high pressure side (outer wall). This is indicated by the isopiestic contours in Fig.4.10. The secondary flow, axial velocity and temperature distributions (Fig.4.8(a)(b)) are qualitatively similar to those shown in Fig.4.4(e)(f) and Fig.4.6(a)(b)(c) by interchanging the inner wall with the outer wall.

Upon increasing the values of L_1 while maintaining the same values for the other parameters, the buoyancy vortex pair shown in Fig.4.8(a)(b)-(i) disappears, and the secondary flow reduces to one pair counter-rotating configuration (Fig.4.8(c)(d)-(i)) with circulating direction opposite to that shown in Fig.4.4(a)(b)(c). In fact, the buoyancy-vortices shown in Fig.4.8(a)(b)-(i) results from the break-up of this one pair vortex flow due to buoyancy-force instability. By interchanging the inner and outer walls, the secondary flow, axial velocity and temperature distributions may be regarded to be qualitatively similar to those shown in Fig.4.4(a)(b)(c). The flow in the channel core is ageostrophic, i.e. pressure gradients are balanced by both convective inertial force and Coriolis force. The reverse direction of the secondary flow indicates that the secondary flow is still dominated by the buoyancy force.

If the Coriolis force is now increased further such that the resulting force of the centrifugal and Coriolis forces is of same order of magnitude as the buoyancy force,

the corner vortices occur and grow with circulating direction opposite to that of vortices in the core region. Figures 4.8(e)(f)(g)(h)-(i) illustrate the process of this formation and development of the corner vortices. The flow in the channel core is neither ageostrophic nor geostrophic. The viscosity effect is not confined in a thin layer along the walls, and exists in the whole cross section of the channel. No counter-part exists in the cases with $L_2 \geq 0$. However, similar results are also found for case of circular cross section using the perturbation method (Chapter3, also see Wang & Cheng 1994a,b).

An important feature of the axial velocity in this flow region is the appearance of strong inflectional profiles (Fig.4.8(e)(f)(g)(h)-(ii) and curves 5-8 in Fig.4.9). This suggest a possible secondary instability problem. No such analysis appears to have been made in the past.

When the rotation becomes more rapid, two corner vortices shown in Fig.4.8(h)-(i) merge together and push the vortices in the center of the cross section to the outer wall. At same time, two vortices near the center in Fig.4.8(h)-(i) merge together and form one-pair of counter- rotating vortices near the center part of the outer wall. They are called *merging-vortices* in this work. Although the secondary flows in Fig.4.8(i)(j)-(i) look quite similar to those in Fig.4.4(e)(f) or Fig.4.6(a)(b)(c), they are different in terms of the mechanism responsible for the appearance of the additional pair of vortices.

A break-up of Ekman-vortices is associated with the Coriolis-vortices due to the

Coriolis instability whereas the merging together of the vortices appearing in the region where centrifugal, Coriolis and buoyancy forces just neutralize each other, characterizes the formation process of the merging-vortices. Here '*just neutralizing*' each other means that one of the three forces (termed as A-force, and it represents the buoyancy force for the cases shown in Fig.4.8) cancel the other two forces (referring the resulting force of these two forces as B-force), and A-force and B-force have the same order of magnitude. The difference in the mechanism results in a smaller size of the merging-vortices than that of the Coriolis-vortices. Furthermore, the axial velocity and temperature distributions are also qualitatively different (see Fig.4.4(e)(f)-(ii)(iii), Fig.4.6(a)(b)(c)-(ii)(iii) and Fig.4.8(i)(j)-(ii)(iii)).

Upon increasing the values of L_1 further, the merging-vortices disappear and the secondary flow becomes a slightly asymmetric one-pair vortex configuration (Fig.4.8(k)-(i)). The axial velocity profile assumes a Taylor-Proudman configuration (Fig.4.8(k)-(ii)) with a maximum located on the horizontal centreline. Similar profile is also observed for the temperature (Fig.4.8(k)-(iii)).

Upon increasing the value of L_1 further, the secondary flow remains qualitatively unchanged (Fig.4.8(l)-(i)). However, the dominant Coriolis force causes the main flow to have a bar-convex dumbbell-like profile with three high velocity regions (Fig.4.8(l)-(ii)). A geostrophic flow is observed in the channel core and Stewartson layers. The temperature profile (Fig.4.8(l)-(iii)), however, remains qualitatively similar to that shown in Fig.4.8(k)-(iii).

4.4.2 The disappearance and reappearance of Dean-, Coriolis- and buoyancy-vortices

The potential sources of instability for flow in rotating curved channels are centrifugal force, Coriolis force and buoyancy force. The instability from such body forces is in the form of streamwise-oriented vortices, i.e. Dean-vortices, Coriolis-vortices and buoyancy-vortices. The onset of these vortices receives much attention in recent years for the Dean, Coriolis and mixed convection problems, respectively. Their disappearance and reappearance, however, have in general suffered comparative neglect. Very little information can be found in the published literature.

Dean-vortices, Coriolis-vortices and buoyancy-vortices perform differently in terms of their characteristics of the disappearance and reappearance although they share some similarities as observed by many investigators. Coriolis-vortices (Fig.4.4(e)(f)-(i) or Fig.4.6(a)(b)(c)-(i)) disappear upon increasing the Coriolis force. The secondary flow restabilizes to a one-pair vortex flow (Fig.4.4(g)-(i) or Fig.4.6(d)-(i)), as discussed in the last section. If the Coriolis force is increased further, this one-pair vortex structure changes to another one-pair vortex flow (Fig.4.4(h)-(i) or Fig.4.6(e)(f)). However, no reappearance of the Coriolis-vortices is observed.

Figure 4.11 shows the disappearance and reappearance of the Dean-vortices (Fig.4.11(i)) and buoyancy- vortices (Fig.4.11(ii)). For the stationary curved channel, one-pair vortex flow (Fig.4.11(a)-(i)) becomes unstable with respect to the cen-

trifugal instability upon increasing the centrifugal force sufficiently. The Dean-vortices are being set up in the region near the center of the outer wall (Fig.4.11(b)-(i)). Upon increasing the centrifugal force further up to that with $Re = 5583$, no disappearance or reappearance is observed in the present calculation (Fig.4.11(c)-(i)).

Figure 4.11(ii) shows the manner in which the buoyancy force affects the disappearance and reappearance of the buoyancy-vortices. Upon increasing the buoyancy-force, the buoyancy instability induces the buoyancy-vortices in the center part near the inner wall or outer wall (Fig.4.11(e)-(ii) or Fig.4.11(i)-(ii)) depending on whether the fluid is cooled or heated. The secondary flow changes from the original one-pair vortex flow (Fig.4.11(f)(g)(h)-(ii)) to two-pair vortex flow (Fig.4.11(e)(i)-(ii)) (Note that the circulation direction of the vortex in (f) is opposite to those in (g)(h)). Upon increasing the buoyancy force further, the buoyancy-vortices disappear. The secondary flow restabilizes to one-pair vortex configuration (Fig.4.11(c)(d)(j)-(ii)). When the buoyancy force is increased further, however, they reappear and remain in a large portion of the parameter space (Fig.4.11(a)(b)(k)(l)-(ii)).

Some contradiction exists in the published literature about whether the Dean-vortices change size and shape with Dean number in fully developed flow region. Experiments by Bara et al (1992) show that the size is about the same at all Dean numbers when the flows are fully developed. Such changes, however, are observed by Cheng et al (1979), Sugiyama et al (1983) and Ligiani & Niver (1988). In addition,

the flow visualizations show that such changes also occur for the Coriolis-vortices in rotating channels (Cheng & Wang 1993a,b,c; Cheng et al 1992).

The present numerical calculations show that the Dean-vortices, Coriolis-vortices and buoyancy- vortices change size and shape as the parameter changes even in the fully developed flow region. This may be seen by comparing Fig.4.11(b)(c)-(i) for the Dean-vortices, Fig.4.4(c)(d)-(i) for the Coriolis-vortices and Fig.4.11(a)(b)(c)(i)(k)(l)-(ii) for the buoyancy-vortices.

4.4.3 Distributions of friction factor and Nusselt number

For engineering applications, the most important results are friction factor and Nusselt number. Since the main flow and temperature fields determine the friction factor and Nusselt number, the flow transitions discussed in the last section will strongly affect the distributions of the friction factor and Nusselt number.

The distributions of the friction factor fRe and Nusselt number Nu along the upper half of the inner wall, upper wall and the upper half of the outer wall, are illustrated in Fig.4.12(a),(b) and (c), respectively. They are shown on the basis of the values for a stationary straight channel ($(fRe)_0$ and Nu_0) to facilitate the understanding of the variations. The distributions are plotted for twelve values of L_1 starting from 1 (curve 1) to 70 (curve 12) at $Dk = 100$, $\sigma = 0.02$ and $L_2 = -5$. The corresponding flow patterns are illustrated in Fig.4.8. Also shown in the figure are friction factor and Nusselt number for curved channel without rotation, i.e.

$L_1 = L_2 = 0$, denoted by the curve 0.

The Dean-vortices, Coriolis-vortices and buoyancy-vortices are of importance in the fundamental research of roll-cell instabilities. They also change the flow resistance and heat transfer characteristics significantly. Curves 1 and 2 show the friction factor and Nusselt number ratios with the buoyancy-vortices in secondary flow (Fig.4.8(a)(b)-(i)). The similarity between main flow and temperature distributions (Fig.4.8(a)(b)-(ii)(iii)) results in a similarity between friction factor and Nusselt number distributions. The asymmetry of the buoyancy-vortices, with respect to the vertical centreline, leads to different distributions of friction factor and Nusselt number at the inner wall from those at the outer wall.

The large velocity (temperature) gradient between high velocity (temperature) core and the inner wall (Fig.4.8(a)(b)-(ii)(iii)) results a peak of the local friction factor (Nusselt number) in that region along the inner wall. A low friction factor (Nusselt number) region is observed in the center of the inner wall. This is induced by the outerwash isovels (isotherms) in that region. The quite uniform axial velocity (temperature) along the outer wall leads to a nearly constant local friction factor (Nusselt number) over a wide region of the outer wall. The friction factor (Nusselt number) along the upper wall reaches a peak near the inner wall because a large velocity (temperature) gradient exists between high velocity (temperature) core and the upper wall as shown in Fig.4.8(a)(b)-(ii)(iii).

Curves 3–5 illustrate the friction factor and Nusselt number ratios corresponding

to one-pair vortex flow in Fig.4.8(c)(d)(e). The distributions along the outer wall is qualitatively similar to those with the buoyancy-vortices (curves 1 and 2) but with lower values in general. The similarity also holds for those along the upper wall with peaks shifted toward the outer wall. The distributions of friction factor (Nusselt number) along the inner wall, however, experience a dramatic change in response to the disappearance of the buoyancy-vortices. The peak regions in curves 1 and 2 are flattened by increasing the values in the region near the center of the inner wall and decreasing those in the other region (curves 3 – 5).

Curves 6 – 8 show the friction factor and Nusselt number distributions in the flow region where the centrifugal, Coriolis and buoyancy forces just neutralize each other (Fig.4.8(f)(g)(h)). The friction factor (Nusselt number), along the inner wall, decreases monotonously from the center to the upper wall, with a decrease in value from curve 6 to 8. The corner vortex in the upper outer corner increases local friction factor (Nusselt number) along the upper wall in the portion near the outer wall, resulting a local peak in that region (Fig.4.12(b)). And a decrease in peak values is observed in curves 6 – 8 (Fig.4.12(b)). Near the boundary between the upper-outer vortex and that located at the center part of the outer wall, the current impinges on the outer wall so that the local friction factor (Nusselt number), along the outer wall, is increased in that region. This results a peak near the vortex boundary (curves 6 – 8 in Fig.4.12(c)).

Once *merging-vortices* appear near the center part of the outer wall, the isovels

(isotherms) along the inner wall become more sparsely spaced (Fig.4.8(i)(j)-(ii)(iii)). Consequently, a dramatic drop in the friction factor (Nusselt number) occurs in curves 9 and 10 (Fig.4.12(a)). The more tightly spaced isovels (isotherms) along the upper wall, however, results a high local friction factor (Nusselt number) along the upper wall as shown by curves 9 and 10 in Fig.4.12(b). The most significant effect of the merging-vortices on the friction factor and Nusselt number occurs along the outer wall as shown by curves 9 and 10 in Fig.4.12(c). The striking feature is that peaks for both friction factor and Nusselt number are located at the boundary between Ekman-type-vortices and merging-vortices. This results from a current impinging on the outer wall in that region (see Fig.4.8(i)(j)-(i)).

After the merging-vortices disappear upon increasing value of L_1 , friction factor and Nusselt number along the inner and upper walls are qualitatively similar to those with the presence of the merging-vortices. And they are quantitatively increased compared with those with the presence of the merging-vortices. This may be seen by comparing curves 11 and 12 with curves 9 and 10 in Fig.4.12(a) and (b). The distributions of the friction factor and Nusselt number along the outer wall, however, experience a qualitative change due to the disappearance of the merging-vortices as shown by curves 11 and 12 in Fig.4.12(c). It is observed that the peak regions in curves 9 and 10 are flattened through increasing local friction factor and Nusselt number in the center part of the outer wall.

Figure 4.13 shows the result for the mean friction factor and Nusselt number

represented by the solid and dotted lines, respectively. They are plotted in the form of $fRe/(fRe)_0$ and Nu/Nu_0 against L_1 at $Dk = 100$, $\sigma = 0.02$ and $L_2 = -5$. The characteristic flow regimes for the secondary flow, main flow and temperature are also shown for reference. It is noted that the flow transitions significantly affect the mean friction factor and Nusselt number. The appearance of the buoyancy-vortices substantially increases the friction factor and Nusselt number. And the increase in Nu is more appreciable.

When the flow is in the region where centrifugal, Coriolis and buoyancy forces just neutralize each other, both friction factor and Nusselt number approach those values for forced convection in stationary straight channel. This is because the secondary flow becomes weaker due to the impaired interaction among the forces. The friction factor and Nusselt number, however, increase significantly once again once the flow moves to the region with merging-vortices. An interesting feature about the friction factor and Nusselt number in this flow region is that their ratios, with respect to those for the stationary straight channel, are nearly identical. After the disappearance of the merging-vortices, the friction factor ratio increases proportionally with L_1 as shown in Fig.4.13. The Nusselt number ratio, however, increases at first, but then decreases with L_1 slightly. The different profiles of the axial velocity and temperature contribute to the different variations of the friction factor and Nusselt number in this Coriolis force dominated flow region.

It is well to compare the friction factor ratio and Nusselt number ratio shown in

Fig.4.13 from a point of view of practical engineering. The Nusselt number ratio is higher than that of the friction factor for the flows shown in Fig.4.8(a)-(h). They are nearly identical if the flow is in the region with the merging-vortices. When the flow is in the region as shown in Fig.4.8(k)(l), however, the Nusselt number ratio is much lower than the friction factor ratio.

4.5 Concluding Remarks

Flow transitions and combined free and forced laminar convective heat transfer were studied numerically for fully developed flow in the rectangular channels with both curvature and rotation, using finite- volume method. Curvature and rotation, in conjunction with heating or cooling, introduce the centrifugal force, Coriolis force and buoyancy force in the momentum equations, which describe the *relative* motion of fluids with respect to the channel. Such body forces cause similar instabilities (centrifugal instability, Coriolis instability and buoyancy instability) in forms of streamwise oriented vortices. In addition, these forces may either enhance or impede each other in the cross-plane depending on the directions of the rotation and heat flux. This produces a rich transition structure for both secondary flow and pressure-driven main flow. The present investigation is confined to examine this structure in the hydrodynamically and thermally fully developed laminar flow region. The work is also limited to the symmetric flow with respect to the horizontal centreline of the cross section by imposing a symmetric condition on that line. The results presented

in this paper are for the case of square cross section of the channel with positive rotation only.

Despite the assumptions made in the present investigation, the calculations cover a rather wide range of the parameters. In particular, the Reynolds number reached up to about six thousand. The rotation rates approached previously studied asymptotic limits of weak rotation and strong rotation where viscous force or Coriolis force dominates. Several flow patterns, hitherto unknown, are revealed in the present study. A one-pair vortex flow with an ageostrophic, virtually inviscid core occurs between a viscous force dominated one-pair vortex flow and two-pair vortex flow with the presence of the Dean-vortices, Coriolis-vortices or buoyancy-vortices. Another two kinds of one-pair vortex flow exist after the disappearance of the Coriolis-vortices upon increasing the Coriolis forces further. The axial velocity profile for the first one assumes a Taylor-Proudman configuration in the core region with one maximum located on the horizontal centreline. That for the second one is dumbbell-like with two maxima or bar-convex dumbbell-like with three high velocity regions. The flow in the core region is also geostrophic for the second kind of one-pair vortex flow. When the fluid is cooled, there exists a parametric region where, overall, the effect of the inward buoyancy force just neutralizes those of the outward centrifugal and Coriolis forces. In this region, new vortices appear and grow around the corners, squeezing the circulation due to the centrifugal and Coriolis forces to the central portion of the cross section of the channel. The flow

thus exhibits a two-pair, three-pair or four-pair structure. Here, the two-pair vortex structure is qualitatively different from the two-pair vortex families encountered in the Dean problem or Coriolis problem.

The remaining domain of the two-pair vortex families may still be divided into two different regions. The distinction is based on the mechanisms responsible for the appearance of an additional pair of vortices. A break-up of the Ekman-vortices (due to the centrifugal, Coriolis or buoyancy force instabilities) is associated with one case, whereas in the other case the merging together represents the formation process of the vortices appearing in the region where the centrifugal, Coriolis and buoyancy forces just meet each other. The additional pair of vortices formed in the second mechanism is called merging-vortices in this paper. They appear in the region near the center of the outer wall (high pressure side) in the case with positive rotation. The circulation direction is the same as that of the Dean-vortices. The size, however, is smaller than that of the Dean-vortices. This flow pattern appears to be new.

The vortices formed in the first mechanism include the Dean-vortices, Coriolis-vortices and buoyancy-vortices. Their shape and size change with the dynamical parameters even in the fully developed flow region. In addition, the Dean-vortices, Coriolis-vortices and buoyancy-vortices behave differently in some aspects although they share some similarities as noted by many investigators. The disappearance of the Coriolis-vortices or buoyancy-vortices is observed with increasing Coriolis or

buoyancy force. No such phenomenon is observed for the Dean-vortices. Furthermore, the reappearance of the buoyancy- vortices, upon increasing the buoyancy force further, is also found in this study. Another important difference is the locations of the vortices. Although the Dean- vortices and Coriolis-vortices always appear in the high pressure side (outer wall) in the case of the positive rotation, the buoyancy-vortices may appear in the high pressure side (outer wall) or low pressure side (inner wall) depending on whether the fluid is heated or cooled. If the fluid is heated, they show up near the center of the outer wall with the same direction of circulation as those of the Dean- vortices and Coriolis-vortices. When the fluid is cooled, however, the inward buoyancy forces cause them to appear near the center of the inner wall with an opposite direction of circulation. The most striking feature is that the fluid near the inner wall still remains low pressure even with the existence of the buoyancy-vortices. It appears to be the first time that the vortices due to body force instabilities are observed in the low pressure side of the channel.

When the fluid is cooled, the inward buoyancy forces cause the direction of the secondary flow to reverse by overcoming the outward centrifugal and Coriolis forces in the plane of the cross section. The flow reversal occurs by passing through a multi-pair vortex flow region where overall, the effect of the buoyancy force just neutralizes those of the centrifugal and Coriolis forces.

The friction factors and Nusselt numbers are significantly affected by the flow transitions. In particular, the Dean-vortices, Coriolis-vortices, buoyancy-vortices

and merging-vortices substantially change the distributions of the local friction factor and Nusselt number with a remarkable increase in their mean values.

The new vortex flows, revealed in the present study, suggest possible further research concerning their instability since usually, an inflectional profile of the main flow is associated with them. Such a study is considered to be very complex because of the full three-dimensional form of the resulting disturbance equations, and is beyond the scope of the present study.

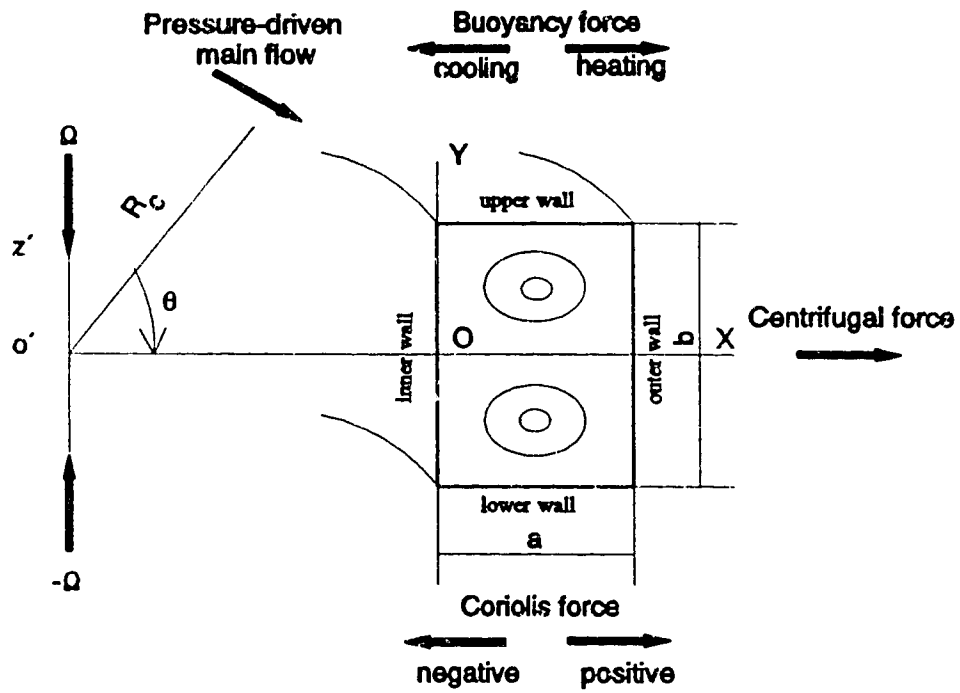


Figure 4.1. Physical problem and rotating toroidal coordinate system

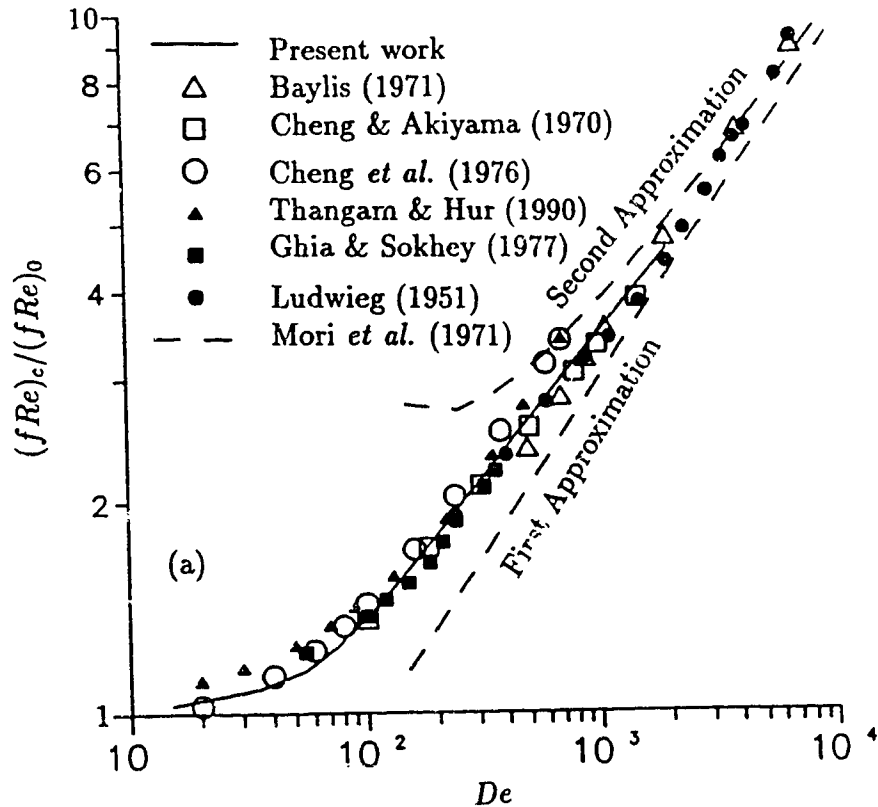


Figure 4.2. Variations of friction factor and Nusselt number with Dean number for a stationary square channel— a comparison of present results with available theoretical, experimental and numerical findings: (a) friction factor (Baylis 1971: experiments; Cheng & Akiyama 1970: numerical analysis; Cheng *et al.* 1976: numerical analysis; Thangam & Hur 1990: numerical analysis; Ghia & Sokhey 1977: numerical analysis; Ludwig 1951: Experiments; Mori *et al.* 1971: boundary layer correlations); (b) Nusselt number (Mori *et al.* 1971: experiments; Cheng & Akiyama 1970: numerical analysis; Cheng *et al.* 1975: numerical analysis; Mori & Uchida 1967: boundary layer correlations)

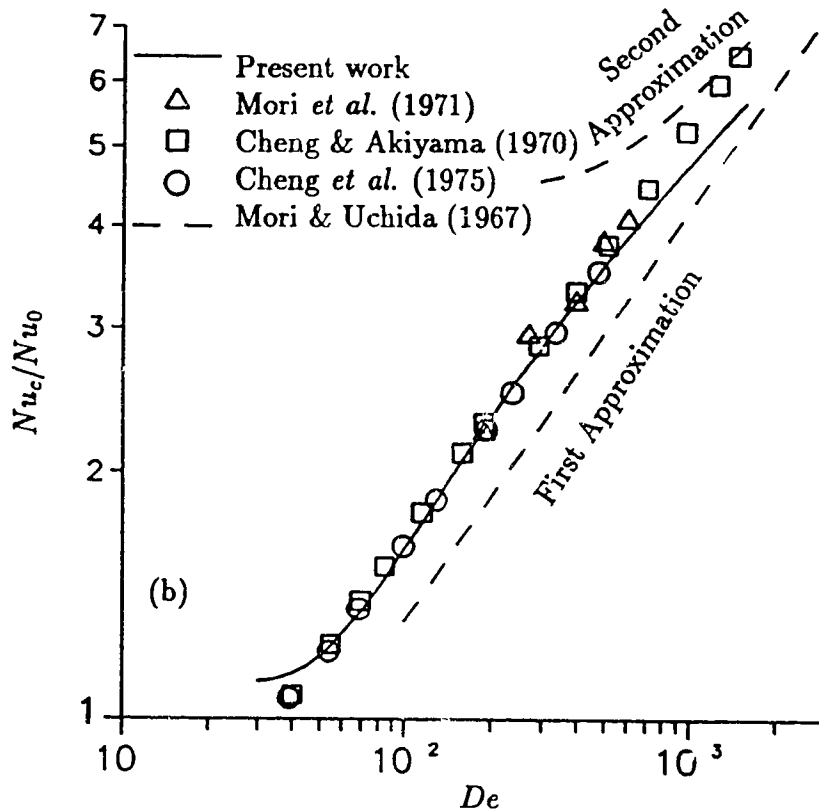


Figure 4.2. Variations of friction factor and Nusselt number with Dean number for a stationary square channel- a comparison of present results with available theoretical, experimental and numerical findings: (a) friction factor (Baylis 1971: experiments; Cheng & Akiyama 1970: numerical analysis; Cheng *et al.* 1976: numerical analysis; Thangam & Hur 1990: numerical analysis; Ghia & Sokhey 1977: numerical analysis; Ludwig 1951: Experiments; Mori *et al.* 1971: boundary layer correlations); (b) Nusselt number (Mori *et al.* 1971: experiments; Cheng & Akiyama 1970: numerical analysis; Cheng *et al.* 1975: numerical analysis; Mori & Uchida 1967: boundary layer correlations)

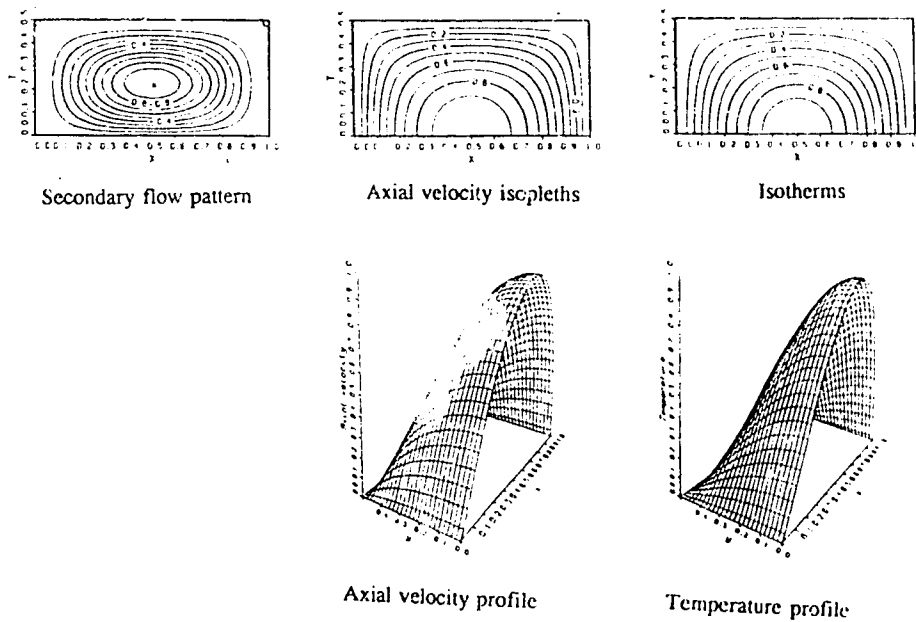
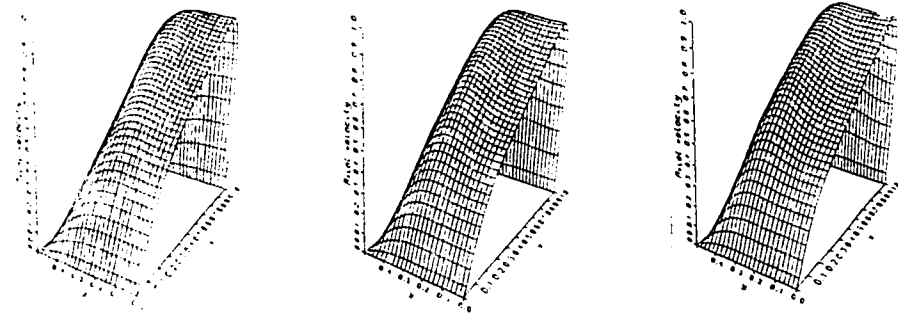
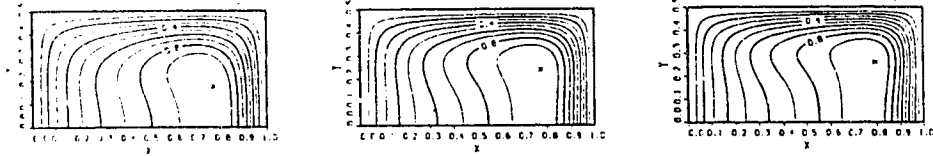


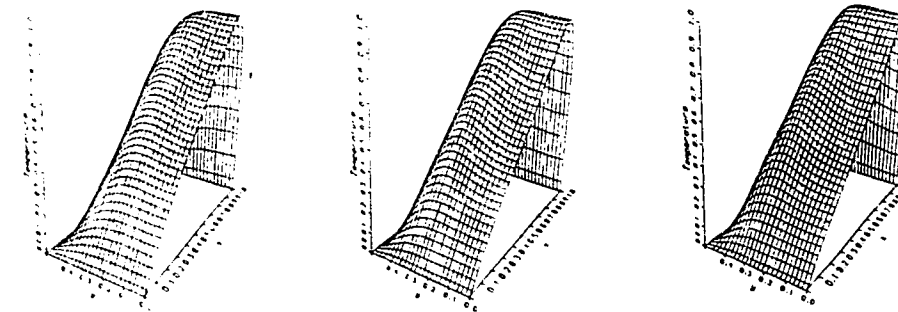
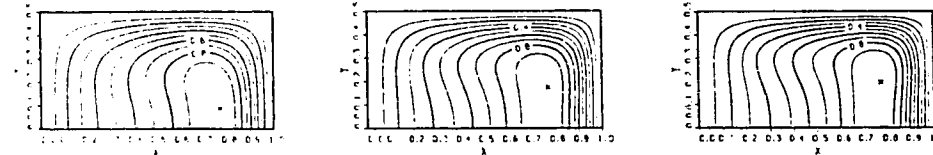
Figure 4.3. Weak curvature and rotation ($Dk = 5, \sigma = 0.02, L_2 = 0, Re = 35$. Maxima of stream function, axial velocity and temperature are 0.0592, 0.0737 and 4.064, respectively.)



(i) Secondary flow patterns



(ii) Axial velocity isopleths and profiles

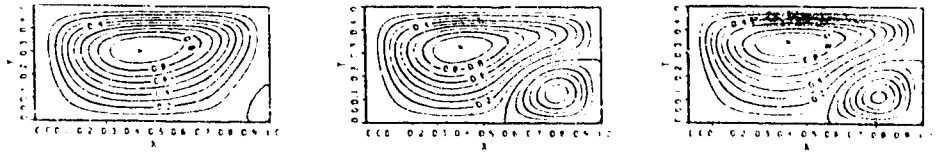


(iii) Isotherms and temperature profiles

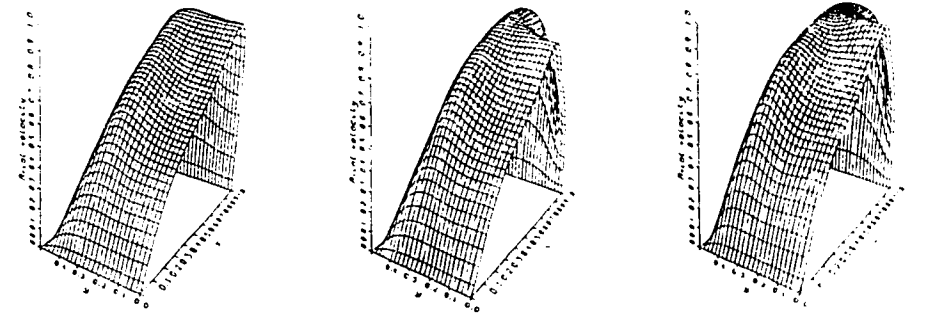
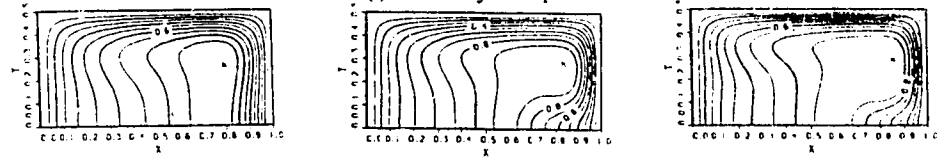
(a) $L_1=0$ $Re=542$
(5.641;0.0496;39.82)

(b) $L_1=1$ $Re=494$
(6.865;0.0440;31.88)

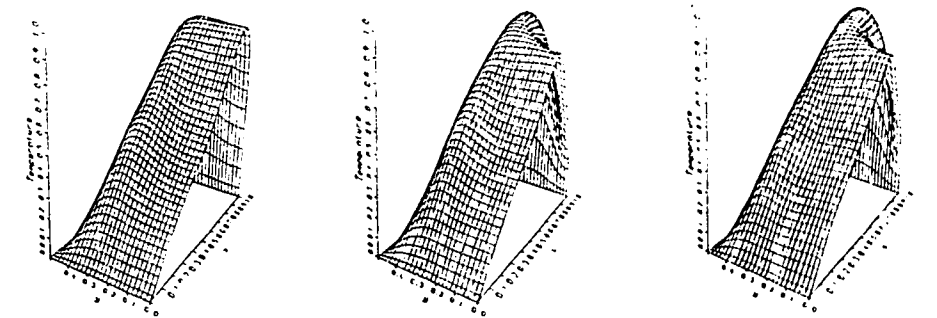
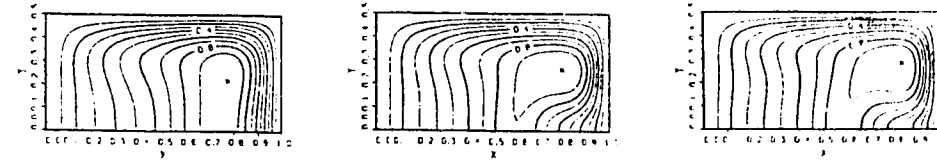
(c) $L_1=2$ $Re=464$
(7.572;0.0406;28.00)



(i) Secondary flow patterns



(ii) Axial velocity isopleths and profiles



(iii) Isotherms and temperature profiles

(d) $L_1=2.5$ $Re=453$
(7.778; 0.0594; 26.65)

(e) $L_1=3$ $Re=423$
(7.256; 0.0353; 22.40)

(f) $L_1=7.5$ $Re=366$
(8.697; 0.0284; 16.92)

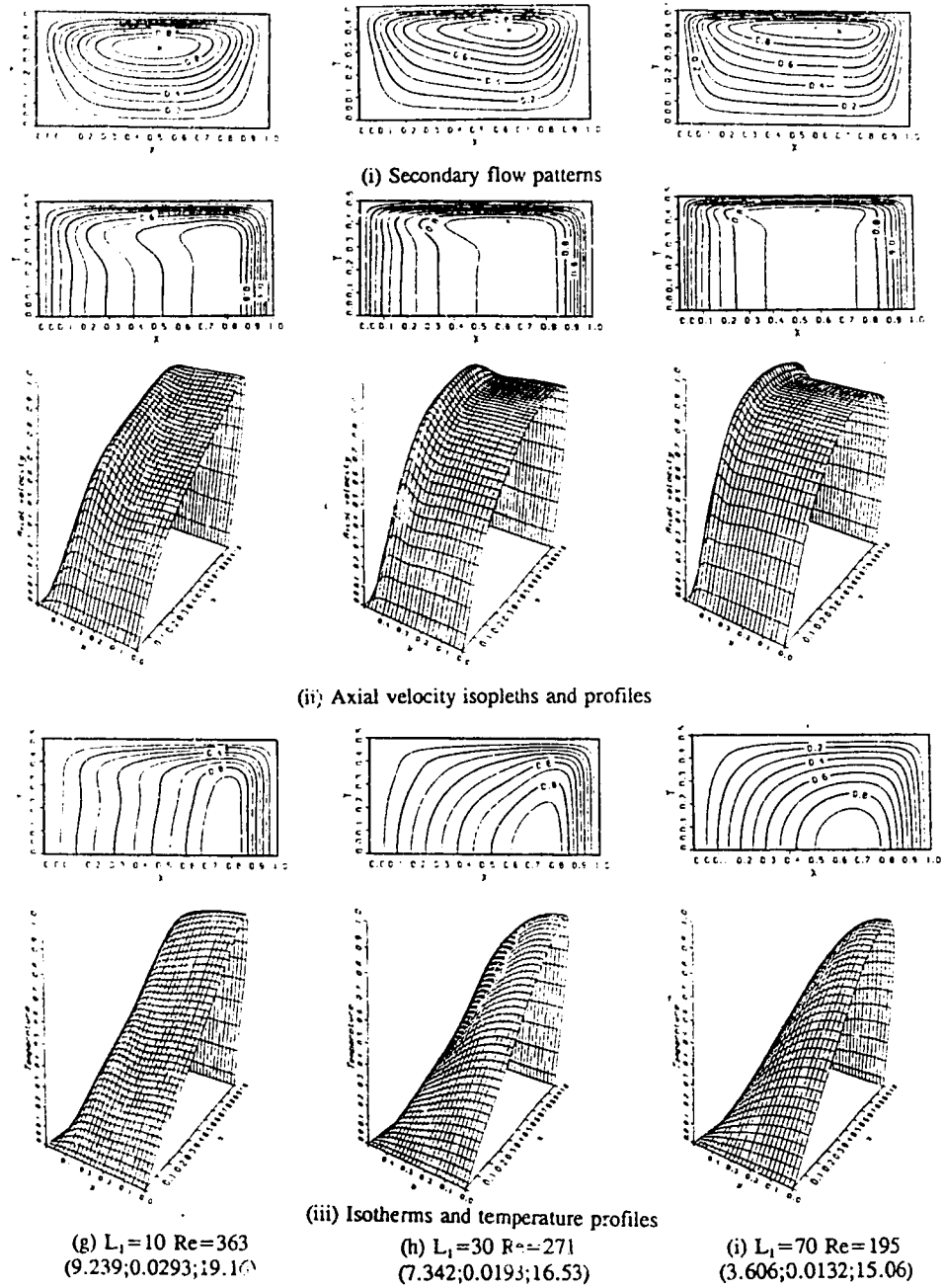
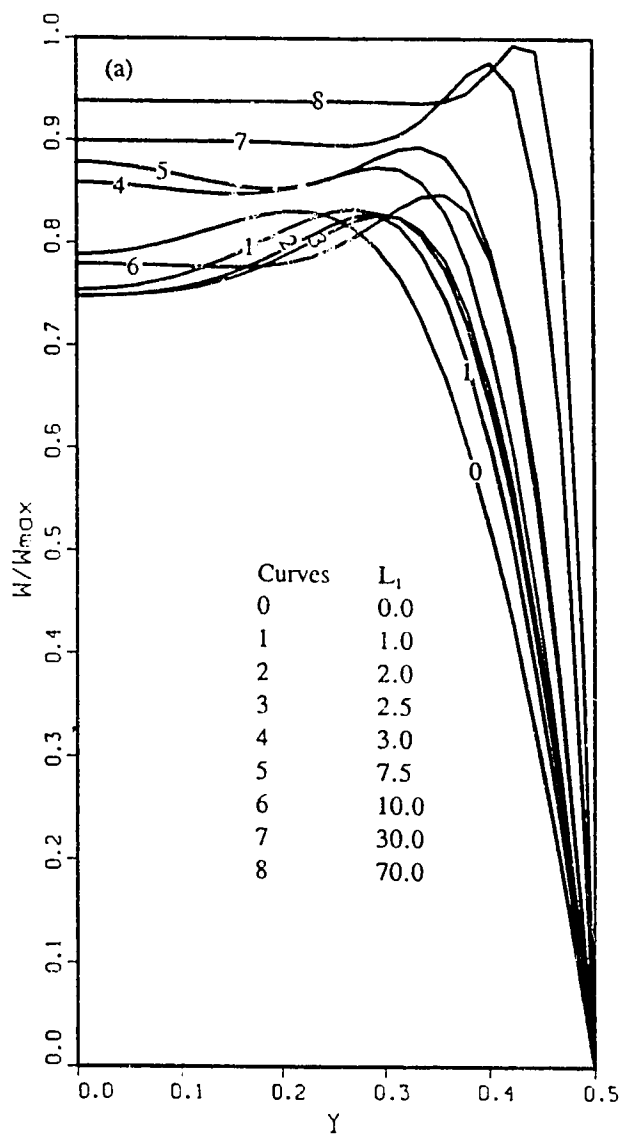
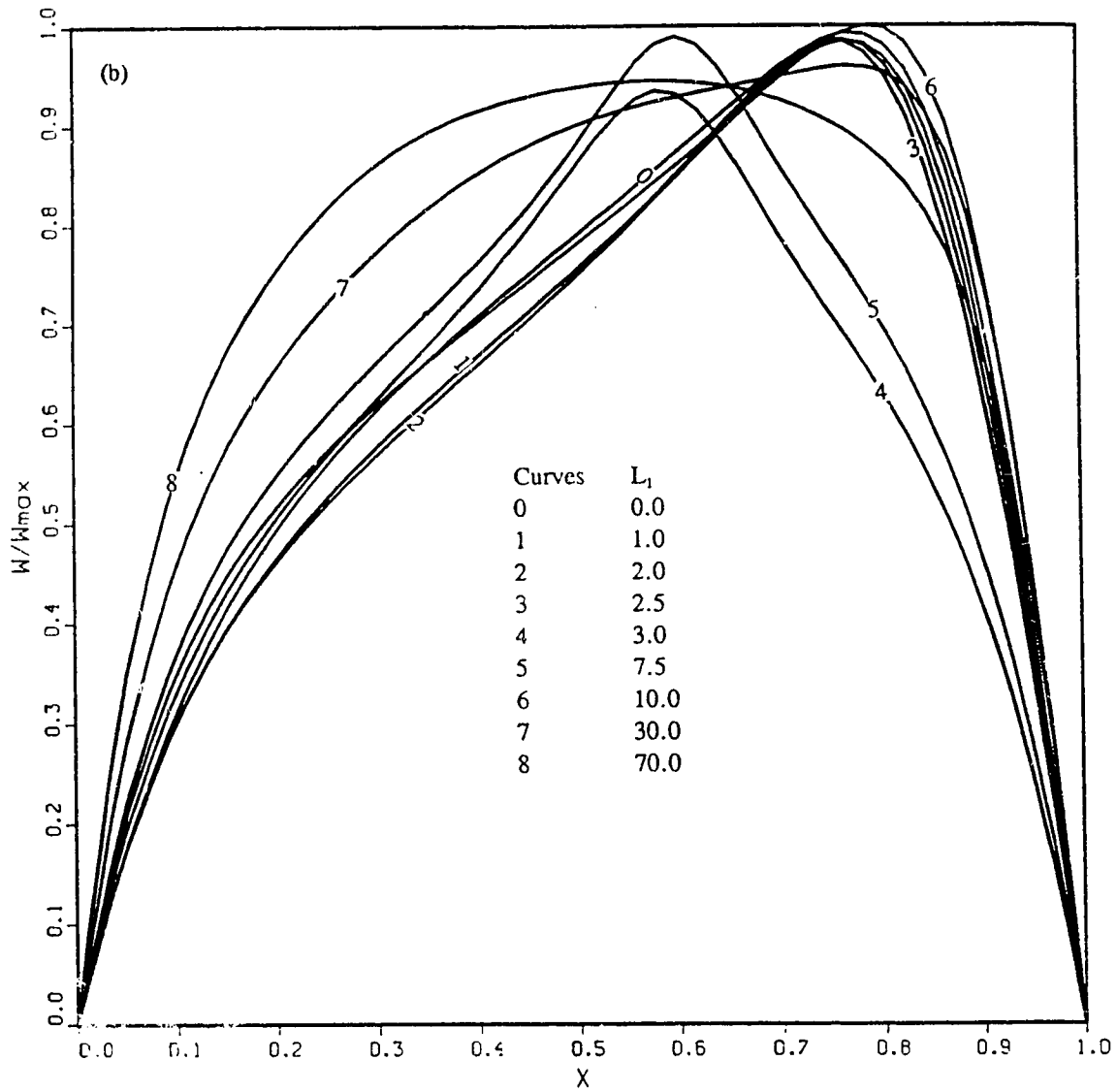


Figure 4.4. Flow transitions and temperature distributions at $Dk = 100, \sigma = 0.02$ and $L_2 = 0$. (Three values for each case are the maxima of stream function, axial velocity and temperature)



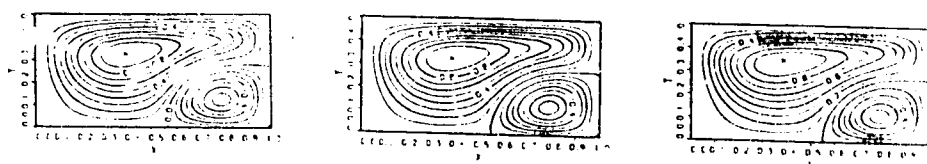
(a) along the vertical centreline of the channel

Figure 4.5. Axial velocity distributions at $Dk = 100$, $\sigma = 0.02$ and $L_2 = 0$: (a) along the vertical centreline of the channel; (b) along the horizontal centreline of the channel

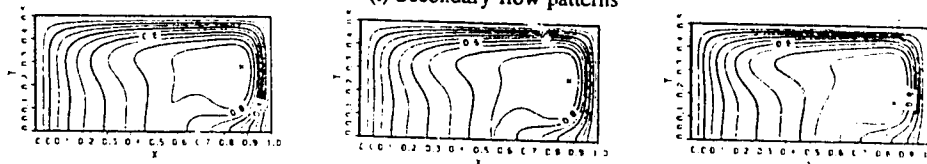


(b) along the horizontal centreline of the channel

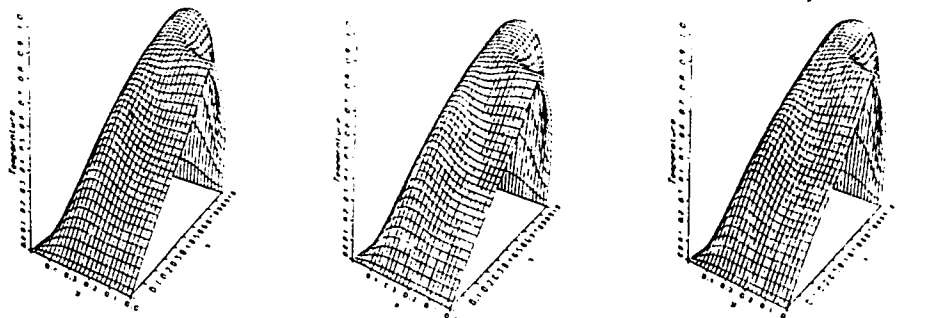
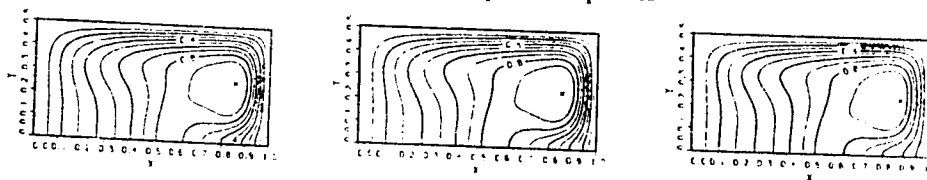
Figure 4.5. Axial velocity distributions at $Dk = 100, \sigma = 0.02$ and $L_2 = 0$: (a) along the vertical centreline of the channel; (b) along the horizontal centreline of the channel



(i) Secondary flow patterns



(ii) Axial velocity isopleths and profiles



(iii) Isotherms and temperature profiles

(a) $L_1=0.1$ $Re=379$
(10.02;0.0312;16.75)

(b) $L_1=1$ $Re=372$
(10.32;0.0301;16.15)

(c) $L_1=4$ $Re=351$
(10.94;0.0275;14.58)

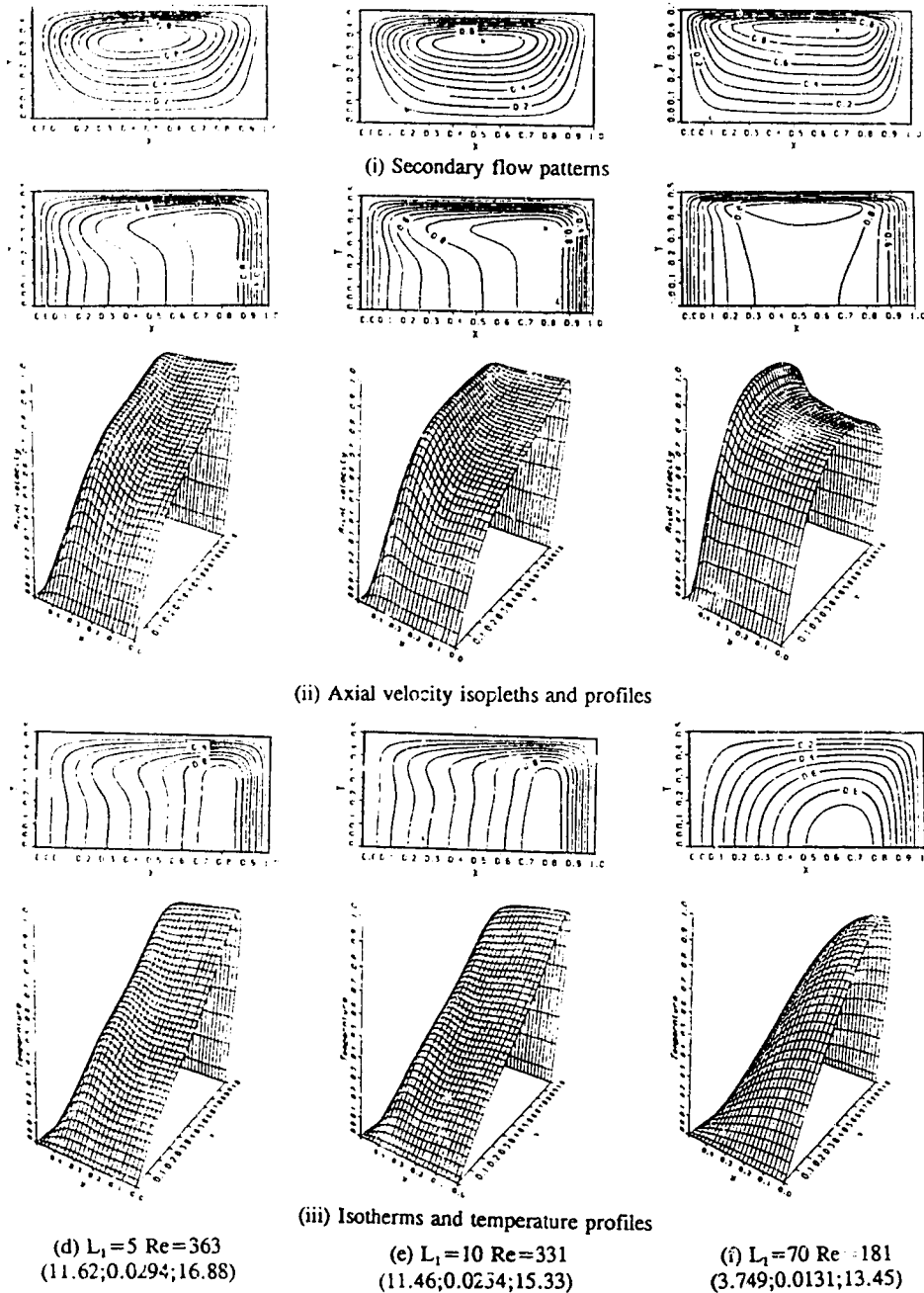
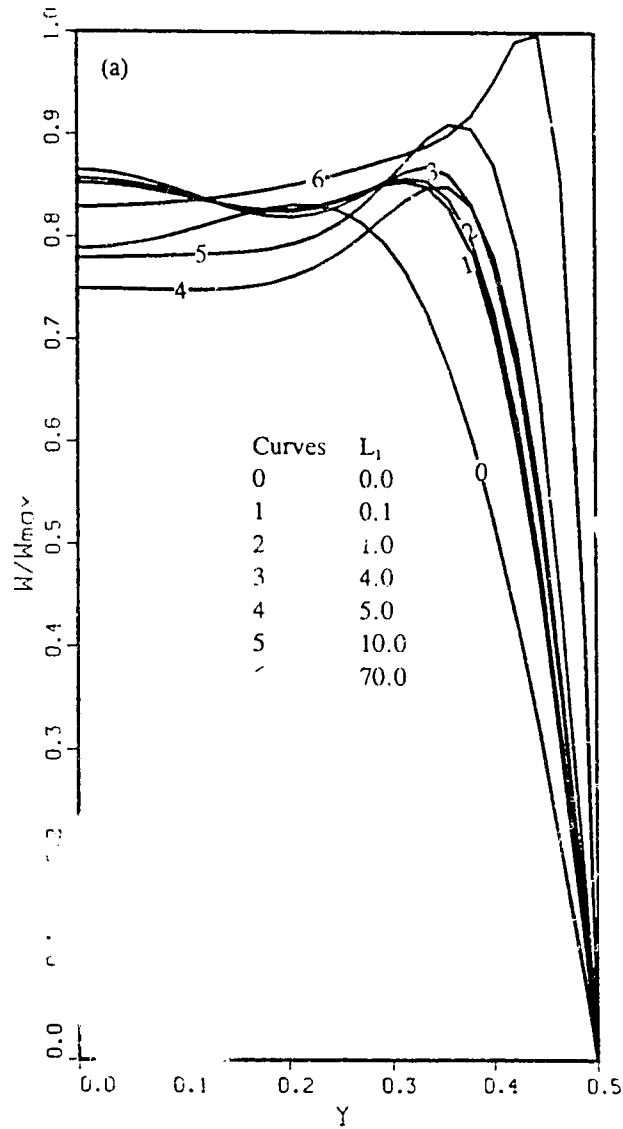
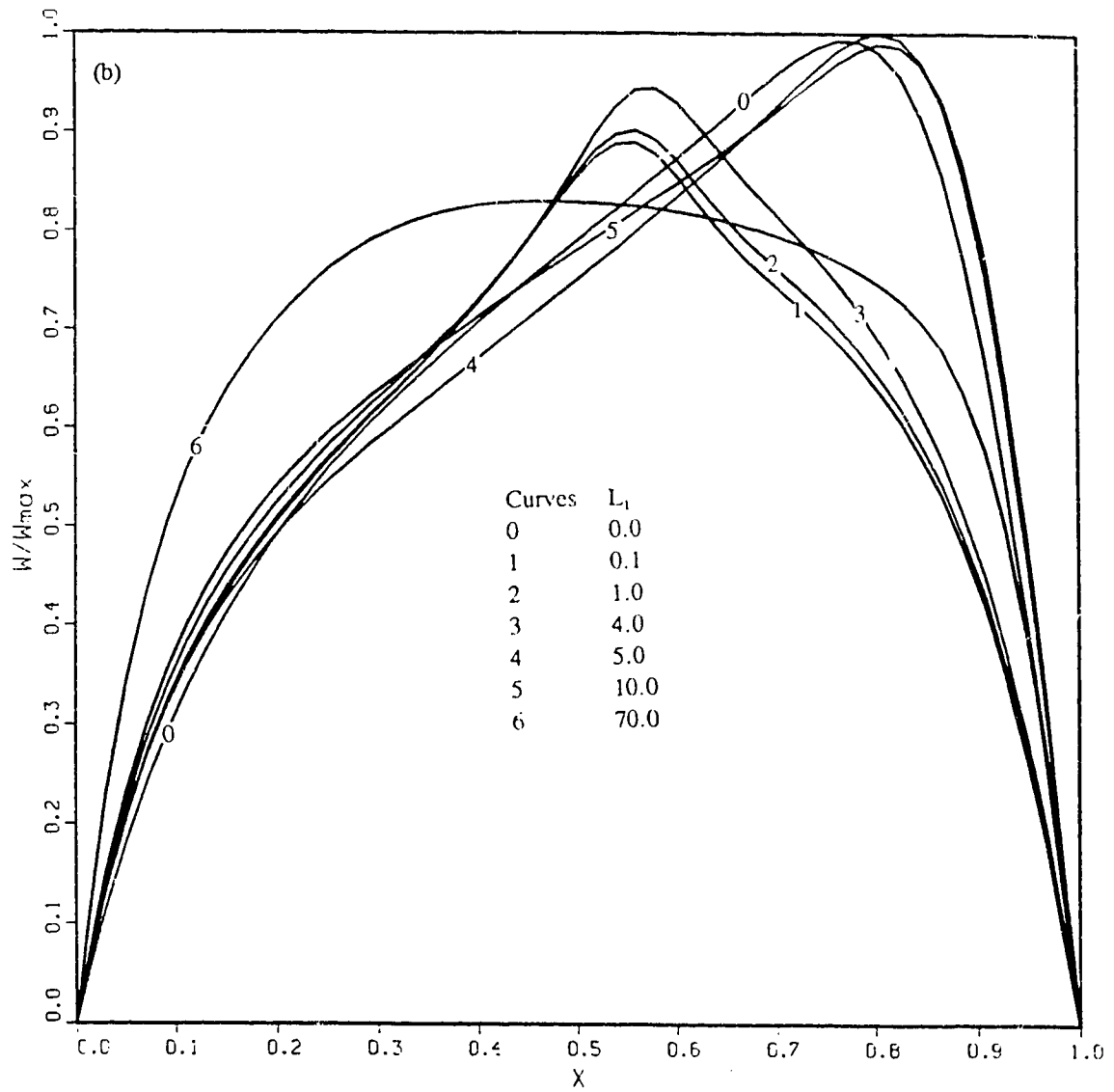


Figure 4.6. Flow transitions and temperature distributions at $Dk = 100, \sigma = 0.02$ and $L_2 = 5$. (Three values for each case are maxima of stream function, axial velocity and temperature)



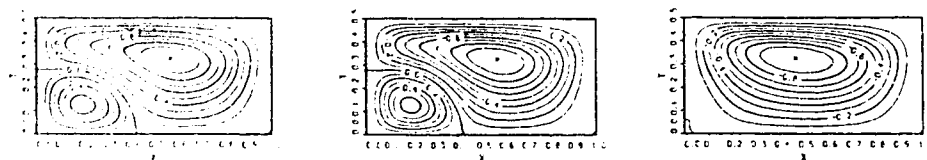
(a) along the vertical centreline of the channel

Figure 4.7. Axial velocity distributions at $Dk = 100, \sigma = 0.02$ and $L_2 = 5$: (a) along the vertical centreline of the channel; (b) along the horizontal centreline of the channel

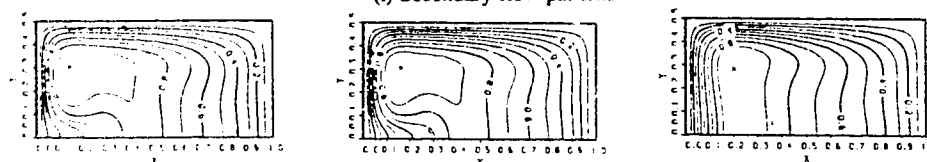


(b) along the horizontal centreline of the channel

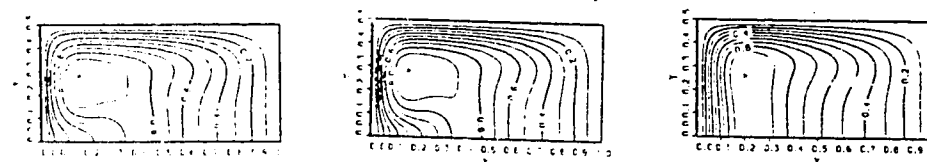
Figure 4.7. Axial velocity distributions at $Dk = 100, \sigma = 0.02$ and $L_2 = 5$: (a) along the vertical centreline of the channel; (b) along the horizontal centreline of the channel



(i) Secondary flow patterns



(ii) Axial velocity isopleths and profiles

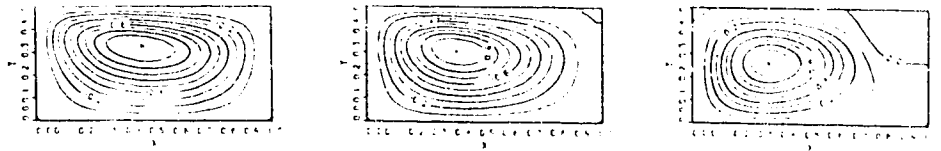


(iii) Isotherms and temperature profiles

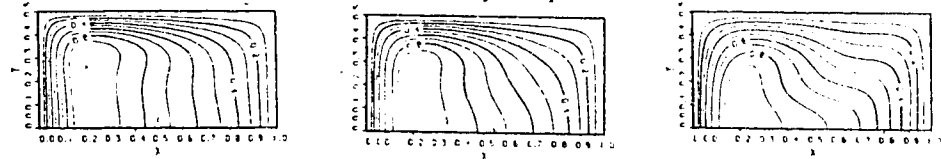
(a) $L_1=1$ $Re=401$
(9.003;0.0341;18.86)

(b) $L_1=1.5$ $Re=408$
(8.764;0.0349;19.47)

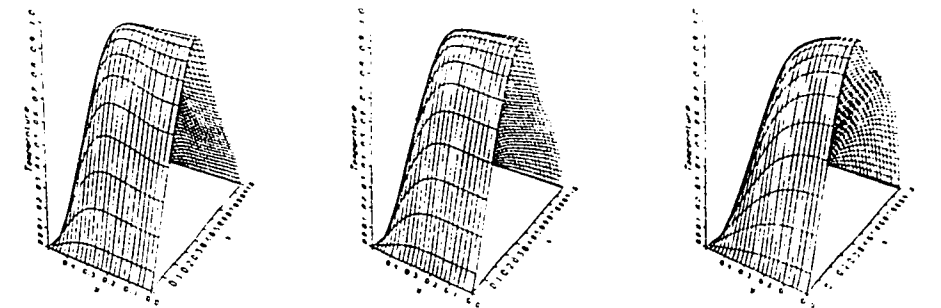
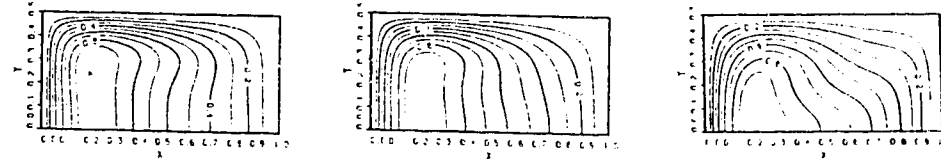
(c) $L_1=2$ $Re=443$
(9.853;0.0396;23.57)



(i) Secondary flow patterns



(ii) Axial velocity isopleths and profiles

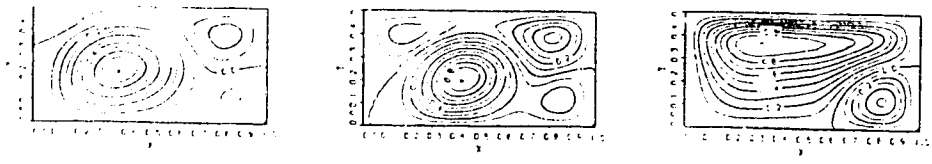


(iii) Isotherms and temperature profiles

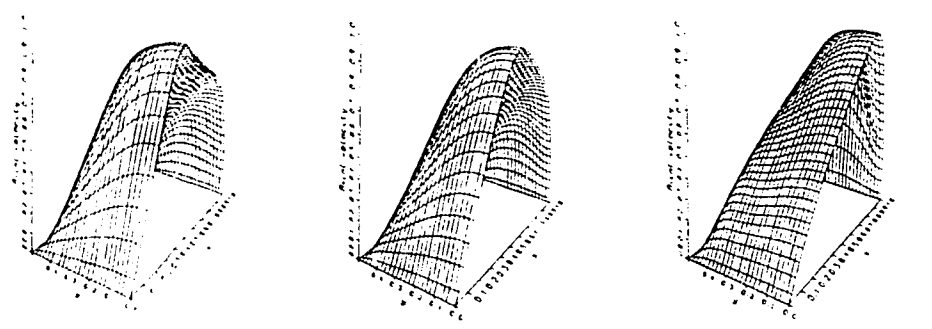
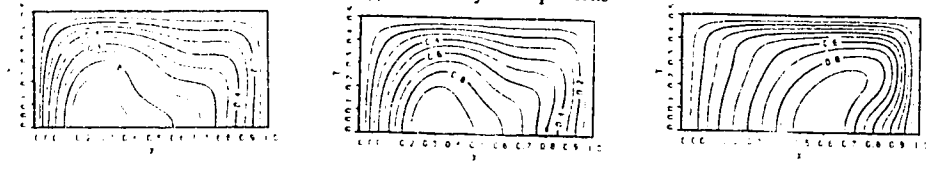
(d) $L_1=3$ $Re=457$
(9.519;0.0414;25.21)

(e) $L_1=5$ $Re=488$
(8.722;0.0460;29.89)

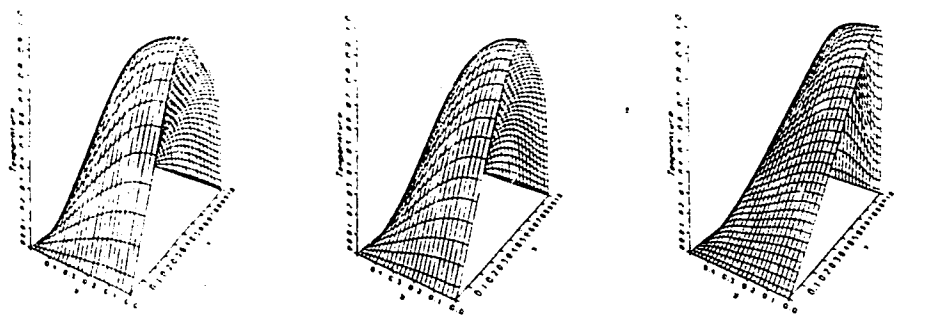
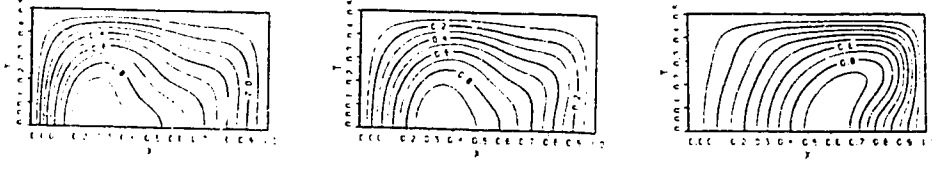
(f) $L_1=8$ $Re=545$
(6.705;0.0543;41.20)



(i) Secondary flow patterns



(ii) Axial velocity isopleths and profiles



(iii) Isotherms and temperature profiles

(g) $L_1 = 10$ $Re = 606$
(4.416; 0.0624; 54.80)

(h) $L_1 = 11.5$ $Re = 652$
(2.716; 0.0688; 67.66)

(i) $L_1 = 12$ $Re = 484$
(3.635; 0.0461; 38.25)

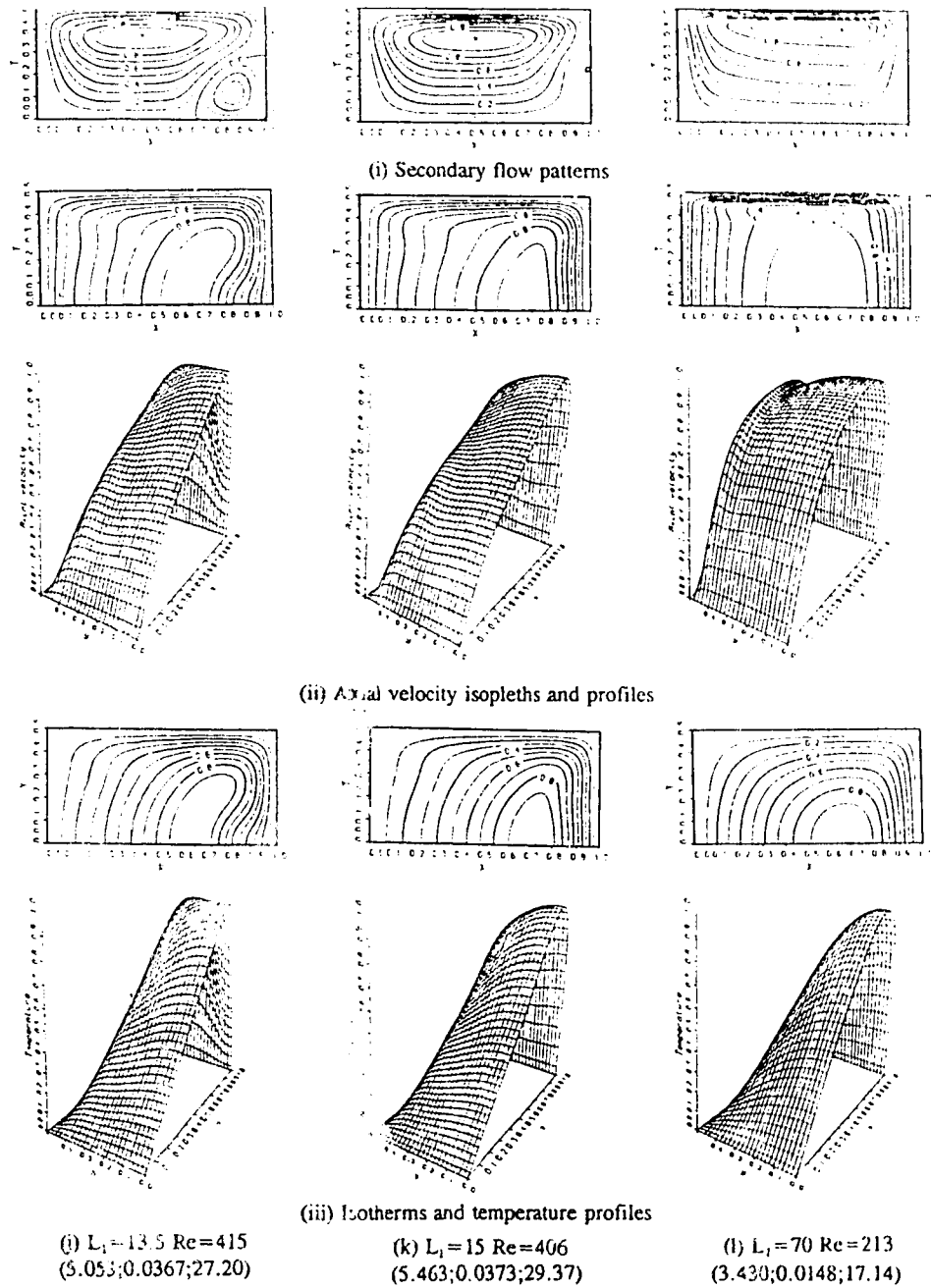
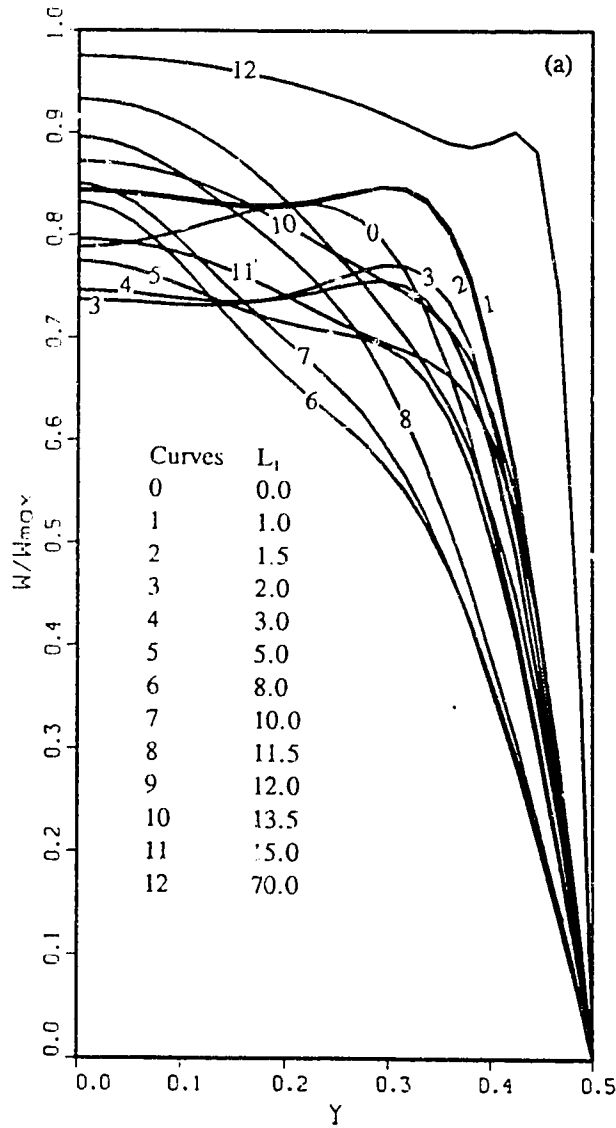
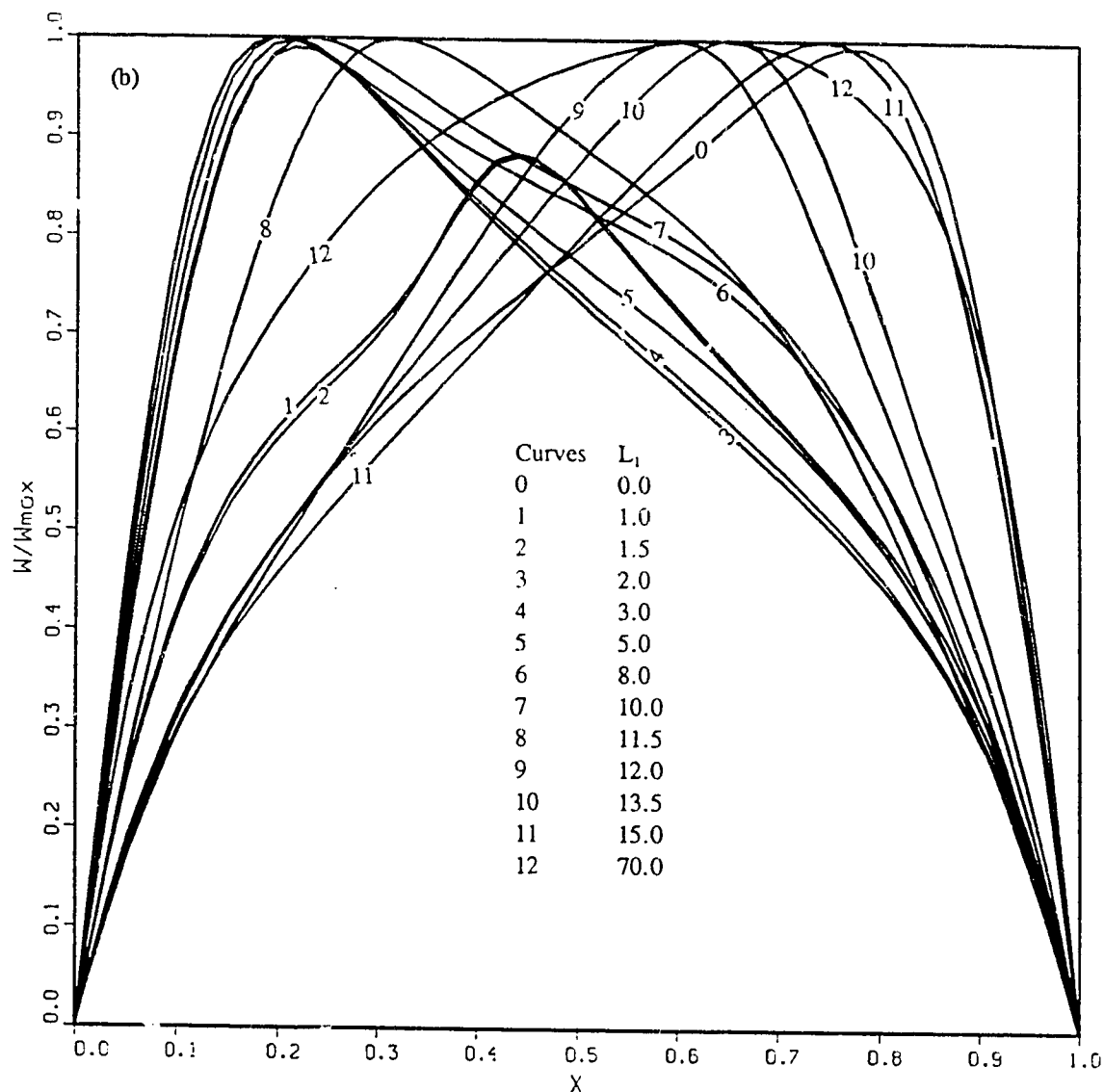


Figure 4.8. Flow transitions and temperature distributions at $Dk = 100, \sigma = 0.02$ and $L_2 = -5$. (Three values for each case are maxima of stream function, axial velocity and temperature)



(a) along the vertical centreline of the channel

Figure 4.9. Axial velocity distributions at $Dk = 100, \sigma = 0.02$ and $L_2 = -5$: (a) along the vertical centreline of the channel; (b) along the horizontal centreline of the channel



(b) along the horizontal centreline of the channel

Figure 4.9. Axial velocity distributions at $Dk = 100, \sigma = 0.02$ and $L_2 = -5$: (a) along the vertical centreline of the channel; (b) along the horizontal centreline of the channel

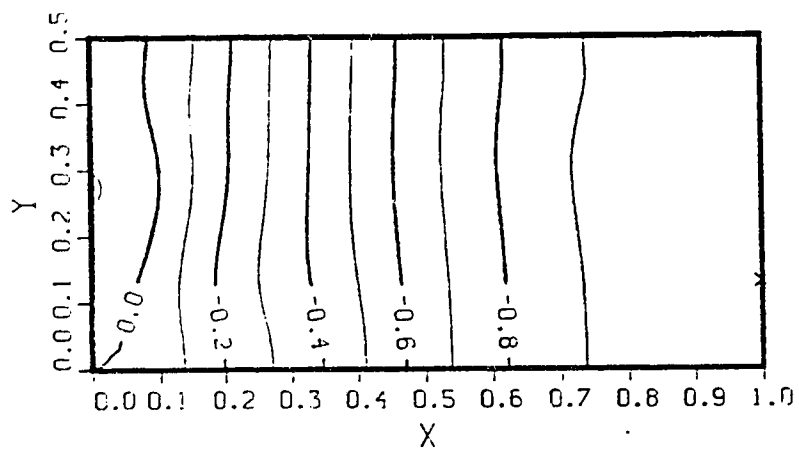
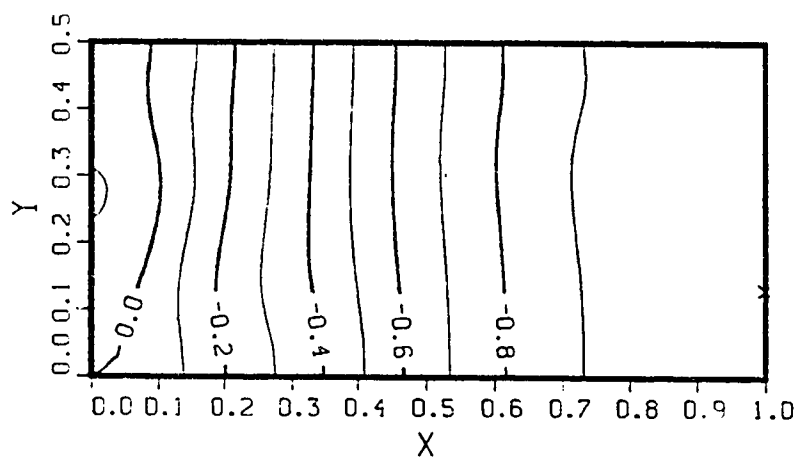
(a) $L_1 = 1.0$ (b) $L_1 = 1.5$

Figure 4.10. Isopiestic contour at $Dk = 100$, $\sigma = 0.02$, $Pr = 0.7$ and $L_2 = -5$

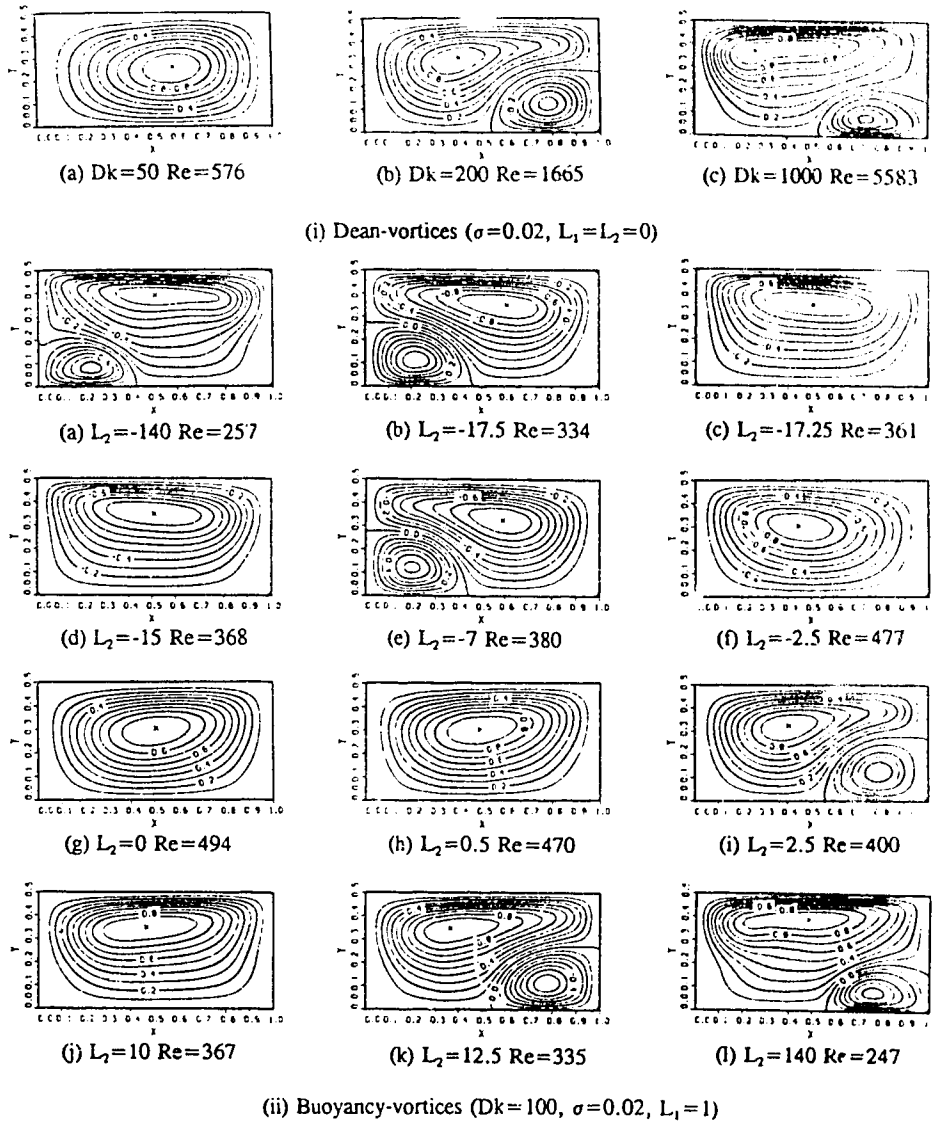


Figure 4.11. Disappearance and reappearance of Dean-vortices and buoyancy-vortices

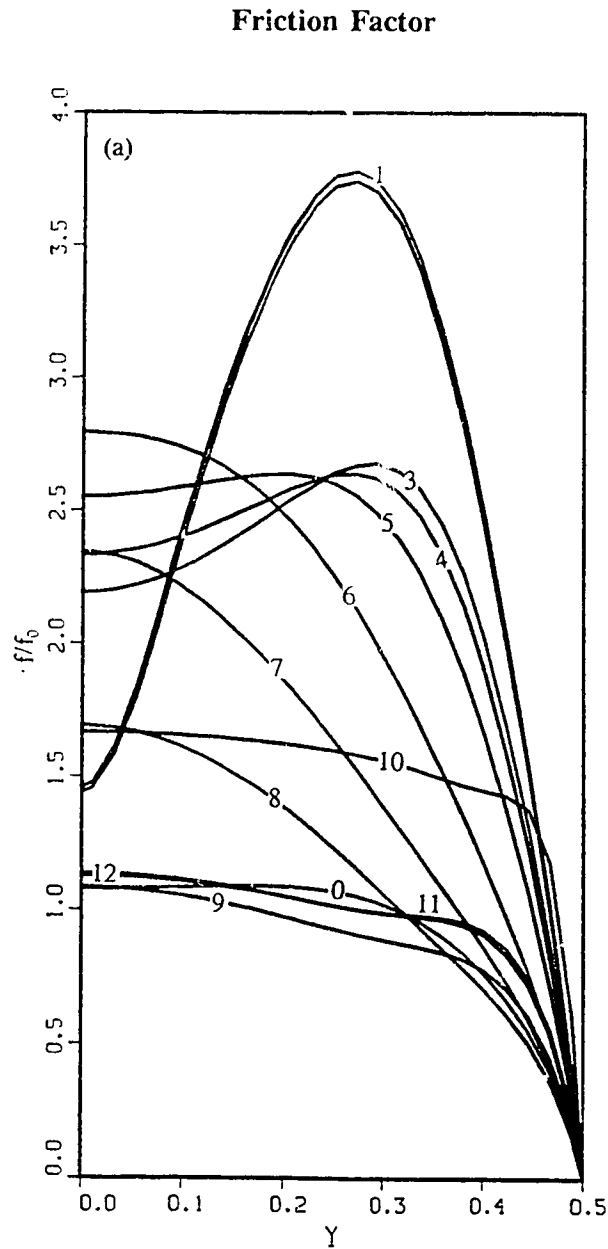


Figure 4.12. Distributions of friction factor and Nusselt number at $Dk = 100$, $\sigma = 0.02$ and $L_2 = -5$ (Curves 1 – 12 correspond to $L_1 = 1, 1.5, 2, 3, 5, 8, 10, 11.5, 12, 13.5, 15$ and 70 . Curve 0 is for the case of $L_1 = L_2 = 0$.) (a) along the inner wall; (b) along the upper wall; (c) along the outer wall

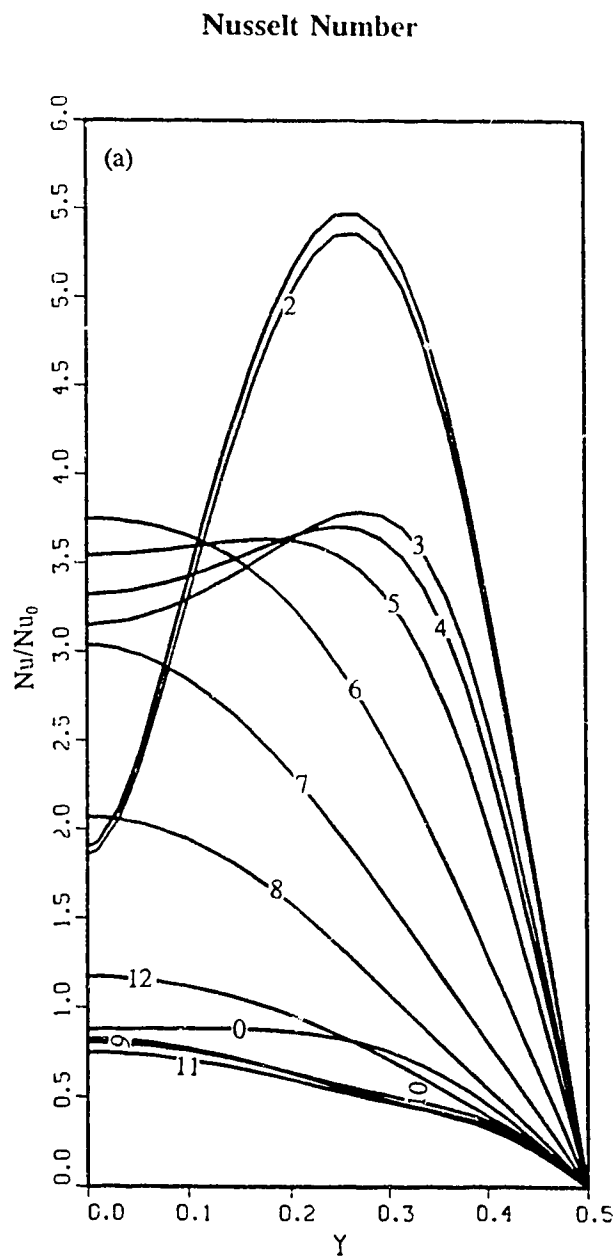
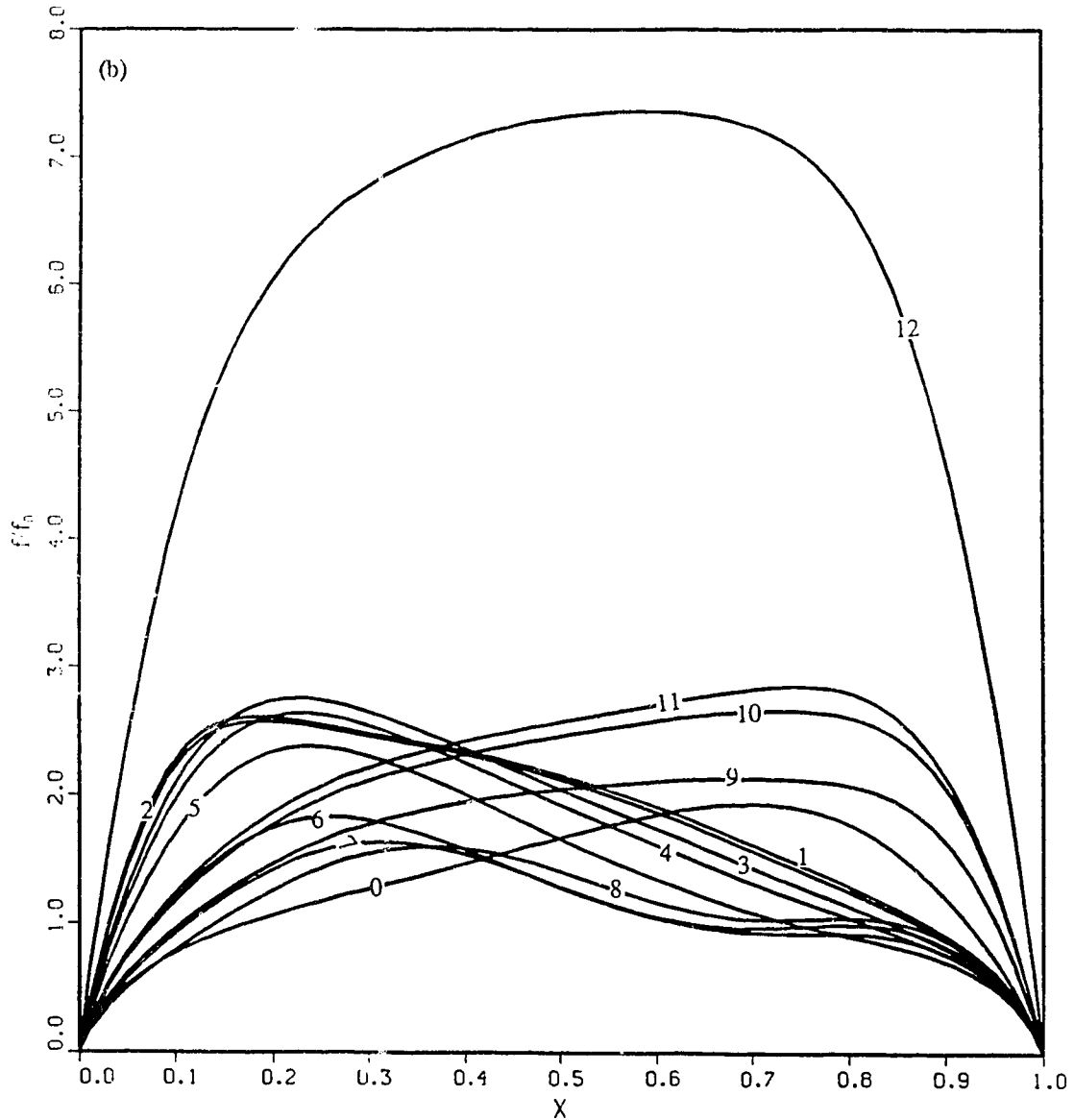


Figure 4.12. Distributions of friction factor and Nusselt number at $Dk = 100$, $\sigma = 0.02$ and $L_2 = -5$ (Curves 1 – 12 correspond to $L_1 = 1, 1.5, 2, 3, 5, 8, 10, 11.5, 12, 13.5, 15$ and 70 . Curve 0 is for the case of $L_1 = L_2 = 0$.) (a) along the inner wall; (b) along the upper wall; (c) along the outer wall!

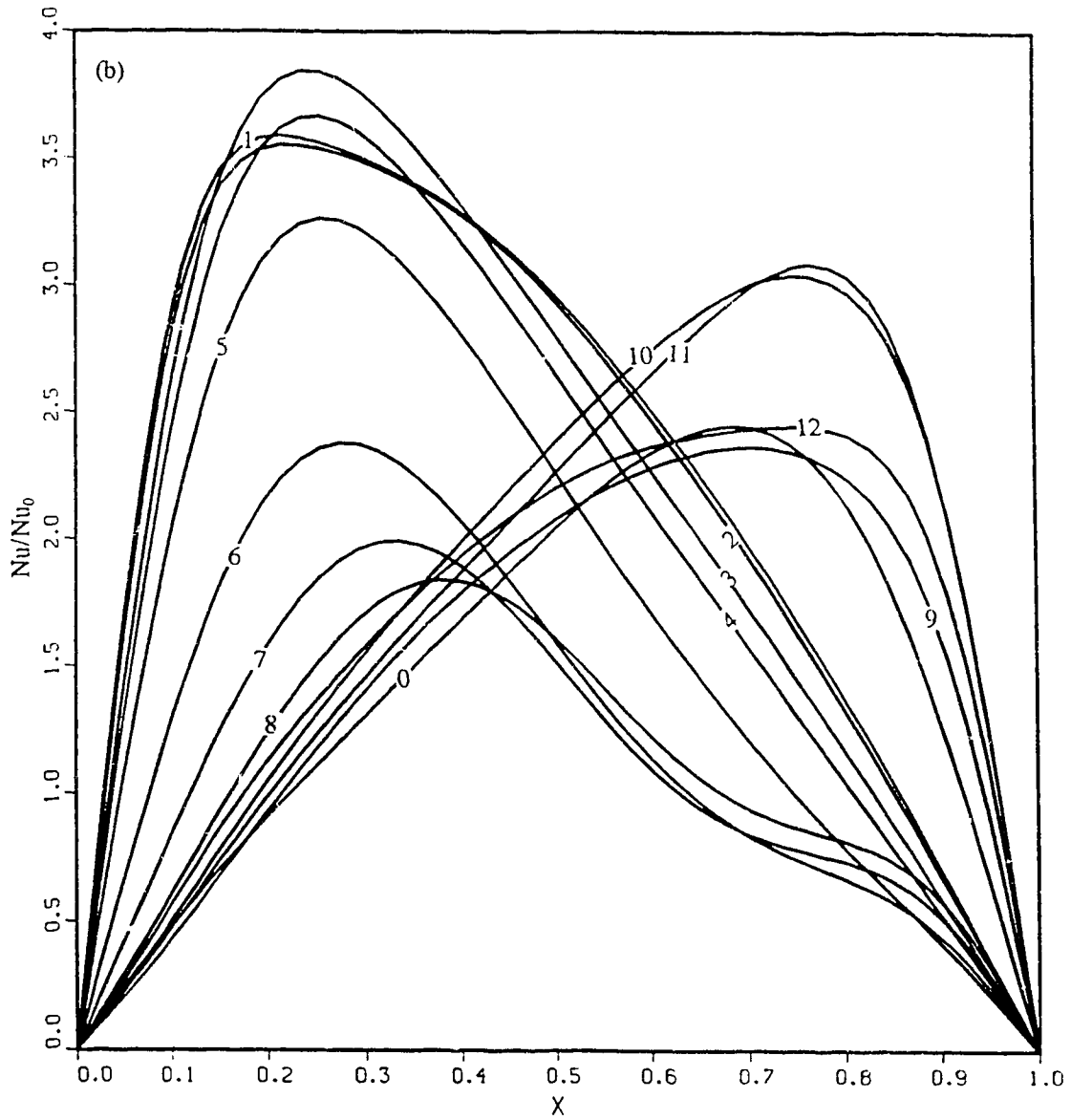
Friction Factor



(b) along the upper wall

Figure 4.12 Distributions of friction factor and Nusselt number at $Dk = 100, \sigma = 0.02$ and $L_2 = -5$ (Curves 1 – 12 correspond to $L_1 = 1, 1.5, 2, 3, 5, 8, 10, 11.5, 12, 13.5, 15$ and 70. Curve 0 is for the case of $L_1 = L_2 = 0$.) (a) along the inner wall; (b) along the upper wall; (c) along the outer wall

Nusselt Number



(b) along the upper wall

Figure 4.12. Distributions of friction factor and Nusselt number at $Dk = 100$, $\sigma = 0.02$ and $L_2 = -5$ (Curves 1 – 12 correspond to $L_1 = 1, 1.5, 2, 3, 5, 8, 10, 11.5, 12, 13.5, 15$ and 70. Curve 0 is for the case of $L_1 = L_2 = 0$.) (a) along the inner wall; (b) along the upper wall; (c) along the outer wall

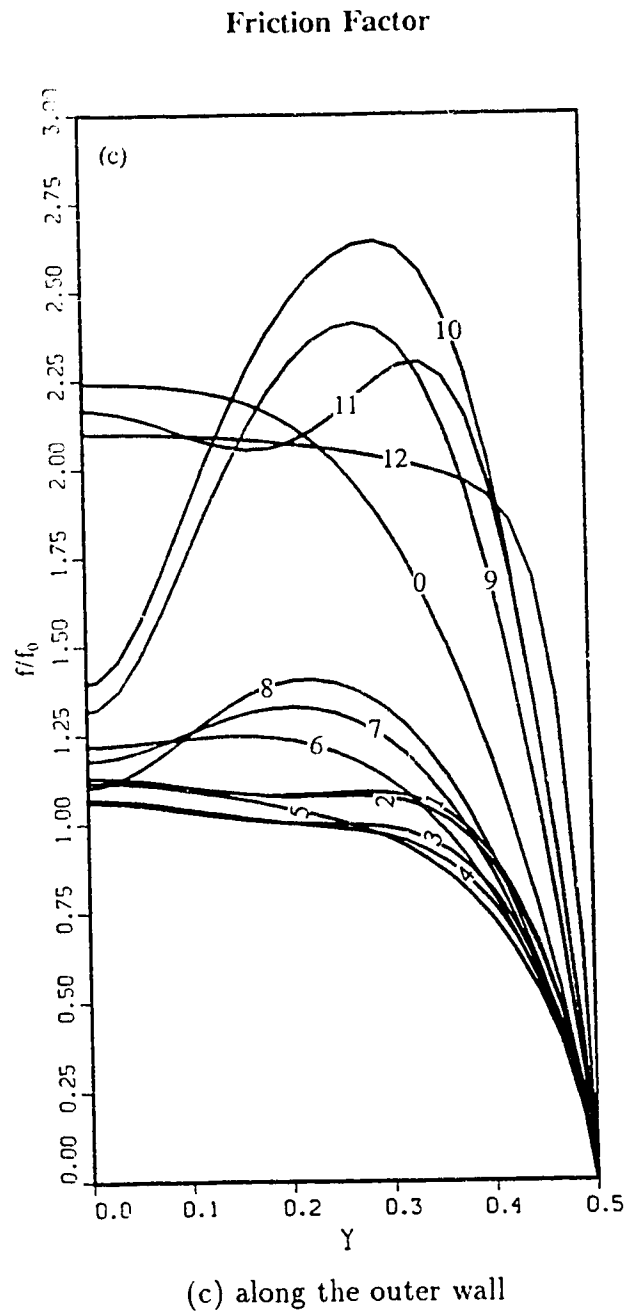


Figure 4.12. Distributions of friction factor and Nusselt number at $Dk = 100$, $\sigma = 0.02$ and $L_2 = -5$ (Curves 1 – 12 correspond to $L_1 = 1, 1.5, 2, 3, 5, 8, 10, 11.5, 12, 13.5, 15$ and 70 . Curve 0 is for the case of $L_1 = L_2 = 0$.) (a) along the inner wall; (b) along the upper wall; (c) along the outer wall

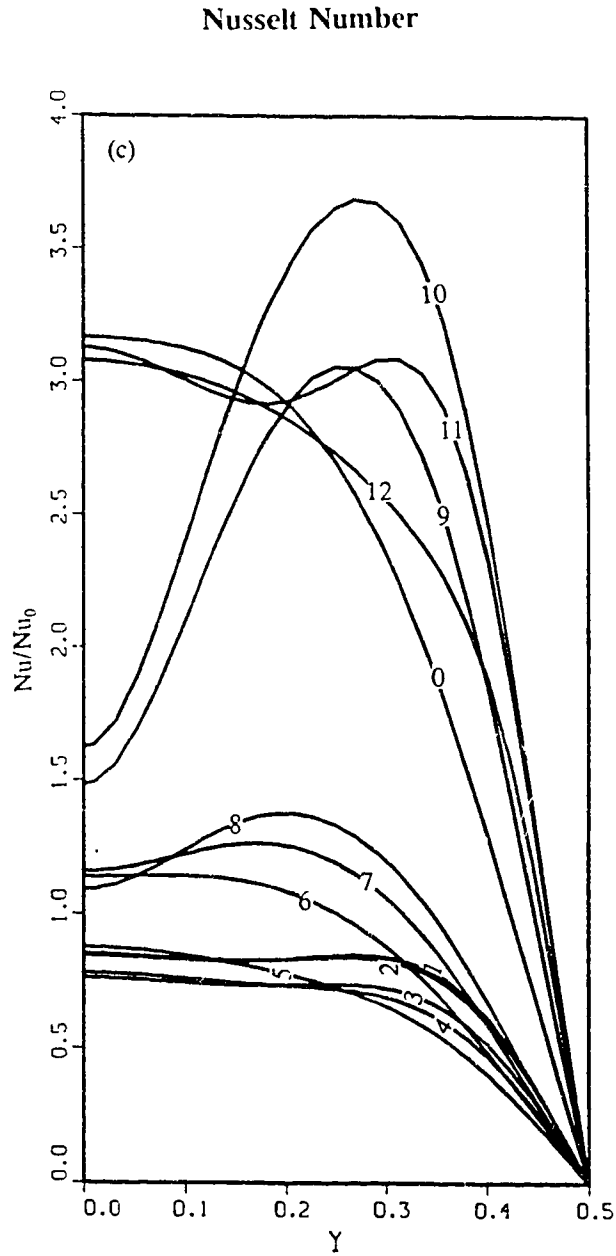


Figure 4.12. Distributions of friction factor and Nusselt number at $Dk = 100$, $\sigma = 0.02$ and $L_2 = -5$ (Curves 1 – 12 correspond to $L_1 = 1, 1.5, 2, 3, 5, 8, 10, 11.5, 12, 13.5, 15$ and 70 . Curve 0 is for the case of $L_1 = L_2 = 0$.) (a) along the inner wall; (b) along the upper wall; (c) along the outer wall

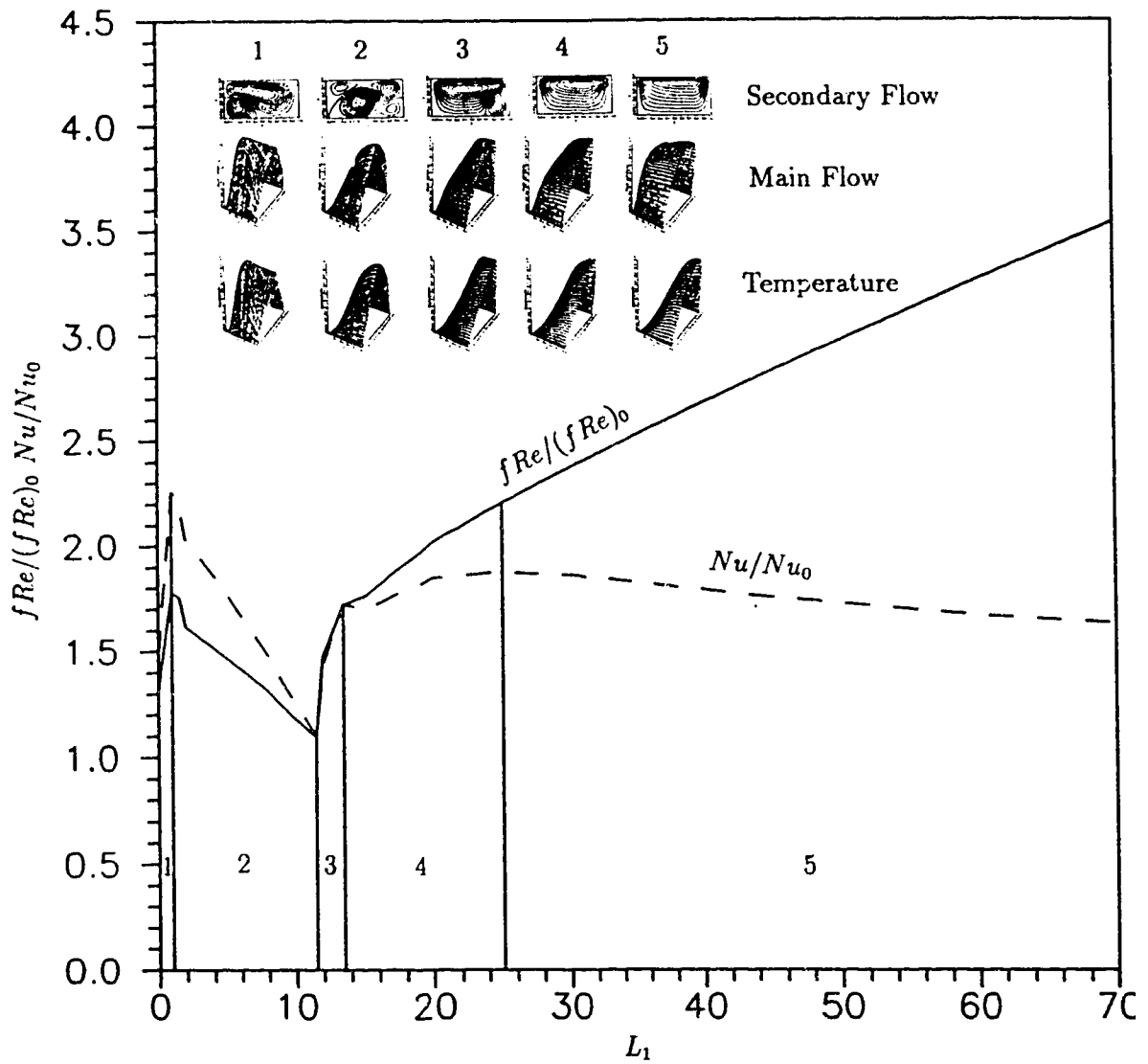


Figure 4.13. Mean friction factor and Nusselt number at $Dk = 100, \sigma = 0.02$ and $L_2 = -5$

References

- [1] Alfredsson, P.A. & Persson, H. 1989 Instabilities in channel flow with system rotation. *J. Fluid Mech.* **202**, 543-557.
- [2] Bara, B., Nandakumar, K. & Masliyah, J.H. 1992 An experimental and numerical study of the Dean problem: flow development towards two-dimensional multiple solutions. *J. Fluid Mech.* **244**, 339-376.
- [3] Baylis, J.A. 1971 Experiments on laminar flow in curved channels of square section. *J. Fluid Mech.* **48**, 417-422.
- [4] Berger, S.A. 1991 Flow and heat transfer in curved pipes and tubes. *AIAA91-0030*.
- [5] Berger, S.A., Talbot, L. & Yao, L.S. 1983 Flow in curved pipes. *Ann. Rev. Fluid Mech.* **15**, 461-512.
- [6] Berman, J. 1985 Fully developed heat transfer in a rotating non-aligned straight tube. *Chem. Eng. Commun.* **39**, 201-216.
- [7] Cheng, K.C. & Akiyama, M. 1970 Laminar forced convection heat transfer in curved rectangular channels. *Int. J. Heat Mass Transfer* **13**, 471-490.
- [8] Cheng, K.C. & Hwang, G.J. 1969 Numerical solution for combined free and forced laminar convection in horizontal rectangular channels. *ASME J. Heat Transfer* **91**, 59-66.

- [9] Cheng, K.C., Lin, R.C. & Ou, J.W. 1975 Graetz problem in curved square channels. *ASME J. Heat Transfer* **97**, 244-248.
- [10] Cheng, K.C., Lin, R.C. & Ou, J.W. 1976 Fully developed laminar flow in curved rectangular channels. *Trans. ASME: J. Fluids Eng.* **98**, 41-48.
- [11] Cheng, K.C., Nakayama, J. & Akiyama, M. 1979 Effect of finite and infinite aspect ratios on flow patterns in curved rectangular channels. In *Flow Visualization* (T.Asanuma, ed.), 181-186. Hemisphere.
- [12] Cheng, K.C. & Wang, L. 1993a The effects of Coriolis and centrifugal forces on transition to turbulence in a rotating curved rectangular channel. *Procs. 6th Int. Symp. on Transport Phenomena in Thermal Eng.*, Begell House, **2**, 1282-1289.
- [13] Cheng, K.C. & Wang, L. 1993b The effects of centrifugal and Coriolis forces on secondary flow phenomena in rotating curved square channels-visualizations for positive and negative rotations. *ASME, FED* **172**, 359-367.
- [14] Cheng, K.C. & Wang, L. 1993c Transition to turbulence and relaminarization phenomena in rotating radial straight pipes. *1993 National Heat Transfer Conference in Atlanta, HTD-* **252**, Visualization of Heat Transfer Processes, ASME, 55-63.
- [15] Cheng, K.C., Wang, L. & Faulkner, B.G., 1992 Visualization of instability phenomena in a rotating curved rectangular channel with aspect ratio 10. *Proc.*

of the Fourth Int. Symp. on Transport Phenomena and Dynamics of Rotating Machinery A, 549-560.

[16] Dean, W.R., 1928 The stream-line motion of a fluid in a curved pipe. *Phil. Mag.* **5**, 673-695.

[17] Dennis, S.C.R. & Ng, M. 1982 Dual solutions for steady laminar flow through a curved tube. *Q.J. Mech. Appl. Maths.* **35**, 305-324.

[18] Finlay, W.H. 1990, Transition to oscillatory motion in rotating channel flow. *J. Fluid Mech.* **215**, 209-227.

[19] Finlay, W.H., Keller, J.B. & Ferziger, J.H. 1988 Instabilities and transition in curved channel flow. *J. Fluid Mech.* **194**, 417-456.

[20] Ghia, K.N. & Sokhey, J.S. 1977 Laminar incompressible viscous flow in curved ducts of regular cross-sections. *Trans. ASME I: J. Fluids Engng* **99**, 640-648.

[21] Guo, Y. & Finlay, W.H. 1991 Splitting, merging and wavelength selection of vortices in curved and/or rotating channel flow due to Eckhaus instability. *J. Fluid Mech.* **228**, 661-691.

[22] Hochrainer, D. 1971 A new centrifuge to measure the aerodynamic diameter of aerosol particles in the submicron range. *J. of Colloid and Interface Science* **36**, 191-194.

- [23] Hocking, L.M., 1967 Boundary and shear layers in a curved rotating pipe. *J. Math. Phys. Sci.* **1**, 123-136.
- [24] Hong, S.W., Morcos, S.M. & Bergles, A.E. 1974 Analytical and experimental results for combined forced and free convection in horizontal tubes. *Proc. Fifth Int. Heat Transfer Conf.* **3**, 154-158.
- [25] Hoover, M.D. & Stöber, W. 1981 Model of particle deposition in spinning duct aerosol centrifuges. *J. Aerosol Science* **12**, 223-232.
- [26] Hoover, M.D., Stöber, W. & Morawietz, G. 1984 Experiment on laminar flow in a rotating, curved duct of rectangular cross section. *J. Fluids Engi.* **106**, 38-44.
- [27] Hwang, G.J. & Chao, C.H. 1991 Forced laminar convection in a curved isothermal square duct. *J. Heat Transfer* **113**, 48-55.
- [28] Hwang, G.J. & Cheng, K.C. 1970 Boundary vorticity method for convective heat transfer with secondary flow-applications to the combined free and forced convection in horizontal tubes. *Heat Transfer 1970* **4**, paper NC3.5.
- [29] Hwang, G.J. & Jen, T.C. 1987 Forced laminar convection in fully developed flow in a rotating isothermal duct with the effect of axial conduction. *Proc. 2nd ASME-JSME Thermal Engineering Joint Conf.*, Honolulu, USA, **2**, 43-49.
- [30] Hwang, G.J. & Jen, T.C. 1990 Convective heat transfer in rotating isothermal ducts. *Int. J. Heat Mass Transfer* **33**, 1817-1828.

- [31] Hwang, G.J. & Kuo, C.R. 1992 Experimental study of convection heat transfer in a radially rotating square duct with uniform heat flux. *The Fourth Int. Symposium on Transport Phenomena and Dynamics of Rotating Machinery (ISROMAC-4)*, Honolulu, USA, April 5-8.
- [32] Hwang, G.J. & Kuo, C.R. 1993 Experimental study of convective heat transfer in a rotating square duct with radial outward flow. *ASME: Gas Turbine Heat Transfer*, HTD-vol.242.
- [33] Hwang, G.J. & Soong, C.Y. 1989 Experimental automation and heat transfer measurement on a rotating thermal system. *Transport Phenomena in Thermal Control* (Ed. by G.J. Hwang), Hemisphere Pub. Corp., New York, 375-388.
- [34] Hwang, G.J. & Soong, C.Y. 1992 Convective heat transfer in rotating channels. *The Fourth Int. Symposium on Transport Phenomena and Dynamics of Rotating Machinery (ISROMAC-4)*, Honolulu, USA, April 5-8.
- [35] Ito, H. 1987 Flow in curved pipes. *JSME Int. J.* **30**, 543-552.
- [36] Ito, H. & Motai, T., 1974 Secondary flow in a rotating curved pipe. *Rep. Inst. High Speed Mech.* **29**, 33-57.
- [37] Jen, T.C., Lavine, A.S. & Hwang, G.J. 1992 Simultaneous developing laminar convection in rotating isothermal square channels. *Int. J. Heat Mass Transfer* **35**, 239-254.

- [38] Kheshgi, H.S. & Scriven, L.E. 1985 Viscous flow through a rotating square channel. *Phys. Fluids* **28**, 2968-2979.
- [39] Kotrappa, P. & Light, M.E. 1972 Design and performance of the lovelace aerosol particle separator. *Review of Scientific Instruments* **43**, 1106-1112.
- [40] Lennartz, J.W., Gorensck, M.B. & Adler, R.J. 1987 Separation of fine-particle dispersions using periodic flows in a spinning coiled tube. Part III: Batch fractionation experiments. *AICH E J.* **33**, 506-509.
- [41] Ligrani, P.M., Finlay, W.H., Fields, W.A., Fuqua, S.T. & Subramaman, C.S. 1992 Features of wavy vortices in a curved channel from experimental and numerical studies. *Phys. Fluids* **A4(4)**, 695-709.
- [42] Ligrani, P. & Niver, R.D. 1988 Flow visualization of Dean vortices in a curved channel with 40 to 1 aspect ratio. *Phys. Fluids* **31**, 3605-3618.
- [43] Ludwig, H. 1951 Die ausgebildete kanalströmung in einem rotierenden system. *Ing.-Arch. Bd.* **19**, 296-308.
- [44] Matsson, O.J.E. & Alfredsson, P.H. 1990 Curvature- and rotation-induced instabilities in channel flow. *J. Fluid Mech.* **210**, 537-563.
- [45] Miyazaki, H. 1971 Combined free and forced convective heat transfer and fluid flow in a rotating curved circular tube. *Int. J. Heat Mass Transfer* **14**, 1295-1309.

- [46] Miyazaki, H. 1973 Combined free and forced convective heat transfer and fluid flow in a rotating curved rectangular tubes. *J. Heat Transfer* **95**, 64-71.
- [47] Mori, Y. & Uchida, Y. 1967 Study on forced convective heat transfer in a curved square channel (1st report, theory of laminar region). *Trans. of JSME* **33**, 1836-1846.
- [48] Mori, Y., Uchida, Y. & Ukon, T. 1971 Forced convective heat transfer in a curved channel with a square cross section. *Int. J. Heat Mass Transfer* **4**, 1787-1805.
- Morris, W.D. 1981, *Heat Transfer and Fluid Flow in Rotating Coolant Channels*. Research Studies Press, John Wiley and Sons.
- [49] Nandakumar, K. & Masliyah, J.H. 1986 Swirling flow and heat transfer in coiled and twisted pipes. *Advances in Transport Processes* **4**, 49-112.
- [50] Nandakumar, K., Masliyah, J.H. & Law, H.S. 1985 Bifurcation in steady laminar mixed convection flow in horizontal ducts. *J. Fluid Mech.* **152**, 145-161.
- [51] Nandakumar, K., Raszillier, H. & Durst, F 1991 Flow through rotating rectangular ducts. *Phys. Fluids* **A3**, 770-781.
- [52] Nandakumar, K. & Weinitschke, H.J. 1991 A bifurcation study of mixed-convection heat transfer in horizontal ducts. *J. Fluid Mech.* **231** 157-187.
- [53] Papanu, J.S., Adler, R.J., Gorensck, M.B. & Menon, M.M. 1986 Separation of

- fine particle dispersions using periodic flows in a spinning coiled tube. *AICHE J.* **32**, 798-808.
- [54] Patankar, S.V. 1980 *Numerical Heat Transfer and Fluid Flow*. McGraw-Hill.
- [55] Pedley, T.J. 1980 *The Fluid Mechanics of Large Blood Vessels*. Cambridge Univ. Press, pp. 160-234.
- [56] Sankar, S.R., Nandakumar, K. & Masliyah, J.H. 1988 Oscillatory flows in coiled square ducts. *Phys. Fluids* **31**, 1348-1358.
- [57] Shah, R.K. & London, A. 1978 *Laminar Flow Forced Convection in Ducts*. Academic Press, New York.
- [58] Smirnov, E.M. 1978 Asymptotic drag formulas for the rapidly rotating radial channels of rectangular cross section. *Izv. Akad. Nauk. SSSR. Mekh. Zhidk. Gaza*, 42-49.
- [59] Soong, C.Y. & Hwang, G.J. 1990 Laminar mixed convection in a radially rotating semiporous channel. *Int. J. Heat Mass Transfer* **33**, 1805-1817.
- [60] Soong, C.Y., Lin, S.T. & Hwang, G.J. 1991 An experimental study of convective heat transfer in radially rotating rectangular ducts. *J. Heat Transfer* **113**, 604-611.
- [61] Speziale, C.G. 1982 Numerical study of viscous flow in rotating rectangular ducts. *J. Fluid Mech.* **122**, 251-271.

- [62] Speziale, C.G. & Thangam, S. 1983 Numerical study of secondary flows and roll-cell instabilities in rotating channel flow. *J. Fluid Mech.* **130**, 377-395.
- [63] Stöber, W. & Flachsbart, H. 1969 Size-separating precipitation of aerosols in a spinning spiral duct. *Environmental science and technology* **3**, 1280-1296.
- Sugiyama S., Hayashi, T. & Yamazaki, K. 1983 Flow characteristics in the curved rectangular channels (visualization of secondary flow). *Bulletin of the JSME* **26**, 964-969.
- [64] Thangam, S. & Hur, N. 1990 Laminar secondary flows in curved rectangular ducts. *J. Fluid Mech.* **217**, 421-440.
- [65] Wang, L. & Cheng, K.C. 1994a Flow transition and combined free and forced convective heat transfer in a rotating curved circular tube-I: perturbation solution. submitted for publication.
- [66] Wang, L. & Cheng, K.C. 1994b Flow transition and combined free and forced convective heat transfer in a rotating curved circular tube II: flow and heat transfer characteristics. submitted for publication.
- [67] Wang, L., Wang, J.C.Y. & Cheng, K.C. 1991 Fluid flow and combined free and forced convective heat transfer in a rotating curved circular tube (Part 1). *ASME Paper: 91-IIT-15*.
- [68] Winters, K.H. 1987 A bifurcation study of laminar flow in a curved tube of rectangular cross-section. *J. Fluid Mech.* **180**, 343-369.

- [69] Yanase, S., Goto, N. & Yamamoto, K. 1988 Stability of dual solutions of the flow in a curved circular tube. *J. Phys. Soc. Japan* **57**, 2602-2604.

Chapter 5

Flow Transitions and Combined Free and Forced Convective Heat Transfer in Rotating Curved Channels: The Case of Negative Rotation

The finite-volume scheme developed in Chapter 4 is used to study the laminar flow transitions and combined free and forced convective heat transfer in a rotating curved channel for the case of negative rotation at relatively high Dean numbers. The results cover both the nature of flow transitions and their effects on temperature

distribution, friction resistance and heat transfer between fluid and wall. Several phenomena shown in the Chapter 4 are confirmed. As well, several new phenomena are revealed. When the rotation is in the negative direction, the inward Coriolis forces cause the Coriolis vortices (due to the Coriolis force instability) to appear near the inner wall of the channel, and the direction of the secondary flow to reverse by overcoming the outward centrifugal and/or buoyancy forces. When the Coriolis vortices appear near the inner wall, the inner side of the channel becomes the high pressure side. The flow reversal (due to negative Coriolis forces) occurs after passing through a multi-pair vortex flow region where overall, the Coriolis, centrifugal and buoyancy forces just neutralize each other. The merging-vortices found in Chapter 4 appear to exist only when the buoyancy forces are taken into consideration.

5.1 Introduction

In Chapter 4, we have discussed the flow transitions for both secondary flow and pressure-driven main flow in a rotating curved channel. Also examined are the effects of the flow transitions on temperature field, flow resistance and heat transfer inside the channel. In this chapter, we constrain ourselves to the case of positive rotation at relatively lower Dean number. Such discussions are extended to the case of negative rotation at relatively high Dean number in this chapter.

The negative rotation of the channel introduces the Coriolis force which may cancel the effect of the curvature in both the cross-plane and the main flow direction.

This is different from the case of positive rotation where the Coriolis force due to the rotation of the channel intensifies the effect of the curvature in both the cross-plane and the main flow direction.

At a relatively high Dean number, the secondary flow may consist of two-pair of counter-rotating vortices even when the channel is just curved (Dean's instability). This differs from the case of low Dean number where it consists of only one-pair of counter-rotating vortices.

Because of the differences, we may expect some different features about the flow transitions when the rotation is negative and the Dean number is relatively high. In §5.2, the flow transitions are examined for both secondary flow and main flow. Also shown in this section are the temperature distributions. The discussions are divided into three parts: (1) the case without effect of buoyancy force (§5.2.1), (2) the heating case (§5.2.2) and (3) the cooling case (§5.2.3). The effects of the flow transition on the friction resistance and heat transfer inside the channel are investigated in §5.3 in terms of local and mean friction factors and Nusselt numbers defined in Chapter 4. The presentation of the results is grouped into the local friction factors and Nusselt numbers along the upper half of the inner wall (§5.3.1), along the upper wall (§5.3.2), along the upper half of the outer wall (§5.3.3) and the mean friction factor and Nusselt number (§5.3.4). The concluding remarks are given in §5.4.

5.2 Flow Transitions and Temperature Distributions

5.2.1 The case without effect of buoyancy force ($L_2 = 0$)

The secondary flow patterns, main velocity isopleths and profiles, and isotherms and temperature profiles are shown in Fig.5.1 for several representative values of L_1 at $\gamma = 1, Dk = 500, \sigma = 0.02, Pr = 0.7$ and $L_2 = 0$. The variations of several representative properties, namely, the Reynolds number, the Dean number, the maximum absolute value of the secondary flow stream function, the maximum values of main velocity and temperature, and the mean friction factor ratio and Nusselt number ratio, are listed in Table 5.1.

Without the effect of the buoyancy force ($L_2 = 0$), the convective heat transfer inside the channel is purely forced convection. In the cross-plane, the Coriolis force (due to the rotation) neutralizes the effect of the centrifugal force due to the curvature of the channel. For the case with vanishing value of L_1 , the Coriolis force disappears and the problem becomes the classical Dean problem which has been well examined by many investigators in recent years. The secondary flow consists of two-pair of counter-rotating vortices as shown in Fig.5.1(a)-(i) for the case of high Dean number. Here the 'high' means that the Dean number is beyond its critical value for the appearance of the Dean vortices, which is about 118 for an aspect ratio of unity found by Cheng *et al.* (1976) and Cheng *et al.* (1979) while Joseph *et al.* (1975) observe that the critical value is about 100. The larger vortices are

Table 5.1: The variations of several representative properties with L_1 at $\gamma = 1$, $Dk = 500$, $\sigma = 0.02$, $Pr = 0.7$ and $L_2 = 0$ ($(fRe)_0 = 14.23$, $Nu_0 = 3.608$)

L_1	Re	De	$ \psi _{max}$	w_{max}	t_{max}	$fRe/(fRe)_0$	Nu/Nu_0
0	1801	255	11.855	0.0297	76.23	1.972	2.534
-0.1	1806	263	11.158	0.0307	81.50	1.909	2.435
-0.3	2030	287	9.574	0.0336	97.73	1.750	2.175
-0.4	2145	303	8.401	0.0356	110.37	1.638	2.004
-0.5	2329	329	10.038	0.0400	135.10	1.530	1.818
-0.6	2456	347	9.994	0.0420	151.60	1.452	1.688
-0.65	2541	359	9.744	0.0441	169.37	1.404	1.575
-0.7	2612	369	8.845	0.0466	188.76	1.367	1.479
-0.75	2143	303	8.261	0.0394	122.64	1.668	1.989
-1.0	1840	260	11.423	0.0325	85.59	1.943	2.449
-3.0	1341	190	16.816	0.0214	42.92	2.678	3.468
-3.5	1298	184	17.278	0.0205	40.38	2.771	3.562

called Ekman-type-vortices which are always present for any non-zero value of Dean number. The smaller vortices are called Dean-vortices which appear only when the Dean number is above the critical value. A strong inward secondary flow exists between two Dean-vortices while a strong outward secondary flow appears between the Ekman-type-vortices and the Dean-vortices.

Figure 5.1(a)-(ii) demonstrates the way in which the Dean-vortices affect the isovels and profile of the main velocity. Significantly distorted isovels are found in the region with the Dean - vortices. In particular, corresponding to the strong inward secondary flow, the isovels are moved inwards by the Dean-vortices in the region between the Dean-vortices. Two high velocity cores are formed which are symmetric about the horizontal centerline. The isovels are more tightly spaced in the region near the outer wall than those near the inner wall. The densely distributed isovels are also found near the upper and lower walls. Consequently, a pronounced peripheral variation is expected for the local friction factor.

The main velocity distributions along the vertical and horizontal centerlines are shown by curve 0 in Fig.5.2 (a) and (b). A striking feature is that the main velocity has inflection points on both vertical and horizontal centerlines. Such profiles may be unstable in accordance with the Rayleigh's inflection point criterion.

For the channel with infinite span, Finally *et al.* (1988) and Finlay (1990) examined the stabilities of the Dean-vortices (the Dean problem) and the Coriolis-vortices (the Coriolis problem) with respect to the streamwise wavy perturbations.

They found that the instability leads to the development of undulating vortex flow and twisting vortex flow. These two different wavy travelling vortex flows have been confirmed experimentally by Ligrani *et al.* (1992) and Ligrani & Niver (1988) for the Dean problem. As well, the Eckhaus stability of the Dean- vortices and Coriolis- vortices was examined numerically by Guo & Finlay (1991) for infinite- span cross section. They found that the Eckhaus instability causes the vortex pairs to split apart or merge together. Experimental observations of the splitting and merging of vortex pairs were made by Ligrani & Niver (1988), Alfredsson & Persson (1989), Matsson & Alfredsson (1990), Ligrani *et al.* (1992). It appears that these types of hydrodynamic stability analyses have not been extended to the geometries with finite cross sections.

Figure 5.1(a)-(iii) illustrates the isotherms and temperature profile affected by the Dean-vortices. The isotherms are drastically distorted inward near the center of the outer wall where the Dean- vortices occur. Two high temperature cores appear in the cross-plane which are symmetric with respect to the horizontal centerline. The isotherms near the outer wall are more tightly spaced than those near the inner wall. The densely distributed isotherms are also found near the upper and lower walls. This will result in a higher heat transfer rate in these regions.

As the channel rotates in the negative direction, the corner vortices appear first at the upper- inner corner (Fig. 5.1(b)-(i)), then at the upper-outer corner (Fig. 5.1(c)-(i)). The circulation direction of these corner vortices is clockwise which is

opposite to that of the Ekman-type-vortices. The formation and development of the corner vortices squeeze the Ekman-type-vortices (Fig. 5.1(b)-(d)-(i)), reduce the maximum absolute value of the secondary stream function (Table 5.1), and increase the maximum values of main velocity and temperature (Table 5.1).

Shown in Fig. 5.1(b)-(d)-(ii) are the main velocity and temperature distributions corresponding to the secondary flow patterns in Fig.5.1(b)-(d)-(i). They are qualitatively similar to those in Fig.5.1(a)-(ii)(iii). However, the formation and development of the corner vortices have two effects on the main flow and temperature distributions. One effect is moving the main velocity and temperature peaks upward to the boundary between the Ekman-type and Dean-vortices. Another effect is reducing the values of the main velocity and temperature in the region with the corner vortices.

The profiles of the main velocity along the vertical centerline and the horizontal centerline for this structure with the coexistence of the Ekman-type-vortices, the Dean-vortices and the corner vortices are illustrated by curves 1-3 in Fig.5.2. They are quite similar to the curve 0. In particular, they have inflection points on both the vertical and horizontal centerlines. This may suggest possible further instability analysis in the future.

When the negative rotation becomes more rapid, the growth of the corner vortices pushes the Ekman-type-vortices further towards the center part of the outer wall. Essentially, the Dean-vortices presented in Fig.5.1(a)-(d)-(i) disappear and

the secondary flow restabilizes to a structure with the Ekman-type-vortices and the corner vortices (Fig.5.1(e)-(i)). The inflection points in the main velocity profiles along the vertical and horizontal centerlines also disappear (curve 4 in Fig.5.2). In addition, the maximum absolute value of the stream function and the maximum values of the main velocity and the temperature are all seen to increase. Furthermore, the main velocity and temperature profiles experience a dramatic change. In particular, the isovels (Fig.5.1(e)-(ii)) and the isotherms (Fig.5.1(e)-(iii)) become more densely spaced near the inner wall while they become more sparsely spaced near the outer wall as compared with the previous case (Fig.5.1(d)-(ii)(iii)). This will result a change in the distributions of the local friction factor ratio and Nusselt number ratio. The flow in the channel core is neither ageostrophic nor geostrophic. The viscous shear is not confined in a thin layer along the walls and exists in the whole cross section of the channel. The boundary layer theory is, apparently, not valid for the analysis in this flow region.

Increasing the rotation speed further in the negative direction, the corner vortices with a clockwise direction of circulation grow, merge together and push the original Ekman-type- vortices towards the horizontal centerline. The maximum absolute value of the stream function decreases while the maximum values of the main velocity and temperature increase (Table 5.1). Figures 5.1(f)-(h)-(i) illustrates this process. In this region, the main velocity and temperature profiles (Fig.5.1(f)-(h)-(ii)(iii), curves 5-7 in Fig.5.2) remain similar to those as shown in Fig.5.1(e)-(ii)(iii) and

curve 4 in Fig.5.2.

Further growth of the corner vortices finally causes the original Ekman-type vortices to disappear and the secondary flow becomes one-pair vortex configuration with a clockwise direction of the circulation, as shown in Fig.5.1(i)(j)-(i). This confirms that the flow reversal can also result from the inward Coriolis force. And the reverse direction of the secondary flow indicates the domination of the Coriolis force. The isovels and the isotherms are observed to be more sparsely spaced near the outer wall than near the inner wall (Fig.5.1(i)(j)-(ii)(iii)). The densely distributed isovels near the center part of the inner wall result in a high pressure region since the centrifugal force and Coriolis force are proportional to w^2 and w , respectively. The flow in the channel core appears ageostrophic. Two main velocity peaks and temperature peaks are seen near the inner wall rather than the outer wall with one on the upper half of the cross section and the other on the lower half. The regions with higher velocity and temperature are moved toward the upper and lower walls while they are shifted toward the inner wall by the rotation in the negative direction. A depression in the main velocity profile near the inner wall shown in Fig.5.1(i)(j)-(ii) foreshadows the onset of the Coriolis instability to be described later.

A striking feature of this ageostrophic one-pair vortex structure can be seen from the profiles of the main velocity along the vertical centerline and the horizontal centerline by curves 8 and 9 in Fig.5.2. The main velocity w changes linearly across the core and a little from the lower wall to the upper wall. The vorticity is, then,

nearly constant. Slow-moving fluid from the outer wall is accelerated across the core mainly at a constant rate until the inner wall is approached. The Coriolis and convective inertial forces dominate the ageostrophic core. Main velocity falls to zero in viscous layers on the outer and inner walls. This constant-vorticity, inviscid core flow structure suggests a possible analysis by the asymptotic method. It appears that no such attempt was made so far.

When the negative rotation becomes more rapid, the ageostrophic one-pair vortex breaks down into a configuration of two-pair of counter-rotating vortices that is asymmetric with respect to the vertical centerline (Fig.5.1(k)(l)-(i)). The additional pair of counter-rotating vortices near the center of the inner wall are called the Coriolis-vortices. They result from the Coriolis instability as discussed in Chapter 4. The secondary flow, main velocity and temperature distributions (Fig.5.1(k)(l)-(i)(ii)(iii)) are qualitatively similar to those shown in Fig.5.1(a)-(i)(ii)(iii) by interchanging the inner wall and the outer wall. Therefore, we neglect the general description about features of flow and temperature fields.

Two salient features, however, are still worthy to note. First an inflectional profile of the main flow is associated with this kind of vortex flow (curves 10 and 11 in Fig.5.2). Second the inner wall, where the Coriolis vortices are located, is the high pressure side. This is indicated by the isopiestic contour in Fig.5.3. Because of this, the Coriolis vortices and the buoyancy vortices behave differently although they all can appear near the center of the inner wall.

Two important points are in order to be noted. First, upon increasing the rotating speed further, we can not obtain the convergent solution in order to observe the disappearance of the Coriolis vortices at higher Dean number. This is true for both positive and negative rotations. For the case of negative rotation at low Dean number, however, we can easily obtain the convergent solution to show the disappearance of the Coriolis vortices. The situation is quite similar to the case of positive rotation at low Dean number as discussed in Chapter 4. The divergence may come from two possible sources: the numerical instability and physical instability. By numerical instability we mean the instability due to the improper numerical scheme. By physical instability we mean the instability caused by the physical problem itself, which means that there exists no steady, two-dimensional solution in this region of the parameter space. At this stage, it is not clear which factor causes the divergence. However, we reasonably suspect that it may be the physical instability based on two facts: (1) we fail to obtain the convergent solution by trying smaller grid sizes and initial guesses for the velocity, temperature and pressure fields for several cases; (2) we can easily find the Coriolis vortices at a higher Dean number. For example, we only need 176 seconds of CPU time to obtain the convergent solution for the case shown in Fig.5.1(1) through 235 iterations. This suggests possible further analysis using unsteady three-dimensional model and bifurcation/instability analysis in this region of the parameter space.

Second, it appears that no merging vortices exist under the condition of vanishing

buoyancy force. We have carried out many calculations for negative rotation with $L_2 = 0$ ranging from low to high Dean numbers. The results shown in Fig.5.1 are typical. The inward Coriolis force causes the secondary flow to reverse and the secondary flow consisting of one-pair of counter-rotating vortices after passing through a multi-pair vortex flow region where overall, the effect of the Coriolis force just neutralizes that of the centrifugal force. Then the Coriolis vortices appear near the center part of the inner wall. No merging vortices are observed.

5.2.2 The heating case with $L_2 > 0$

If the fluid is heated, both centrifugal and centrifugal-type buoyancy forces act radially outwards. The Coriolis force, however, acts radially inwards for the case of negative rotation. This is different from the case of positive rotation discussed in Chapter 4. Because of this different effect, we can intuitively expect a complex structure of flow transition and secondary flow reversals as the rotation speed is gradually increased in the negative direction. Figure 5.4 shows the secondary flow patterns, main velocity isopleths and profiles, and isotherms and temperature profiles for several representative values of L_1 with $\gamma = 1$, $Dk = 500$, $\sigma = 0.02$, $Pr = 0.7$ and $L_2 = 1$. The variations of the Reynolds number, Dean number, maximum absolute value of secondary flow stream function, the maximum values of main velocity and temperature and mean friction factor ratio and Nusselt number ratio, are listed in Table 5.2.

Table 5.2: The variations of several representative properties with L_1 at $\gamma = 1$, $Dk = 500$, $\sigma = 0.02$, $Pr = 0.7$ and $L_2 = 1$ ($(fRe)_0 = 14.23$, $Nu_0 = 3.608$)

L_1	r^2	De	$ \psi _{max}$	w_{max}	t_{max}	$fRe/(fRe)_0$	Nu/Nu_0
-0.5	1599	226	15.338	0.0255	56.45	2.218	2.975
-1.0	1717	243	14.151	0.0276	64.60	2.066	2.714
-1.5	1865	264	12.200	0.0300	77.38	1.904	2.395
-1.65	1931	273	11.298	0.0309	82.98	1.841	1.286
-1.85	2111	299	13.694	0.0356	106.83	1.686	2.046
-2.0	2147	304	14.550	0.0359	110.73	1.660	1.996
-2.1	2183	309	14.740	0.0367	115.49	1.634	1.940
-2.25	2264	320	14.175	0.0384	127.44	1.576	1.821
-2.3	2294	324	13.861	0.0391	132.00	1.556	1.780
-2.5	1638	232	12.035	0.0290	73.14	2.186	2.601
-3.0	1472	208	13.770	0.0245	54.92	2.435	3.046
-4.0	1334	189	15.556	0.0213	44.04	3.375	3.382

Shown in Fig.5.4(a)-(i) is one secondary flow with an additional pair of vortices occurring in the center part near the outer wall. A comparison with Fig.5.1(e)-(i) indicates that they result from the buoyancy force instability, and are called buoyancy-vortices.

The presence of the buoyancy-vortices leads to a highly disturbed main flow field (Fig.5.4(a)-(ii)) and temperature field (Fig.5.4(1)-(iii)), with strong inflectional profiles developing for both vertical and horizontal centerlines (curve 1 in Fig.5.5). This can result in a secondary instability as mentioned previously. The secondary flow, main velocity and temperature distributions (Fig.5.4(a)-(i)(ii)(iii)) are qualitatively similar to those shown in Fig.5.1(a)-(i)(ii)(iii).

If the rotation speed is increased in the negative direction such that the Coriolis force is of the same order of magnitude as the resulting force of the centrifugal and buoyancy forces, the corner vortices occur and grow with circulating direction opposite to that of the Ekman-type-vortices (Fig.5.4(b)-(d)-(i)). The formation and development of the corner vortices squeeze the Ekman-type-vortices, reduce the maximum absolute value of the stream function, increase the maximum values of the main velocity and temperature (Table 5.2), and have two effects on the main flow and temperature distributions. One effect is to move the main velocity peak and temperature peak upward towards the boundary between the Ekman-type and buoyancy vortices (Fig.5.4(b)-(d)-(ii)(iii)). Another effect is to reduce the value of the main velocity and temperature in the region with the corner vortices (Fig.5.4(b)-

(d)-(ii)(iii)). The main velocity and temperature profiles, however, are qualitatively similar to those shown in Fig.5.4(a)-(ii)(iii) in general, with strong inflectional profiles of main velocity along the vertical and horizontal centerlines (curves 2-4 in Fig.5.5).

Upon increasing the rotation speed, the further growth of the corner vortices leads to the disappearance of the buoyancy vortices (Fig.5.4(c)-(i)) and the increase on the maximum absolute value of the stream function (Table 5.2). This changes the distributions of the main flow and temperature dramatically (Fig.5.4(e)-(ii)(iii)). In particular, the isovels and isotherms become more sparsely spaced near the outer wall. The flow in the channel core is neither ageostrophic nor geostrophic. The viscous shear is not confined in a thin layer along the walls and exists in the whole cross section of the channel. A major difference from that shown in Fig.5.1(e)-(i) is the appearance of the vortices near the center of the inner wall. Such vortices are always observed in some regions of the parameter space if the fluid is heated or cooled. For convenience, we call them the center vortices.

When the rotation speed is increased further, the corner and center vortices grow. As well, two corner vortices merge together and push the original Ekman-type-vortices towards the inner wall to merge with the center vortices. Figure 5.4(f)-(i)-(i) illustrates this merging and pushing process. In this process, the maximum values of the main velocity and temperature are seen to increase (Table 5.2). The inflection points on the profiles of the main velocity along the vertical and horizontal

centerline: disappear gradually. (curves 6-9 in Fig.5.5).

Finally, this merging process leads the secondary flow to a two-pair vortex configuration as shown in Fig.5.4(j)-(l)-(i). The one-pair vortices near the center of the inner wall, which is the high pressure side as shown in Fig.5.6, result from the merging of the Ekman-type-vortices with the center vortices. We call them merging vortices. The profiles of the main velocity and temperature change dramatically from those in Fig.5.4(i)-(ii)(iii) with a significantly decrease of their maximum values, and are qualitatively similar to those in Fig.5.1(k)(l)-(ii)(iii) for the case of the high Dean number (Fig.5.4(j)-(l)-(ii)(iii)). Furthermore, the strong inflectional profiles develop along both vertical and horizontal centerlines (curves 10-12 in Fig.5.5).

Similarly, we have failed to observe the disappearance of the merging vortices upon increasing the rotation speed further possibly because of the physical instability in the region.

5.2.3 The cooling case with $L_2 < 0$

For the cooling case, both Coriolis force and centrifugal-type buoyancy force act inward in the cross-plane, if the rotation is in the negative direction. The secondary flow reversal can take place either by the Coriolis or buoyancy forces depending on the value of $|L_2|$. Shown in Fig.5.7 are the secondary flow patterns, main velocity and temperature profiles at $\gamma = 1, Dk = 500, \sigma = 0.02, Pr = 0.7$ and

Table 5.3: The variations of several representative properties with L_1 at $\gamma = 1$, $Dk = 500$, $\sigma = 0.02$, $Pr = 0.7$ and $L_2 = -1$ ($(fRe)_0 = 14.23$, $Nu_0 = 3.608$)

L_1	Re	De	$ \psi _{max}$	w_{max}	t_{max}	$fRe/(fRe)_0$	Nu/Nu_0
0	1792	253	13.722	0.0311	75.91	1.993	2.613
-0.02	1785	252	13.773	0.0310	75.32	2.001	2.625
-0.5	1540	218	15.001	0.0247	53.25	2.320	3.112
-1.0	1463	207	16.174	0.0235	48.65	2.443	3.277
-3.0	1276	180	18.612	0.0200	38.10	2.818	3.690

$L_2 = -1$. The corresponding profiles of the main velocity along the vertical and horizontal centerlines are shown in Fig.5.8. Table 5.3 lists the Reynolds number, Dean number, the maximum absolute value of the stream function, the maximum values of the main velocity and temperature, and mean friction factor ratio and Nusselt number ratio for each case.

A comparison of Figs.5.7 and 5.8 with Figs. 5.1 and 5.2 shows that the flow transitions in the secondary flow, the main flow and the temperature distribution in Fig.5.7 resemble those shown in Fig.5.1(i)-(l). The secondary flow has already been reversed even in the case of $L_1 = 0$ (Fig.5.7(a)-(i)). The flow regions with the presence of the multi-pair vortices and merging vortices are in the region of the parameter space with $L_1 > 0$. The inward Coriolis forces cause the Coriolis vortices to appear near the center of the inner wall which is the high pressure side as shown

in Fig.5.9.

Once again, we have failed to observe the disappearance of the Coriolis vortices possibly because of the physical instability.

5.3 Distributions of Friction Factor and Nusselt Number

As is well understood, variations in profiles of main flow and temperature change the peripheral distributions of the friction factor and Nusselt number along the wall, which are important in practical applications. The flow transition discussed in the last section will, then, significantly affect the distributions of the friction factor and Nusselt number.

Shown in Fig.5.10 are fRe and Nu along the upper half of the inner wall (Fig.5.10(a)), the upper wall (Fig.5.10(b)) and the upper half of the outer wall (Fig.5.10(c)) for twelve representative values of L_1 at $Dk = 500$, $\sigma = 0.02$, $Pr = 0.7$ and $L_2 = 1$. They are shown on the basis of those for a stationary straight channel, namely, $(fRe)_0 (=14.23)$ and $Nu_0 (=3.608)$. The corresponding flow patterns and temperature profiles are illustrated in Fig.5.4. Also shown in the figure are friction factor and Nusselt number for the curved channel without rotation, i.e., $L_1 = L_2 = 0$, denoted by the curve 0.

A reexamination of Fig.5.4 shows that the flow and temperature profiles may be, qualitatively, divided into three groups. The secondary flows for the first group show

the presence of the buoyancy vortices, as shown in Fig.5.4(a)-(d). The distributions of fRe and Nu for this group are shown by curves 1-4 in Fig.5.10. Curves 5-9 in Fig.5.10 show the profiles of fRe and Nu for group two. The secondary flows for this group consist of multi- pair of counter-rotating vortices characterizing by the presence of the corner and center vortices as shown in Fig.5.4(e)-(i). The last group, which includes Fig.5.4(j)-(l), is characterized by the merging vortices in secondary flow. The curves 10-12 are drawn in Fig.5.10 to show the distributions of fRe and Nu for this group.

An interesting feature can be inferred by comparing the distributions of fRe with those of Nu in Fig.5.10. They are qualitatively similar in general. This results from the similarity between the main flow profile and temperature profile in the flow region (Fig.5.4.).

5.3.1 Distributions along the upper half of the inner wall

For the flow in Group one, the main flow and temperature distribution are quite uniform over a wide range of the inner wall. This leads to a relatively constant local friction factor and Nusselt number (curves 1-4 in Fig.5.10(a)). The formation and development of the corner vortices in the upper-inner corner destroy this uniformity more or less, and cause the isovels and isotherms to be more densely distributed along the inner wall (Fig.5.4(a)-(d)). This results in a more notable variation of the friction factor and Nusselt number along the inner wall with an increase in value

from the curve 1 to curve 4. In this flow region, the friction factor ratio is higher than the Nusselt number ratio. However, both ratios are relatively low because of the sparsely distributed isovels and isotherms.

When the flow is in Group two, the formation and growth of the corner and the center vortices have three major effects on the distributions of the friction factor and Nusselt number along the inner wall. First an increase in the ratios of the frictions factor and the Nusselt number is observed through the more densely distributed isovels and isotherms (curves 5-9 in Fig.5.10(a)). Second the appearance of the two local peaks in the friction factor (Nusselt number) is noted through impinging on and retreating from the inner wall. Third the decrease in the ratios of the friction factor and Nusselt number near the center of the inner wall occurs through the retreating effect of the center vortices in that region. A comparison shows that the friction factor ratio is lower than the Nusselt number ratio.

The formation of the merging vortices changes the distributions of isovels and isotherms along the inner wall significantly. Consequently, a dramatic change is observed in the distributions of the friction factor and the Nusselt number (curves 10-12 in Fig.5.10(a)). The high values of the friction factor and Nusselt number result from the very densely distributed isovels and isotherms along the inner wall. The large velocity (temperature) gradient between the high velocity (temperature) core and the inner wall (Fig.5.4((j)-(l)-(ii)(iii))) results in a peak of the local friction factor (Nusselt number) in that region. Another peak is seen around the boundary

of the layer along the upper wall. As well, a relatively low friction factor (Nusselt number) region is observed in the center of the inner wall. It is induced by the outwash isovels (isotherms) due to the retreating effect of the merging vortices in that region.

5.3.2 Distributions along the upper wall

For the flow in Group one, the isovels and isotherms along the upper wall gradually become densely distributed from the inner wall to the outer wall except a very short region from the outer wall (Fig.5.4(a)-(d)). Consequently, the friction factor and the Nusselt number increase in general from the inner wall to the outer wall along the upper wall. The large velocity (temperature) gradient between the high velocity (temperature) core and the upper wall results a peak of the local friction factor (Nusselt number) in that region. The formation and development of the corner vortices in the upper-inner corner increase the values of the friction factor and Nusselt number in the corresponding region, and decrease those in the other region. In response to this, another peak is formed near the inner wall side. In this flow region, the Nusselt number ratio is higher than the friction factor ratio.

When the flow is in Group two, the disappearance of the buoyancy vortices leads to a sparsely spaced isovels and isotherms along the upper wall. Consequently, a decrease in the friction factor and Nusselt number is observed. With the growth of the corner vortices, this decrease continues from curve 5 to curve 9. The peak,

resulting from the large velocity (temperature) gradient between the high velocity (temperature) core and the upper wall, still exists, but is shifted inwards in response to the inward shift in the location of the high velocity (temperature) core. A further growth of the upper-inner corner vortices increases the values of friction factor and Nusselt number in that region, and decrease those in the other region. The difference in the peak values between the two peaks decreases from curve 5 to curve 9. In this flow region, the Nusselt number ratio is still higher than the friction factor ratio. But, the difference becomes less notable than that in Group one.

When the flow moves to Group three, the appearance of the merging vortices dramatically changes the distributions of the main flow and temperature (Fig.5.4(j)-(l)-(ii)(iii)). The densely spaced isovels and isotherms along the upper wall lead to a high value of the friction factor and the Nusselt number (curves 10-12 in Fig.5.10(b)). The large velocity (temperature) gradient between the high velocity (temperature) core and the upper wall results a peak of the local friction factor (Nusselt number) in that region. As well, the values of the friction factor and the Nusselt number increase with the peak shifting inward from curve 10 to curve 11. In this flow region, the Nusselt number ratio is much higher than the friction factor ratio.

5.3.3 Distributions along the upper half of the outer wall

For the flow in Group one, the buoyancy vortices affect the distributions of the friction factor and the Nusselt number along the outer wall significantly. The densely

distributed isovels and isotherms along the outer wall result in a relative high values of the friction factor and the Nusselt number. A peak in the local friction factor (Nusselt number) appears in the region where a large velocity (temperature) gradient occurs between the high velocity (temperature) core and the outer wall (Fig.5.4(a)-(d)-(ii)(iii)). A relatively low friction factor (Nusselt number) is observed near the center of the outer wall. This results from the inwarsh isovels (isotherms) due to the retreating effect of the buoyancy vortices in that region. The appearance and development of the corner vortices reduce the strength of the buoyancy vortices, causing a decrease in the friction factor and Nusselt number from curve 1 to curve 4. In this flow region, the Nusselt number ratio is much higher than the friction factor ratio.

When the flow moves to Group two, the inwarsh isovels and isotherms disappear near the center of the outer wall because of the disappearance of the buoyancy vortices. The friction factor and the Nusselt number, therefore, increase significantly in that region (curves 5-9 in Fig.5.10(c)). But their values decrease in the other regions due to the decrease in the strength of the secondary flow. The growth of the corner vortices shifts the main velocity (temperature) peak inward, causing a decrease in the friction factor and the Nusselt number from curve 6 to curve 9. In this region, the Nusselt number ratio is still higher than the friction factor ratio although the difference is less notable than that in Group one.

The appearance of the merging vortices near the inner wall results in the quite

uniform and sparsely spaced isovels and isotherms along the outer wall (Fig.5.4(j)-(l)-(ii)(iii)). This induces a low and nearly constant local friction factor (Nusselt number) over a wide region of the outer wall as shown by curves 10-12 in Fig.5.10(c). Only in this region, the friction factor ratio is slightly higher than the Nusselt number ratio.

5.3.4 Mean friction factor and Nusselt number

The mean friction factor and Nusselt number are shown in Fig.5.11 by the solid and dashed lines, respectively. They are presented in the form of $fRc/(fRc)_0$ and Nu/Nu_0 against L_1 at $Dk = 500$, $\sigma = 0.02$, $Pr = 0.7$ and $L_2 = 1$. It is observed that they are affected significantly by the flow transition. The formation and development of the corner vortices and center vortices reduce both the friction factor and Nusselt number with a more significant decrease for the Nusselt number. The friction factor and Nusselt number, however, increase considerably once the flow transitions to the region with merging vortices occur. As well, the increase in Nu is more remarkable. An interesting feature about the friction factor and the Nusselt number is that the Nusselt number ratio is higher than the friction factor ratio, and the difference becomes more appreciable as the flow moves away from the region with secondary flow of multi-pair of counter-rotating vortices.

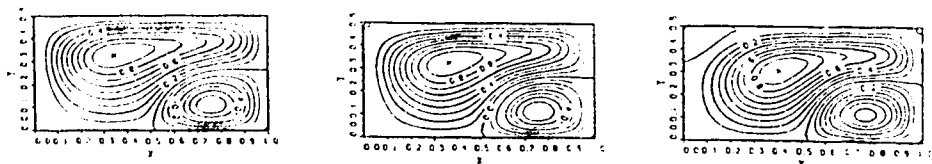
5.4 Concluding Remarks

The problem studied in Chapter 4 has been extended to the case of negative rotation at relatively high Dean numbers. Several phenomena, hitherto unknown, have been revealed in the present study. A one-pair vortex flow with an ageostrophic and virtually inviscid core exists between a multiple-vortex flow and two-pair vortex flow with the presence of the Coriolis vortices near the side of the inner wall. Its circulating direction is opposite to that of one-pair ageostrophic vortex flow found in Chapter 4. When the channel rotates in the negative direction, the inward Coriolis force can cause the secondary flow to reverse its direction, and the Coriolis vortices to appear near the center of the inner wall with an counterclockwise direction of the circulation. The flow reversal is found to occur after passing through a multi-pair vortex flow regime where overall, the centrifugal, Coriolis and buoyancy forces just neutralize each other in the cross-plane. This multi-pair vortex flow differs from that found in Chapter 4 mainly in its coexistence of the Dean-vortices, buoyancy-vortices or Coriolis-vortices. When the Coriolis vortices appear near the inner side, the inner wall becomes the high pressure side. This is different from the case of the buoyancy-vortices appearing near the inner wall. As well, the merging vortices are found to appear only when the buoyancy force is present.

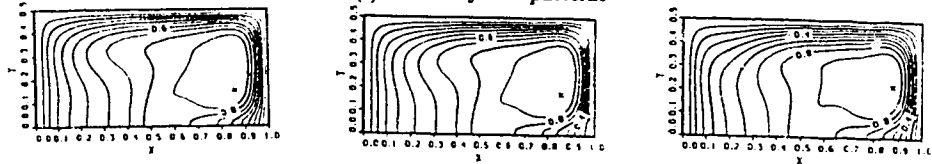
Upon increasing the Coriolis force, we fail to observe the disappearance of the Coriolis vortices for both positive and negative cases at higher Dean number. This is believed to be caused by the possible physical instability of the problem, and merits

further investigation by using an unsteady, three-dimensional analysis.

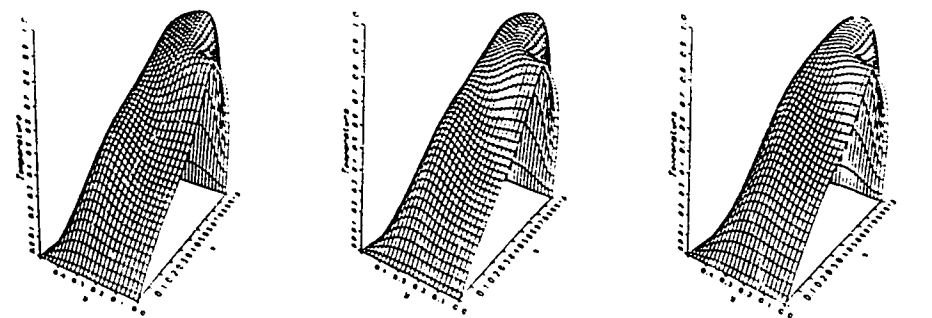
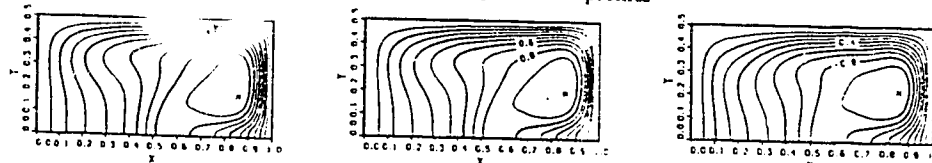
The flow transition changes the distributions of the main flow and temperature. They affect both the local and mean values for friction resistance and convective heat transfer between the fluid and the wall significantly.



(i) Secondary flow patterns



(ii) Axial velocity isopleths and profiles

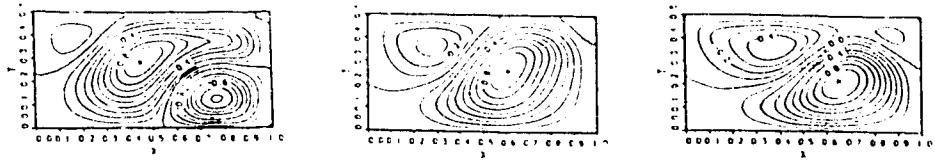


(iii) Isotherms and temperature profiles

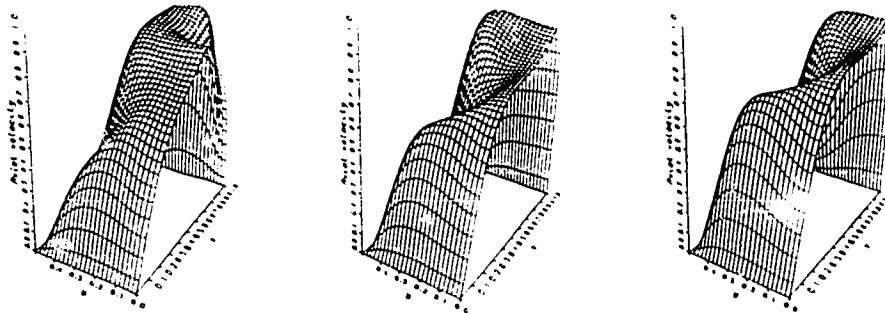
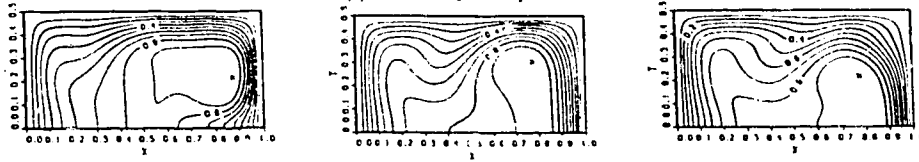
(a) $L_1 = 0, Re = 1801$
(11.805; 0.0297; 76.23)

(b) $L_1 = -0.1, Re = 1806$
(11.158; 0.0307; 81.50)

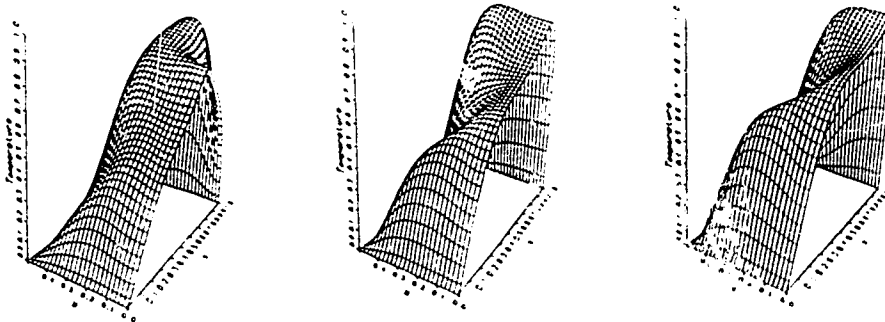
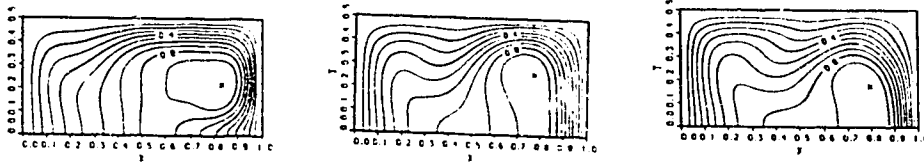
(c) $L_1 = -0.3, Re = 2030$
(9.574; 0.0336; 97.73)



(i) Secondary flow patterns



(ii) Axial velocity isopleths and profiles:



(iii) Isotherms and temperature profiles:

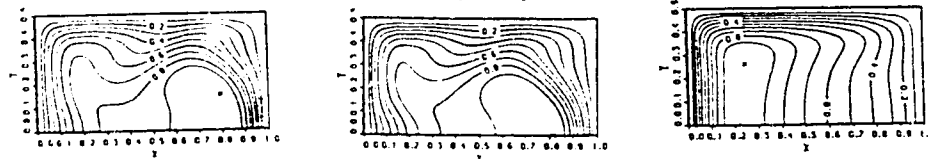
(d) $L_1 = -0.4, Re = 2145$
(8.401;0.0356;110.37)

(e) $L_1 = -0.5, Re = 2329$
(10.038;0.0400;135.10)

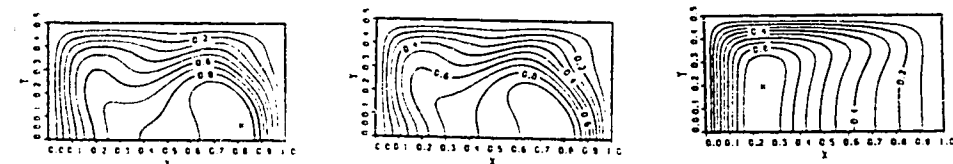
(f) $L_1 = -0.6, Re = 2456$
(9.994;0.0420;151.60)



(i) Secondary flow patterns



(ii) Axial velocity isopleths and profiles



(iii) Isotherms and temperature profiles

(g) $L_1 = -0.65, Re = 2541$
(9.744; 0.0441; 169.37)

(h) $L_1 = -0.7, Re = 2612$
(8.846; 0.0466; 188.76)

(i) $L_1 = -0.75, Re = 2143$
(8.261; 0.0394; 122.64)

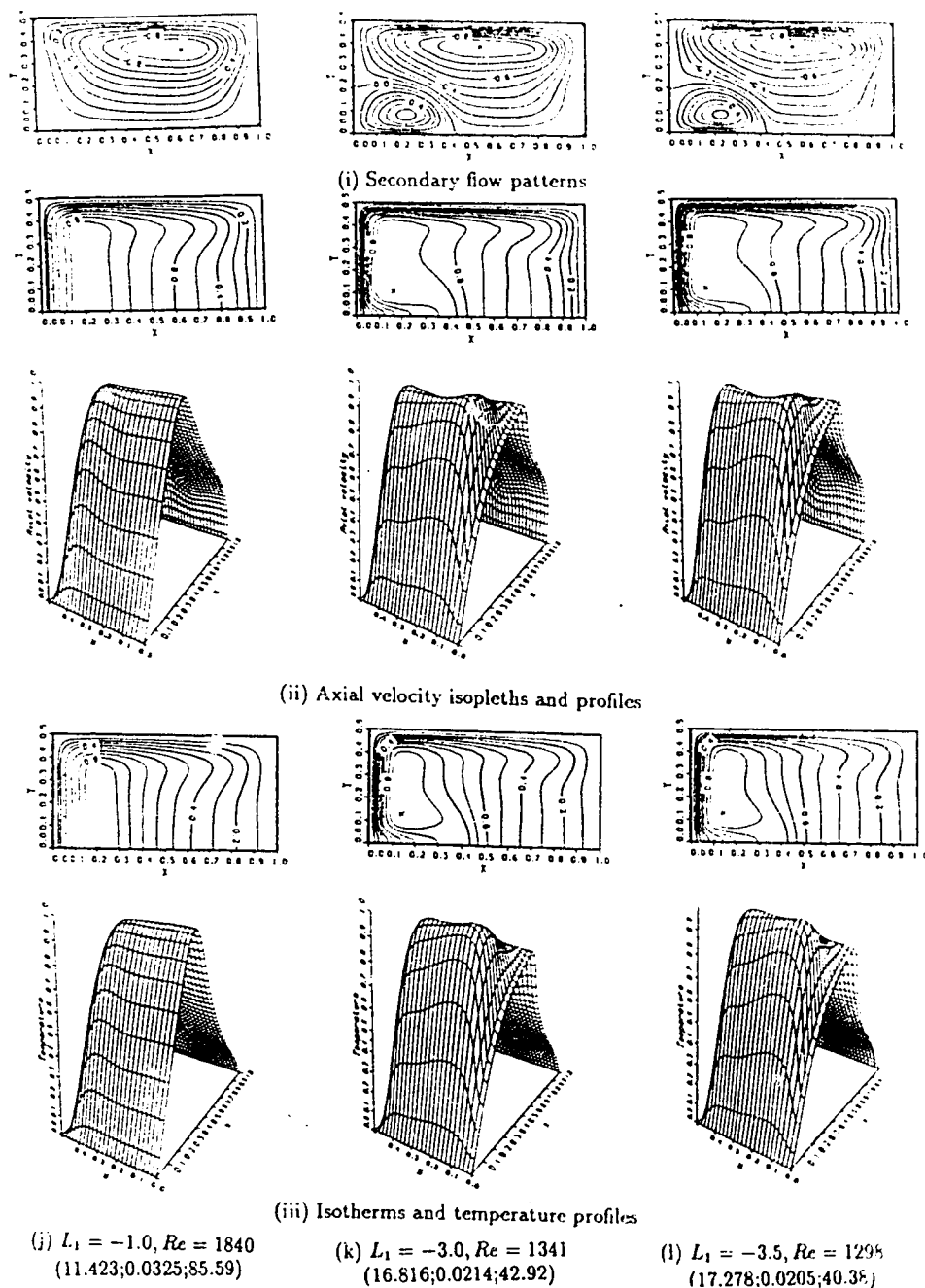
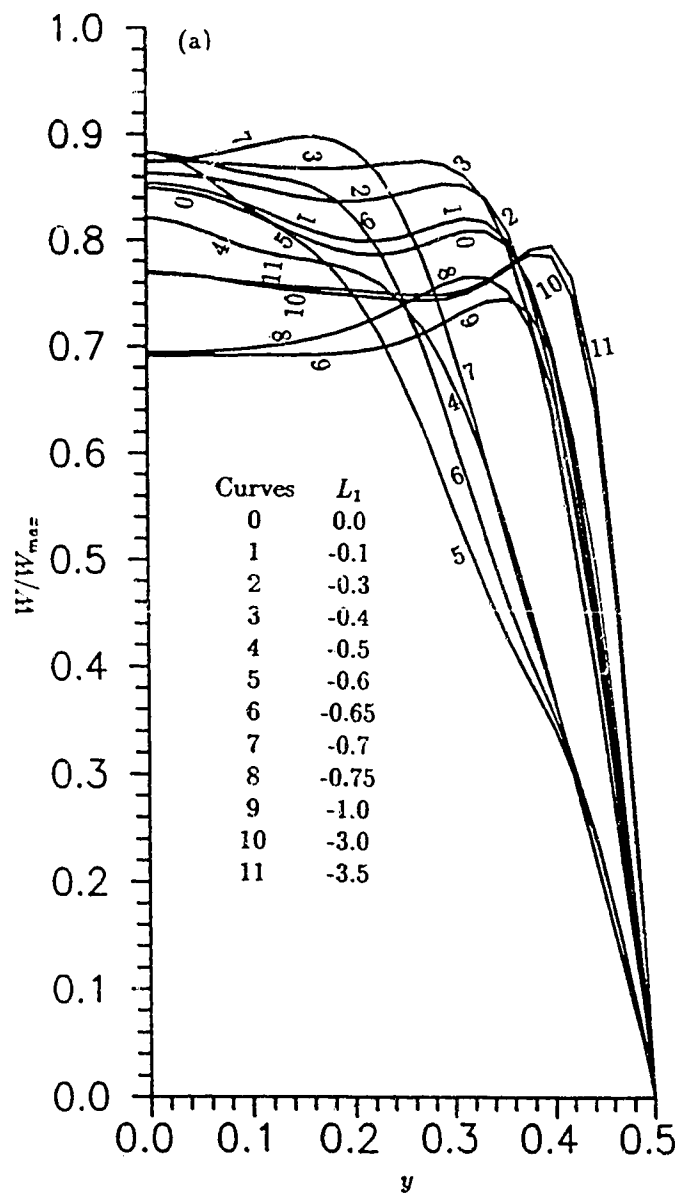
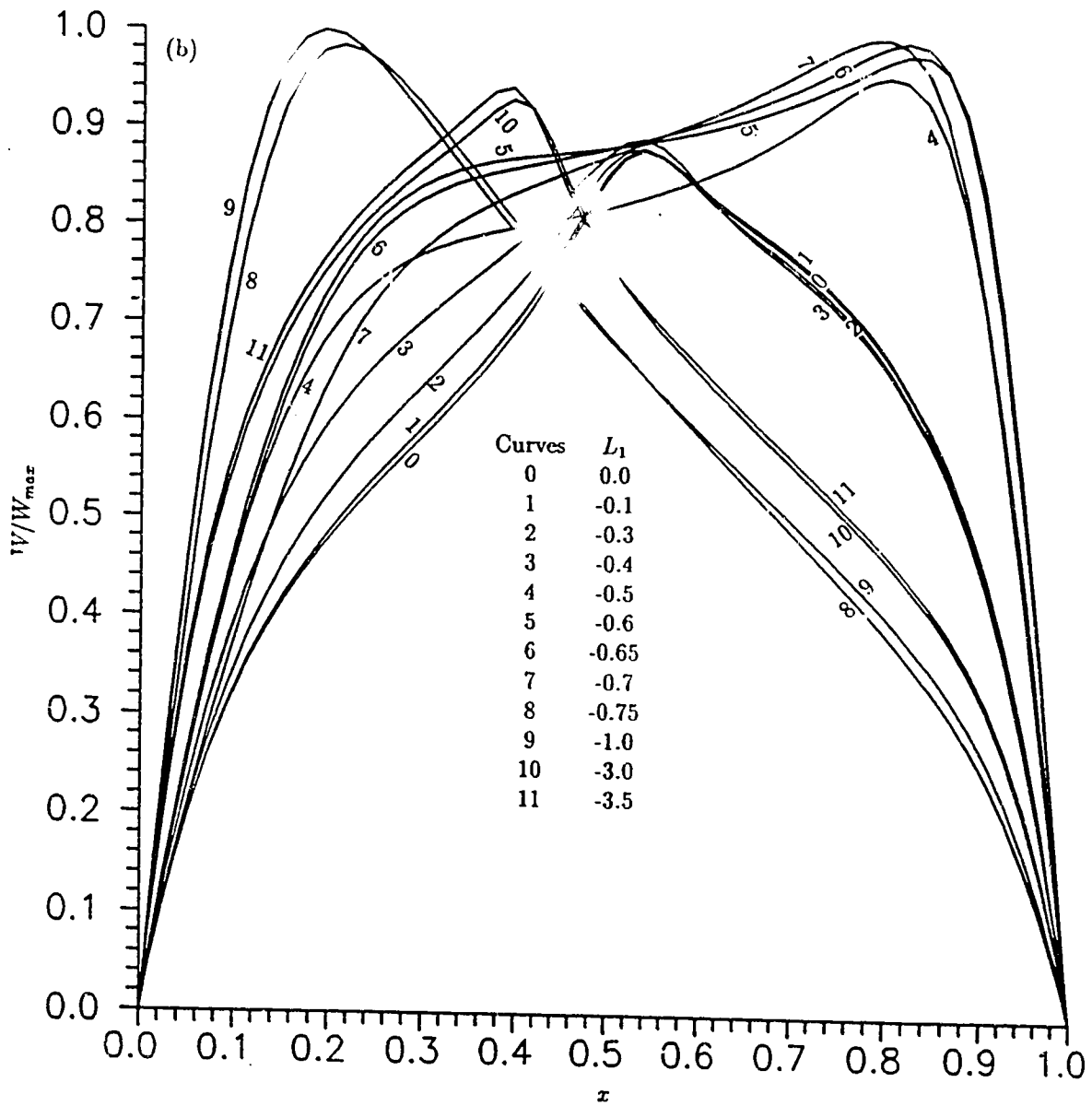


Figure 5.1. Flow transitions and temperature distributions at $\gamma = 1, Dk = 500, \sigma = 0.02, Pr = 0.7$ and $L_2 = 0$. (Three values for each case are the maxima of the stream function, main velocity and temperature)



(a) along the vertical centreline of the channel

Figure 5.2. Main velocity distributions at $\gamma = 1$, $Dk = 500$, $\sigma = 0.02$, $Pr = 0.7$ and $L_2 = 0$: (a) along the vertical centreline of the channel; (b) along the horizontal centreline of the channel



(b) along the horizontal centreline of the channel

Figure 5.2. Main velocity distributions at $\gamma = 1, Dk = 500, \sigma = 0.02, Pr = 0.7$ and $L_2 = 0$: (a) along the vertical centreline of the channel; (b) along the horizontal centreline of the channel

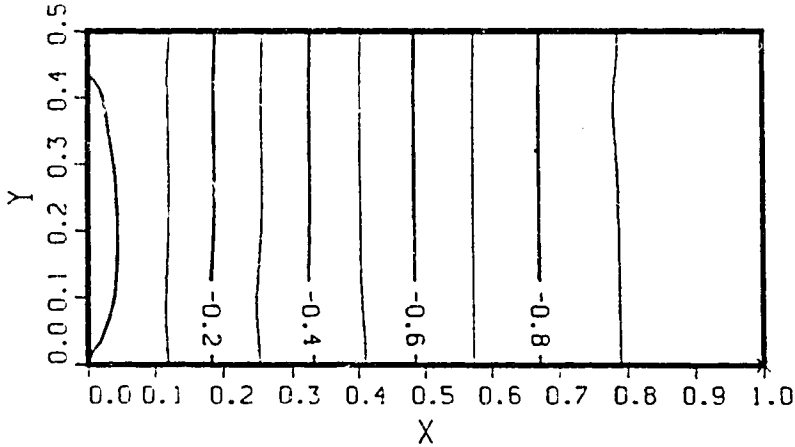
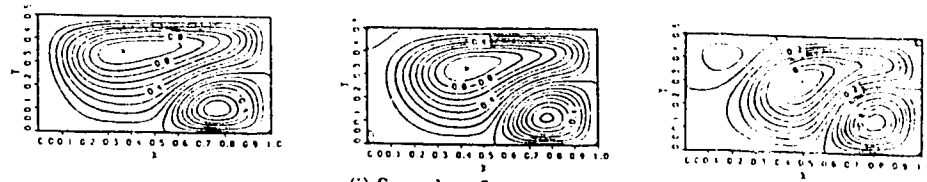
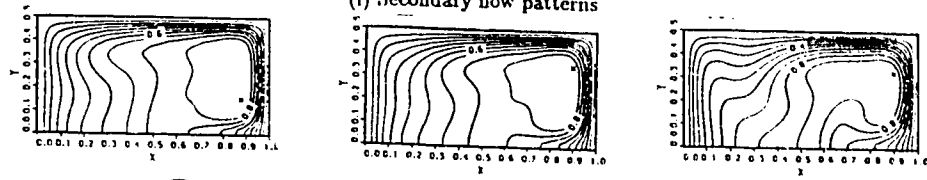


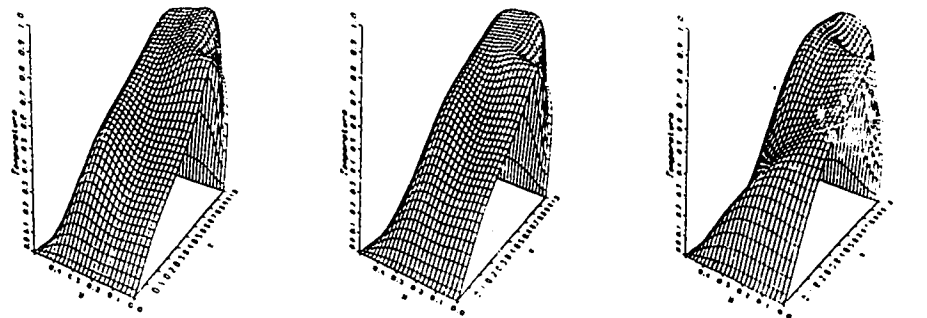
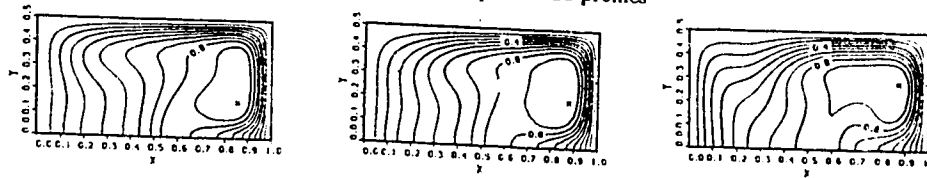
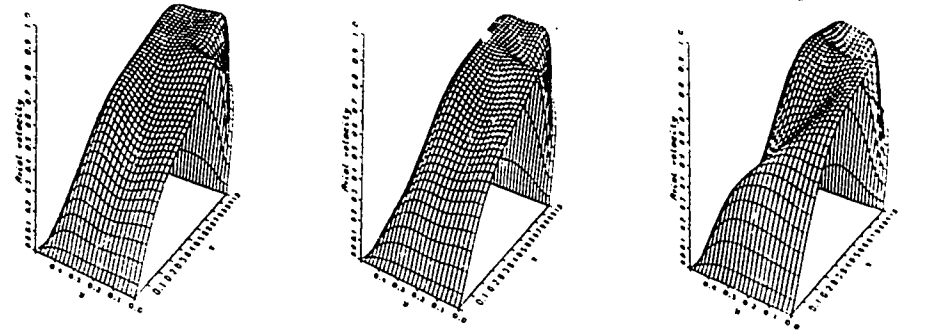
Figure 5.3. Isopiestic contour at $\gamma = 1, Dk = 500, \sigma = 0.02, Pr = 0.7, L_1 = -3.5$ and $L_2 = 0$



(i) Secondary flow patterns



(ii) Axial velocity isopleths and profiles



(iii) Isotherms and temperature profiles

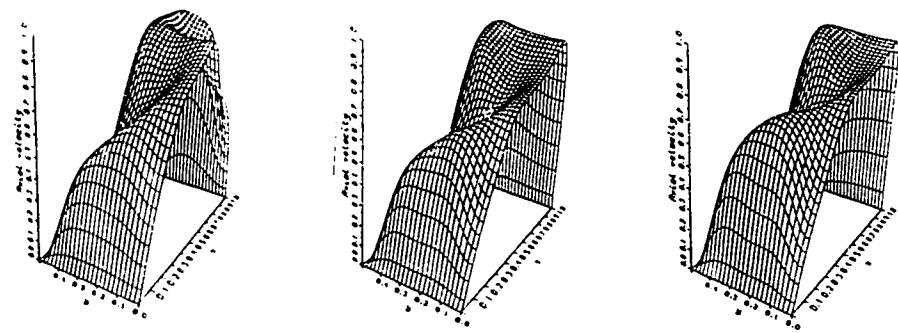
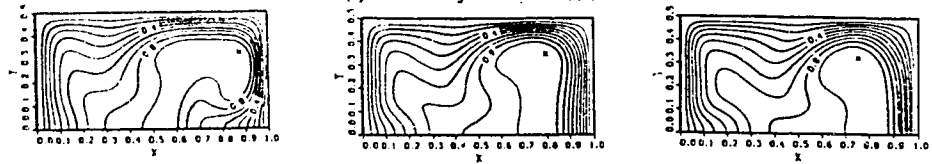
(a) $L_1 = -0.5, Re = 1599$
(15.338;0.0255;56.45)

(b) $L_1 = -1.0, Re = 1717$
(14.151;0.0276;64.60)

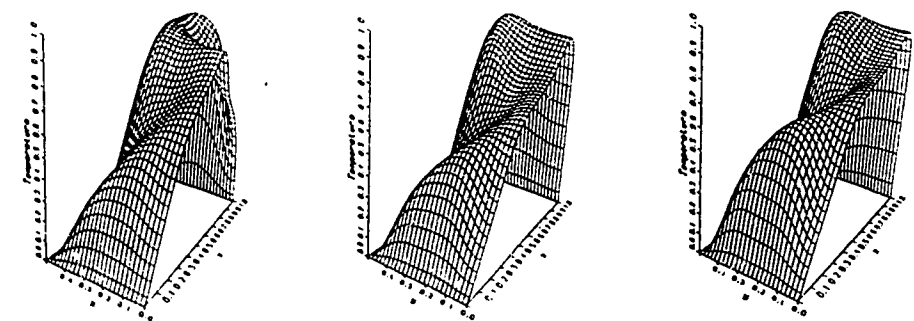
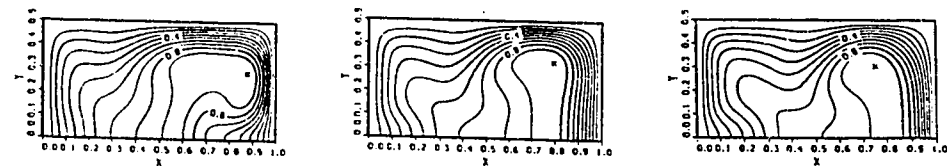
(c) $L_1 = -1.5, Re = 1865$
(12.200;0.0300;77.38)



(i) Secondary flow patterns



(ii) Axial velocity isopleths and profiles

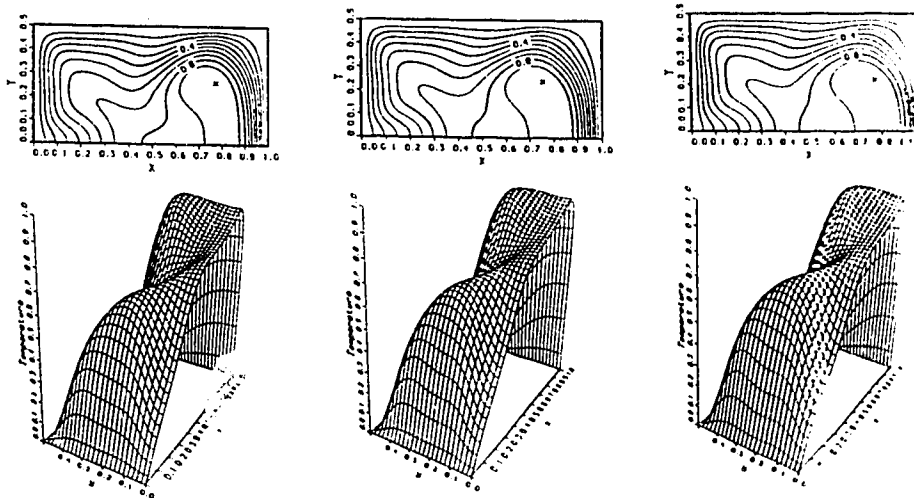
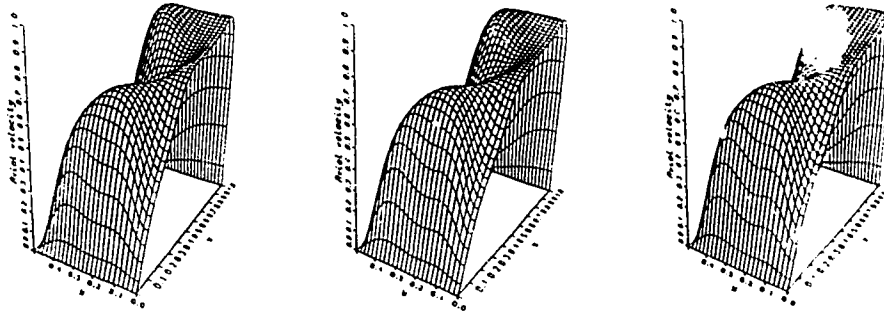
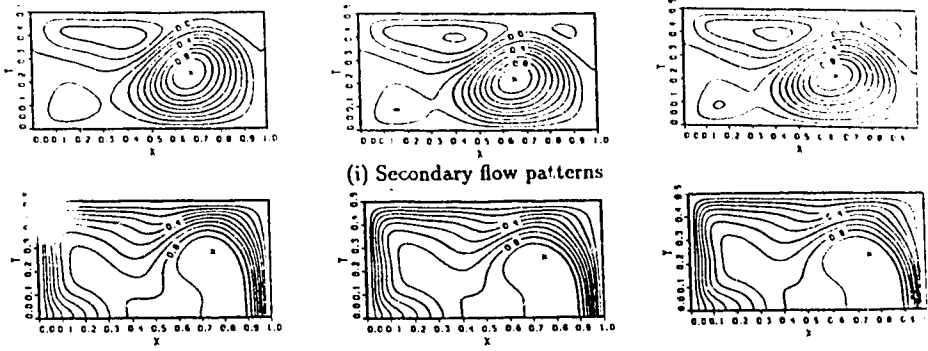


(iii) Isotherms and temperature profiles

(d) $L_1 = -1.65, Re = 1931$
(11.298; 0.0309; 82.98)

(e) $L_1 = -1.85, Re = 2111$
(13.694; 0.0356; 106.83)

(f) $L_1 = -2.0, Re = 2147$
(14.550; 0.0359; 110.73)



(g) $L_1 = -2.1, Re = 2183$
(14.740;0.0367;115.49)

(h) $L_1 = -2.25, Re = 2264$
(14.175;0.0384;127.44)

(i) $L_1 = -2.3, Re = 2294$
(13.861;0.0391;132.00)

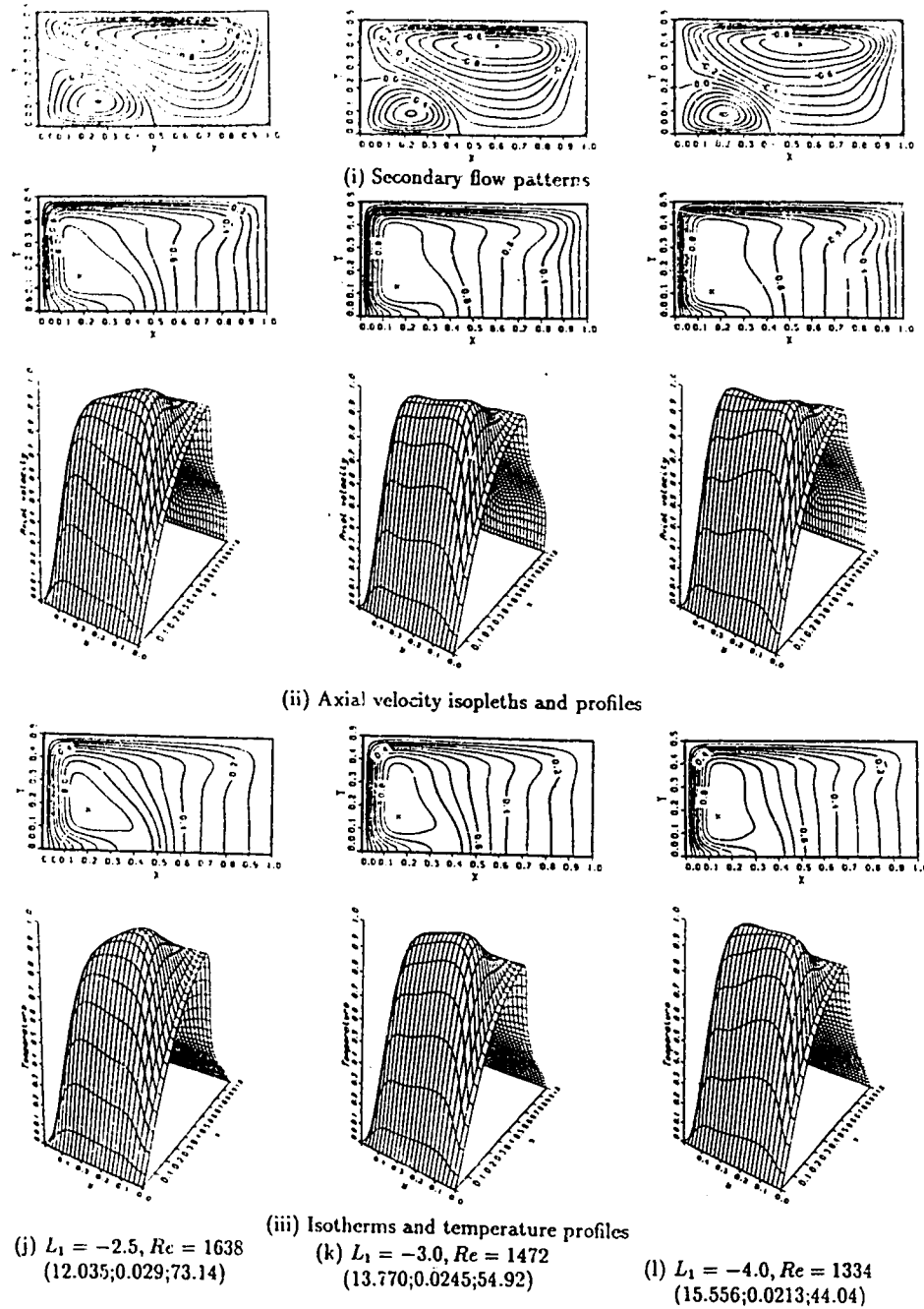
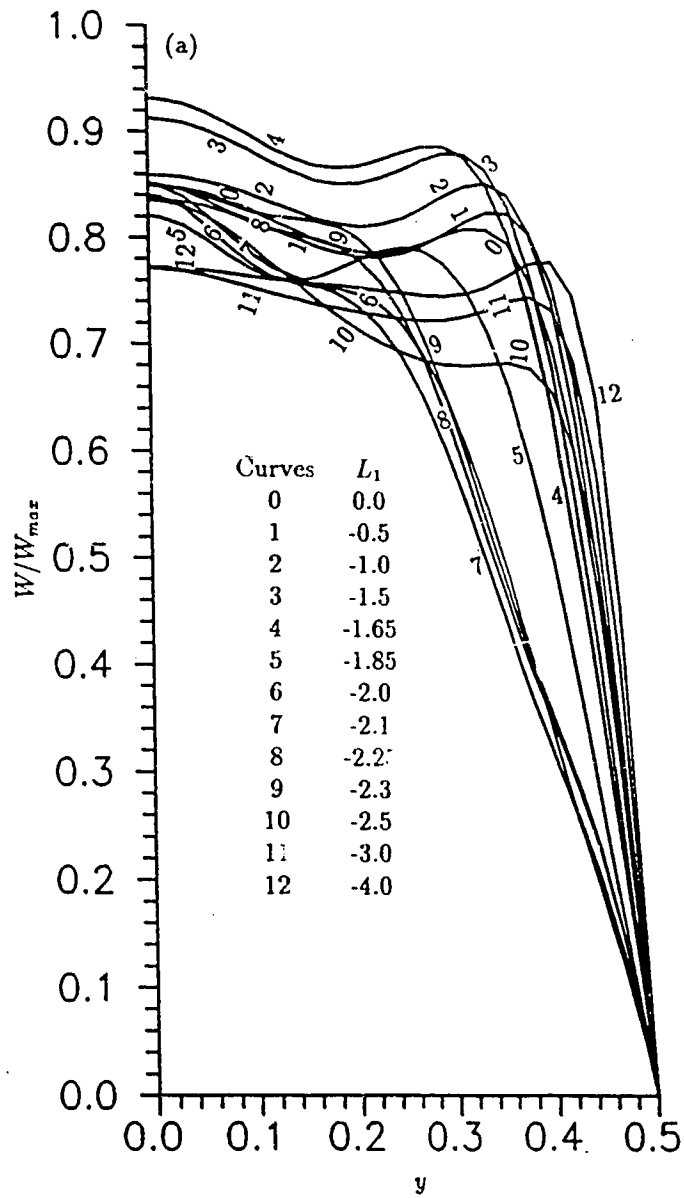
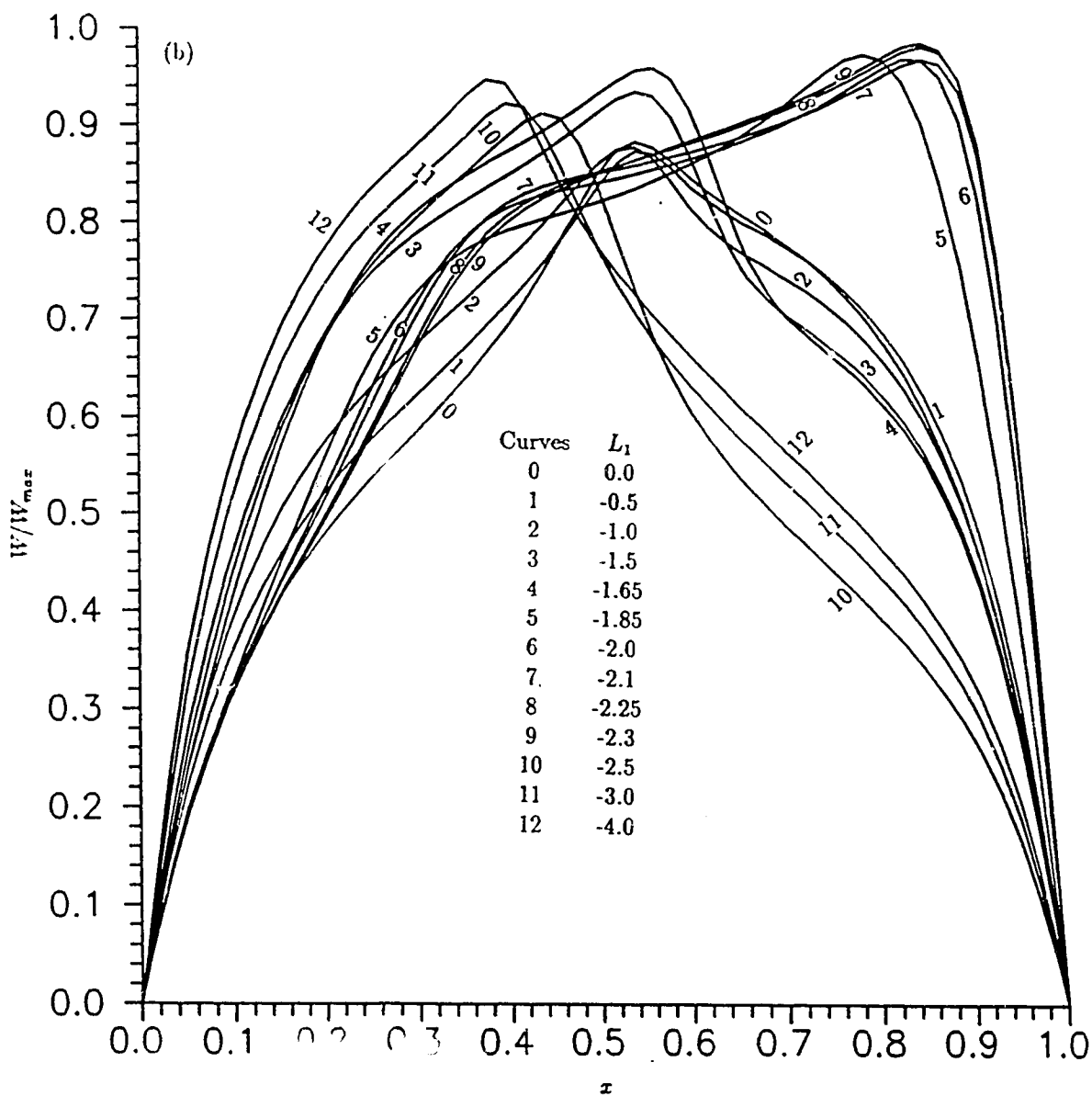


Figure 5.4. Flow transitions and temperature distributions at $\gamma = 1, Dk = 500, \sigma = 0.02, Pr = 0.7$ and $L_2 = 1$. (Three values for each case are the maxima of the stream function, main velocity and temperature)



(a) along the vertical centreline of the channel

Figure 5.5. Main velocity distributions at $\gamma = 1, Dk = 500, \sigma = 0.02, Pr = 0.7$ and $L_2 = 1$: (a) along the vertical centreline of the channel; (b) along the horizontal centreline of the channel



(b) along the horizontal centreline of the channel

Figure 5.5. Main velocity distributions at $\gamma = 1, Dk = 500, \sigma = 0.02, Pr = 0.7$ and $L_2 = 1$: (a) along the vertical centreline of the channel; (b) along the horizontal centreline of the channel

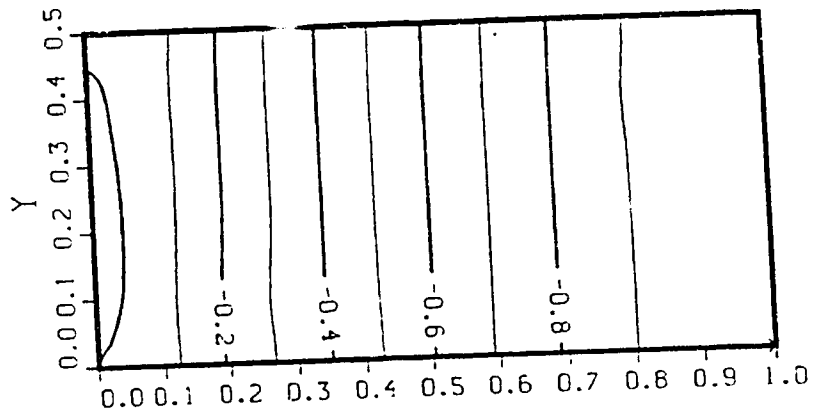
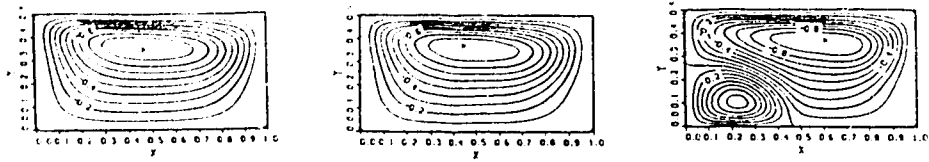
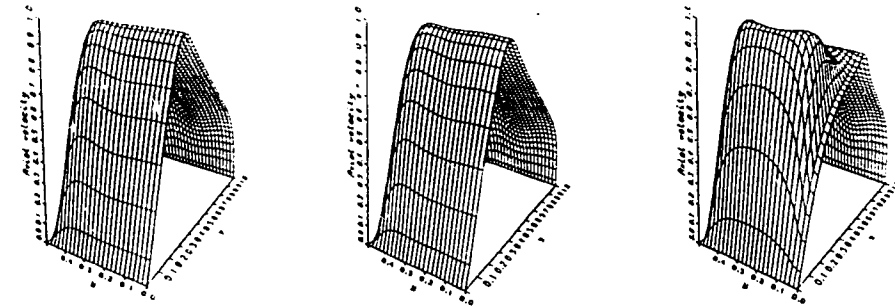
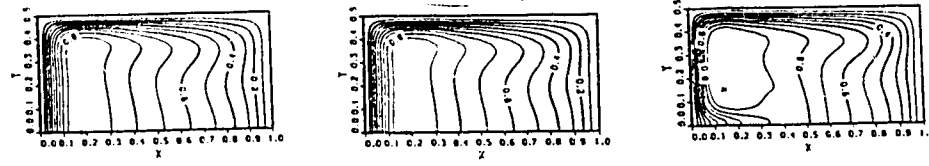


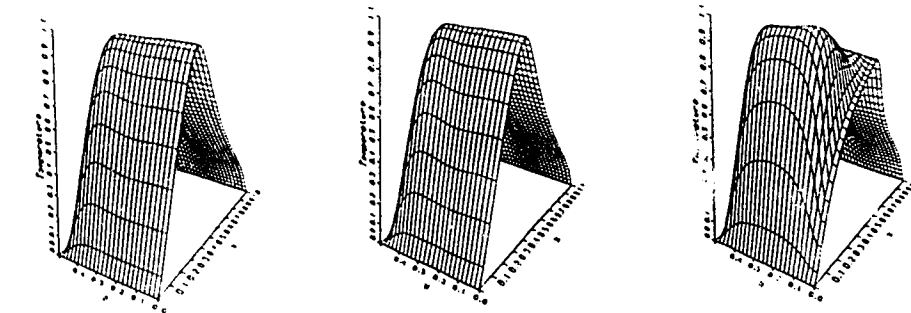
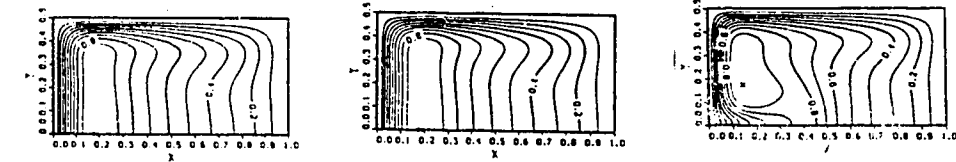
Figure 5.6. Isopiestic contour at $\gamma = 1$, $Dk = 500$, $\sigma = 0.02$, $Pr = 0.7$, $L_1 = -4.0$ and $L_2 = 1$



(i) Secondary flow patterns



(ii) Axial velocity isopleths and profiles



(iii) Isotherms and temperature profiles

(a) $L_1 = 0, Re = 1792$
(13.723;0.0311;75.91)

(b) $L_1 = -0.02, Re = 1785$
(13.773;0.0310;75.32)

(c) $L_1 = -0.5, Re = 1540$
(15.001;0.0247;53.25)

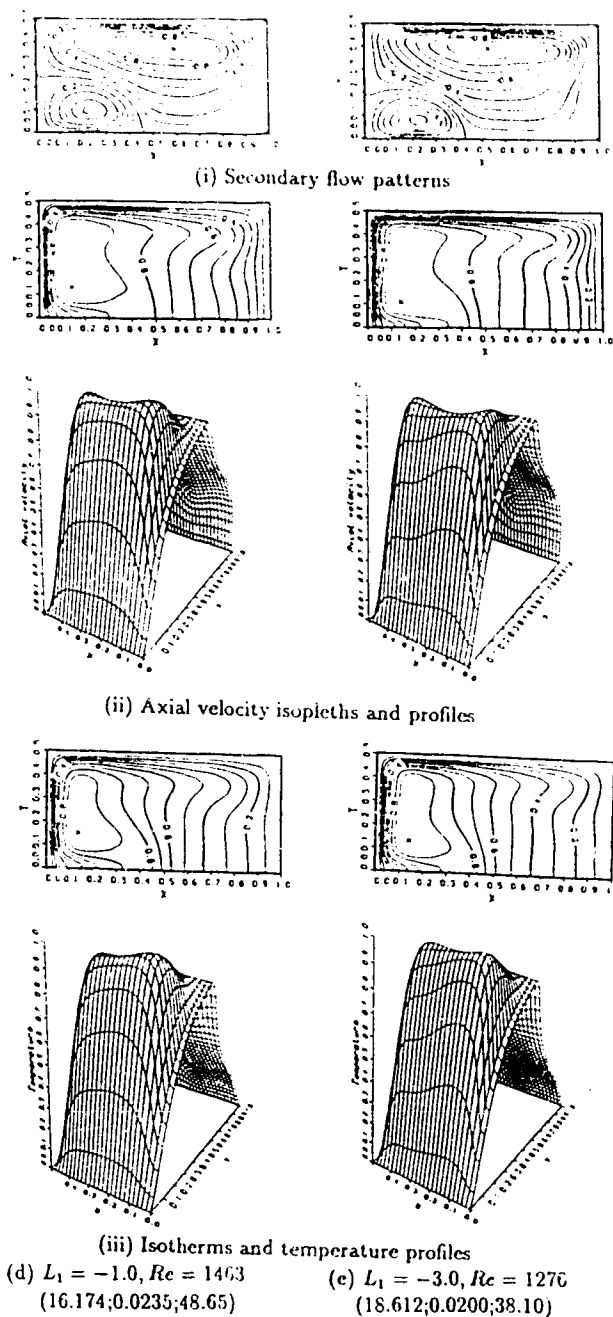
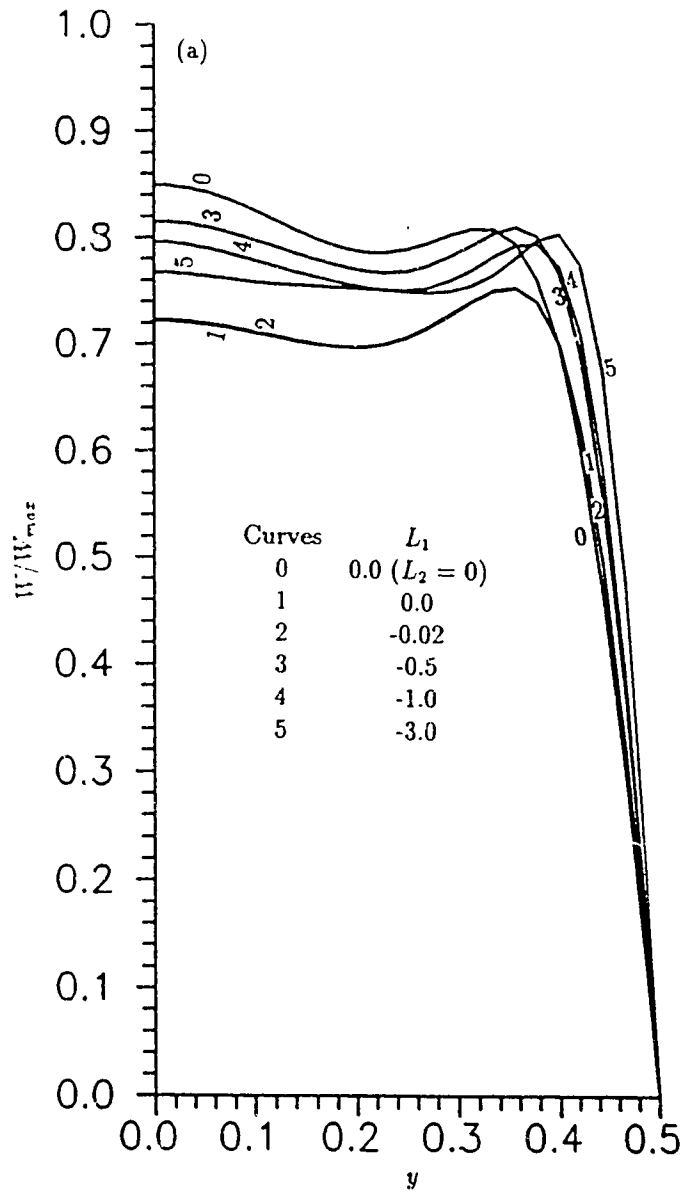
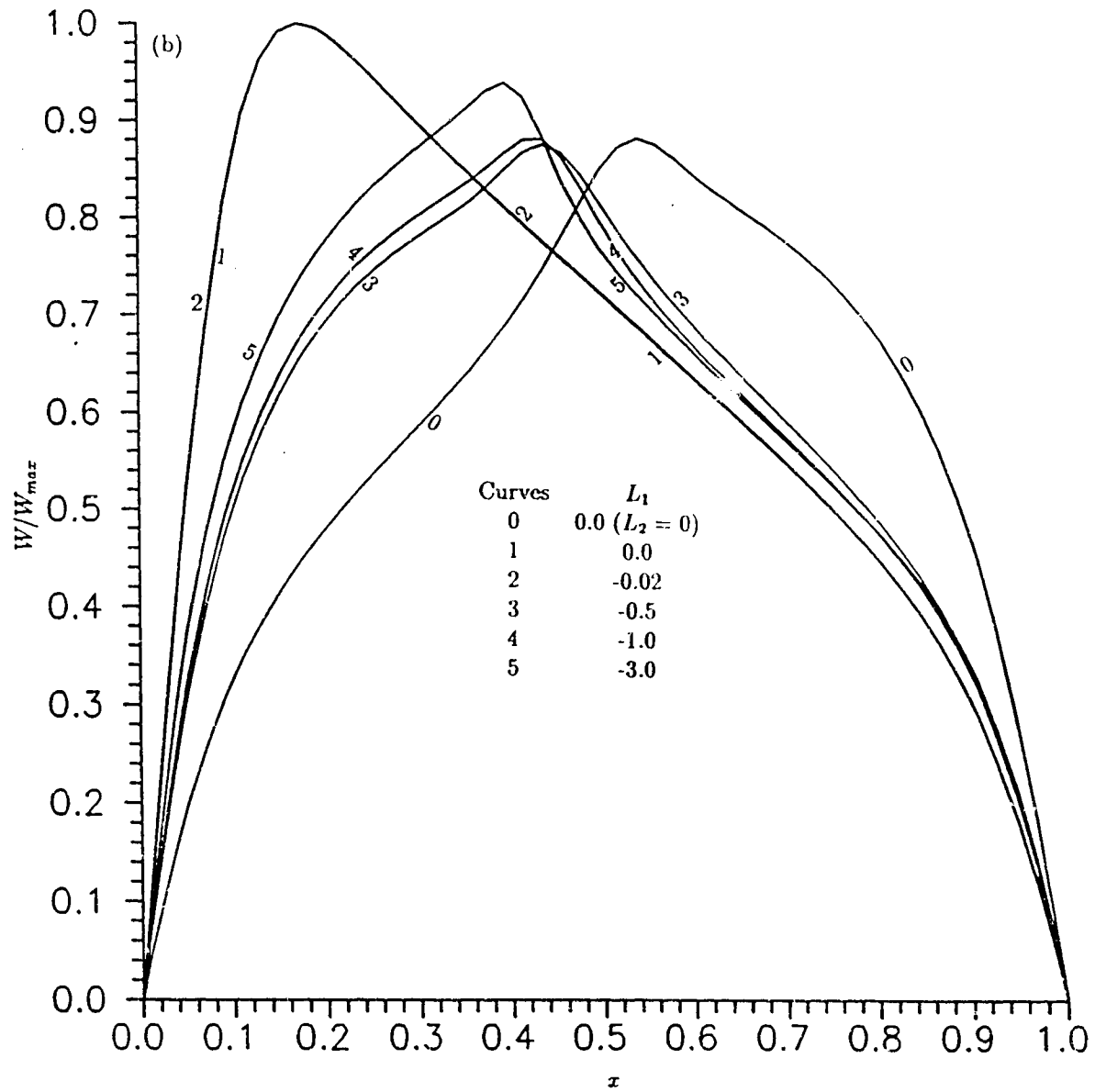


Figure 5.7. Flow transitions and temperature distributions at $\gamma = 1, Dk = 500, \sigma = 0.02, Pr = 0.7$ and $L_2 = -1$. (Three values for each case are the maxima of the stream function, main velocity and temperature)



(a) along the vertical centreline of the channel

Figure 5.8. Main velocity distributions at $\gamma = 1$, $Dk = 500$, $\sigma = 0.02$, $Pr = 0.7$ and $L_2 = -1$: (a) along the vertical centreline of the channel; (b) along the horizontal centreline of the channel



(b) along the horizontal centreline of the channel

Figure 5.8. Main velocity distributions at $\gamma = 1$, $Dk = 500$, $\sigma = 0.02$, $Pr = 0.7$ and $L_2 = -1$: (a) along the vertical centreline of the channel; (b) along the horizontal centreline of the channel

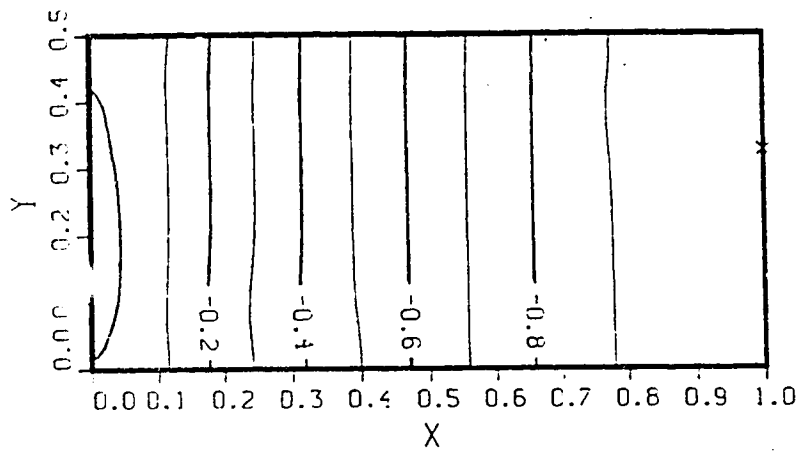


Figure 5.9. Isopiestic contour at $\gamma = 1$, $Dk = 500$, $\sigma = 0.02$, $Pr = 0.7$, $L_1 = -3.0$ and $L_2 = -1$

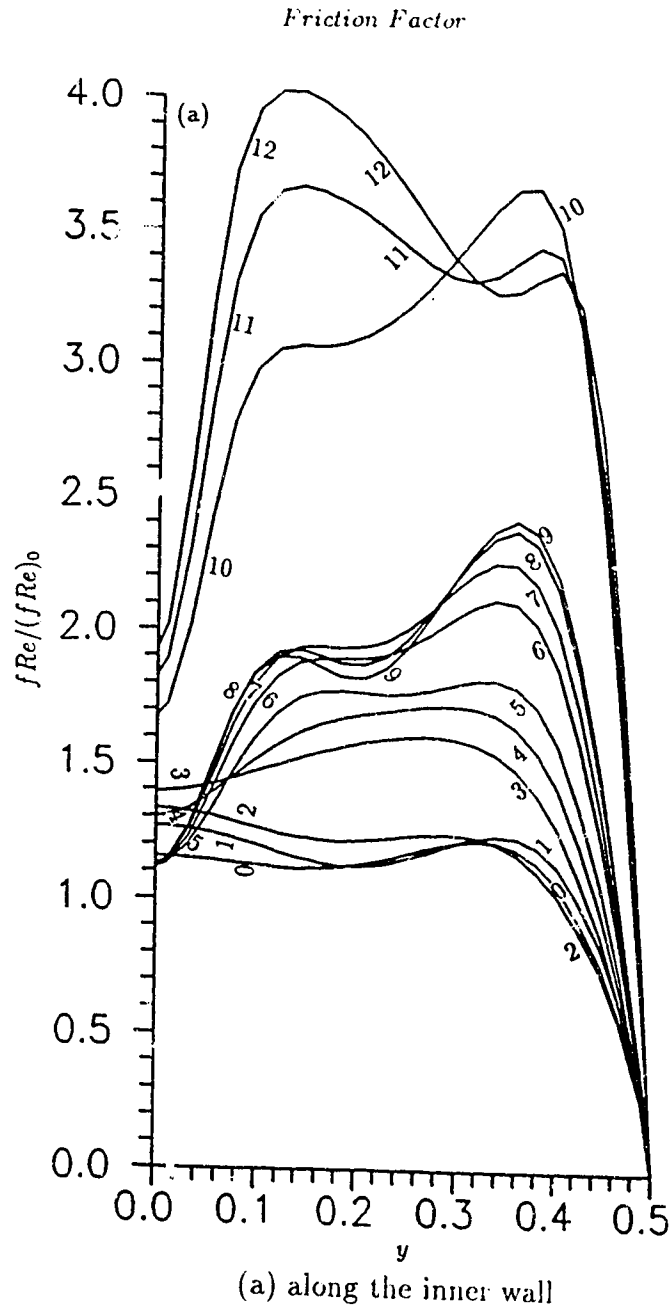


Figure 5.10. Distributions of friction factor and Nusselt number at $\gamma = 1$, $Dk = 500$, $\sigma = 0.02$, $Pr = 0.7$ and $L_2 = 1$ (Curves 1–12 correspond to $L_1 = -0.5, -1.0, -1.5, -1.65, -1.85, -2.0, -2.1, -2.25, -2.3, -2.5, -3.0$ and -4.0 . Curve 0 is for the case of $L_1 = L_2 = 0$.) (a) along the inner wall; (b) along the upper wall; (c) along the outer wall

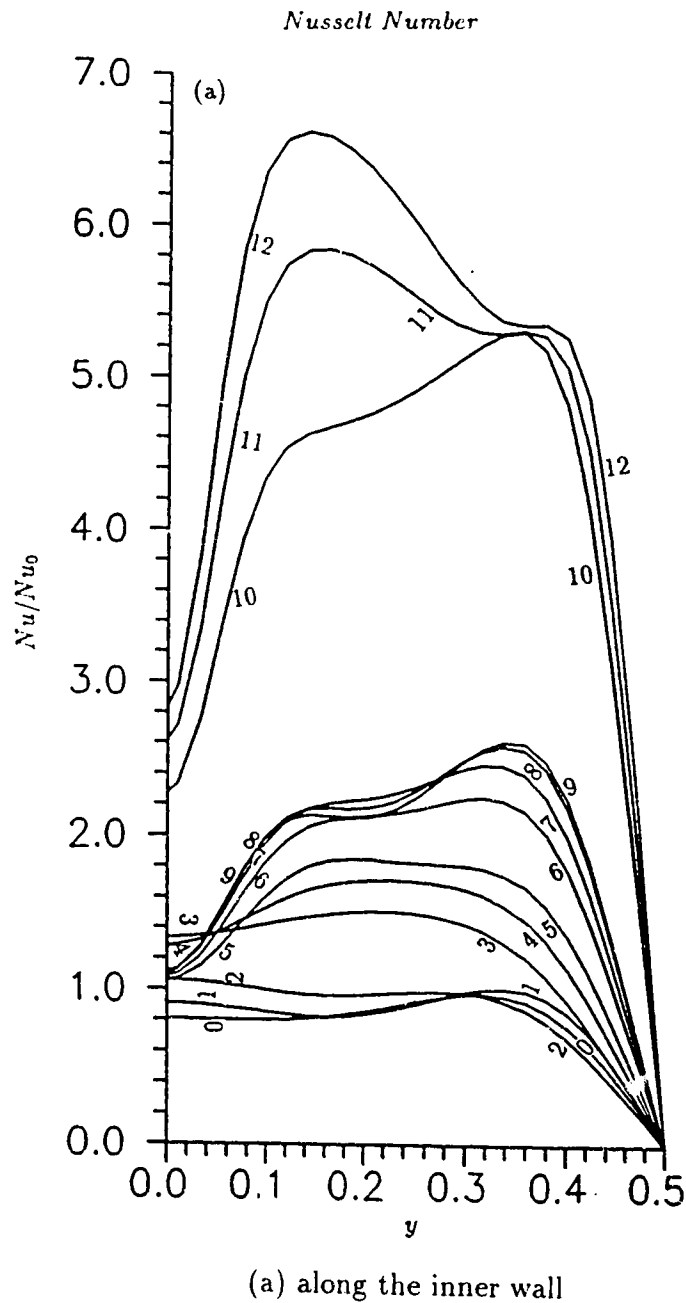
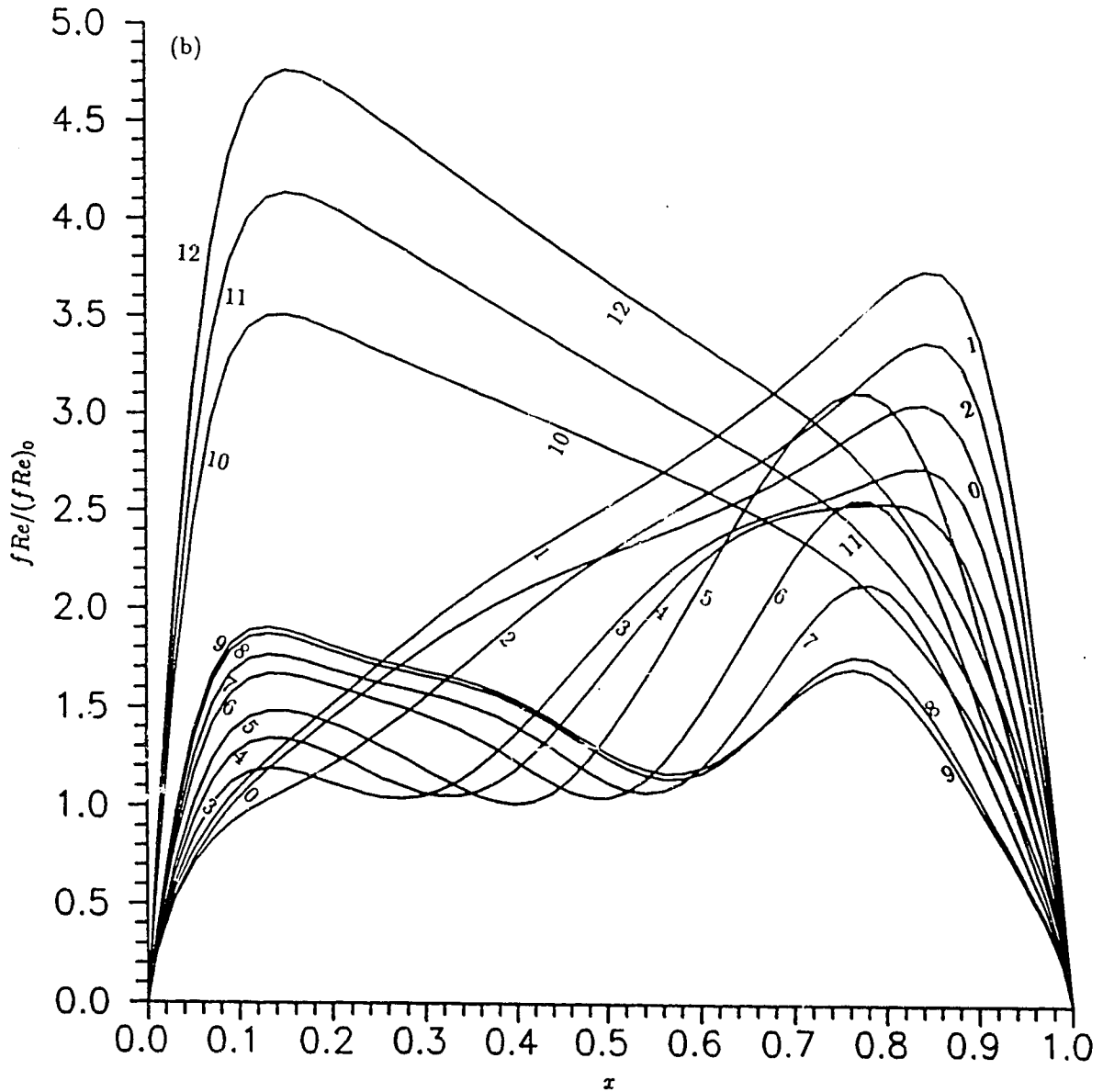


Figure 5.10. Distributions of friction factor and Nusselt number at $\gamma = 1$, $Dk = 500$, $\sigma = 0.02$, $Pr = 0.7$ and $L_2 = 1$ (Curves 1–12 correspond to $L_1 = -0.5, -1.0, -1.5, -1.65, -1.85, -2.0, -2.1, -2.25, -2.3, -2.5, -3.0$ and -4.0 . Curve 0 is for the case of $L_1 = L_2 = 0$.) (a) along the inner wall; (b) along the upper wall; (c) along the outer wall

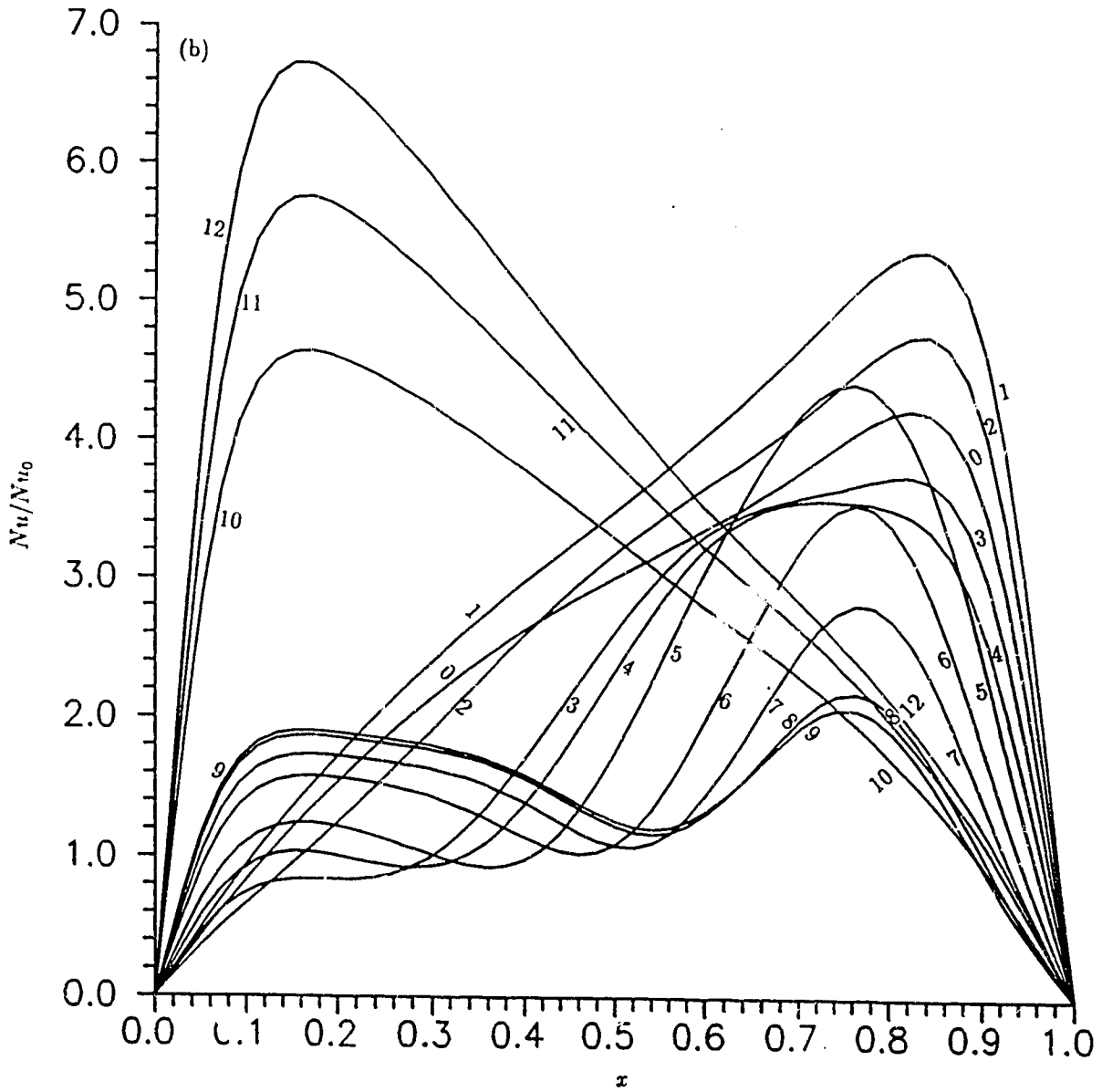
Friction Factor



(b) along the upper wall

Figure 5.10. Distributions of friction factor and Nusselt number at $\gamma = 1$, $Dk = 500$, $\sigma = 0.02$, $Pr = 0.7$ and $L_2 = 1$ (Curves 1–12 correspond to $L_1 = -0.5, -1.0, -1.5, -1.65, -1.85, -2.0, -2.1, -2.25, -2.3, -2.5, -3.0$ and -4.0 . Curve 0 is for the case of $L_1 = L_2 = 0$.) (a) along the inner wall; (b) along the upper wall; (c) along the outer wall

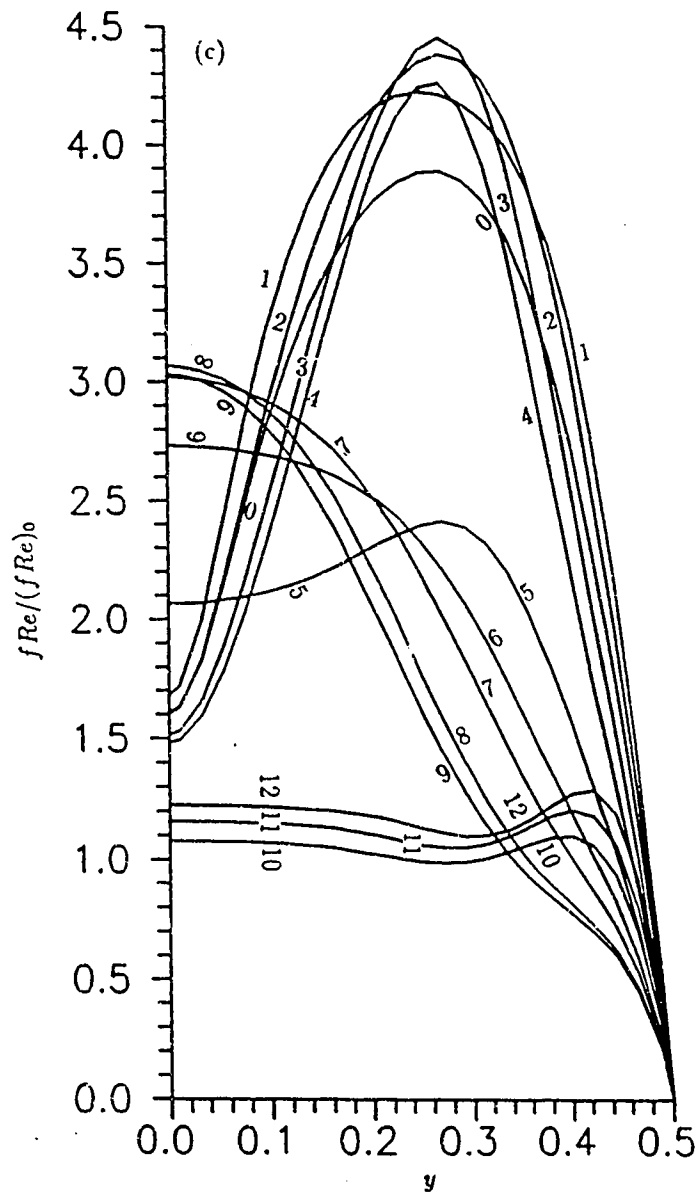
Nusselt Number



(b) along the upper wall

Figure 5.10. Distributions of friction factor and Nusselt number at $\gamma = 1, Dk = 500, \sigma = 0.02, Pr = 0.7$ and $L_2 = 1$ (Curves 1–12 correspond to $L_1 = -0.5, -1.0, -1.5, -1.65, -1.85, -2.0, -2.1, -2.25, -2.3, -2.5, -3.0$ and -4.0 . Curve 0 is for the case of $L_1 = L_2 = 0$.) (a) along the inner wall; (b) along the upper wall; (c) along the outer wall

Friction Factor



(c) along the outer wall

Figure 5.10. Distributions of friction factor and Nusselt number at $\gamma = 1$, $Dk = 500$, $\sigma = 0.02$, $Pr = 0.7$ and $L_2 = 1$ (Curves 1–12 correspond to $L_1 = -0.5, -1.0, -1.5, -1.65, -1.85, -2.0, -2.1, -2.25, -2.3, -2.5, -3.0$ and -4.0 . Curve 0 is for the case of $L_1 = L_2 = 0$.) (a) along the inner wall; (b) along the upper wall; (c) along the outer wall

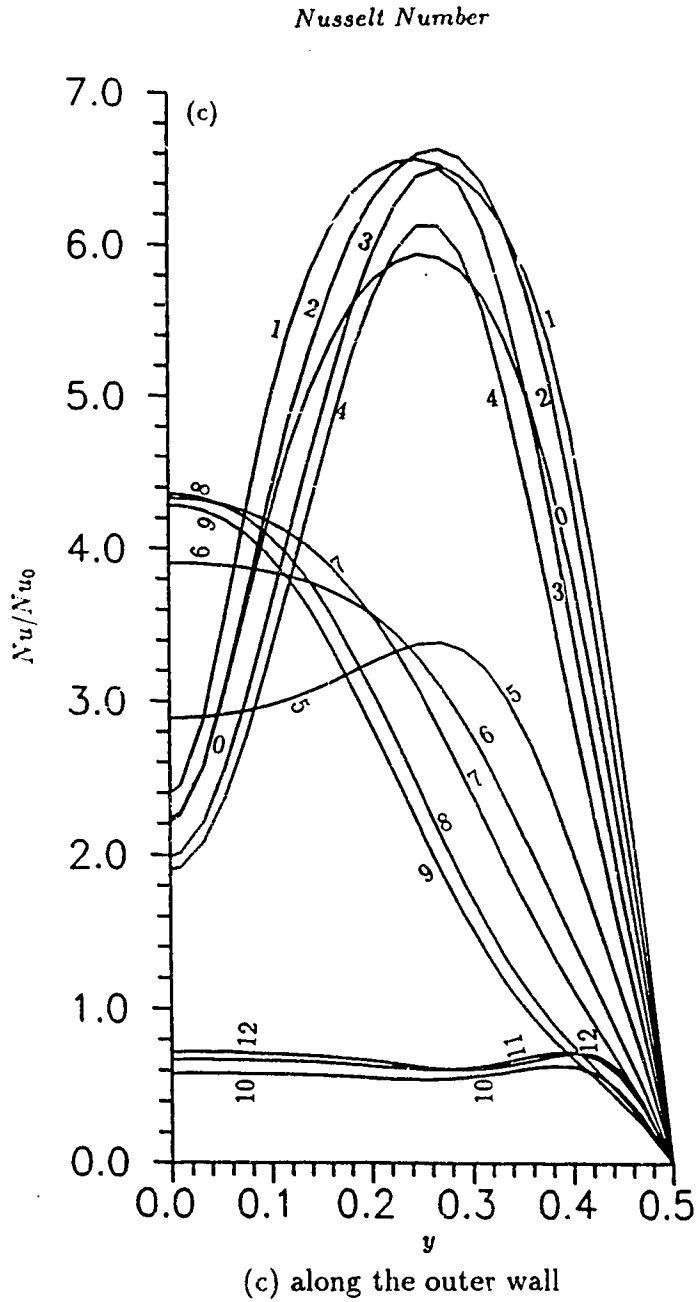


Figure 5.10. Distributions of friction factor and Nusselt number at $\gamma = 1, Dk = 500, \sigma = 0.02, Pr = 0.7$ and $L_2 = 1$ (Curves 1–12 correspond to $L_1 = -0.5, -1.0, -1.5, -1.65, -1.85, -2.0, -2.1, -2.25, -2.3, -2.5, -3.0$ and -4.0 . Curve 0 is for the case of $L_1 = L_2 = 0$.) (a) along the inner wall; (b) along the upper wall; (c) along the outer wall

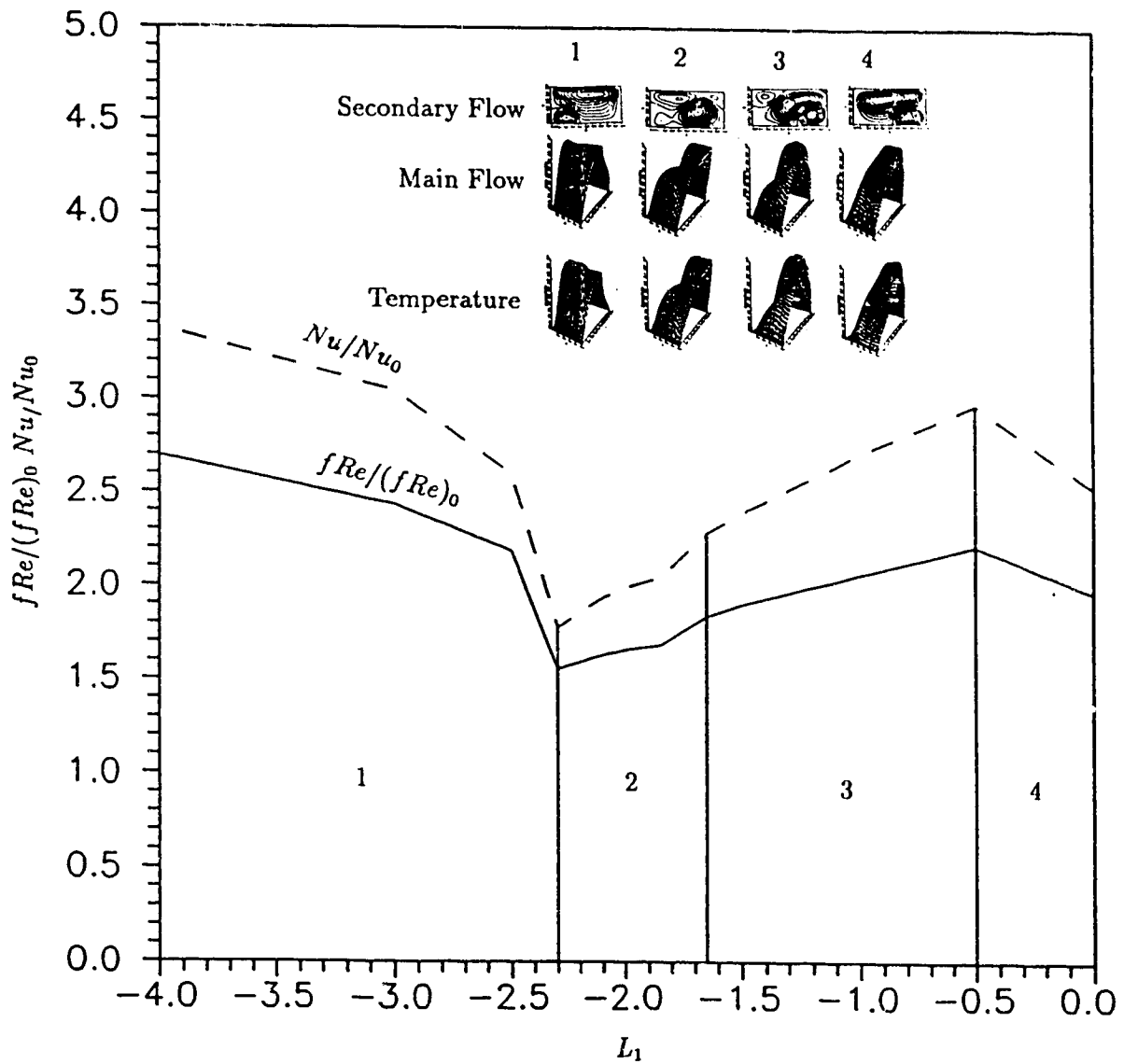


Figure 5.11. Mean friction factor and Nusselt number at $\gamma = 1$, $Dk = 500$, $\sigma = 0.02$, $Pr = 0.7$ and $L_2 = 1$

References

- [1] Alfredsson, P.A. & Persson, H. 1989 Instabilities in channel flow with system rotation. *J. Fluid Mech.* **202**, 543-557.
- [2] Cheng, K.C., Lin, R.C. & Ou, J.W. 1976 Fully developed laminar flow in curved rectangular channels. *Trans. ASME: J. Fluids Eng.* **98**, 41-48.
- [3] Cheng, K.C., Nakayama, J. & Akiyama, M. 1979 Effect of finite and infinite aspect ratios on flow patterns in curved rectangular channels. In *Flow Visualization* (T.Asanuma, ed.), 181-186. Hemisphere.
- [4] Finlay, W.H. 1990 Transition to oscillatory motion in rotating channel flow. *J. Fluid Mech.* **215**, 209-227.
- [5] Finlay, W.H., Keller, J.B. & Ferziger, J.H. 1988 Instabilities and transition in curved channel flow. *J. Fluid Mech.* **194**, 417-456.
- [6] Guo, Y. & Finlay, W.H. 1991 Splitting, merging and wavelength selection of vortices in curved and/or rotating channel flow due to Eckhaus instability. *J. Fluid Mech.* **228**, 661-691.
- [7] Joseph, B., Smith, E.P. & Adler, R.J., 1975 Numerical treatment of laminar flow in helically coiled tubes of square cross section, Part I: stationary helically coiled tubes. *AIChE J.* **21**, 965-974.

- [8] Ligrani, P.M., Finlay, W.H., Fields, W.A., Fuqua, S.T. & Subramaman, C.S. 1992 Features of wavy vortices in a curved channel from experimental and numerical studies. *Phys. Fluids* **A4(4)**, 695-709.
- [9] Ligrani, P. & Niver, R.D. 1988 Flow visualization of Dean vortices in a curved channel with 40 to 1 aspect ratio. *Phys. Fluids* **31**, 3605-3618.
- [10] Matsson, O.J.E. & Alfredsson, P.H. 1990 Curvature- and rotation-induced instabilities in channel flow. *J. Fluid Mech.* **210**, 537-563.

Chapter 6

Visualization of Stabilizing/Destabilizing Flows in Channels with Curvature and/or Rotation

Experiments on visualization of stabilizing/destabilizing flows in channels with curvature and/or rotation are described. Several test sections have been used, and the results shown here are some typical ones for four test sections. Although the main objective is to draw some general features about the stabilizing/destabilizing flows from the visualization experiments, a generalized Rayleigh criterion is formulated about the primary instability of flows in rotating curved channels to help

understanding of some experimental results.

6.1 Introduction

The curvature and rotation of a channel can stabilize the channel flow in some flow domain, and destabilize the flow in the other domain. This was first recognized by Reynolds in 1884. The knowledge of this stabilizing/destabilizing phenomenon is essential in order to have the ability to predict and control the performance for technical applications of the flow in blade passages of radial flow pump, compressor impellers, centrifuges and cooling channels of rotating machinery etc.

The mechanism for this stabilizing/destabilizing phenomenon can be intuitively understood. For flows over concave surfaces, the centrifugal force is mainly balanced by a normal pressure gradient. The fluid particles moving outward across mean streamlines into regions of higher mean velocity should on average retain some memory of their previous (lower) mean velocity history. Their individual centrifugal forces will, thus, be less than the new mean normal pressure gradient, resulting in a net restoring force. Therefore, convex boundary layers should act a stabilizing influence on the flow. On concave surfaces, the opposite destabilizing effect should occur.

The spanwise rotation of a straight channel introduces Coriolis forces into the flow which play a similar role as that of the centrifugal forces in curved channels. Here, the flows near the antirotating wall are destabilized while the flows near the

corotating wall are stabilized. By the *antirotating (corotating) wall*, we mean the side on which the imposed rotation and the basic flow vorticity have the opposite (the same) sense. They are also called pressure (leading) and suction (trailing) walls, respectively.

The combined effects of both curvature and rotation occur in a curved channel with spanwise system rotation. Depending on the direction of rotation, the stabilizing/destabilizing effects due to the curvature and rotation will either enhance or counteract each other. The stabilizing/destabilizing flows in a curved rotating channel is, then, endowed with some more complex features.

If the centrifugal force and/or Coriolis force are strong enough, we can expect an early transition of flow from laminar to turbulent state in the destabilizing region. As well, we can also expect flow relaminarization from turbulence to laminar state in the stabilizing region.

Insights of the stabilizing/destabilizing flows can be examined theoretically through hydrodynamic stability and bifurcation theory and experimentally through the quantitative measurements of flow fields. Four major experimental difficulties discussed by Swinney & Gollub (1985) limit the extensive application of quantitative detailed measurements of the flow field at present. The study of this phenomenon was, then, performed mainly through the stability and bifurcation analyses in the past. In order to model the flows properly, the knowledge of the appearance of the stabilizing/destabilizing flows is essential. Flow visualization is an approach which can be

used to visualize the whole flow field.

In this part of work, a smoke visualization apparatus is designed to visualize the stabilizing/destabilizing flows in the channels with curvature, rotation or both. The cross section of the channel can be circular or rectangular with various aspect ratios. Although the apparatus designed may be used to visualize flows in the developing region, only fully developed flows will be considered in this work.

We have observed several stabilizing/destabilizing related phenomena in the channel flows with curvature, rotation or both. (1) The curvature and /or rotation can decrease the tendency of flows to undergo transition to a turbulent state, resulting an high-Reynolds number laminar flow, i.e., the curvature and/or rotation can suppress turbulent transition. (2) The curvature and/or rotation can increase turbulence production in the locally destabilized region, resulting in low-Reynolds number turbulence. (3) It is possible to completely cancel the Dean vortices by rotation and to give rise to vortices on the convex wall due to the Coriolis force. (4) At high rotation speeds, both primary and secondary instabilities show symmetry with respect to the direction of rotation. (5) The flows at high rotation speeds appear to be controlled by the secondary instabilities rather than the primary instability. (6) When the curved channels rotate with slow negative speed, two potentially unstable regions are separated by two stable regions in the cross-plane, resulting a complicated vortex flow. (7) The Dean/Coriolis vortices can also appear on the unstable side in the relaminarizing flows. (viii) The secondary instabilities lead the Dean/Coriolis

vortices oscillating in various forms.

Here we will deal specifically with experimental observations on these phenomena. No analytic studies of stability are made. However, a generalized Rayleigh criterion formulated in §6.2 should help to understand some experimental results. With the same purpose, a subsection is also included in §6.2 to reproduce the mechanism model for formation and break-up of the low-speed streaks in turbulent boundary layers, originally proposed by Kline *et al.* (1967). The present status regarding the stabilizing/destabilizing flows in channels with curvature, rotation or both are briefly discussed in §6.3. A discussion of the experimental apparatus and technique is given in §6.4, and the discussion of typical results in §6.5. In §6.6, we summarize the important results from the present study.

The objectives of this study are to give some new information on the stabilizing/destabilizing flows and flow changes with the Reynolds number and rotation number, as observed from flow visualizations and photographs. No experimental measurement is attempted in this study. It is interesting to note that relation between smoke pattern and secondary flow is somewhat uncertain (Finlay *et al.* 1993) at present. However, since little information from experiments is currently available, some qualitative information is believed to be useful.

6.2 Generalized Rayleigh's Theory and Mechanics of Streak Formation and Breakup in Turbulent Boundary Layers

6.2.1 Generalized Rayleigh's theory

In order to better understand the stable/unstable regions, we use a displaced particle argument (Tritton & Davis 1985) to derive a stability criterion including both centrifugal and Coriolis force effects. This can be regarded as the generalization of the Rayleigh's theory to include both curvature and rotation effects.

To simplify the analysis, consider an undisturbed flow in a rotating curved channel with an infinite span, as shown in Fig.6.1. If a fluid particle moving with streamwise velocity W at a distance r from the center of curvature o , be displaced by a radial disturbing force, the variation in moment of the momentum of the particle, taken around the axis perpendicular to W through o , can be written as (applying the principle of moment of momentum)

$$\tilde{W}(r + dr) - W r = -2\Omega \int_0^{\Delta t} v r dt \quad (6.1)$$

where v is the displacement speed, and Δt the time required for the particle to move from r to $r + dr$. This gives the streamwise velocity \tilde{W} of the particle at the new position,

$$\tilde{W} = W - \frac{W dr}{r} - 2\Omega dr \quad (6.2)$$

to the first order of dr .

With a streamwise velocity \tilde{W} , the particle at the new position is subjected to a centrifugal force F_1 and a Coriolis force F_2 along the radial direction as

$$F_1 = \frac{\rho \tilde{W}^2}{r + dr} \quad F_2 = 2\rho\Omega\tilde{W} \quad (6.3)$$

In the undisturbed flow, the centrifugal force and Coriolis force acting on a particle with a streamwise velocity $W + \frac{dW}{dr}dr$ at $r + dr$, is balanced by a pressure gradient in the radial direction, i.e.

$$\frac{\partial P}{\partial r} \Big|_{r+dr} = \rho \frac{(W + \frac{dW}{dr}dr)^2}{r + dr} + 2\rho\Omega(W + \frac{dW}{dr}dr) \quad (6.4)$$

This pressure gradient will also act on the displaced particle (Tritton & Davis 1985). Hence, the restoring force per unit volume acting on the displaced particle is (Eqs.(6.3) and (6.4))

$$F = \rho \frac{(W + \frac{dW}{dr}dr)^2}{r + dr} + 2\rho\Omega(W + \frac{dW}{dr}dr) - \frac{\rho \tilde{W}^2}{r + dr} - 2\rho\Omega\tilde{W} \quad (6.5)$$

Substituting Eq.(6.2) into Eq.(6.5) gives

$$F = \rho\Theta(r)dr + o(dr^2) \quad (6.6)$$

where

$$\Theta(r) = \frac{2W}{r} \left(\frac{dW}{dr} + \frac{W}{r} \right) + \frac{6\Omega W}{r} + 2\Omega \left(\frac{dW}{dr} + 2\Omega \right) \quad (6.7)$$

Nondimensionalizing $\Theta(r)$, Ω , W and r by $(W_m/a)^2$, W_m/a , W_m and a , with W_m as the mean streamwise velocity across the channel ($W_m = \frac{1}{a} \int_{r_i}^{r_o} W(r)dr$), we have

$$\Pi = \frac{\Theta}{(W_m/a)^2} = 2 \left[\frac{\sigma w}{1 + \sigma(x - 1/2)} + Ro \right] \left[\frac{dw}{dx} + \frac{\sigma W}{1 + \sigma(x - 1/2)} + 2Ro \right] \quad (6.8)$$

or

$$\Pi = \underbrace{\frac{2\sigma w}{1 + \sigma(x - 1/2)} \left(\frac{dw}{dx} + \frac{\sigma w}{1 + \sigma(x - 1/2)} \right)}_{1st \text{ term}} + \underbrace{\frac{6\sigma w Ro}{1 + \sigma(x - 1/2)}}_{2nd \text{ term}} + \underbrace{2Ro \left(\frac{dw}{dx} + 2Ro \right)}_{3rd \text{ term}} \quad (6.9)$$

where

$$x = \frac{r - R}{a} \quad w = \frac{W}{W_m} \quad Ro = \frac{\Omega d}{W_m} \quad \sigma = \frac{c}{R_c} \quad (6.10)$$

Ro , the inverse of a Rossby number, represents the ratio of the Coriolis force to the inertia force.

Π may be called the generalized Rayleigh stability criterion which includes both centrifugal and Coriolis force effects. The intermediate term on the right side of Eq.(6.9) is the coupling term between the curvature and rotation, while the first term and last term are centrifugal instability-related and Coriolis instability-related effects, respectively. The flow is stable in the flow domain with $\Pi > 0$, and unstable in the domain with $\Pi < 0$.

It is interesting to note that Eq.(6.8) is identical to that obtained by a linear stability theory (Matterson, 1993a).

For the flow in a curved channel with rotation around the axis of curvature, the base flow is unaffected by the rotation (Chandrasekhar 1961). Chandrasekhar (1961) obtained solution for the base flow. For the small gap ($\sigma \ll 1$), it can be written as

$$w(x) = 6x(1 - x) \quad (6.11)$$

We analyze the stable/unstable regions through Eq.(6.8) or (6.9) for two special cases, namely, small gap with low rotation rate and small gap with high rotation rate next.

the case of small gap with low rotation rate

For the small gap ($\sigma \ll 1$) and low rotation rate ($Ro \sim o(\sigma)$), the generalized Rayleigh's criterion Π reduces to

$$\Pi = 2(\sigma w + Ro) \frac{dw}{dx} \quad (6.12)$$

The condition $\Pi(x) = 0$, which can be obtained either by $\sigma w + Ro = 0$ or by $\frac{dw}{dx} = 0$, gives the boundary between the stable region and unstable region. By $\frac{dw}{dx} = 0$, we have

$$x_{01} = \frac{1}{2} \quad \forall Ro \quad (6.13)$$

which is the midplane of the channel.

By $\sigma w + Ro = 0$, we have

$$\left. \begin{aligned} x_{02} &= \frac{1}{2}(1 + \sqrt{1 + 2Ro/(3\sigma)}) \\ x_{03} &= \frac{1}{2}(1 - \sqrt{1 + 2Ro/(3\sigma)}) \end{aligned} \right\} \quad (6.14)$$

for all values of Ro satisfying

$$-1.5 \leq \frac{Ro}{\sigma} \leq 0 \quad (6.15)$$

The sign of Π in different region is listed in Table 6.1. Thus, the stable/unstable

Table 6.1: Sign of Π for the case of small gap and low rotation rate

Ro/σ	Region with Positive Π	Region with Negative Π
$Ro/\sigma \leq -1.5$	$0 < x < 1/2$	$1/2 < x < 1$
$-1.5 \leq Ro/\sigma \leq 0$	$x_{03} < x < 1/2$ $x_{02} < x < 1$	$0 < x < x_{03}$ $1/2 < x < x_{02}$
$Ro/\sigma \geq 0$	$0 < x < 1/2$	$1/2 < x < 1$

regions can be determined, as shown in Fig.6.2.

It is interesting that, in the region $-1.5 < Ro/\sigma < 0$, there exist two potentially unstable regions separated by two stable regions. We could expect that the competition of the destabilizing mechanisms in the two regions will lead to a complicated flow.

Although we show all the regions of Ro in Table 6.1 and Fig.6.2, the results are valid only for lower $|Ro|$. The analysis for the high rotation rate is shown below.

the case of small gap with high rotation rate

For the small gap ($\sigma \ll 1$) and high rotation rate ($Ro \sim o(1)$), the generalized Rayleigh's criterion Π can be approximated as

$$\Pi(x) = 2Ro\left(\frac{dw}{dx} + 2Ro\right) \quad (6.16)$$

Table 6.2: Sign of Π for the case of small gap and high rotation rate

Ro	Region with Positive Π	Region with Negative Π
$Ro \leq -3$	$0 < x < 1$	
$-3 < Ro \leq 0$	$x_0 < x < 1$	$0 < x < x_0$
$0 \leq Ro < 3$	$0 < x < x_0$	$x_0 < x < 1$
$Ro \leq 3$	$0 \leq x \leq 1$	

which vanishes at a radial position x_0 satisfying

$$\frac{dw}{dx} + 2Ro = 0 \quad (6.17)$$

This gives

$$x_0 = \frac{1}{2} \left(1 + \frac{Ro}{3} \right) \quad \forall |Ro| \leq 3 \quad (6.18)$$

The sign of Π in different regions is summarized in Table 6.2. The stable/unstable regions are shown in Fig.6.3.

This shows that the unstable regions reduces as $|Ro|$ increases, and the high rotation with $|Ro| > 3$ always stabilizes the flow in the whole cross section.

Although Table 6.2 and Fig.6.3 show the results for the whole range of Ro , we should use the results shown in Table 6.1 and Fig.6.2 for the case with low rotation rate. We show all here because this case is identical to the case only with spanwise rotation of straight channels.

6.2.2 Mechanics of Streak Formation and Breakup in Turbulent Boundary Layers

In a study on the structure of turbulent boundary layers along a flat plate, Kline *et al.* (1967) found that the low-speed streak formation and breakup play a central role in turbulent boundary layer processes. In particular, the break up of the wall-layer streak was found to make a substantial contribution to the turbulence energy production. As well, the dominance of the streaks is not confined to the region of their origin or breakup. They affect most of the flow directly or indirectly.

This *bursting* phenomenon was also found in the middle stages of natural laminar-turbulent transition (Elder 1960, Klebanoff *et al.* 1962), and has been confirmed by many independent experiments. Here, we briefly describe the *bursting* phenomenon and mechanisms for the formation and break-up of the low-speed streaks as proposed by Kline *et al.* (1967), Lighthill (1963) and Klebanoff *et al.* (1962). We are interested in this phenomenon because we have observed a quite similar phenomenon in the flows with high rotation rates.

In a series of visual studies on the structure of the flat plate turbulent boundary layer, Kline *et al.* (1967) observed the formation, gradual *lift-up*, then sudden oscillation, *bursting* and ejection of the low-speed streaks in fully developed turbulent boundary layers, as sketched in Fig.6.4. The flow pattern appears to consist of an array of *streaks*, which are interspaced with areas of fluids with high

streamwise velocity. The streaks appear as long stretched filaments in the streamwise direction which move downstream more slowly than the surrounding fluid. The primary orientation of the vortex elements is streamwise¹, but each streak stands at a slight angle to the wall so that its distance from the wall increases as it moves downstream. Within the sublayer, the streaks waver and oscillate much like a flag, and intermittently leap outwards from the wall, sometimes passing rapidly clear to the outer edge of the boundary layer, but more frequently following trajectories within the wall layer. As they enter the outer region of the flow, the streaks ejected from the wall region become tangled, suddenly oscillating and bursting, and making the apparent streamwise and spanwise scales of motion more nearly equal.

A physical explanation for the formation of the low-speed streaks was essentially proposed by Lighthill 1963 (Kline *et al.* 1967). The effect of flow towards and away from a wall could act to convect and change the spanwise vorticity component as sketched in Fig.6.5. In particular, the outflows (inflows) compress (stretch) the vortex lines in the corresponding regions. This results in a spanwise variation in w near the wall because the spanwise component of vorticity is mainly due to $\frac{\partial w}{\partial y}$. More precisely, the local w in the sublayer is increased where the flow is towards the wall, and is reduced in regions of outflow. Therefore, a variation in w can develop spanwisely due to the inherent three-dimensionality of the coexisting turbulence.

¹The use of the word *streamwise* here refers only to the observed primary orientation of the streak, and should not be constructed as necessarily implying a connection to a Görtler, Dean or Coriolis type vortices.

The gathering of low-speed fluid near the wall, due to the streamwise vorticity so generated, forms the streaks which could be observed when the tracer such as smoke and dye are put into the fluid. As well, the same secondary vorticity accounts for the lifting of the low-speed wall-layer streaks (observed experimentally) prior to the breakup process (Fig.6.6).

A picture of the mechanism for the low-speed wall-layer streak breakup is shown in Fig.6.6 (Kline *et al.* 1967). This sketch was drawn according to the experimental measurements and physical explanations by Klebanoff *et al.* (1962), Kovasnay *et al.* (1962) and Stuart (1965). The vortex stretching at the outer edge of the boundary layer leads to the intermittent formation of the intense local shear layers (vorticity concentrations) there. These local shear layers become locally unstable intermittently, break down in violent oscillation, and eject into the outer flow along the streak trajectory (Kline *et al.* 1967).

6.3 Brief Review of Previous Works

6.3.1 Dean flow

By imposing a small gap approximation, velocity profile $w(x)$ is near-parabolic as expressed by Eq.(6.11). On substitution of Eq.(6.11), with $Ro = 0$, into Eq.(6.8), one concludes that the flow is stable in the region

$$0 < x < \frac{1}{2} - \frac{1}{\sigma} + \sqrt{\frac{1}{\sigma^2} + \frac{1}{4}} \quad (6.19)$$

and unstable in the region

$$\frac{1}{2} - \frac{1}{\sigma} + \sqrt{\frac{1}{\sigma^2} + \frac{1}{4}} < x < 1 \quad (6.20)$$

This means that the flow may be inviscidly stable (unstable) from the inner wall (outer wall) to slightly outside the centreline.

relaminarization by curvature

The stabilizing effect of the curvature on the flow can be visualized through the relaminarization from the turbulence to laminar. Indeed, as long ago as 1884, Reynolds had listed ‘curvature with the velocity greatest on the outside’ as one of the factors ‘conductive to direct or steady (=laminar) motion’, and had noted how a small curvature may have a large effect. However, this stabilizing effect has not been well understood even today, mainly because of the lack of precise definition of relaminarization and the effective methods of measurements.

To simplify the study and eliminate the interaction between the stabilizing and destabilizing effects, the previous investigations are mainly concerned with the boundary layer flow on convex surfaces. One measure of the curvature is the parameter $k\delta$ with k^{-1} and δ as the radius of curvature (considered positive when convex) and the boundary layer thickness, respectively. The streamwise curvature introduces additional terms, consisting of a source of strength $-\frac{\partial(kvy)}{\partial y}$ and the body forces $(-kuv, ku^2)$ along the streamwise and normal directions respectively, into the

governing equations of the flow (So & Mellor, 1972). Here the w, v are the velocity components along the curved surface (x-direction) and the normal to it (y-direction).

Because of the centrifugal component kw^2 , a normal pressure gradient (the pressure being lower toward the convex wall) is induced in the convex boundary layer. This gradient then acts as a stabilizing force for the flow. For example, a slow lump of turbulence thrown outward from a convex wall is subjected to a lower centrifugal force than the faster ambient fluid, and so is driven back by the normal pressure gradient that balances the mean flow. Similarly, a faster lump moving toward the convex wall will be thrown out. Consequently, there is a tendency to the suppression of turbulence.

Another way to see the nature is to examine the Reynolds stress transport equations for curved layers. This was performed by Rotta (1967) and So & Mellor (1972). The curvature introduces some *absorption* terms for the Reynolds stress.

Bradshaw (1969) used an analogy theory between streamline curvature and buoyancy in turbulent shear flow, and calculated the curved turbulent flows using this analogy theory. In particular, he defines a Richardson number for curvature, which serves as a measure of the ratio of the absorption term to the production term. As well, this Richardson number was found to be very small near the convex wall.

As in buoyant flows, however, even a relatively small value of Richardson number

can cause significant changes in the turbulent structure. This is confirmed by the experiments by Thomann (1968) and Bradshaw (1973). Thus, even when the magnitude of the terms explicitly involving curvature in the stress transport equations is very small, the effects of curvature are not negligible, and clearly affect the other terms as well.

Ramapriam & Shivaprasad (1978) made the detailed measurements on the structure of turbulent boundary layers along mildly convex curved surfaces. They found that the curvature affects not only the amplitudes of the fluctuating motion but also the turbulence structure. In particular, the stabilizing influence of curvature was found to destroy the organization of the motion in the large-scale structures in the boundary layer. And the effects also affect the high wave number and the bursting process (Rao *et al.* 1971, Badri Narayanan *et al.* 1977, and Brown & Thomas 1977).

On summary, the centrifugal forces have been found to destroy the organization of the motion and suppress the Reynolds shear stress in the turbulent boundary layers along the convex curved walls. This results in an absorption of the turbulence energy and leads to a relaminarization from the turbulent to laminar flow. Such a study of stabilizing effect, however, needs to be extended to the case of curved channel flows. And the visualization of stabilizing flows is desirable to evaluate the existing theoretical considerations with the goal of providing a sound physical model as a basis for theory.

destabilization of flows by curvature

Both theoretical and experimental investigations on the destabilizing effect of curvature on the curved channel flows have been carried further than those on the stabilizing effect. The quantitative details of the flow fields are therefore more extensive in the literature concerning the destabilizing effect of curvature.

Using analytic means for small gap channels with infinite span, Dean (1928) first demonstrated that curved channel flow is unstable to small amplitude disturbances for values of $Rc\sqrt{\sigma}$ greater than a critical value. This parameter is now referred to as the Dean number De . In terms of Dean number versus spanwise wavenumber at a particular curvature ratio, the neutral stability curve separates unstable flow at higher Dean numbers from *curved channel Poiseuille flow* (CCPF) at lower Dean numbers. The focus of points along the neutral stability curve defines the critical Dean number De_c and critical spanwise wavenumber α_c . With CCPF, the velocity in the channel is purely streamwise with a profile similar to the parabola of plane channel flow. The main difference is evident in the maximum velocity, which is shifted slightly toward the outer wall. Dean (1928) found that

$$\left. \begin{aligned} De_c &= 35.94 \\ \alpha_c &= 3.96 \end{aligned} \right\} \quad (6.21)$$

Confirmation of Dean's results was provided by the independent theoretical analyses of Yih & Sangster (1957), Reid (1958) and Hammer & Lin (1958) using different

methods and by the experiments of Brewster *et al.* (1959) who find that

$$\left. \begin{aligned} De_c &= 36.5 \pm 1.1 \\ \alpha_c &= 4.9 \pm 0.8 \end{aligned} \right\} \quad (6.22)$$

The results are in good agreement with the predicted values by Dean (1928).

It is of interest to compare the Reynolds number for the onset of instability given by Dean with the Reynolds number at which Tollmien-Schlichting waves may set in for strictly straight plane channel flows. It is known that in the latter case, the onset of instability occurs when $Re_c \doteq 7070$ (Lin 1955 and Gibson & Cook 1974). Clearly, the criterion given by Dean must cease to be valid when

$$\sigma < 2.6 \times 10^{-5}$$

which is very small. Therefore, we typically expect to observe streamwise oriented vortices instead of TS-waves in curved channel flow when the Reynolds number is increased from zero.

Kelleher *et al.* (1980) and Ligrani & Niver (1988) made flow visualization experiments in the curved channels with a high spanwise aspect ratio. They observed mushroom shaped smoke patterns, which are believed to be indicative of Dean vortices. As shown by the hot-wire measurements (Kelleher *et al.* 1980), the vortices give rise to large variations of the streamwise velocity in the spanwise direction.

The secondary instability of Dean-vortices was first examined numerically by Finlay *et al.* (1988) for a curved channel with infinite span. Two different wavy

travelling vortex flows, namely, undulating vortex flow and twisting vortex flow, are developed on top of the primary instability due to the instability of the Dean-vortices subjected to the streamwise wavy disturbances. These two kinds of vortex flows were confirmed experimentally by Ligrani *et. al.* (1992) and Ligrani & Niver (1988). The linear stability analysis of the one-dimensional streamwise profiles in the spanwise and radial directions (Le Cunff & Bottaro 1993) shows that the spanwise inflectional profile is associated with the secondary twisting motion while the undulating motion is related to the normal profiles.

The secondary instability of Dean-vortices with respect to two dimensional spanwise-periodic perturbations (i.e. Eckhaus stability) was investigated numerically by Guo & Finlay (1991) for infinite-span cross section. Because of this instability, the merging and splitting of vortex pairs appear. Experimental confirmation of splitting and merging of vortex pairs was made by Ligrani & Niver (1988), Alfredsson & Persson (1989) and Matsson & Alfredsson (1990). The further developments on the Eckhaus instability problem have been made by Matsson & Alfredsson (1992) and Bottaro (1993).

The three-dimensional spatially developing vortices were studied by Guo & Finlay (1994). They found that the spanwise wave number selection depends on the energy level of the vortices. Different spanwise wave lengths could appear simultaneously without interaction when the energy level is low. However, merging and splitting of vortices occur if the vortices have reached a certain non-linear level.

The measurements on the streamwise development of the Dean instability (Mattsson & Alfredsson 1992) show that the merging and splitting of vortex pairs are not time dependent as the case for Ligrani & Niver (1988). Numerical simulations by Bottaro (1993), however, show that the Eckhaus instability is time-dependent in the temporal model, and steady in the spatial model.

6.3.2 Straight channel flow with spanwise rotation

Substituting Eq.(6.11) with $\sigma = 0$ for straight channel flows into Eq.(6.8) leads to a result about the stable/unstable regions which is identical to those discussed in §6.2.1.2. (see Table 6.2 and Fig.6.3).

relaminarization by rotation

The rotation of the channel introduces two additional forces, namely, the centrifugal and Coriolis forces, in the rotating frame of reference. For the fluids with constant properties, the centrifugal force can be combined with the static pressure and does not then explicitly enter into the equations of motion. The Coriolis force, on the other hand, will have to be considered explicitly. An important effect of the Coriolis force is to generate a normal pressure gradient proportional to the angular velocity of rotation. As in the curved channel, this pressure gradient has a stabilizing effect in the corotating side of the channel where the imposed rotation and the basic flow vorticity have the same sense, but a destabilizing effect in the antirotating

side where the imposed rotation is opposite to the basic flow vorticity.

A direct result of the stabilizing effect is the relaminarization of flows in the corotating side. Unfortunately, this relaminarization-related phenomenon has not been studied extensively. Consequently, the literature on this is quite limited.

From an analogy with curved and stratified flows, Bradshaw (1969) introduces an criterion for relaminarization, namely, the Richardson number, for rotating flows, which is the ratio of the additional *absorption* term due to the Coriolis force over the conventional production terms for Reynolds stress.

Based on the flow visualization studies in the wall region, Johnston *et al.* (1972) found that, with increasing Reynolds number, the relaminarization occurs at an increasingly higher value of rotation, and that no unique value of rotation number describes the boundaries between the different flow regimes (fully turbulent, relaminarization-transitional and laminar states).

Halleen & Johnston (1967), Lezius & Johnston (1971) and Johnston *et al.* (1972) made flow visualization studies in an two-dimensional channel rotating about a spanwise axis. They observed the relaminarization on the corotating side. For small rotation rates, the flow remains essentially turbulent although it is slightly modified, but for rotation rates higher than a certain value, the following changes occur progressively on the corotating side: (i) intermittent appearance of streaky wall-layer, (ii) basic laminar flow interspaced with turbulent spot-like characteristics, and (iii) purely laminar layer close to the wall. Furthermore, it is found that turbulent

bursting ceases, turbulence intensities decrease, the velocity profile departs from the standard log-law form, and the skin- friction decreases considerably.

destabilization of flows by rotation

Hart (1971) first proved experimentally and theoretically by a linear stability analysis the existence of roll-cell instability in rotating channel flows. His experiments were conducted with water to allow for dye injection visualization in a rectangular channel with an aspect ratio 7. The linear stability analysis is for the rotating plane Poiseuille flow, i.e., the limiting case of a rectangular channel with an infinite aspect ratio. Hart also demonstrated that the general stability problem for rotating Poiseuille flow is exactly analogous to that of a temperature- stratified fluid with the appropriate stratification.

A more detailed theoretical analysis was performed by Lezius & Johnston (1976) about the roll- cell instabilities in rotating channel flow. They found that the critical disturbance occurs at a Reynolds number $Re = 88.53$ and a rotation number $Ro = 0.5$ in plane Poiseuille flow. For higher Reynolds number, however, they found that unstable conditions can exist for $0 < Ro < 3$. As well, their theoretical results are in good agreement with the experiments (Johnston *et al.* 1972).

The roll-cell instabilities in rotating laminar channel flows are also observed numerically for the channels with aspect ratio of 1, 2 and 8 by Speziale (1982), Speziale & Thangam (1983), Speziale (1986), and Hwang & Jen (1990).

Two different streamwise travelling vortex flows, namely, WVF1 and WVF2, can develop due to the secondary instability of the roll-cell instability with respect to the streamwise wavy disturbances. This was first found by Finlay (1990) in a numerical study of secondary instabilities for a rotating channel flow with an infinite span by a three-dimensional spectral method. For low rotation rates, WVF1 is similar to the twisting vortices in curved channel flow. However at higher rotation rates, the similarity disappears. WVF2 is very similar to the undulating vortex motion in curved channel flows (Finlay *et al.* 1988).

The Eckhaus instability was found to cause the roll-cell vortices to split and merge by Guo & Finlay (1991). This was confirmed experimentally by Alfredsson & Persson (1989) and Matsson & Alfredsson (1990).

Direct numerical simulations with random disturbances was carried out by Yang & Kim (1991) for rotating plane Poiseuille flow. Initially, the wave number was found to agree with the linear theory. However, the spanwise wave number is found to decrease during the non-linear stage. This is believed to be due to the merging of vortex pairs in an Eckhaus mechanism of wave number selection.

6.3.3 Curved channel flow with spanwise rotation

The combined effects of curvature and rotation result in the stabilizing/destabilizing flows with some new features in a rotating curved channel, especially when the Coriolis force counteracts the centrifugal force. The criterion to determine the inviscid

stability is the generalized Rayleigh' criterion derived in §6.2.1. Also shown in §6.2.1 are stable/unstable regions for the two cases at small gap approximation: low rotation rate and high rotation rate.

It appears that the literature on the stabilizing/destabilizing flows in a rotating curved channel is rather limited. Matsson & Alfredsson (1990) made a linear stability analysis for a channel with infinite span and small curvature ratio, and flow visualizations for a channel with spanwise aspect ratio of 28 and a curvature ratio of 0.025. From the linear stability theory, they show that there is a region where centrifugal and Coriolis effects nearly completely cancel each other. This increases the critical Reynolds number for the onset of instability significantly. The flow visualization experiments show that a complete cancellation of Dean vortices can be obtained for low Reynolds number at a rotation rate agreement with predictions by linear stability theory. Furthermore, the rotation is found to be capable to completely cancel the secondary instability occurring at high Reynolds number in curved channel flows. As well, there are evidence that the principle of exchange of stabilities is not valid in a certain parametric region.

In this region, the critical Reynolds number was found by Matsson (1993b) to be determined by an instability in the form of travelling, slightly inclined, stream-wise vortices. However, for an axisymmetric oscillatory motion, the experimental observation of the time dependent motion is still lacking.

The Eckhaus instability analysis by Guo & Finlay (1991) also includes the rotat-

ing curved channel flows. They show that the splitting and merging of vortex pairs can also occur in the rotating curved channel flows due to the secondary instability with respect to the two-dimensional, space-wise-periodic disturbances.

6.4 Experimental Apparatus and Technique

A schematic diagram of the experimental apparatus is shown in Fig.6.7. It consists of a test section, a rotating table with the rotating seal, an air supply system and a smoke generator.

The rotating table is driven by an electric motor with adjustable speed drive and the range of the rotating speed is $n = 0 \sim 500 \text{ rpm}$ for this work. The rotational speed is measured by using an optical slot switch running on a disc with equally spaced 60 holes near its perimeter. The signal from the switch is fed to a Hewlett Packard HP 5314A Universal counter. With 60 holes in the disc, the frequency in Hz equals the rotational speed in rpm .

A second disc with a single hole provides the signal for firing the General Radio 1540 Strobolume by way of a delay generator/single flash flip-flop which allows visual observation using a slit light source with one flash per rotation and also permits a single, properly timed flash for photographing the whole flow field.

The building compressed air is used as the fluid. The air flow rate is measured by a Meriam flow element with a calibrated differential pressure transducer. The

smoke generated by burning Chinese incense sticks is injected through a dispersing tube before the test section as shown in Fig.6.7. The very tiny smoke particle, subjected to neglected gravitational and *rotational* buoyancy forces relative to the drag forces, marks fluid particle trajectories. The smoke patterns are photographed instantly at the exit of the test section revealing the flow pattern. This provides an end-view of the secondary flow pattern for an *observer* looking upstream into the channel cross-section. A Nikon FM2 single lens reflex camera and Kodak T-Max black and white film P3200 are used.

The various test sections may be installed on the turning table. The test sections used are summarized in Table 6.3. A square cross section represents a special case of rectangular channel.

Four typical test sections, denoted by *Ts-A*, *Ts-B*, *Ts-C* and *Ts-D*, are shown in Fig.6.8. *Ts-A* consists of an entrance spiral square channel with axial length $0.85m$ and a curved square channel (270° bend with axial length of $1.2m$) with constant radius of curvature $R_c = 25.4cm$. The top view and the exit cross-section are shown in Fig.6.8(a). The curved square channel has cross-section $5.08 \times 5.08cm^2$. The air flows through a rotating straight tube (inside diameter= $4cm$) along the axis of rotation, and then enters the spiral square channel before entering the test section. The test section was made from acrylic sheets.

Ts-B, also made from acrylic sheets, consists of an entrance spiral rectangular channel with axial length $1.25m$ and a curved rectangular channel (270° bend) with

Table 6.3: Test Sections

Case	Curvature		Rotation		Curvature+Rotation	
	circular	rectangular	circular	rectangular	circular	rectangular
Cross Section						
$d(cm), \gamma$	3.18,	1,10	3.81	1/6, 1, 2,	3.18,	1,10
	3.81,4.8			6,12	3.81,4.8	
σ	0.1,0.174,0.2	0.1,0.182	0	0	0.1,0.174,0.2	0.1
Re	100-4000	200-1000	100-4500	200-4000	100-10000	200-4000
n, rpm	0	0	0-350	0-350	0-450	0-450

constant radius of curvature $R_c = 25.4\text{cm}$. The top view and the exit cross section for *Ts-B* are shown in Fig.6.8(b). The air flows through a rotating straight tube (inside diameter= 4cm) along the axis of rotation and then enters the spiral rectangular channel before flowing into the curved channel.

Ts-C consists of a plenum box (15.24cm cube), a smooth contraction from 15cm dia. to 3.81cm dia. over the length of 12cm , and a plexiglass test tube (dia. $d = 3.81\text{cm}$, length $l = 82\text{cm}$). The top view of *Ts-C* is shown in Fig.6.8(c). The plenum box and contraction section were designed to obtain an approximately uniform entrance velocity to the test section. The air flows through a rotating vertical straight tube (inside diameter= 4cm) along the axis of rotations and then enters the plenum box and contraction section before entering the straight tube.

Ts-D, Fig.6.8(d), is basically similar to *Ts-C*. The differences are plexiglass test channel and the contraction section from the plenum box to the test channel. The plexiglass test channel for *Ts-D* is a square channel with cross section= $2.54 \times 2.54\text{cm}^2$ and length= 52cm . The contraction is a smooth section from a cross-section ($15.24 \times 15.24\text{cm}^2$) to a cross-section ($2.54 \times 2.54\text{cm}^2$) over a length of 12cm .

6.5 Results and Discussion

This discussion will focus only on the phenomena relating the stabilizing/destabilizing influence caused by the centrifugal and/or Coriolis forces. As mentioned in §6.2, both influences occur simultaneously. Although the generalized Rayleigh's criterion may

offer a possibility of determining the boundary between the stable and unstable regions for an inviscid fluid in the sense of the primary instability, the precise division between stable and unstable regions is not possible from the flow visualization for a real fluid. Furthermore, the secondary instabilities may introduce further difficulty for determining the boundary.

The end-view photographs are to be shown for $Ts-A$, $Ts-B$, $Ts-C$ and $Ts-D$ with spanwise direction vertical and radial direction horizontal. For the cases of $Ts-A$ and $Ts-B$, the convex (inner) wall is on the left and the concave (outer) wall is on the right. For the cases of $Ts-C$ and $Ts-D$, the corotating side (low pressure) is on the left and the antirotating side (high pressure) is on the right. Different test condition for a given test section is characterized by two parameters, namely, Reynolds number Re and rotation number Ro . The channel width is used as the characteristic length in Re and Ro for the cases of $Ts-A$, $Ts-B$ and $Ts-D$ while the diameter of the tube is employed as the characteristic length for the case of $Ts-C$. For a given set of Re and Ro , several photographs, with each taken at different instant, are usually given to show the time variation of the flow.

Two typical cases are shown in Fig.6.9 for $Ts-C$ and $Ts-A$ respectively to show the overall effects of stabilization (Fig.6.9(a)) and destabilization (Fig.6.9(b)). As shown in these photographs, the stabilizing effect can cause flow relaminarization from turbulence to laminar (Fig.6.9(a)). The destabilizing effect can lead to an early transition from laminar to turbulence (Fig.6.9(b)).

The results of Fig.6.9 show only the end result of two of the phenomena under investigation. Our discussion here is first to present some detailed, typical visual results that bear on these phenomena, and how they are affected by both Reynolds number and rotation number. Next, we shall examine some visual evidence concerning the several interesting structures of the stabilizing /destabilizing flows due to the centrifugal and/or Coriolis forces.

In §6.5.1, we observe the effect of rotation number on the visual results of flow for $Ts-B$ at low Reynolds number ($Re = 110$). This Reynolds number represents a Dean number of 35 which is below the critical Dean number De_c for the onset of Dean vortices in a stationary curved rectangular channel with an aspect ratio of 10 ($De_c = 41$, see Cheng *et al.* 1977). The discussion in §6.5.1 is extended to the case of intermediate Reynolds number of 452 in §6.5.2. This Reynolds number gives a Dean number of 143 which is higher than De_c .

In §6.5.1 and §6.5.2, we are mainly concerned with the destabilizing related phenomena. We shift our attention to the stabilizing phenomena in §6.5.3 through examining the effect of rotation number on the visual results of flow for $Ts-C$ at higher Reynolds number ($Re = 3000$).

In §6.5.4, we show the visual evidences of Dean/Coriolis vortices oscillating in various modes and flows in the region with two potentially unstable layers. The more complete results are shown in Cheng *et al.* 1992, Cheng & Wang 1993a, 1993b, 1993c, 1994a, 1994b, 1994c and Wang & Cheng (1995).

6.5.1 Visual results for $Ts-B$ at $Re = 110$

For fully developed laminar flow in a stationary curved rectangular channel ($n = 0$) with an aspect ratio of 10, the critical Dean number for the onset of Dean vortices (streamwise vortex rolls) is known to be 41 with the gap size a as the characteristic length (Cheng *et al.* 1977). With an entrance spiral channel length of $1.25m$ and a subsequent curved rectangular channel (length= $1.2m$) with constant radius of curvature, the flow at the exit of the channel is believed to be fully developed ($l/d \doteq 96.5$)

The end-view of flow in the cross section is illustrated in Fig.6.10. With vanishing rotational speed ($n = 0$), The stabilizing/destabilizing effect on flow is caused by the centrifugal force alone. The analysis based on the Rayleigh's criterion in §6.2 and §6.3 shows that the base flow is stabilized near the inner wall by the centrifugal force, and is destabilized near the outer wall. The flow near the inner wall appears, therefore, steady and laminar. This can be seen by comparing the two photos taken at different instants. The flow near the outer wall, however, appears unsteady and wavy due to the destabilizing effect of the centrifugal force. Some smaller vortices in the destabilizing region are also observed. The effect of the upper and lower side walls causes the end vortices to appear near the upper and lower side walls. The size of the end vortices is of the order of the gap size a . For this low Reynolds number, the centrifugal force is not strong enough to form Dean vortices, and the unsteadiness of the flow in the destabilizing region is also rather weak.

The value of Ro for the case of $n = -21$ falls in the region where two potentially unstable regions separated by two stable regions exist. The competition of the two destabilizing mechanisms (centrifugal instability and Coriolis instability) leads to a more complicated flow as shown in Fig.6.10. In particular, the secondary flow in the cross section appears as four elongated vortices, and the oscillating feature can be inferred by a comparison between the photos taken at different instants.

Two resources possibly contribute to this oscillating feature, i.e. the secondary instability of the primary instability or invalidation of the principle of exchange of instabilities in this region. The flow visualization experiments are not appropriate to determine the exact cause. However, the linear stability analysis by Matsson & Alfredsson (1990) shows that the principle of exchange of stabilities is not valid in a parameter region with low negative rotation where the two unstable regions, separated by two stable regions, appear (§6.2). As well, they found an oscillating mode in this region. Hence, it may be reasonable to suggest that the invalidation of the principle of exchange of stabilities is responsible for the oscillatory phenomenon.

When the rotation becomes more rapid to $n = -44$ ($Ro = -1.659$) in the negative direction, the flow becomes fairly steady in the whole cross section. This indicates that the Coriolis instability can completely cancel the centrifugal instability. However, the flow near the inner wall becomes unsteady again when the rotation speed reaches at $-65rpm$ ($Ro = -2.45$), and an additional pair of vortices appears near the inner wall. The additional pair of vortices becomes more notable

at $n = -86$ ($Ro = -3.242$).

Upon increasing the rotation speed further in the negative direction, the vortices become distorted, one observes a gradual breakdown and a vigour busting from the inner wall. The flow near the inner wall appears highly unsteady, and is somewhat similar to the *bursting* flow in the turbulent boundary layer (Kline *et al.* 1967) described in §6.2. This process can be seen from Fig.6.10 for $n \leq -153$. This *bursting* phenomenon, resulting smaller scales of motion, becomes stronger as the rotation speed increases in the negative direction.

The *bursting* phenomenon is believed to be due to the secondary instability and has two interesting features: (i) It appear only along the inner wall; and (ii) As the rotation speed increases in the negative direction, the region where the *bursting* occurs becomes smaller toward the inner wall.

According to the generalized Rayleigh's criterion, the flow is stable with respect to the primary instability in the whole cross section for the high $|Ro|$ (see §6.2). The highly unstable, turbulent-like flow near the inner wall implies that for the case with rapid negative rotation, the instability is determined by the secondary instability rather than the primary instability. As well, at high negative rotation the secondary instability leads to a low Reynolds number turbulence (say, $Re = 110$) near the inner wall.

According to the generalized Rayleigh's criterion, the base flow is stable near the inner wall, unstable near the outer wall when the rotation is positive. As the

rotation becomes more rapid, the stable region extends towards the outer wall (§6.2). Finally, the flow becomes the stable in the whole cross section at high Ro .

At low positive Ro ($Ro = 0.377, n = 10$), the flow is fairly steady and laminar near the inner wall, and weakly wavy near the outer wall. Upon increasing the rotation speed to $n = 26$ ($Ro = 0.98$), the large scale vortices begin to appear along the outer wall. At $n = 44$ ($Ro = 1.659$), many different scales of vortex motions become distinctive, and the flow becomes more unsteady.

Upon increasing the rotation speed further, the bursting phenomena occur along the outer wall, resulting a smaller scale, turbulent-like flow near the outer wall. This shows that the instability is also determined by the secondary instability at high positive rotation speed. Once again, the secondary instability results in a low Reynolds number turbulence near the outer wall at higher positive rotation speed. The symmetry between the directions of rotation is, then, valid not only for the primary stability (§6.2) but also for the secondary stability.

6.5.2 Visual results for $Ts-B$ at $Re = 452$

The end-view of the flow is shown in Fig.6.11 for several rotation numbers Ro at $Re = 452$. This Reynolds number corresponds to a Dean number 143 which is higher than the critical Dean number $De_c (=41)$ for the onset of Dean vortices in a stationary channel with an aspect ratio of 10. The pairs of counter-rotating Dean vortices at $n = 0$ is indicated by mushroom-shaped smoke patterns near the

outer wall. The differences in shape and spacing at different spanwise positions may be due to different amplitudes and locations of the small upstream disturbances which trigger initial vortex development. Some mushroom-shaped smoke patterns have a rocking type of motion while the others oscillate radially or spanwisely. The merging/splitting of vortex pairs is also evident. This is believed to be due to a different type of secondary instability of the Dean vortices.

At $n = -10$ ($Ro = -0.0914$), there exist two potentially unstable regions alternating by two stable regions. Once again, the competition of the two destabilizing mechanisms results in a more complicated flow in the whole cross section as shown in Fig.6.11. At $n = -44$, the mushroom-shaped smoke patterns along the outer wall (Dean vortices) at $n = 0$ are completely cancelled by the negative rotations, and the Coriolis force instability gives rise to Coriolis vortices on the inner (convex) wall as indicated by the mushroom-shaped smoke patterns. The different types of vortex motions are observed, and are believed to be due to different types of the secondary instabilities of the Coriolis vortices.

Upon increasing the rotation speed to $n = -107$ and -188 , the Coriolis vortices on the convex wall become smaller, fairly steady and symmetric. Further increase in the rotation speed, however, leads the Coriolis vortices to be broken. The flow near the inner wall becomes highly unsteady and small scale motion, and is similar to the bursting flow in the turbulent boundary layers. This confirms one previous result that the instability is determined by the secondary instability rather than the

primary instability at high negative rotation rates.

The positive rotation enhances the secondary instabilities of the Dean vortices. This leads to a twisting Dean vortex flow at $n = 38$ ($Ro = 0.347$) with a strong rocking type of motion. With further increase of the rotational speed, the size of the Dean vortices on the outer wall becomes smaller ($n = 84$). The different kinds of vortex flows are observed to coexist due to various possible secondary instabilities.

When the rotation speed increases to $n = 125$, the secondary instabilities cause the vortex to be broken, and the flow becomes highly unsteady. Continuity of this process results in a flow near the outer wall very like the bursting flow in the turbulent boundary layer at high positive rotation rates. This complex process is visualized in Fig.6.11 through a series of photos for different rotational speeds.

6.5.3 Visual results for $Ts-C$ at $Re = 3000$

When $Re = 3000$, the flow is fully turbulent in a stationary straight tube. Our failure to visualize the flow field for zero or small Ro indicates that the flow is or very near the fully turbulent since the smoke injection method is not valid to visualize turbulent flow. It is widely accepted today that the bursting phenomena discussed in §6.2 are the source of the largest part of the newly produced Reynolds shear stress and turbulence energy. The basic bursting structure of the wall-layer flow is then believed not to be changed by the rotation for low rotation number Ro . However, the relaminarization will occur if the rotation number is high enough.

Shown in Fig.6.12 is the end-view of flow for $Ts-C$ at $Re = 3000$. At $n = 59$, the large scale vortex flow appears in the whole cross section. The pair of vortices near the high pressure side is the Coriolis vortices. The secondary instability causes these vortices to oscillate and twist. The flow appears to be laminar in the whole cross section. This implies that the formation of large scale vortex flow annihilates turbulence, and the relaminarization process, whose detailed features can not be visualized clearly through smoke injection method, takes place at lower rotation rates.

Upon increasing the rotation speed to $n = 118$, the secondary instabilities of the Coriolis vortices make the flow near the high pressure side difficult to discern. Further increasing of rotation speed leads the flow near the high pressure side to be like the Taylor-Proudman flow.

6.5.4 The Dean/Coriolis vortices and flows in the region with two unstable layers

Two important stabilization/destabilization related features are the appearance of the Dean/Coriolis vortices and two unstable regions alternating by two stable regions in a curved channel spanwisely rotating with a slow negative rotation rate. They are of special interest because they may cause significant alternations to flow structure and wall heat transfer distribution. In addition, they have an important effect on transition from laminar to turbulent flow and relaminarization from turbu-

lent to laminar flow. Further discussions are made here about these two phenomena.

The Dean/Coriolis vortices

The Dean/Coriolis vortices may be present as a result of centrifugal/Coriolis instabilities imposed on the flow by curvature/rotation. Experimentally, these vortices are identified by the mushroom-shaped smoke patterns. Such patterns form because of spanwise variations of streamwise velocity due to the different inwash and outwash regions associated with pairs of counter-rotating vortices. The stems of individual mushroom shapes mark the region of flow away from the wall surface between the vortices which make up one pair.

Possible various kinds of secondary instabilities of the Dean/Coriolis vortices may produce the Dean/Coriolis vortices with various different features in different parameter regions. The properties of disturbances triggering initial vortex development (such as their steadiness, uniformness along the spanwise direction etc.) may also lead to various different Dean/Coriolis vortices. Consequently, we may observe different mushroom-shaped smoke patterns due to single or combined effect of two causes. In a fully developed region at larger downstream locations, which the present work is mainly concerned with, the Dean/Coriolis vortices become fully developed and should be less sensitive to the initial disturbances because once initiated, vortex behaviour and development are strongly controlled by the centrifugal/Coriolis instabilities from the curvature/rotation of the channel. The different Dean/Coriolis

vortices observed in our experiments are, therefore, believed to be caused by their secondary instabilities.

The Dean/Coriolis vortices observed can be divided into two groups: symmetric and nonsymmetric vortices with respect to radial-streamwise planes. The symmetric Dean/Coriolis vortices appear usually at dynamic parameters close to their critical values for the onset of the Dean/Coriolis vortices. Such vortices are identified by mushroom *stems* which form the radial symmetry lines. The mushroom-shaped smoke patterns are mirror images on each side of the line. In other words, the two vortices in each pair are similar. The nonsymmetric Dean/Coriolis vortices are often observed at higher dynamic parameters. When viewed in radial-spanwise planes, such vortices are distorted generally by spanwise and/or radial unsteadiness in the flow such that no symmetric line is observed.

symmetric Dean/Coriolis vortices Examples of smoke patterns from symmetric Coriolis vortex flow are illustrated in Fig.6.13. They are obtained for $Ts-D$ at $Re = 1000, Ro = 0.066$; $Re = 1000, Ro = 0.111$ and $Re = 1500, Ro = 0.107$. The patterns are especially interesting because they show only small unsteadiness. No significant time variations on shape and size can be observed. The narrow *mushroom stems* indicate narrow innerwash regions from the high pressure wall. And the large *mushroom petals* imply large, spread-out sidewash and outwash regions. A comparison of the smoke patterns at $Re = 1000, Ro = 0.066$ with those for $Re = 1000, Ro = 0.111$ and $Re = 1500, Ro = 0.107$ shows that the location of the

symmetric Coriolis vortices can be at the center or off the center of the high pressure wall for a square cross section.

The mushroom-shaped smoke patterns at $Re = 452$, $Ro = -1.718$ in Fig. 6.11 are also for symmetric Coriolis vortex flow. An additional set is presented in Fig.6.14. They are obtained for $Ts-B$ at $Re = 193.6$, $Ro = -1.18$. The fairly uniform size and shape at different spanwise positions indicate that the flow is fully developed since otherwise the difference will result from the sensitivity of developing vortices to initial disturbances.

A comparison of the smoke patterns in Fig.6.13 with those in Fig.6.11 (at $Ro = -1.72$) and Fig.6.14 shows that the shape of the symmetric Coriolis vortices changes with the operating parameters. This is consistent with the simulations (Finlay 1990) which indicate that vortex shape changes occur with spanwise wavenumber, Reynolds number and rotation number.

radially oscillating Dean/Coriolis vortex flow Two examples of radially oscillating Coriolis vortices are presented in Fig.6.15. They occur at $Re = 600$, $Ro = -1.37$ for $Ts-A$ and at $Re = 193.6$, $Ro = -0.663$ for $Ts-B$ respectively. At this stage of flow, very little spanwise oscillation is present and mushroom patterns seem to move almost exclusively in the radial direction. When these oscillations appear by themselves, they are mostly symmetric Coriolis vortices, and the radial unsteadiness decreases in magnitude as overall average vortex height increases.

The vortex heights at different span locations in Fig.6.15.(b) show relatively small variations in height and spacing. This indicates that the Coriolis vortices are fully developed along the streamwise direction and the oscillation is caused by the secondary instability of the Coriolis vortices.

spanwisely oscillating Dean/Coriolis vortex flow The mushroom-shaped smoke patterns at $Re = 500, Ro = 0$ for *Ts-A* and at $Re = 581, Ro = -1.12$ for *Ts-B* are shown in Fig.6.16. The time variations in shape show that very little radially oscillation is present and mushroom patterns seem to move almost exclusively in the spanwise direction. When these oscillations occur by themselves, they are mostly symmetric. The uniform height and spacing in spanwise direction provide evidence of fully developed vortices. As well, the oscillation is believed to be caused by the secondary instability.

simultaneous spanwise and radial oscillating Dean/Coriolis vortex flow
The Mushroom-shaped smoke patterns, oscillating simultaneously in the spanwise and radial directions are observed without a twisting motion. Two examples are shown in Fig.6.16 for *Ts-A* at $Re = 550, Ro = 0$ and *Ts-D* at $Re = 1000, Ro = 0.194$. The vortices in this vortex flow are also nearly symmetric, and generally have larger-scale oscillations and greater unsteadiness than the smoke patterns identified with radial, span or twisting modes.

twisting Dean/Coriolis vortex flow Finlay *et al.* (1988) and Finlay (1990) simulated curved and rotating channel flows using three-dimensional incompressible time-dependent Navier-Stokes equations. They found evidence that the Dean and Coriolis vortices develop two different types of travelling waves in the streamwise direction. Undulating Dean/Coriolis vortex flow contains long streamwise wavelengths and very small growth rates which make them difficult to observe experimentally. Twisting Dean/Coriolis vortex flow contains much shorter streamwise wavelengths than undulating Dean/Coriolis vortex flow. This makes them to be observed more readily.

Streamwise fully developed travelling waves result in same events at one time but different streamwise location, as at one streamwise location but different times. With twisting, the vortex centers oscillate only a little in the spanwise direction. Most motion occurs in the radial direction as the vortices in one pair oscillate in shape and strength.

The smoke patterns for twisting Dean/Coriolis vortices are mushroom-shaped with a rocking type of motion. Examples of smoke patterns from twisting Dean/Coriolis vortices are presented in Fig.6.18. They were obtained at $Re = 1000, Ro = 0.309$ for *Ts-D*, at $Re = 600, Ro = 0$ for *Ts-A* and at $Re = 581, Ro = 0$ for *Ts-B*. It is observed that the twisting Dean/Coriolis vortices are nonsymmetric. The Reynolds number for the two cases with twisting Dean vortices ($Ro = 0$) are large than $1.96Re_c$ with Re_c as the critical Reynolds number for onset of the Dean vortices.

These are consistent with the numerical simulations by Finlay *et al.* (1988).

For *Ts-B*, we found that the rocking motion is rarely observed alone, rather it is usually observed in conjunction with at least one other mode of oscillation. In many cases, rocking vortex pairs are adjacent to pairs with a different type of motion.

small vortex pairs Using linear stability theory and spectral methods, Guo & Finlay (1991) examined the Eckhaus stability of the Dean/Coriolis vortices. Their results have also been confirmed by nonlinear flow simulations. They found that the Eckhaus stability boundary is a small closed loop. Outside the boundary, the Eckhaus instability causes the vortex pair to split apart by the formation of a new vortex pair or merge together, and no vortex flow is stable to spanwise disturbances when $Re > 1.7Re_c$. When Re is not too high ($Re < 4Re_c$), the wavenumber of vortices are selected by the Eckhaus instability. Similar phenomena have also been reported by Finlay *et al.* (1988), Finlay (1990) and Bland & Finlay (1991) in their numerical simulations of channel flows with curvature or rotation.

The vortex splitting/merging and readjustment of the spanwise wavenumber are clearly evidenced in the radial-span cross section by the presence of small vortex pairs at some instants. Examples are shown in Fig.6.11 for *Ts-B* at $Re = 452$, $Ro = 0$, -0.0914 , -0.384 and -0.978 . Additional examples are shown in Fig.6.19 for *Ts-B* at $Re = 193.6$, $Ro = 0.150$; $Re = 323.3$, $Ro = -0.819$; $Re = 581$, $Ro = -0.696$ and 1.12.

complex oscillating models In some cases, usually with high dynamical parameters, the oscillation of the Dean/Coriolis vortices appear to be so chaotic that mushroom-shaped patterns are barely recognizable or can not be identified clearly. Photographs of such patterns are shown in Fig.6.20 for *Ts-B* at $Re = 193.6$, $Ro = 0$ and $Re = 581$, $Ro = 0.554$.

flow patterns in rotating curved channels with slow negative rotation

For flows in a curved channel rotating spanwisely with a low negative rotation speed, there are two potentially unstable regions alternating with two stable layers (§6.2). The competition of the two destabilizing mechanisms causes the flow to become very complicated. We have already seen two examples of such flows in Fig.6.10 ($Ro = -0.792$) and in Fig.6.11 ($Ro = -0.0914$) for *Ts-B* with aspect ratio of 10. Such flows for *Ts-A* are presented in Fig.6.21 for four pairs of Re and Ro . It is worthy to note that the flows in Fig.6.21 are qualitatively similar to those predicted numerically in the region where overall, the Coriolis forces just neutralize the centrifugal forces. However, a further detailed stability analysis is required in this region to fully understand the features of such flows.

6.6 Concluding Remarks

An experimental apparatus was designed and constructed especially to visualize the fully developed stabilizing/destabilizing flows in channels with curvature, span-wise rotation or both in terms of end-view of flow at the exit of the test sections. Several different test sections were used, and the results shown here are some typical ones for four test sections. Although the main objective is to obtain some general features about the stabilizing/destabilizing flows from the visualization experiments, a generalized Rayleigh criterion has been formulated about the primary instability of flows in rotating curved channels to understand some experimental results.

The stability of flows in rotating curved channels is, on average, characterised by three parameters, namely, curvature ratio σ , Reynolds number Re and rotation number Ro . For large values of $|Ro|$, both primary and secondary instabilities exhibit a reasonable symmetry between the directions of rotation. As well, the flows at large $|Ro|$ were found to be controlled by the secondary instabilities rather than the primary instability. In particular, the secondary instabilities lead the flow at large $|Ro|$ to be unsteady and turbulent somewhat like the *bursting* flow in the turbulent boundary layers. This appear to produce the low Reynolds number turbulent flows.

For flows in rotating curved channels with slow negative rotation, there exist two potentially unstable regions alternating by two stable regions. The competition of the two instability mechanisms leads to a complicated flow. The detailed

nature of such flows remains to be explored in future through stability analysis and experimental measurements.

The Dean/Coriolis vortices can also exist on the unstable side in the relaminarization process of the flow from turbulent to laminar. In particular, their formation in the flows with high Reynolds number annihilates the turbulence, and leads to a high Reynolds number laminar flow.

Pairs of counter-rotating Dean/Coriolis vortices are observed as the mushroom-shaped smoke patterns. The narrow *mushroom stems* indicates the narrow outwash flow regions while large *mushroom petals* imply the large, spread-out sidewash and inwash regions. The fairly steady, symmetric Dean/Coriolis vortices have been observed in some parameter regions. They can appear in the center or off the center of the high pressure wall for a square cross section. As well, their size and shape change with the operating parameters.

Secondary instabilities of the Dean/Coriolis vortices lead them to oscillate in various forms even in the streamwise fully developed flow regions. We have observed several oscillating modes including (1) one with mostly radial motion, (2) one with mostly spanwise motion, (3) one with significant simultaneous radial and spanwise motion, and (4) one with rocking motion. In addition, the oscillating modes are also present with motion so complicated that they are difficult to describe from the flow visualization results. The experimental results are to be confirmed theoretically and numerically in the future.

In radial-spanwise planes, the twisting Dean/Coriolis vortices are evidenced by nonsymmetric mushroom-shaped smoke patterns with rocking motion. The region where the twisting Dean/Coriolis vortices are observed appears to be in agreement with that predicted by Finlay *et al.* (1988) and Finlay (1990). This kind of vortex flow differs from that with simultaneous radial and spanwise motion mainly in three aspects: (i) the twisting vortices are nonsymmetric but the simultaneous radial and spanwise oscillating vortices are symmetric, (ii) with twisting, the spanwise locations of vortex centers oscillating only a little. With simultaneous radial and spanwise oscillating, the spanwise locations of vortex centers can oscillate significantly, and (iii) the simultaneous radial and spanwise oscillating Dean/Coriolis vortices usually have larger-scale oscillation and greater unsteadiness than the twisting Dean/Coriolis vortices.

Vortex pairs sometimes seem to appear and disappear as indicated by small vortex pairs observed temporarily in radial-spanwise planes for some experimental conditions. This is believed to be caused by the Eckhaus instability discussed by Guo & Finlay (1991).

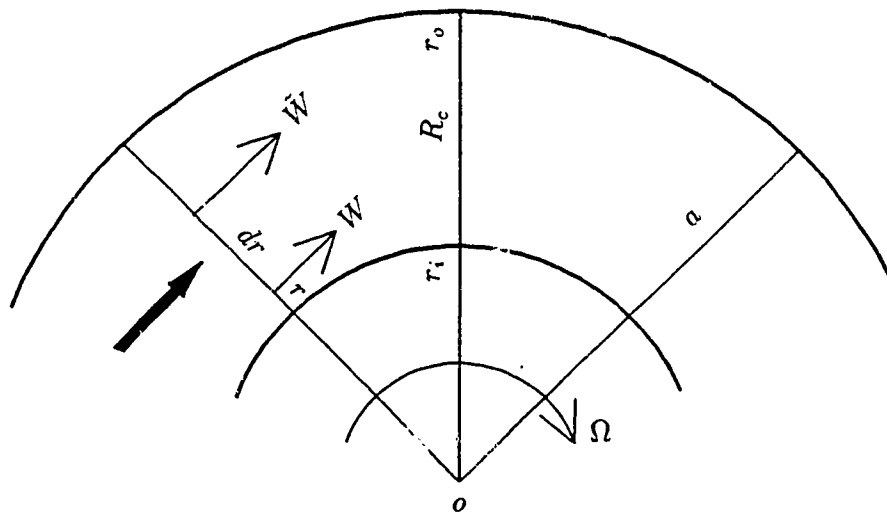


Figure 6.1. Sketch relating to displaced particle discussion

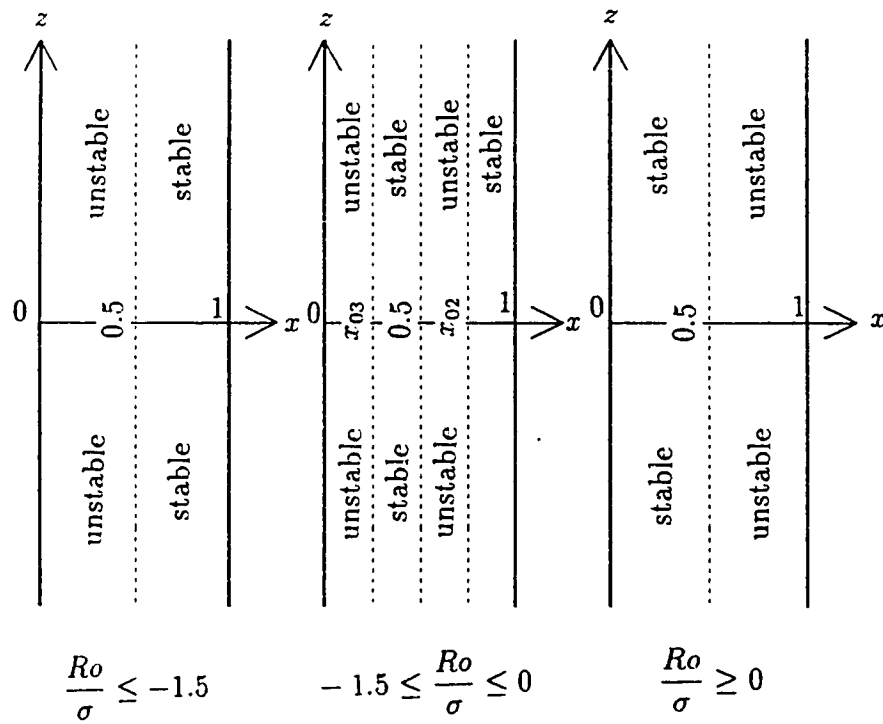


Figure 6.2. Stable/unstable regions for the case of small gap with low rotation rate

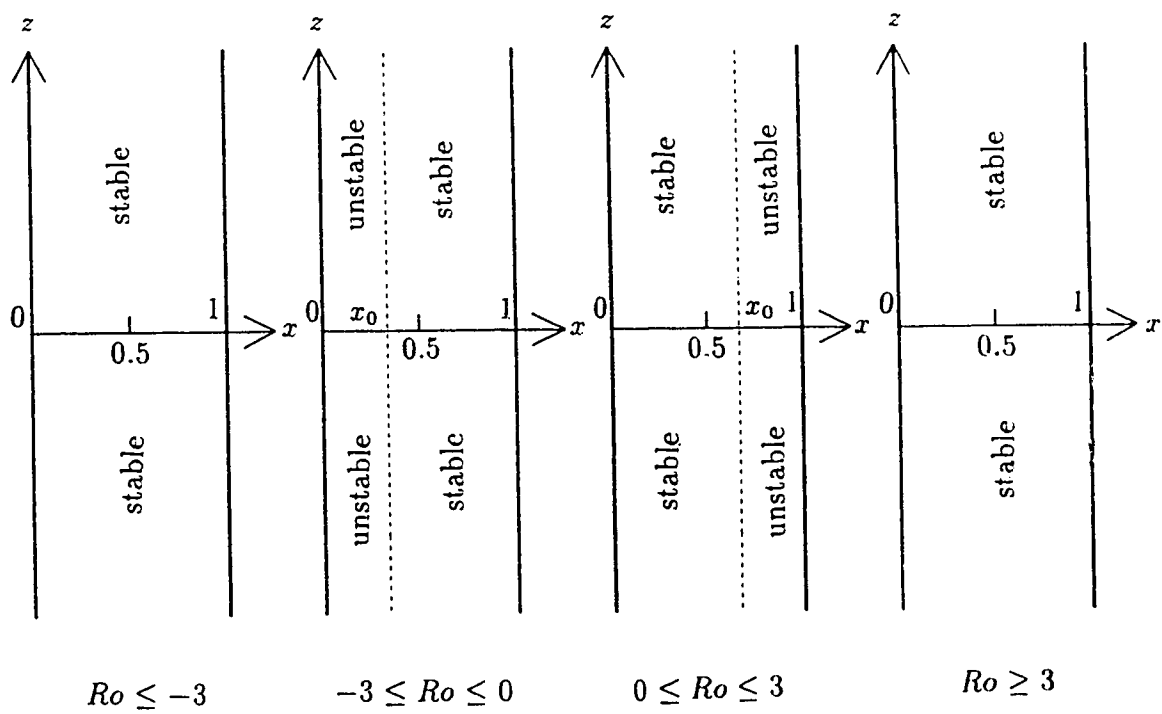


Figure 6.3. Stable/unstable regions for the case of small gap with high rotation rate

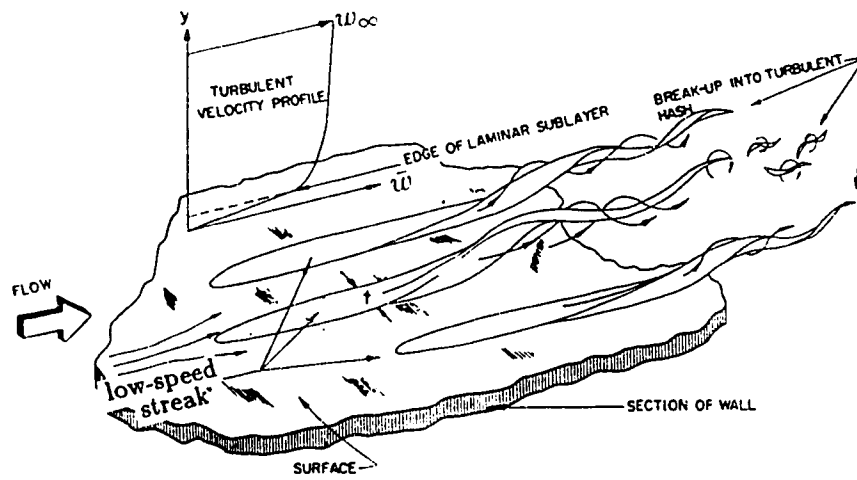


Figure 6.4. Sketch of flow model in wall layers of fully developed turbulent boundary layer (Kline & Runstadler 1959)

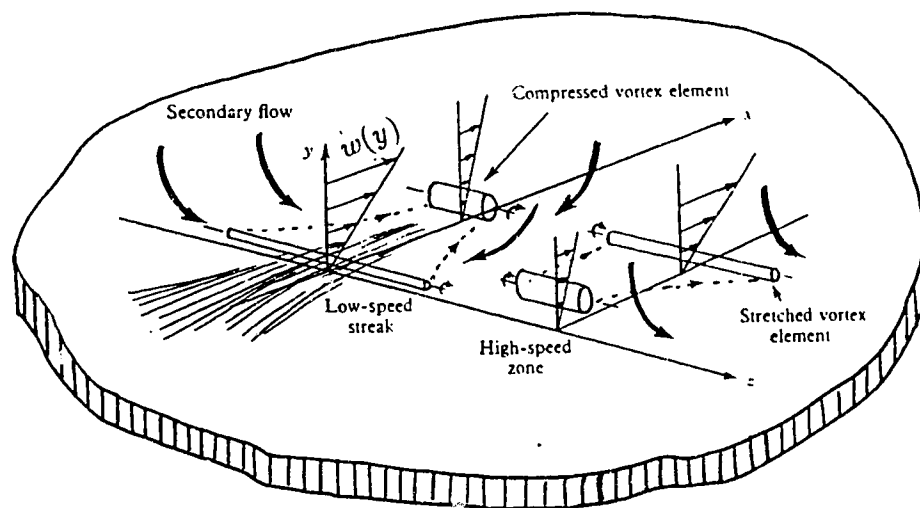


Figure 6.5. The mechanics of streak formation (Kline *et. al.* 1967)

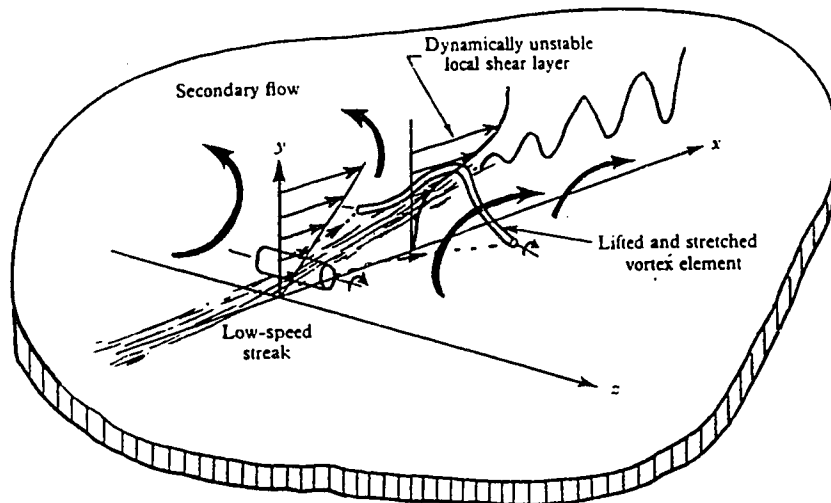


Figure 6.6. The mechanics of streak breakup (Kline *et. al.* 1967)

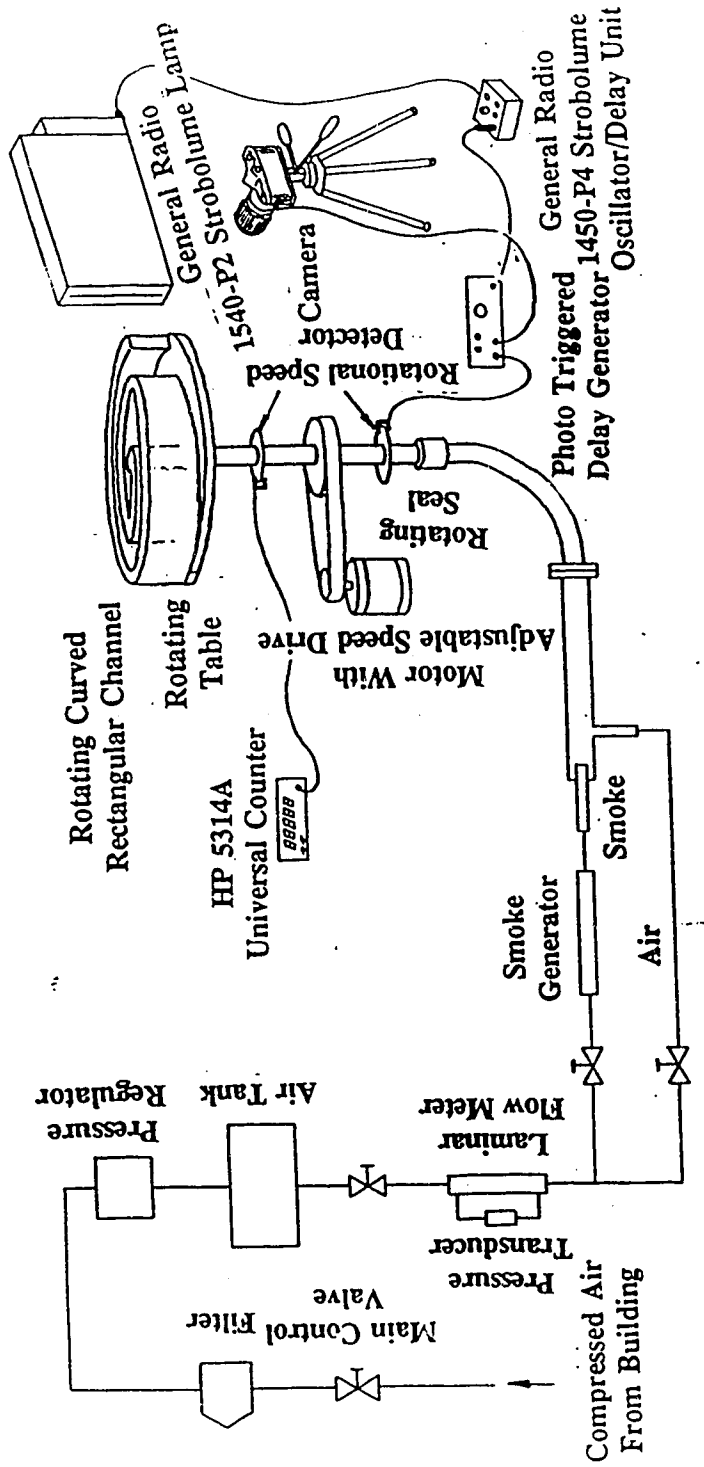


Figure 6.7. Schematic diagram of experimental apparatus

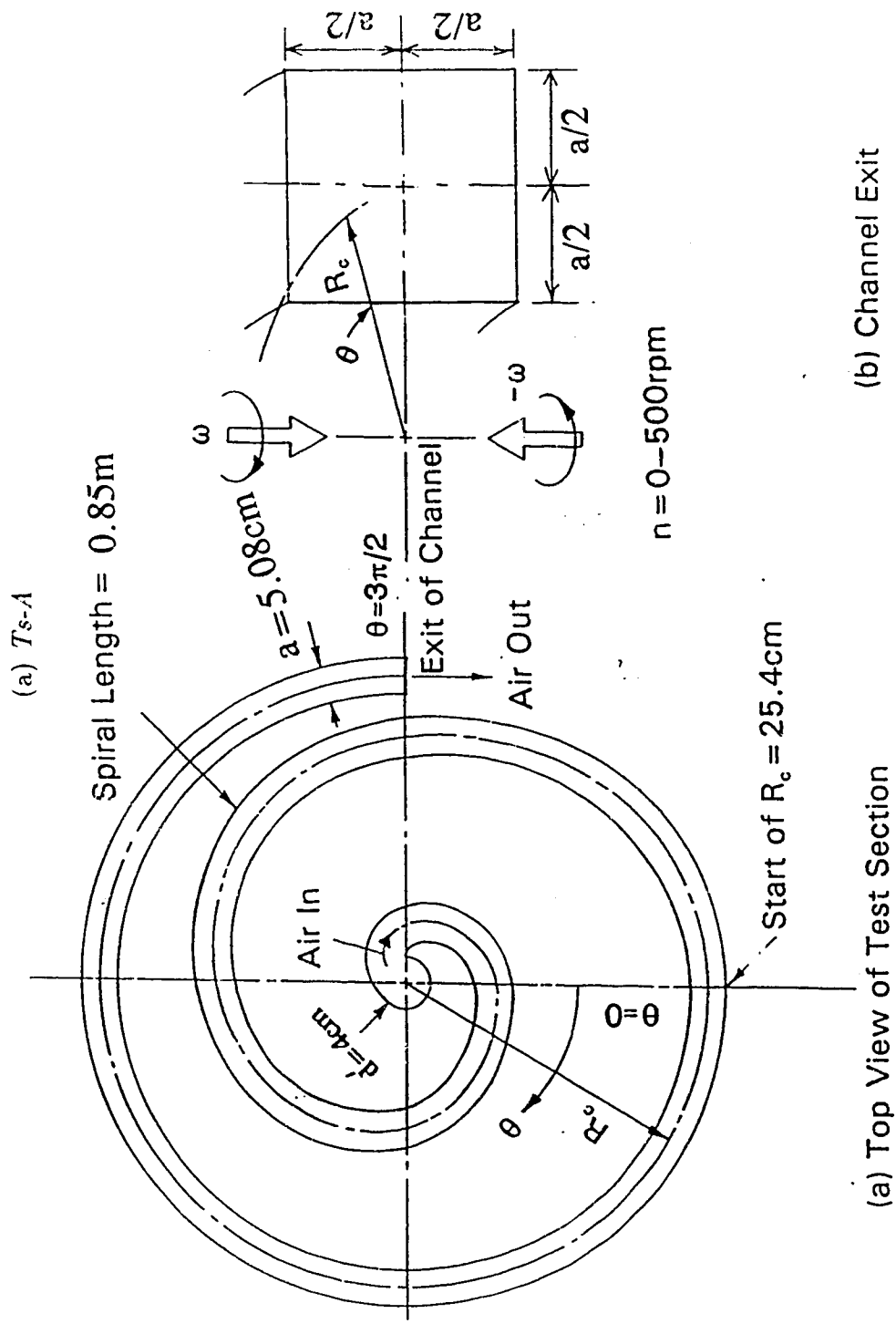


Figure 6.8. Four typical test sections

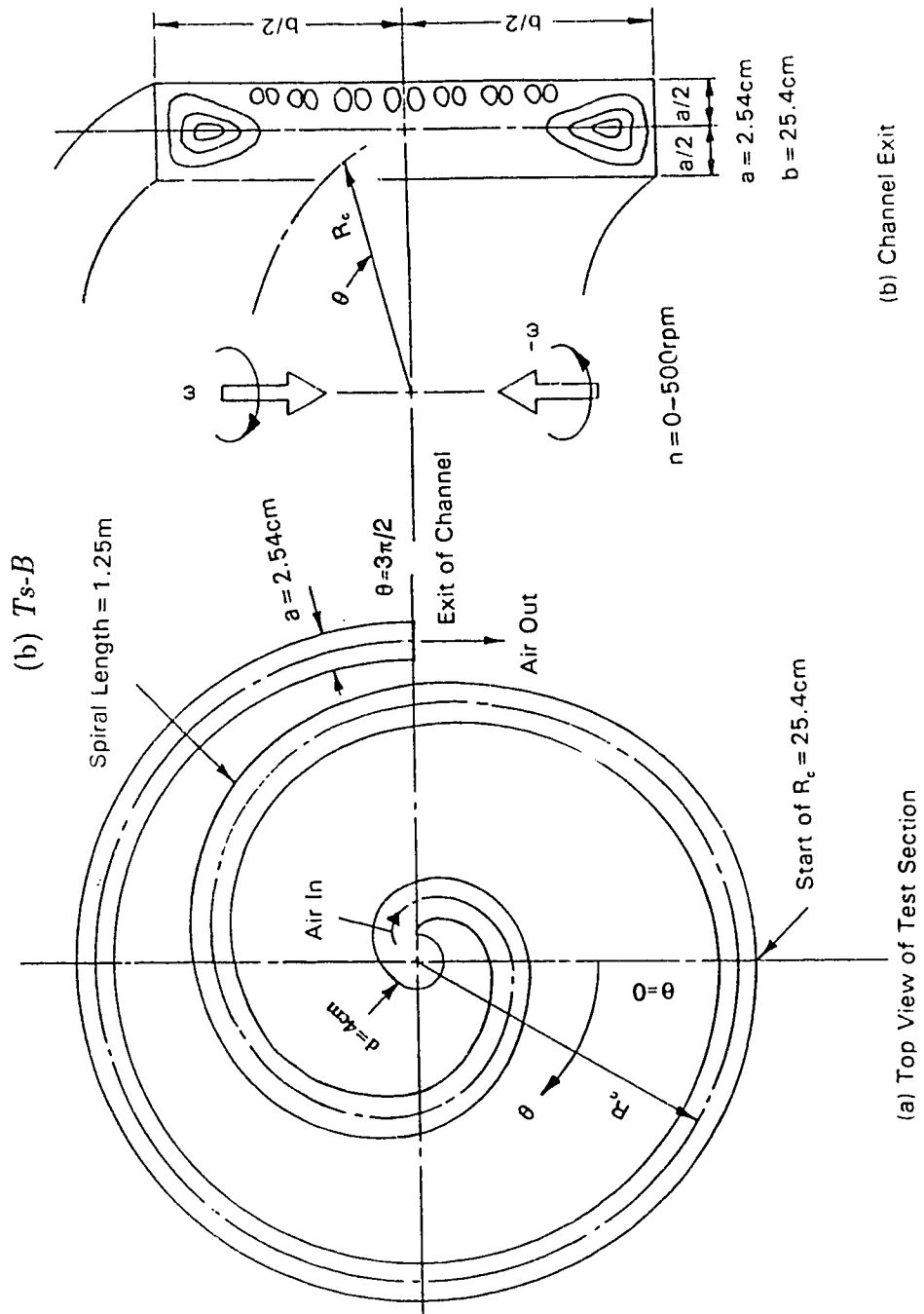


Figure 6.8. Four typical test sections

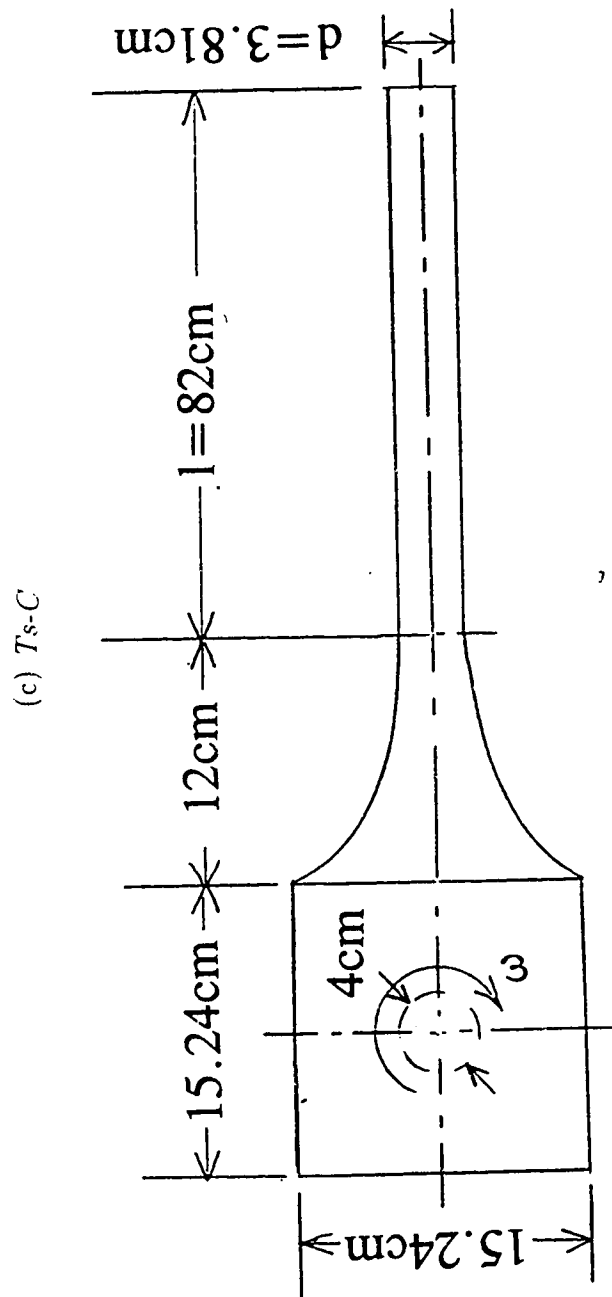


Figure 6.8. Four typical test sections

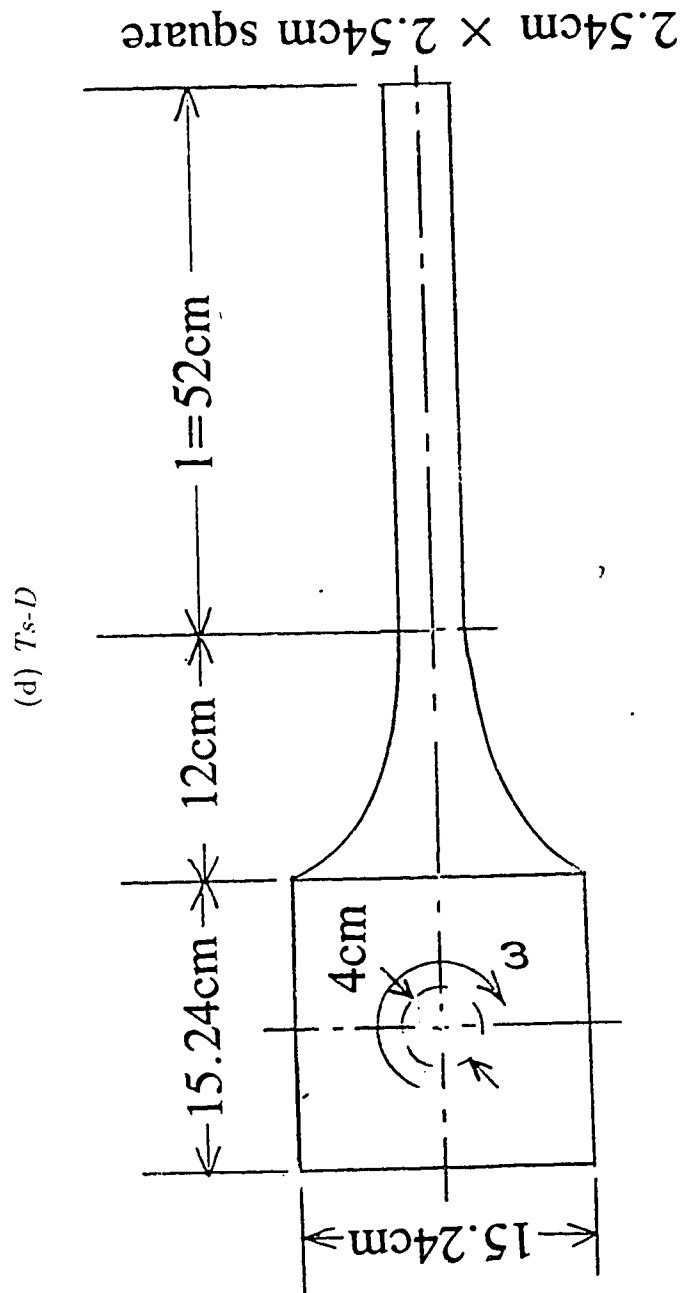
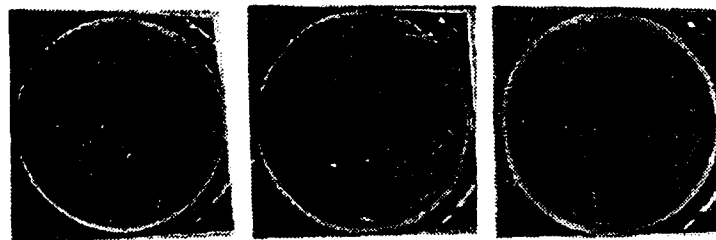


Figure 6.8. Four typical test sections



$Ro = 0$

$Ro = 0.142$

$Ro = 0.367$

(a) $Re = 4500$ ($Ts-C$)



$Ro = 0$

$Ro = 0.274$

$Ro = 9.77$

(b) $Re = 600$ ($Ts-A$)

Figure 6.9. Variations of flows with Ro

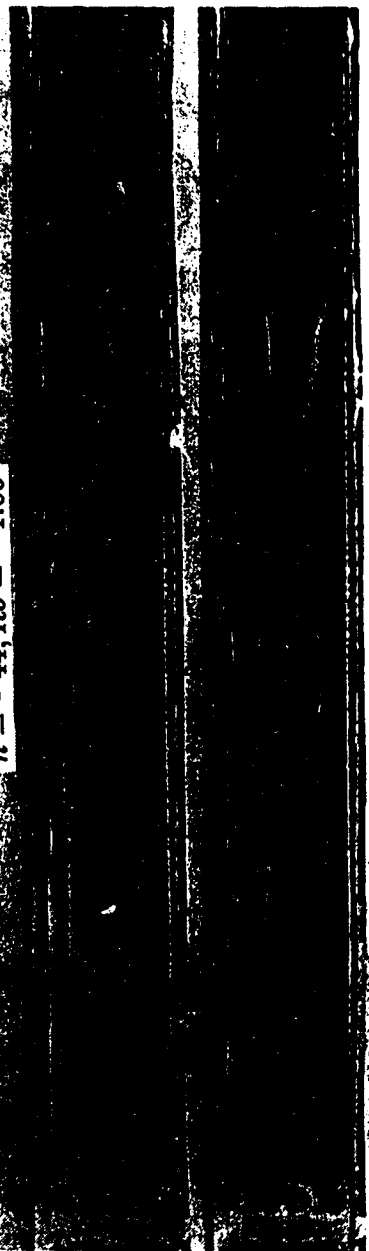
$n = 0, Ro = 0$



$n = -21, Ro = -0.792$



$n = -44, Ro = -1.66$





$n = -215, Ro = -8.11$

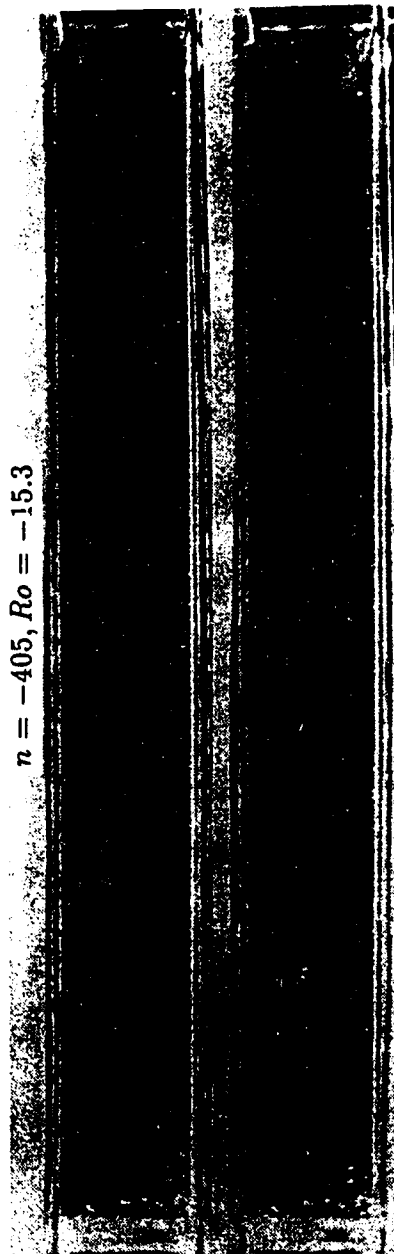


$n = -302, Ro = -11.4$

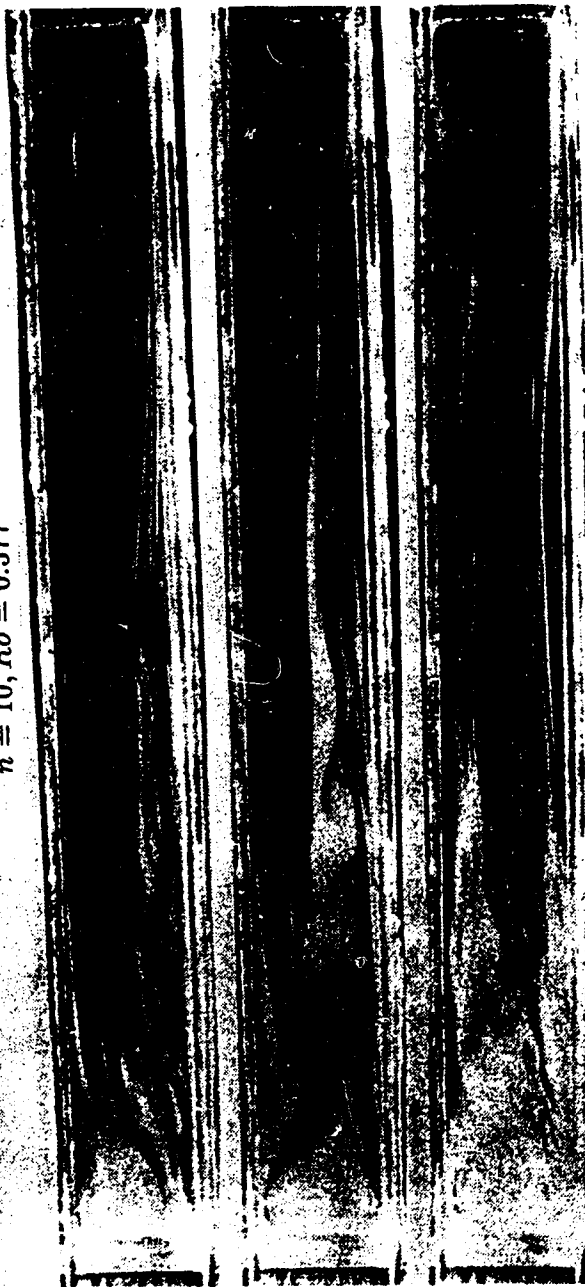


$n = -366, Ro = -13.8$

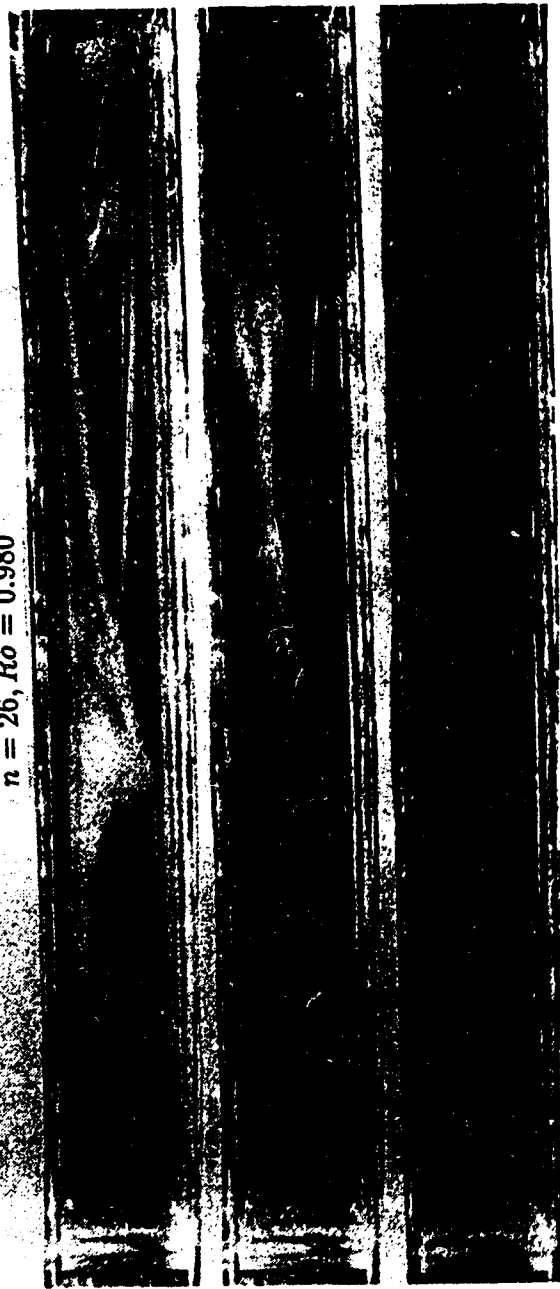




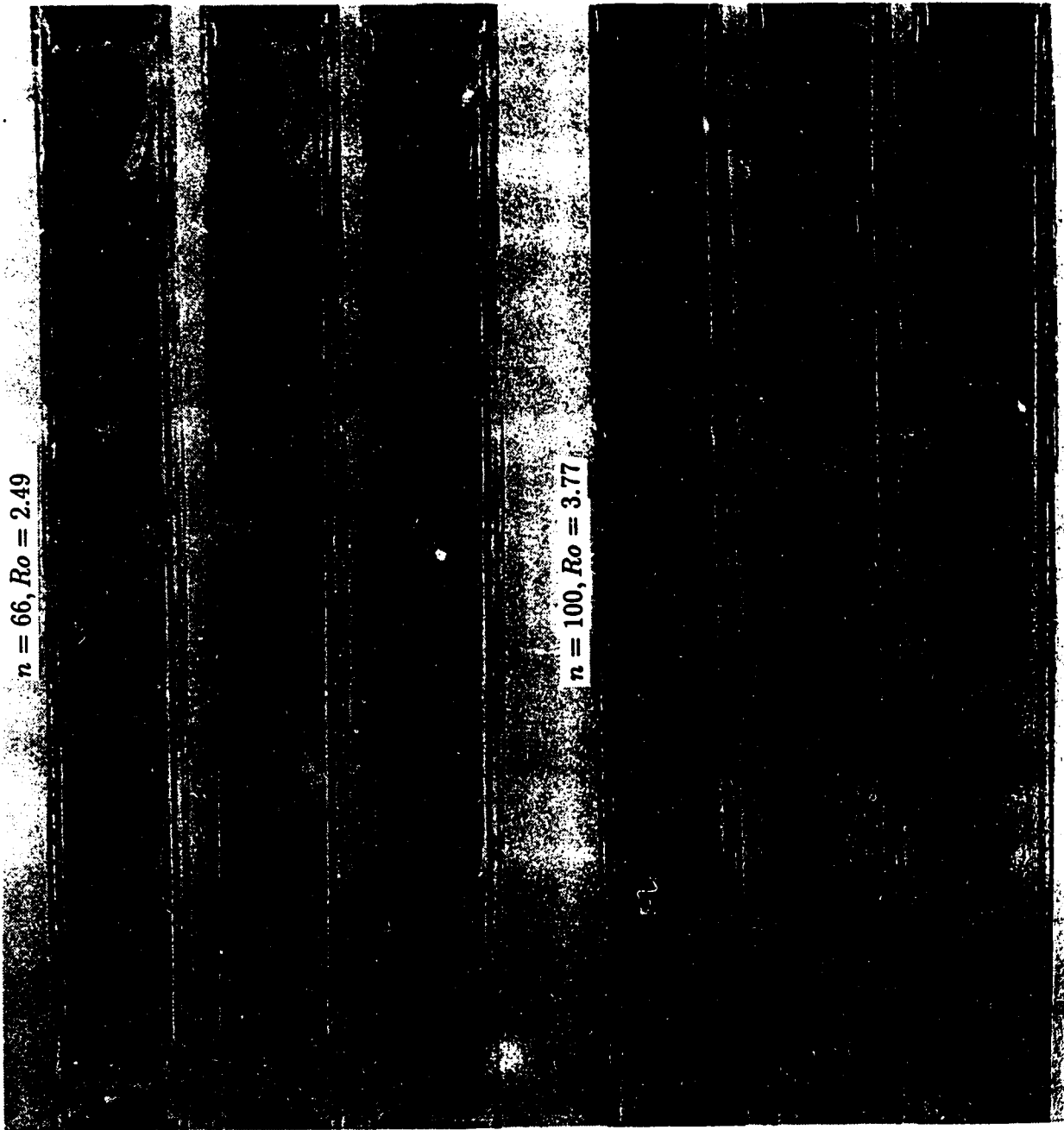
$n = 10, Ro = 0.377$



$n = 26, Ro = 0.980$







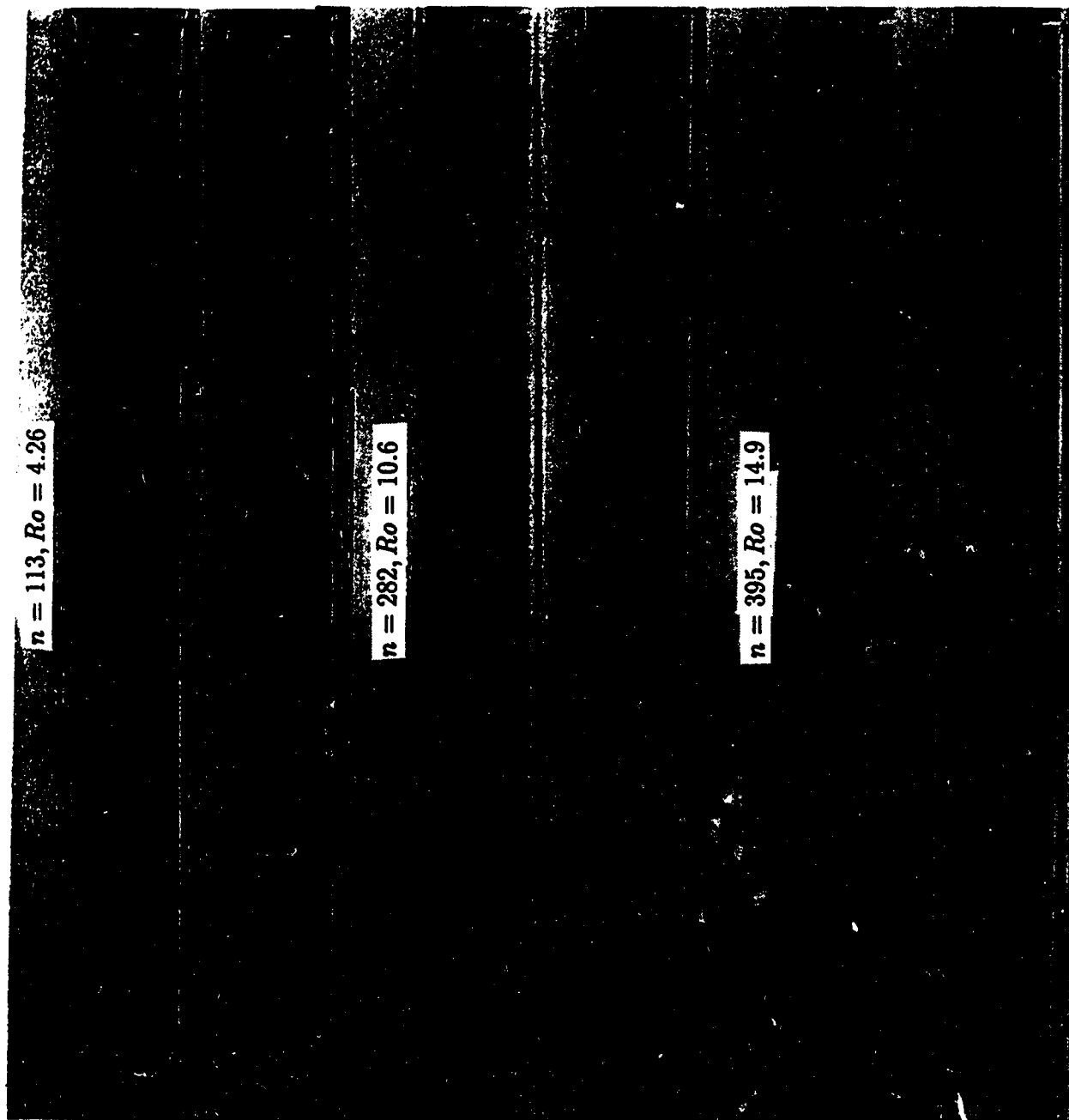
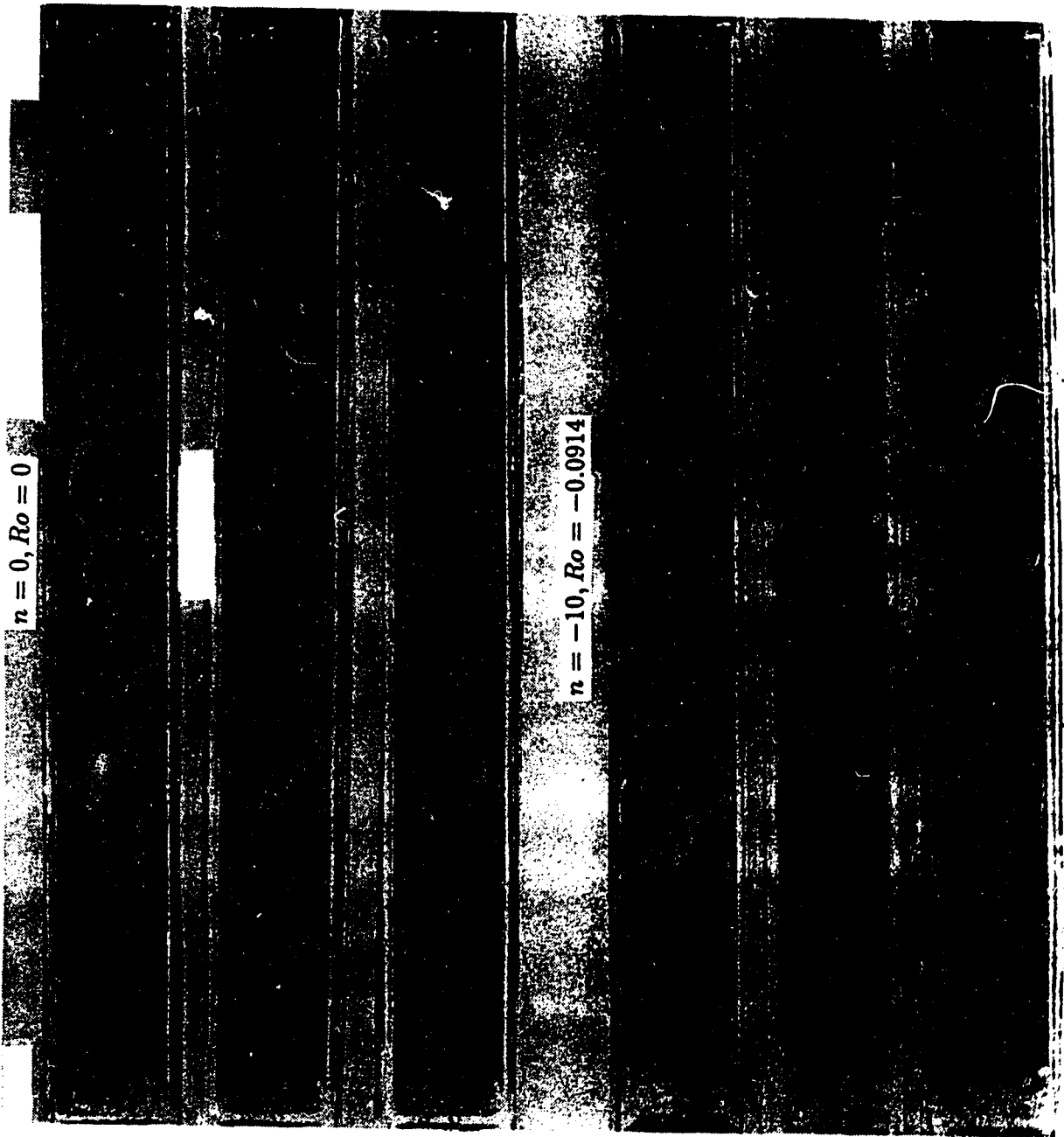


Figure 6.10. Variations of flows with Ro and time at $Re = 110$ for $Ts-B$

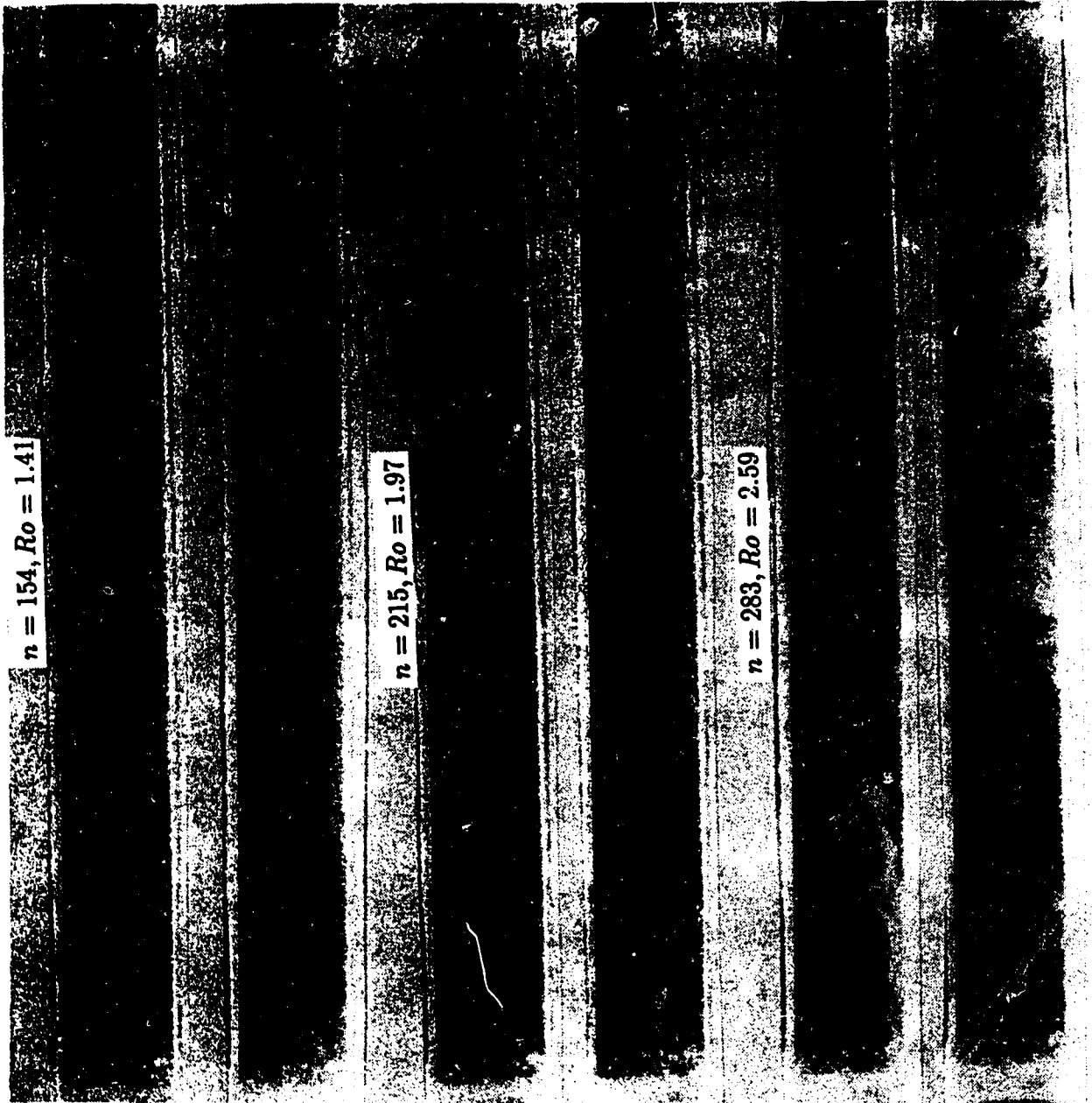














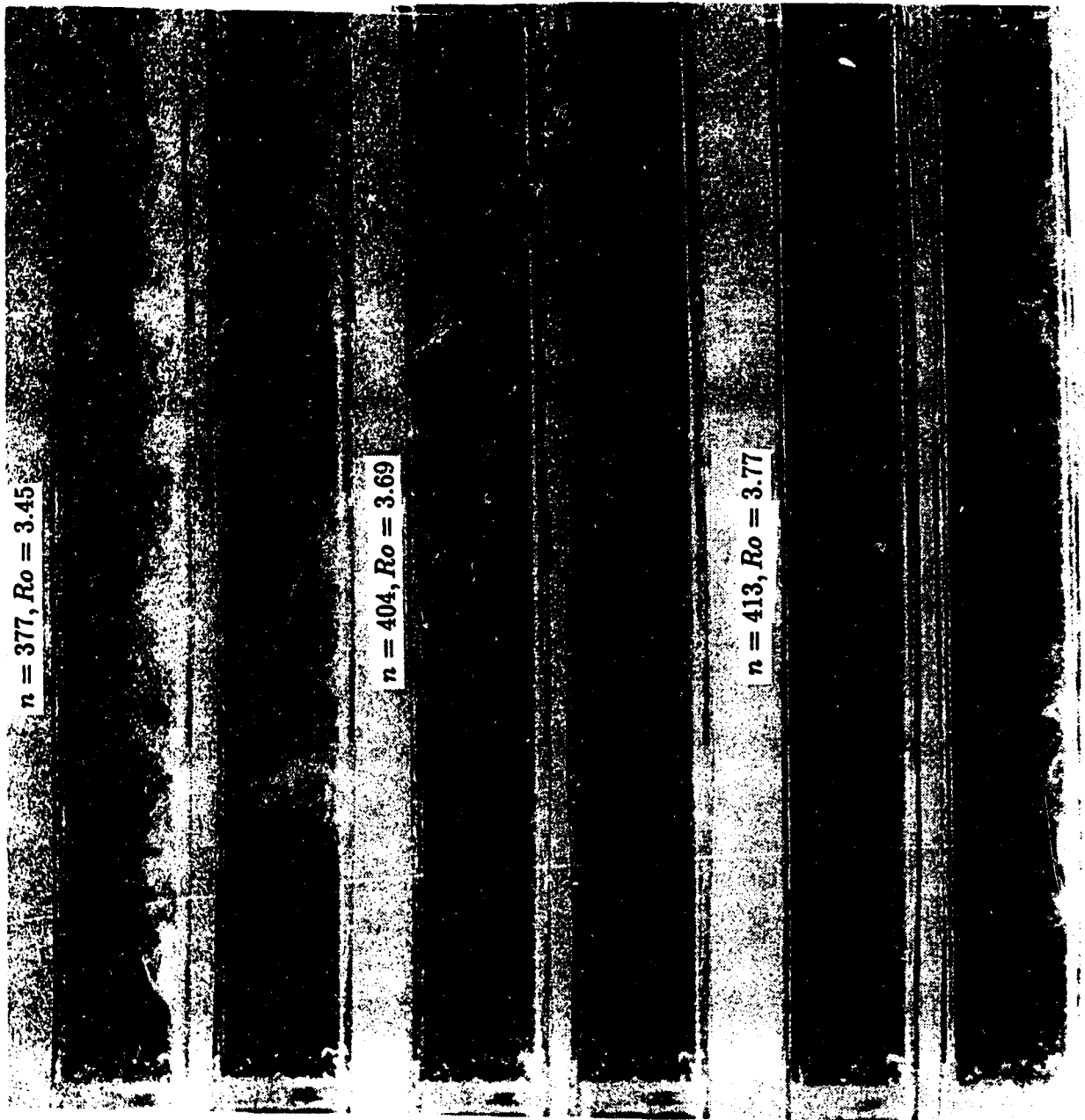


Figure 6.11. Variations of flows with Ro and time at $Re = 452$ for $Ts-B$

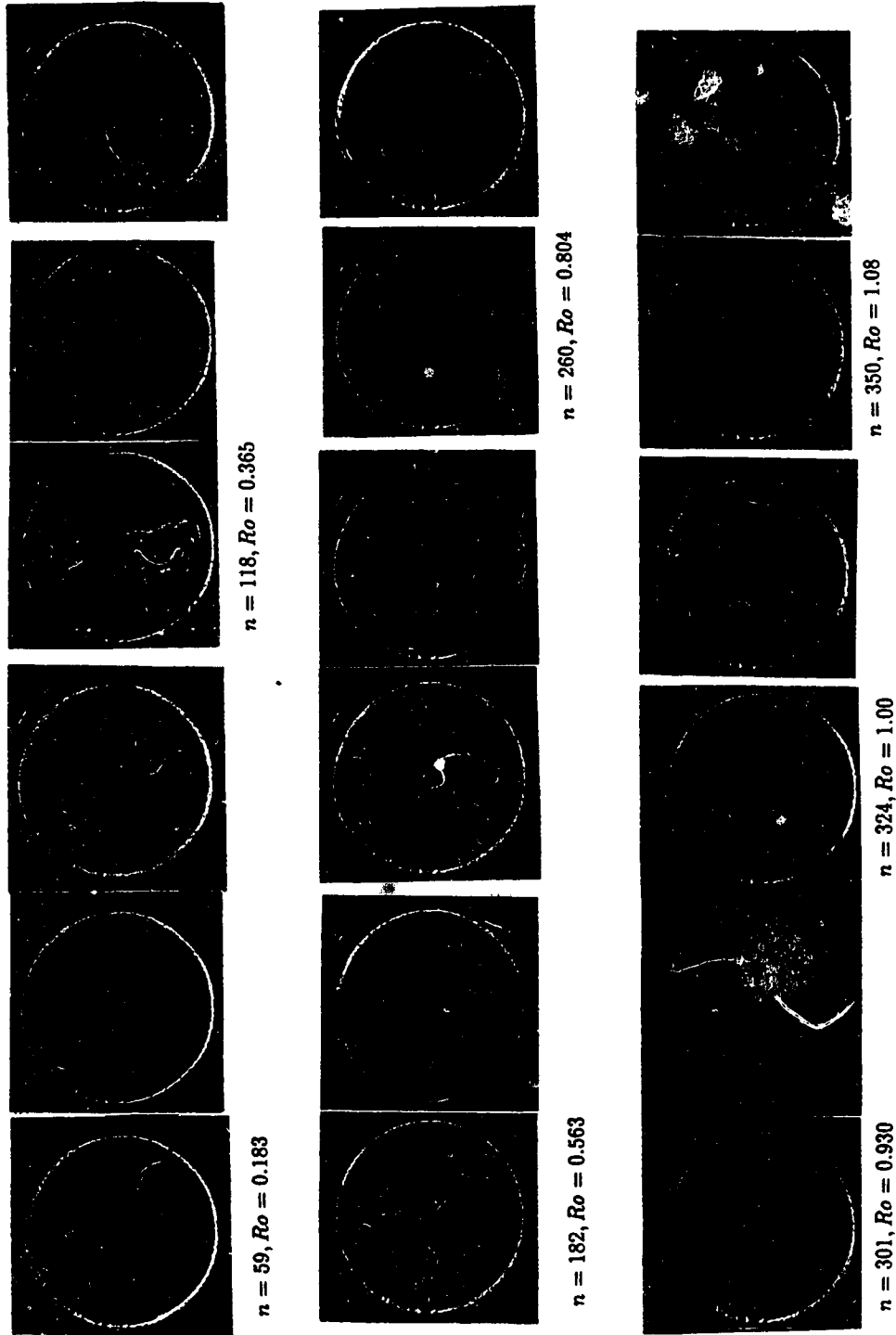


Figure 6.12. Variations of flows with Ro and time at $Re = 3000$ for $Ts-C$

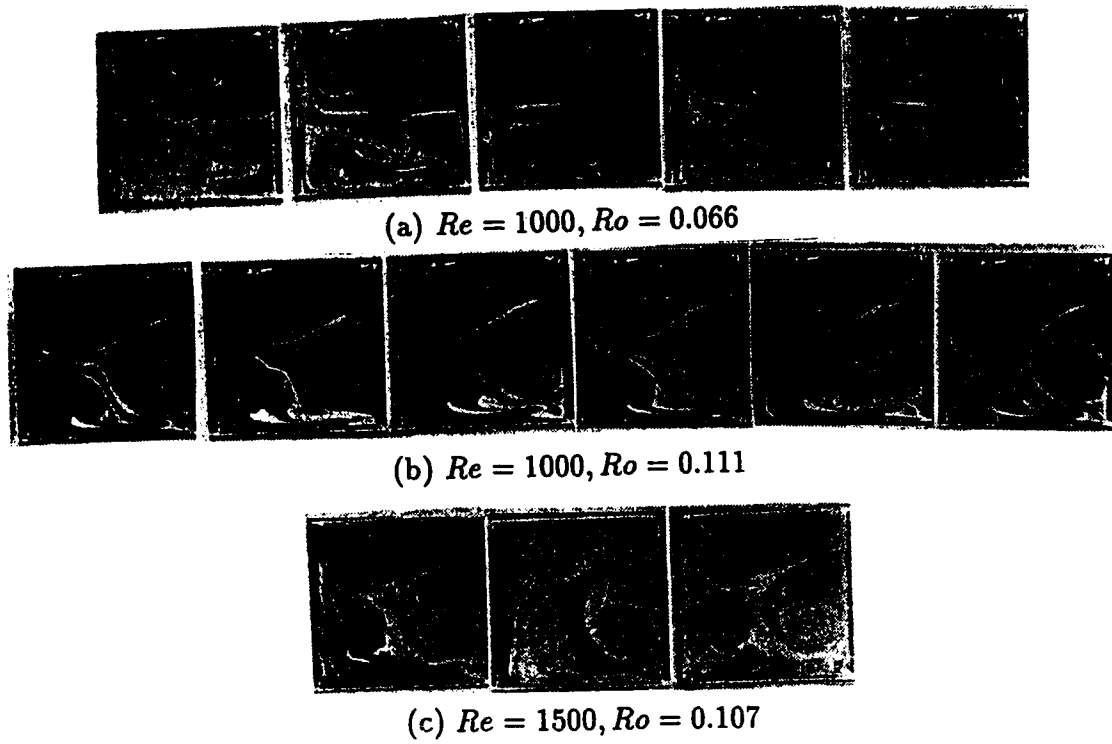
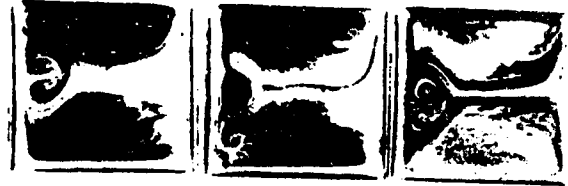


Figure 6.13. Symmetric Coriolis Vortices for $Ts-D$



Figure 6.14. Symmetric Coriolis Vortices at $Re = 193.6$, $Ro = -1.18$ for $Ts-B$)



(a) $Re = 600, Ro = -1.37$ ($Ts-A$)



(b) $Re = 193.6, Ro = -0.663$ ($Ts-B$)

Figure 6.15. Radial oscillating Coriolis vortices



(a) Spanwise oscillating Dean vortices
at $Re = 563$, $Ro = 0$ for $Ts-A$

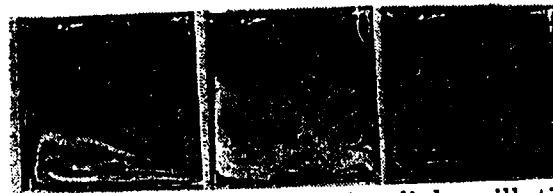


(b) Spanwise oscillating Coriolis vortices
at $Re = 581$, $Ro = -1.12$ for $Ts-B$

Figure 6.16. Spanwise oscillating Dean/Coriolis vortices



(a) Simultaneous spanwise and radial oscillating Dean vortices at $Re = 550, Ro = 0$ for $Ts-A$



(b) Simultaneous spanwise and radial oscillating Coriolis vortices at $Re = 1000, Ro = 0.194$ for $Ts-D$

Figure 6.17. Simultaneous spanwise and radial oscillating Dean/Coriolis vortices



(a) Twisting Coriolis vortices at $Re = 1000, Ro = 0.309$ for $Ts-D$



(b) Twisting Dean vortices at $Re = 600, Ro = 0$ for $Ts-A$



(c) Twisting Dean vortices at $Re = 581, Ro = 0$ for $Ts-B$

Figure 6.18. Twisting Dean/Coriolis vortices

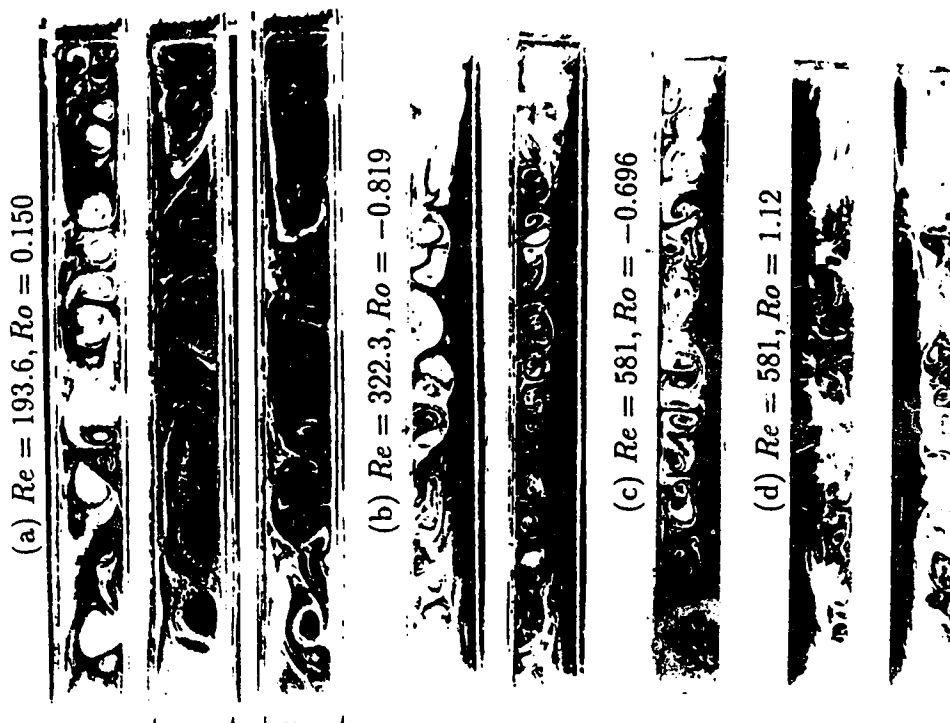


Figure 6.19. Small vortex pairs for $Ts-B$

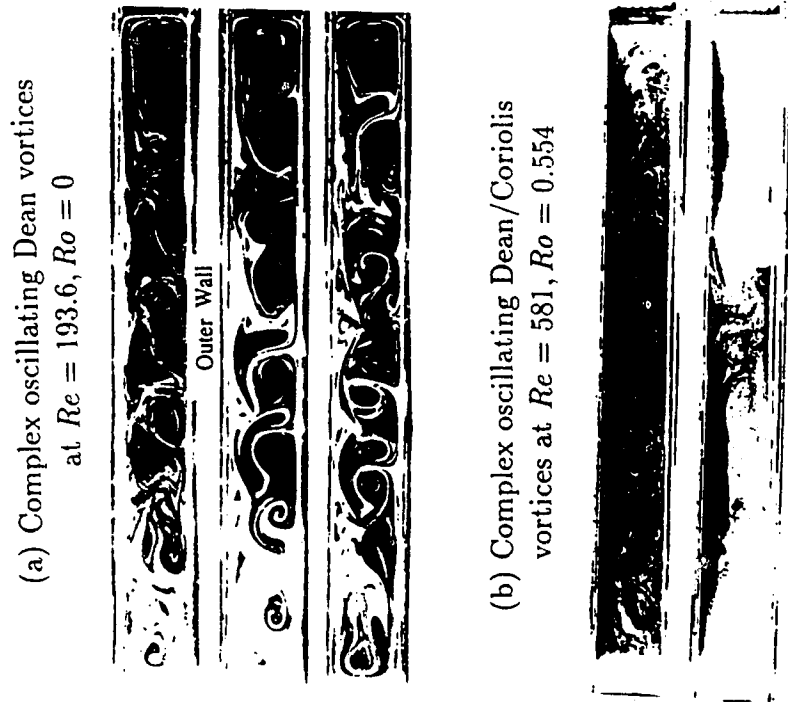


Figure 6.20. Complex oscillating Dean/Coriolis vortices for $Ts-B$



(a) $Re = 500, Ro = -0.330$



(b) $Re = 600, Ro = -0.274$



(c) $Re = 1000, Ro = -0.279$



(d) $Re = 2000, Ro = -0.165$

Figure 6.21. Flows in the region with two unstable layers for $Ts-A$

References

- [1] Alfredsson, P.A. & Persson, H. 1989 Instabilities in channel flow with system rotation. *J. Fluid Mech.* **202**, 543-557.
- [2] Badri Narayanan, M.A., Rajaopalan, S. & Narasimha, R. 1977 Experiments on the fine structure of turbulence. *J. Fluid Mech.* **80**, 237.
- [3] Bland, S.B. & Finlay, W.H. 1991 Transitions towards turbulence in a curved channel. *Phys. Fluids* **A3**, 106-114.
- [4] Bottaro, A. 1993 On longitudinal vortices in curved channel flow, *J. Fluid Mech.* **251**, 627-660.
- [5] Bradshaw, P. 1969 The analogy between streamline curvature and buoyancy in turbulent shear flow. *J. Fluid Mech.* **36**, 177-191.
- [6] Bradshaw, P. 1973 Effects of streamline curvature on turbulent flow. AGAR Dograph, 169.
- [7] Brewster, D.B., Grosberg, P. & Nissan, A.H. 1959 The stability of viscous flow between horizontal concentric cylinders. *Proc. Roy. Soc. A* **251**, 76-91.
- [8] Brown, G.L. & Thomas, A.S.W. 1977 Large structure in a turbulent boundary layer. *Phys. Fluids* **20**, S243-S252.
- [9] Chandrasekhar, S. 1961 *Hydrodynamic and Hydromagnetic Stability*, Oxford University Press, London.

- [10] Cheng, K.C., Nakayama, J. & Akiyama, M. 1977 Effect of finite and infinite aspect ratios on flow patterns in curved rectangular channels. In *Flow Visualization* (T. Asanuma, ed.), 181-186. Hemisphere.
- [11] Cheng K.C. & Wang L. 1994a Flow visualization and laminar heat transfer in rotating curved square channels, In *Heat Transfer 1994*, Procs. 10th International Heat Transfer Conference, Brighton, UK, Taylor & Francis, 4, Paper 8-IC4.
- [12] Cheng K.C. & Wang L. 1994b Visualization of secondary flow phenomena in rotating curved square channels with positive and negative rotations, In *Proc. Fourth Triennial International Symposium on Fluid Control, Fluid Measurement, Fluid Mechanics, Visualization and Fluidics* (Ed. by P. Hebrand). Aug.29-Sept.1, 1994, Toulouse, France, CERT, ONERA, 1, 561- 569.
- [13] Cheng K.C. & Wang L. 1994c Secondary flow phenomena in rotating radial straight pipes, In *Proc. of the 5th International Symposium on Transport Phenomena and Dynamics of Rotating Machinery*.
- [14] Cheng, K.C. & Wang L. 1993a Transition to turbulence and relaminarization phenomena in rotating radial straight pipes, *ASME: Visualization of Heat Transfer Processes*, HTD- Vol.252, 55-63.
- [15] Cheng, K.C. & Wang L. 1993b The effects of Coriolis and centrifugal forces on transition to turbulence in a rotating curved rectangular channel, In *Proc. of the 6th International Symposium on Transport Phenomena in Thermal Engineering*,

egell House, **2**, 1282-1289.

Cheng K.C. & Wang L. 1993c The effects of centrifugal and Coriolis forces on secondary flow phenomena in rotating curved square channels-visualization for positive and negative Rotations, *ASME: Experimental and Numerical Flow Visualization* FED-Vol.172, 359-367.

Cheng.K.C., Wang L. & Faulkner, B.G., 1992 Visualization of instability phenomena in a rotating curved rectangular channel with aspect ratio 10, In *Proc. of the Fourth International Symposium on Transport Phenomena and Dynamics of Rotating Machinery*, Vol.A, 549-560.

Dean, W.R. 1928 Fluid motion in a curved channel. *Proc. Roy. Soc. A* **121**, 392-420.

Elder, J.W. 1960 An experimental investigation of turbulent spots and breakdown to turbulence. *J. Fluid Mech.* **9**, 235-246.

Finlay, W.H. 1990 Transition to oscillatory motion in rotating channel flow. *J. Fluid Mech.* **215**, 209-227.

Finlay, W.H., Guo, Y. & Olsen, D. 1993 Inferring secondary flows from smoke or dry flow visualization: two case studies. *Phys. Fluids* **A5**, 2689-2701.

Finlay, W.H., Keller, J.B. & Ferziger, J.H. 1988 Instabilities and transition in curved channel flow. *J. Fluid Mech.* **194**, 417-456.

- [23] Gibson, R.D. & Cook, A.E. 1974 The stability of curved channel flow. *Q. J. Mech. Appl. Maths.* **27**, 149-160.
- [24] Guo, Y. & Finlay, W.H. 1991 Splitting, merging and wavelength selection of vortices in curved and/or rotating channel flow due to Eckhaus instability. *J. Fluid Mech.* **228**, 661-691.
- [25] Guo, Y. & Finlay, W.H. 1994, Wavenumber selection and irregularity of spatially developing nonlinear Dean & Görtler vortices. *J. Fluid Mech.* **264**, 1-40.
- [26] Hallen, R.M. & Johnston, J.P. 1967 The influence of rotation on flow in a long rectangular channel- an experimental study. Rep. MD. 18. Thermosci. Div., Dept. Mech. Eng., Stanford University, Stanford, California.
- [27] Hammerlin, G. 1958 Die stabilität der strömung in einem gekrümmten kanal. *Arch. Rat. Mech. and Anal.* **1**, 212-224.
- [28] Hart, J.E. 1971 Instability and secondary motion in a rotating channel flow. *J. Fluid Mech.* **45**, 341-353.
- [29] Hwang, G.J. & Jen, T.C., Convective heat transfer in rotating isothermal ducts. *Int. J. Heat Mass Transfer* **33**, 1817-1828.
- [30] Johnston, J.P., Halleen, R.M. & Lezius, D.K. 1972 Effects of spanwise rotation on the structure of two-dimensional fully developed turbulent channel flow. *J. Fluid Mech.* **56**, 533-557.

- [31] Kelleher, M.D., Flentie, D.L. & Mckee, R.J. 1980 An experimental study of the secondary flow in a curved rectangular channel. *J. Fluids Eng.* **102**, 92-96.
- [32] Klebanoff, P.S., Tidstrom, K.D. & Sargent, L.M. 1962 The three-dimensional nature of boundary-layer instability, *J. Fluid Mech.* **12**, 1-34.
- [33] Kline, S.J., Reynolds, W.C., Schraub, F.A. & Runstadler, P.W. 1967 The structure of turbulent boundary layers. *J. Fluid Mech.* **30**, 741-773.
- [34] Kline, S.J. & Runstadler, P.W. 1959 Some preliminary results of visual studies of the flow model of the wall layers of the turbulent boundary layer. *J. of Applied Mechanics* **81**, 166-170.
- [35] Kovasnay, L.S., Komoda, H. & Vasuedva, B.R. 1962 *Proc. Heat Transfer and Fluid Mech. Institute*, P.1, Stanford University Press.
- [36] Le Cunff, C. & Bottaro, A. 1993 Linear stability of shear profiles and relation to the secondary instability of the Dean flow. *Phys. Fluids* **A5**, 2161-2171.
- [37] Lezius, D.K. & Johnston, J.P. 1971 The structure and stability of turbulent wall layers in rotating channel flow. Rep. MD. 29. Thermosci. Div., Dept. Mech. Eng., Stanford University, Stanford, California.
- [38] Lezius, D.K. & Johnston, J.P. 1976 Roll-cell instabilities in rotating rectangular ducts. *J. Fluid Mech.* **122**, 251-271.

- [39] Lighthill, M.J. 1963 Introduction: boundary layer theory. In *Laminar Boundary Layers* (Ed. L. Rosenhead), Clarendon Press, Oxford, p.99.
- [40] Ligrani, P.M., Finlay, W.H., Fields, W.A., Fuqua, S.T. & Subramaman, C.S. 1992 Features of wavy vortices in a curved channel from experimental and numerical studies. *Phys. Fluids A4*, 695-709.
- [41] Ligrani, P. & Niver, R.D. 1988, Flow visualization of Dean vortices in a curved channel with 40 to 1 aspect ratio. *Phys. Fluids*, 31, 3605-3618.
- [42] Lin, C.C. 1955 *The Theory of Hydrodynamic Stability*. Cambridge, England.
- [43] Matsson, O.J.E. 1993a Channel Flow Instabilities Induced by Curvature and Rotation, Ph.D. Dissertation, Dept. of Mechanics/Fluid Physics, Royal Institute of Technology, Sweden.
- [44] Matsson, O.J.E. 1993b Time-dependent instabilities in curved rotating channel flow. *Phys. Fluids A5*, 1514-1516.
- [45] Matsson, O.J.E. & Alfredsson, P.H. 1990 Curvature- and rotation-induced instabilities in channel flow. *J. Fluid Mech.* **210**, 537-563.
- [46] Matsson, O.J.E. & Alfredsson, P.H. 1992 Experiments on instabilities in curved channel flow. *Phys. Fluids A4*, 1666-1676.
- [47] Ramaprian, B.R. & Shivaprasad, B.G. 1978 The structure of turbulent boundary layers along mildly curved surfaces. *J. Fluid Mech.* **85**, 273-303.

- [48] Rao, K.N., Narasimha, R. & Badri Narayanan, M.A. 1971 The bursting phenomenon in a turbulent boundary layer. *J. Fluid Mech.* **48**, 339-352.
- [49] Rayleigh, L. 1916 On convection current in a horizontal layer of fluid, when the higher temperature is on the under side. *Phil. Mag.* **32**, 529-546.
- [50] Reid, W.H. 1958 On the stability of viscous flow in a curved channel. *Proc. Roy. Soc. A* **244**, 186-198.
- [51] Reynolds, O. 1884 *Scientific Papers* **2**, 157, Cambridge University Press.
- [52] Rotta, J.C. 1967 Effect of streamwise wall curvature on compressible turbulent boundary layers,. *Phys. Fluids* **10**, S174-S180.
- [53] So, R.M.G. & Mellor, G.L. 1972 An experimental investigation of turbulent boundary layers along curved surfaces. NASA Contract. Rep. NASA CR-1940.
- [54] Speziale, C.G. 1982 Numerical study of viscous flow in rotating ducts. *J. Fluid Mech.* **122**, 251-271.
- [55] Speziale, C.G. 1986 The effect of the earth's rotation on channel flow. *J. Appl. Mech.* **53**, 198-202.
- [56] Speziale, C.G. & Thangam, S. 1983 Numerical study of secondary flows and roll- cell instabilities in rotating channel flow. *J. Fluid Mech.* **130**, 377-395.
- [57] Stuart, J.T. 1965 *NPL Sero. Rept.* 1147.

- [58] Swinney, H.L. & Gollub, J.P. 1985 Introduction. In *Hydrodynamic Instabilities and the Transition to Turbulence* (2nd edn.) (Ed. by Swinney, H.L. & Gollub, J.P.), **45**, 1-6, Springer.
- [59] Tomann, H. 1968 Effects of streamwise wall curvature on heat transfer in a turbulent boundary layer. *J. Fluid Mech.* **33**, 283-292.
- [60] Tritton, D.J. & Davies, P.A. 1985 Instabilities in geophysical dynamics. In *Hydrodynamic Instabilities and the Transition to Turbulence* (2nd edn.) (Ed. by Swinney, H.L. & Gollub, J.P.), **45**, 229-270, Springer.
- [61] Wang, L. & Cheng, K.C. 1995 Flow in curved channels with a low negative rotation speed. *Physical Review E* **51**, No.2.
- [62] Yang, K. & Kim, J. 1991 Numerical investigation of instability and transition in rotating plane Poiseuille flow. *Phys. Fluids* **A3**, 633-641.
- [63] Yih, C.S. & Sanyster, W.M. 1957 Stability of laminar flows in curved channels, *Phil. Mag.* **2**, 305-310.

Chapter 7

Conclusions and Recommendations

Three different approaches are used to study the laminar flow transitions, instabilities, and combined free and forced convective heat transfer problems for fully developed flows in rotating, curved channels with circular and rectangular cross sections.

In particular, a three-parameter regular perturbation method and a finite-volume numerical method are developed to solve the governing equations for the flow and heat transfer in channels with simultaneous curvature, rotation and heating/cooling. The perturbation method is for the circular tubes, and the numerical method for the rectangular channels. In these two parts of the work, we constrain ourselves to the steady, hydrodynamically and thermally fully developed flow under the condition of

uniform wall heat flux with peripherally uniform wall temperature. We also confine ourselves to examine the symmetric flows with respect to the horizontal center plane of the channel by imposing a symmetric condition on the plane in our numerical scheme. The results cover the nature of the flow transition and its effect on the flow resistance and combined free and forced convective heat transfer for both heating and cooling cases under positive or negative rotations.

Using air as the fluid, the flows in channels with curvature and/or rotation are visualized in terms of end-view at the exit of the test sections through injecting smoke into the flows. In this part of the work, we also confine ourselves to the fully developed flows, and focus our attention on the phenomena due to the stabilizing/destabilizing influence of the curvature and/or rotation. Several test sections are used, and the results shown here are some typical ones for the four test sections.

7.1 Perturbation Solutions

A unique, uniformly convergent polynomial is found to be associated with any continuous function of one or more variables. It can be used as the approximation of the function, and can be obtained from the governing partial differential equations of the function.

Assuming that the stream function ϕ of the secondary flow, the main velocity w and the temperature η are continuous on the curvature ratio σ , the rotational Reynolds number Re_{Ω} and the rotational Rayleigh number Ra_{Ω} , a three-parameter

regular perturbation method is developed to obtain an approximate analytical solution for velocity and temperature fields in a rotating curved circular tube

In the method, each of the functions ϕ , w and η is expanded in a triple power series in terms of σ , Re_Ω and Ra_Ω . The coefficients in these expansion series are governed by a set of nonhomogeneous harmonic and biharmonic differential equations. The successive solutions of these equations will produce as many terms as desired for the three series depending upon the accuracy required. In this work, the solution is carried up to and including the second-order terms.

All the first order terms for the series of secondary flow result in a secondary flow of two-cell counter-rotating vortices with the centers of circulation located on the vertical centerline while all the second order terms cause the secondary flow to exhibit a four-cell pattern with the centers of circulation located away from the vertical centerline. As well, the secondary flows resulting from either the first order terms or the second order terms alone are all symmetric with respect to both horizontal and vertical centerlines. The asymmetric effect of the second order terms on the first order terms about the vertical centerline, however, destroys the symmetry with respect to the vertical centerline in the secondary flow from all the first order and second order terms in the series.

The solutions of velocity and temperature are found to be infinite series in powers of the three pairs of parameters with each characterizing the flow and heat transfer in the Dean problem, the Coriolis problem and mixed convection problem, respectively.

The resultant secondary flow due to the simultaneous effect of the curvature, rotation and heating/cooling may be grouped under three broad patterns depending on the values of the two dimensionless parameters L_1 and L_2 . The former represents the ratio of the Coriolis force to the centrifugal force, and the latter donates the ratio of the buoyancy force to the centrifugal force.

The inward Coriolis force and/or buoyancy force can arise in the cross plane when the rotation is negative and/or when the fluid is cooled. They may cause the direction of the secondary flow to reverse by overcoming the outward centrifugal forces. The flow reversal occurs (after passing through a four-cell vortex flow region) either along the wall or from the center part of the cross plane depending on the value of L_2 , i.e. the ratio of buoyancy force over the centrifugal force.

The secondary flow changes the main velocity and temperature profiles and causes the locations of the maximum main velocity and the extreme temperature to move away from the center of the tube in the direction of the secondary velocities in the middle of the tube. This causes a pronounced peripheral variation of friction factor and Nusselt number, and increases the mean friction factor and Nusselt number significantly. However, in the region where the secondary flow appears as a four-cell pattern, the secondary flow is too weak to modify the main velocity and temperature profiles effectively, such that they are essentially axisymmetric and parabolic with extreme value appearing along the horizontal centerline at or very close to the center of the cross section. As well in this region, the friction factor and Nusselt

number are identical or very close to those for constant property forced convection problem in a stationary straight tube.

The profiles of the main velocity and temperature show that the boundary layer theory is not valid for the analysis of the flow and heat transfer in a rotating curved tube for a range of parameters considered in this work.

By setting any one or two of σ , Re_{Ω} and Ra_{Ω} to be zero, the solution reduces to the corresponding six special cases, i.e., Dean problem, Coriolis problem, mixed convection problem, Dean problem with the effect of rotation, Dean problem with the effect of heating/cooling and Coriolis problem with the effect of heating/cooling. As well depending on the region of the governing parameters, the secondary flow with the simultaneous effect of more than one of the curvature, rotation and heating/cooling may be qualitatively similar to or completely different from that with only one factor.

One area of future study is to extend the solution to include the higher order terms by a computer, to identify the location and nature of singularities, and to recast the perturbation solution series. Another is to expand the analysis to contain the effects of unsteadiness and flow development.

A final area of future study is to perform the analysis of the second law of the thermodynamics for the present problem. In particular, the properties of entropy at points of flow transitions are of special interest because they may be used to classify and determine the different bifurcation points and instabilities.

7.2 Numerical Solutions

Numerical scheme developed in this work is capable to examine the laminar flow transitions and heat transfer ranging from a weak rotation limit where the viscous force dominates to a strong rotation limit where the Coriolis force dominates. Several flow patterns, hitherto unknown, are revealed in the present study.

Curvature and rotation, in conjunction with heating/cooling introduce the centrifugal, Coriolis and buoyancy forces in the momentum equations. Such body forces cause similar instabilities (Centrifugal instability, Coriolis instability and buoyancy instability) in the forms of streamwise oriented vortices (Dean-vortices, Coriolis-vortices and buoyancy-vortices), resulting a two-pair vortex flow in a square channel. Although the Dean-vortices always appear along the outer wall, the Coriolis-vortices and buoyancy-vortices can occur either along the outer wall or along the inner wall depending on the directions of rotation and heat flux respectively. The Coriolis-vortices always appear in the high pressure side, along the outer wall when the rotation is positive, but along the inner wall when the rotation is negative. The buoyancy-vortices may appear either in the high pressure side or in the low pressure side depending on the direction and the rate of heat flux. They occur along the outer wall when the fluid is heated, but along the inner wall when the fluid is cooled.

The shape and size of the Dean-vortices, the Coriolis-vortices and the buoyancy-vortices are found to change with the dynamical parameters even in the fully developed flow region. Upon increasing Coriolis or buoyancy force, the disappearance of

the Coriolis-vortices or the buoyancy-vortices is observed. No such phenomenon is seen for the Dean-vortices. Furthermore, the reappearance of the buoyancy-vortices, upon increasing the buoyancy force further, is also found in this study.

For a non-isothermal flow, there is another mechanism responsible for the appearance of an additional pair of vortices, i.e. the merging of the vortices in the region where the centrifugal, Coriolis and buoyancy forces just neutralize each other. The additional pair of vortices formed in this mechanism is called merging-vortices in this work. They may appear in the region near the center of the outer wall or inner wall depending on the direction of rotation.

Between a viscous force dominated one-pair vortex flow and two-pair vortex flow with the presence of the Dean-vortices, Coriolis-vortices or buoyancy-vortices, there exist a one-pair vortex flow with an ageostrophic, virtually inviscid core. Another two kinds of one-pair vortex flow exist after the disappearance of the Coriolis-vortices upon increasing the Coriolis forces further. The axial velocity profile for the first one assumes a Taylor-Proudman configuration in the core region with one maximum located on the horizontal centreline. That for the second one is dumbbell-like with two maxima or bar-convex dumbbell-like with three high velocity regions. The flow in the core region is also geostrophic for the second kind of one-pair vortex flow.

When the rotation is negative and/or when the fluid is cooled, the inward Coriolis force and/or buoyancy force can completely cancel the Dean-vortices and to give rise to vortices on the inner wall. These inward forces can also cause the direction of

the secondary flow to reverse by overcoming the outward forces in the plane of the cross section. The flow reversal occurs by passing through a multi-pair vortex flow region where overall, the centrifugal, the Coriolis and the buoyancy forces just neutralize each other.

The profiles of the main velocity and the temperature are quite similar when the rotation speed is not so high. The similarity will, however, be broken at the rapid rotation rate.

The flow resistance and heat transfer are significantly affected by the flow transitions. In particular, the Dean-vortices, Coriolis-vortices, buoyancy-vortices and merging-vortices substantially change the distributions of the local friction factor and Nusselt number with a remarkable increase in their mean values.

The new vortex flows, revealed in the present study, suggest possible further research concerning their instability since usually, an inflectional profile of the main flow is associated with them. The analysis needs also further extension by removing the limitations of symmetry (with respect to the horizontal centerline), steadiness and fully development. Another area for further study is the properties of entropy associated with the flow transitions.

7.3 Visualization of Flows

The visualizations of stabilizing/destabilizing flows in channels with curvature and/or rotation reveal five stabilizing/destabilizing related phenomena: (1) For large values of $|Ro|$, both primary and secondary instabilities exhibit a symmetry about the directions of rotation. As well, the flows at large $|Ro|$ are found to be controlled by the secondary instabilities rather than the primary instability. In particular, the secondary instabilities lead the flow at large $|Ro|$ to be unsteady and turbulent very like the *bursting* flow in the turbulent boundary layers. This produces the low Reynolds number turbulent flows. (2) When the curved channels rotate with slow negative speed, two potentially unstable regions alternating by two stable regions, exist in the cross-plane, resulting in a complicated vortex flow. (3) The Dean/Coriolis vortices can also exist on the unstable side in the relaminarization process of the flow from turbulent to laminar. In particular, their formation in the flows with high Reynolds number annihilates the turbulence, and leads to a high Reynolds number laminar flow. (4) Secondary instabilities of the Dean/Coriolis vortices lead the vortices to oscillate in various forms even in the streamwise fully developed flow regions. We have observed several oscillating modes including one with mostly radial motion, one with mostly spanwise motion, one with significant simultaneous radial and spanwise motion, and one with rocking motion. In addition, the oscillating modes are also present with the motion so complicated that they are difficult to describe from the flow visualization results. (5) It is possible to completely

destroy the Dean vortices by rotation and to give rise to vortices on the convex wall due to the Coriolis force.

Further work concerning the experimental measurements and stability analyses are required to confirm the results obtained in the present study. The experiments based on the stratified flow - rotating flow analogy and electromagnetic flow - rotating flow analogy may be of special interest because they allow one to investigate the flow and heat transfer under the effect of the centrifugal and Coriolis forces in a stationary analogous system, and to measure the quantities of flow and heat transfer under the isolated centrifugal force or Coriolis force. However, the experiments may be rather difficult to perform.

Appendix A

Two Fundamental Theorems for the Perturbation Method

Theorem 1 Any continuous function $f(x)$ in x in the interval $c^l \leq x \leq c^h$ may be approximated uniformly by polynomials in this interval (Weierstrass's Approximation Theorem¹).

Proof Since we can always find a proper mathematical transformation to map the interval $c^l \leq x \leq c^h$ into an interval in $0 < x < 1$, we assume that the interval $c^l \leq x \leq c^h$ lies in the interior of the interval $0 < x < 1$ without loss of the generality.

¹K.T.W. Weierstrass, über die analytische Darstellbarkeit sogenannter Willkürlicher Funktionen reeller Argumente, Sitzungsber. K. Akad. Wiss. Berlin, 1885, pp.633-639, 789-805; Werke, vol.3, pp.1-37, Berlin, 1903.

Then there exist two numbers β^l and β^h such that

$$0 < \beta^l < c^l < c^h < \beta^h < 1$$

We may assume that the continuity of the function $f(x)$, which is continuous in the interval $c^l \leq x \leq c^h$ by the hypothesis, has been extended to the entire interval $\beta^l \leq x \leq \beta^h$.

Consider the integral

$$I_n = \int_0^1 (1 - y^2)^n dy$$

with n as the positive integers. This converges to zero with increasing n .

Note that

$$\begin{aligned} I_n &= \int_0^1 (1 - y^2)^n dy > \int_0^1 (1 - y)^n dy = \frac{1}{n+1} \\ \hat{I}_n &= \int_\alpha^1 (1 - y^2)^n dy < (1 - \alpha^2)^n (1 - \alpha) < (1 - \alpha^2)^n \\ 0 &\leq \frac{\hat{I}_n}{I_n} < (n+1)(1 - \alpha^2)^n \end{aligned}$$

where α is a fixed number in the interval $0 < \alpha < 1$. Then

$$\lim_{n \rightarrow \infty} \frac{\hat{I}_n}{I_n} = 0$$

which implies that for a sufficiently large n the integral from 0 to α constitute the dominant part of the whole integral from 0 to 1.

By making the substitution

$$v = y + x$$

we have

$$\int_{\beta^l}^{\beta^h} f(v)[1 - (v - x)^2]^n dv = \int_{\beta^l - x}^{\beta^h - x} f(y + x)(1 - y^2)^n dy = A + B + C$$

where

$$\begin{aligned} A &= \int_{\beta^l - x}^{-\alpha} f(y + x)(1 - y^2)^n dy \\ B &= \int_{-\alpha}^{\alpha} f(y + x)(1 - y^2)^n dy \\ C &= \int_{-\alpha}^{\beta^h - x} f(y + x)(1 - y^2)^n dy \end{aligned}$$

and α is a positive number in the interval $0 < \alpha < 1$.

Let M be the maximum of $|f(x)|$ for $\beta^l \leq x \leq \beta^h$, then

$$\begin{aligned} |A| &< M \int_{-1}^{-\alpha} (1 - y^2)^n dy = M \hat{I}_n \\ |C| &< M \int_{\alpha}^1 (1 - y^2)^n dy = M \hat{I}_n \end{aligned}$$

Now rewriting B as

$$\begin{aligned} B &= f(x) \int_{-\alpha}^{\alpha} (1 - y^2)^n dy + \int_{-\alpha}^{\alpha} [f(y + x) - f(x)](1 - y^2)^n dy \\ &= 2f(x)(I_n - \hat{I}_n) + D \end{aligned}$$

where

$$D = \int_{-\alpha}^{\alpha} [f(y + x) - f(x)](1 - y^2)^n dy$$

Note that the function $f(x)$ is continuous in the interval $\beta^l \leq x \leq \beta^h$, then for arbitrary small $\delta > 0$, we can find an $\alpha = \alpha(\delta)$ in the interval $0 < \alpha < 1$, depending only on δ , such that, for $|y| \leq \alpha$ and $\beta^l \leq x \leq \beta^h$,

$$|f(y + x) - f(x)| \leq \delta$$

And we have

$$|D| \leq \delta \int_{-\alpha}^{\alpha} (1 - y^2)^n dy < \delta \int_{-1}^1 (1 - y^2)^n dy = 2\delta I_n$$

Then

$$\begin{aligned} & \left| \int_{\beta^l}^{\beta^h} f(v)[1 - (v - x)^2]^n dv \right| = |A + B + C| \leq |A| + |B| + |C| \\ & < 2M\hat{I}_n + 2\delta I_n + 2|f(x)|(I_n - \hat{I}_n) < 2M\hat{I}_n + 2\delta I_n + 2|f(x)|I_n \end{aligned}$$

Consider the polynomials $P_n(x)$ in x

$$P_n(x) = \frac{\int_{\beta^l}^{\beta^h} f(y)[1 - (y - x)^2]^n dy}{\int_{-1}^1 (1 - y^2)^n dy}$$

then

$$|P_n(x) - f(x)| < M \frac{\hat{I}_n}{I_n} + \delta$$

Since

$$\lim_{n \rightarrow \infty} \frac{\hat{I}_n}{I_n} = 0$$

the term $|P_n(x) - f(x)|$ may be made arbitrarily small for any $x \in [c^l, c^h]$ by a suitable choice of n . This means that $f(x)$ is indeed approximated by $F_n(x)$ uniformly in the interval $c^l \leq x \leq c^h$.

In exactly the same way we may show that a function f of m variables x_1, x_2, \dots, x_m , which is continuous for $c_k^l \leq x_k \leq c_k^h$ ($k = 1, 2, \dots, m$), may be approximated uniformly by the polynomials

$$P_n(x_1, \dots, x_m) = \frac{\int_{\beta_1^l}^{\beta_1^h} \dots \int_{\beta_m^l}^{\beta_m^h} f(y_1, \dots, y_m)[1 - (y_1 - x_1)^2]^n \dots [1 - (y_m - x_m)^2]^n dy_1 \dots dy_m}{[\int_{-1}^1 (1 - y^2)^n dy]^m}$$

where β_k^l and β_k^h satisfy

$$0 < \beta_k^l < c_k^l < c_k^h < \beta_k^h < 1$$

Theorem 2 The representation of a function $f(x)$ by a power series is unique in an interval which contains the point $x = 0$.

Proof Suppose that two power series

$$P_1 = \sum_{k=0}^{\infty} f_{1k} x^k$$

$$P_2 = \sum_{k=0}^{\infty} f_{2k} x^k$$

both converge uniformly to the same function $f(x)$ in an interval which contains the point $x = 0$ in its interior. The power series $\sum_{k=0}^{\infty} g_k x^k$ with coefficients

$$g_k = f_{1k} - f_{2k}$$

then converges to the function

$$g(x) = f(x) - f(x) = 0$$

for any x in the interval. The power series, formed by taking n -th derivative of the series $\sum_{k=0}^{\infty} g_k x^k$, are

$$\sum_{k=n}^{\infty} k(k-1)\cdots(k-n+1)g_k x^{k-n} \quad (n = 1, 2, \dots)$$

which converge uniformly to $g^{(n)}(x)$, i.e., zero throughout the interval. Then we have

$$0 = \sum_{k=0}^{\infty} g_k x^k$$

$$0 = \sum_{k=n}^{\infty} k(k-1)\cdots(k-n+1)g_k x^{k-n} \quad (n = 1, 2, \dots)$$

for any x in the interval. For $x = 0$, in particular, the series must be zero. This gives

$$g_k = 0 \quad (k = 0, 1, \dots)$$

so that

$$f_{1k} = f_{2k} \quad (k = 0, 1, \dots)$$

i.e., P_1 and P_2 are identical as stated by the theorem.